

## Pellet-plasma interaction in a tokamak

**Citation for published version (APA):**

Kloe, de, J. (2000). *Pellet-plasma interaction in a tokamak*. [Phd Thesis 1 (Research TU/e / Graduation TU/e), Applied Physics and Science Education]. Technische Universiteit Eindhoven. <https://doi.org/10.6100/IR534799>

**DOI:**

[10.6100/IR534799](https://doi.org/10.6100/IR534799)

**Document status and date:**

Published: 01/01/2000

**Document Version:**

Publisher's PDF, also known as Version of Record (includes final page, issue and volume numbers)

**Please check the document version of this publication:**

- A submitted manuscript is the version of the article upon submission and before peer-review. There can be important differences between the submitted version and the official published version of record. People interested in the research are advised to contact the author for the final version of the publication, or visit the DOI to the publisher's website.
- The final author version and the galley proof are versions of the publication after peer review.
- The final published version features the final layout of the paper including the volume, issue and page numbers.

[Link to publication](#)

**General rights**

Copyright and moral rights for the publications made accessible in the public portal are retained by the authors and/or other copyright owners and it is a condition of accessing publications that users recognise and abide by the legal requirements associated with these rights.

- Users may download and print one copy of any publication from the public portal for the purpose of private study or research.
- You may not further distribute the material or use it for any profit-making activity or commercial gain
- You may freely distribute the URL identifying the publication in the public portal.

If the publication is distributed under the terms of Article 25fa of the Dutch Copyright Act, indicated by the "Taverne" license above, please follow below link for the End User Agreement:

[www.tue.nl/taverne](http://www.tue.nl/taverne)

**Take down policy**

If you believe that this document breaches copyright please contact us at:

[openaccess@tue.nl](mailto:openaccess@tue.nl)

providing details and we will investigate your claim.

# Pellet-plasma interaction in a tokamak

Joost de Kloe

Pellet-plasma interaction in a tokamak

Joost de Kloet

2000

Pellet-plasma interaction in a tokamak

PROEFSCHRIFT

ter verkrijging van de graad van doctor aan de  
Technische Universiteit Eindhoven, op gezag van de  
Rector Magnificus, prof.dr. M. Rem, voor een  
commissie aangewezen door het College voor  
Promoties in het openbaar te verdedigen  
op dinsdag 23 mei 2000 om 16.00 uur

door

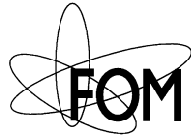
Joost de Kloe

geboren te Gameren (gemeente Zaltbommel)

Dit proefschrift is goedgekeurd door de promotoren:

prof.dr. N.J. Lopes Cardozo  
en  
prof.dr. D.C. Schram

Copromotor: dr. A.A.M. Oomens



The work described in this dissertation is a part of a research program of the “Stichting voor Fundamenteel Onderzoek der Materie” (FOM) with financial support from the “Nederlandse Organisatie voor Wetenschappelijk Onderzoek” (NWO) and EUR-ATOM. The work was carried out at the “FOM-instituut voor Plasmafysica” in Nieuwegein in The Netherlands.

*Aan Mariska*

# Samenvatting

Een van de mogelijke bijdragen om ons toekomstige energiegebruik veilig te stellen is het opwekken van beheerste kernfusie van waterstofisotopen. Een mogelijke opstelling waarin dit bereikt kan worden is de zogenaamde “tokamak”. Deze is gebaseerd op de magnetische opsluiting van de zeer hete deeltjes (het plasma) die bij dit proces gebruikt worden.

Dit proefschrift is een studie naar de invloed op het plasma van het injecteren van verse brandstof in zo een machine. Dit injecteren gebeurt door “pellets” (kleine klontjes of pilletjes vast waterstof) met hoge snelheid het plasma in te schieten. In het bijzonder wordt gekeken naar de menging van het geïnjecteerde materiaal met het achtergrond plasma, en de invloed die dit heeft op de opsluiting van de deeltjes in het magneetveld.

Op het moment dat ik aan deze studie begon werd getwijfeld aan de praktische mogelijkheid van brandstof injectie met pellets in een fusiereactor. Dit omdat het extra verhitten van het plasma, iets dat nodig is om kernfusie te kunnen bereiken, er tevens voor zorgde dat het geïnjecteerde materiaal voor een groot deel weer het plasma uitvloog op een onbegrepen manier.

Na de ontdekking op de Duitse tokamak ASDEX-Upgrade dat deze verslechterde opname van geïnjecteerd materiaal niet optreedt wanneer het pellet met de gradient van het magneetveld mee wordt geschoten, is in deze studie het experimentele bewijs gevonden voor het mechanisme dat hiervoor verantwoordelijk is. Het bleek dat “wolkjes” verdampt materiaal afkomstig van het pellet zich met grote snelheid naar gebieden met lager magneetveld verplaatsen, en dat dit effect groter wordt bij toenemende temperatuur (hoofdstuk 4). Het is nu dus mogelijk het punt van injectie zo te kiezen dat deze “wolkjes” zich naar het plasma centrum toebewegen, in plaats van naar de rand van het plasma en eruit. Door deze observaties lijkt het probleem van brandstof injectie in een fusiereactor nu opgelost te zijn.

Een volgend onderwerp dat bestudeerd is, is de mate van opsluiting van de deeltjes in het magneetveld. Het blijkt dat in bepaalde omstandigheden een ingeschoten pellet kan worden gebruikt om plaatselijk deze opsluiting enorm te verbeteren. Dit gebeurt dan vooral op de grens van het wel en niet door het pellet bijgevoerde plasma (hoofdstuk 5).

Tot slot is gekeken naar de invloed van rotatie van het plasma op het pellet en vice versa. Door de toevoeging van massa wordt het plasma duidelijk afgeremd,

maar ook blijkt het in een richting loodrecht op de oorspronkelijke rotatierichting te gaan roteren. Deze rotaties verklaren waarom het geïnjecteerde materiaal zo snel vermengd raakt met het al aanwezige plasma (hoofdstuk 6).

Al deze gevonden inzichten kunnen worden gebruikt om dit proces van brandstof injectie beter te kunnen voorspellen voor een nog te bouwen fusiereactor.



# Summary

One of the possible contributions to secure our future supply of energy is the generation of controlled nuclear fusion of hydrogen isotopes. A possible machine in which this can be achieved is a device called “tokamak”. It is based on magnetic confinement of these very hot particles (the plasma) that are used in this process.

This thesis is a study of the influence on the plasma of the injection of fresh fuel in such a device. This is done by injecting small pellets of hydrogen ice with high velocity in the plasma. Special attention is given to the mixing of the injected matter with the background plasma, and the influence that this injection has on the confinement of the particles in the magnetic field.

Before I started this study it was doubted whether this fuel injection by pellets would be feasible in a fusion device, or not. This doubt existed because the heating of the plasma, something necessary to achieve nuclear fusion in the first place, also causes a large loss of the injected material in an un understood way.

After the discovery on the German tokamak ASDEX-Upgrade that this particle loss does not occur when the pellet is injected along the gradient of the magnetic field, in this study the experimental evidence was found that causes this behaviour. It was found that “clouds” of ablated material originating from the pellet move with high velocity to regions with lower magnetic field, and that this effect increases with increasing temperature (chapter 4). Knowing this, it is possible to choose the point of injection of the pellet, in such a way that these “clouds” move towards the plasma center, and not to the plasma edge and out of the plasma. After these observations the problem of fueling a fusion reactor seems to be solved.

A next subject that was studied, is the confinement of the plasma particles in the magnetic field. It was found that in certain conditions an injected pellet can be used to dramatically improve the confinement locally. This happens especially on the boundary of the fueled part of the plasma, and the not by the pellet perturbed center of the plasma (chapter 5).

Finally the influence of the rotation of the plasma on the pellet, and of the pellet on the plasma rotation, was studied. A clear slowing down occurs due to the insertion of a large quantity of mass, but in the same time in a direction perpendicular to the original plasma rotation, a rotation is induced. These rotations explain why the injected material mixes as fast with the background plasma as we observe (chapter 6).

The results obtained in this thesis may be used to better predict the process of

fuel injection in a fusion reactor.

# Contents

|   |            |
|---|------------|
| <b>Frontpage</b>  | <b>i</b>   |
| <b>Samenvatting</b>                                       | <b>v</b>   |
| <b>Summary</b>  | <b>vii</b> |
| <b>Contents</b>   | <b>ix</b>  |
| <b>1 Introduction</b>                                     | <b>1</b>   |
| 1.1 Introduction . . . . .                                | 1          |
| 1.2 Why pellet injection ? . . . . .                      | 1          |
| 1.3 The energy problem . . . . .                          | 2          |
| 1.3.1 Energy . . . . .                                    | 2          |
| 1.3.2 Nuclear fusion . . . . .                            | 2          |
| 1.3.3 Fueling a plasma . . . . .                          | 3          |
| 1.4 Objective of this thesis . . . . .                    | 4          |
| 1.5 This thesis . . . . .                                 | 5          |
| 1.5.1 Outline of this thesis . . . . .                    | 5          |
| 1.5.2 Publications related to this thesis . . . . .       | 5          |
| <b>1A Plasmas and pellets</b>                             | <b>8</b>   |
| 1A.1 Plasmas . . . . .                                    | 8          |
| 1A.1.1 Definition of a plasma . . . . .                   | 8          |
| 1A.1.2 Creating and confining a plasma . . . . .          | 8          |
| 1A.1.3 Plasma devices . . . . .                           | 9          |
| 1A.1.4 Heating a plasma . . . . .                         | 10         |
| 1A.1.5 Why don't we have a fusion reactor yet ? . . . . . | 11         |
| 1A.1.6 Present status of fusion plasma devices . . . . .  | 11         |
| 1A.2 Pellets . . . . .                                    | 11         |
| 1A.2.1 What is a pellet ? . . . . .                       | 11         |
| 1A.2.2 Short history of pellet injection . . . . .        | 11         |

|          |  |           |
|----------|--|-----------|
| <b>2</b> | <b>Instrumentation</b>   | <b>14</b> |
| 2.1      | The RTP tokamak . . . . .  | 14        |
| 2.1.1    | RTP, history and future . . . . .                                    | 14        |
| 2.1.2    | RTP, parameters . . . . .  | 14        |
| 2.1.3    | Coordinate system used . . . . .                                     | 15        |
| 2.1.4    | Additional heating . . . . .   | 16        |
| 2.1.5    | Fueling systems . . . . .  | 16        |
| 2.2      | The pellet injector at RTP . . . . .                                 | 16        |
| 2.3      | Diagnosing the plasma and the pellet . . . . .                       | 18        |
| 2.3.1    | Pellet diagnostics . . . . .   | 18        |
| 2.3.2    | Triggering the Thomson scattering diagnostic by the pellet . . . . . | 19        |
| 2.3.3    | Diagnosing the pellet during the ablation . . . . .                  | 21        |
| 2.3.4    | Plasma diagnostics at RTP . . . . .                                  | 25        |
| 2.3.5    | Location of the diagnostics . . . . .                                | 30        |
| 2.4      | Time and length scales for RTP . . . . .                             | 30        |
| <b>3</b> | <b>Status of pellet physics</b>                                      | <b>33</b> |
| 3.1      | Introduction . . . . .   | 33        |
| 3.2      | The ablation itself . . . . .  | 34        |
| 3.3      | Behaviour and movement of the ablatant . . . . .                     | 37        |
| 3.3.1    | Parallel ablatant expansion . . . . .                                | 38        |
| 3.3.2    | Cloud movement . . . . .   | 39        |
| 3.4      | Changes in the pellet movement . . . . .                             | 40        |
| 3.5      | Plasma response to the pellet . . . . .                              | 40        |
| 3.6      | Using the pellet as a plasma diagnostic . . . . .                    | 43        |
| 3.6.1    | Diagnosing the magnetic field . . . . .                              | 43        |
| 3.6.2    | Diagnosing temperature profiles . . . . .                            | 43        |
| 3.6.3    | Diagnosing fast particles . . . . .                                  | 44        |
| 3.6.4    | Diagnosing fluctuations in E or B . . . . .                          | 44        |
| 3.6.5    | Diagnosing $Z_{\text{eff}}$ . . . . .                                | 44        |
| 3.6.6    | Diagnosing (impurity) transport . . . . .                            | 45        |
| <b>4</b> | <b>Diagnosing pellet penetration</b>                                 | <b>46</b> |
| 4.1      | Introduction . . . . .   | 46        |
| 4.2      | Structure of this Chapter . . . . .                                  | 49        |
| 4.3      | The fiber array diagnostic . . . . .                                 | 49        |
| 4.3.1    | Some history of the fiber-array diagnostic at RTP . . . . .          | 49        |
| 4.3.2    | Examples of data taken by the new diagnostic . . . . .               | 50        |
| 4.3.3    | Pellet velocity measured by the fiber array . . . . .                | 57        |
| 4.3.4    | Ablation cloud size . . . . .  | 59        |
| 4.3.5    | Toroidal movement of the ablation cloud . . . . .                    | 60        |
| 4.3.6    | Radial movement of the ablation cloud . . . . .                      | 60        |
| 4.3.7    | Size of the drifting cloud . . . . .                                 | 61        |
| 4.3.8    | Penetration depth measured by the fiber array . . . . .              | 62        |

|          |  |           |
|----------|--|-----------|
| 4.4      | Connection between fueling and drift effects . . . . .                                     | 63        |
| 4.5      | Radial inward drifts . . . . .   | 64        |
| 4.6      | Striations . . . . .   | 67        |
| 4.7      | Summary . . . . .  | 69        |
| 4.8      | Conclusion . . . . .   | 71        |
| 4.9      | Fast backward drift of pellet ablatant in tokamak plasmas . . . . .                        | 72        |
| <b>5</b> | <b>Radial particle transport</b>   | <b>77</b> |
| 5.1      | Introduction . . . . .   | 77        |
| 5.2      | The transport equations . . . . .  | 78        |
| 5.3      | Strategy for extracting D and $v_{pinch}$ . . . . .  | 80        |
| 5.3.1    | Density scale length . . . . .   | 81        |
| 5.3.2    | Sawtooth density pulse . . . . .   | 81        |
| 5.4      | Modeling of particle transport . . . . .   | 82        |
| 5.4.1    | Implementation of the numerical model . . . . .  | 82        |
| 5.4.2    | The initial conditions . . . . .   | 83        |
| 5.4.3    | The boundary conditions . . . . .  | 83        |
| 5.4.4    | The particle source function . . . . .   | 83        |
| 5.4.5    | The pellet source function . . . . .   | 84        |
| 5.4.6    | The pellet source function on shorter time scales . . . . .                                | 84        |
| 5.4.7    | Measuring the flux surface averaged density . . . . .                                      | 85        |
| 5.4.8    | Expectations . . . . .   | 86        |
| 5.5      | Density evolution without pellet (step A) . . . . .  | 87        |
| 5.5.1    | Choosing D and $v_{pinch}$ profiles . . . . .  | 87        |
| 5.5.2    | Estimation of the internal particle source . . . . .                                       | 88        |
| 5.5.3    | Modulated gas puff . . . . .   | 88        |
| 5.5.4    | Summary . . . . .  | 90        |
| 5.6      | Short time scale simulation (step B) . . . . .   | 93        |
| 5.6.1    | Validation of assumptions . . . . .  | 94        |
| 5.6.2    | On-axis pellet in Ohmic plasma (case a) . . . . .  | 95        |
| 5.6.3    | Off-axis pellet in Ohmic plasma (case b) . . . . .   | 98        |
| 5.6.4    | On-axis pellet in slide-away plasma (case c) . . . . .                                     | 99        |
| 5.6.5    | Summary of all simulated cases . . . . .   | 102       |
| 5.6.6    | Interpretation of the difference in D with on-axis and off-axis pellet injection . . . . . | 102       |
| 5.7      | Long time scale simulation (Step C) . . . . .  | 104       |
| 5.7.1    | Stationary D profile . . . . .   | 104       |
| 5.7.2    | Time dependent D . . . . .   | 105       |
| 5.8      | Conclusion and discussion . . . . .  | 108       |

---

|          |  |              |
|----------|--|--------------|
| <b>6</b> | <b>Transport on a flux surface</b>                   | <b>113</b>   |
| 6.1      | Introduction . . . . .                               | 113          |
| 6.2      | Mixing on a flux surface: experiment . . . . .       | 113          |
| 6.3      | Mixing on a flux surface: a challenge . . . . .      | 115          |
| 6.4      | Cross-field transport: experiment . . . . .          | 117          |
| 6.5      | Cross-field transport: summary . . . . .             | 123          |
| 6.6      | Plasma rotation theory . . . . .                     | 124          |
| 6.6.1    | Stationary rotation . . . . .                        | 124          |
| 6.6.2    | Pellet induced rotation change . . . . .             | 126          |
| 6.7      | Ion rotation measurements . . . . .                  | 128          |
| 6.7.1    | Movement on photographs . . . . .                    | 129          |
| 6.7.2    | Spectroscopic measurements . . . . .                 | 130          |
| 6.8      | Summary and conclusion . . . . .                     | 132          |
| <b>7</b> | <b>Other pellet related research at RTP</b>          | <b>134</b>   |
| 7.1      | Introduction . . . . .                               | 134          |
| 7.2      | Cold pulse experiments . . . . .                     | 134          |
| 7.2.1    | Description of the experiments . . . . .             | 134          |
| 7.2.2    | Observations . . . . .                               | 135          |
| 7.2.3    | Interpretation . . . . .                             | 137          |
| 7.2.4    | Extremely fast temperature rise . . . . .            | 137          |
| 7.3      | Limited energy reservoir . . . . .                   | 138          |
| 7.3.1    | Description of the experiment . . . . .              | 138          |
| 7.3.2    | Interpretation . . . . .                             | 139          |
| 7.4      | Ablation pattern in off-axis heated plasma . . . . . | 139          |
| 7.4.1    | Description of the experiment . . . . .              | 140          |
| 7.4.2    | Interpretation . . . . .                             | 141          |
| <b>8</b> | <b>Discussion and future work</b>                    | <b>144</b>   |
| 8.1      | Conclusions . . . . .                                | 144          |
| 8.2      | Answers to the posed questions . . . . .             | 145          |
| 8.3      | Future work . . . . .                                | 147          |
|          | <b>References</b>                                    | <b>148</b>   |
|          | <b>Appendix A:Implementation of the model</b>        | <b>A i</b>   |
|          | <b>Dankwoord</b>                                     | <b>A vi</b>  |
|          | <b>Curriculum Vitae</b>                              | <b>A vii</b> |

*Aan Mariska*

# Chapter 1

## Introduction

### 1.1 Introduction

The subject of this thesis is the interaction of a cold, solid state pellet with a high temperature plasma. The strange combination of a solid with an extremely low temperature (only 8 K above the absolute zero) and a thermonuclear plasma with its incredible high temperatures ( $10^7$  to  $10^8$  K) causes a behaviour that is often counter-intuitive.

A drop of water on a very hot plate of metal, a situation more familiar to most of us, might be a useful analogy to envisage what is happening in this situation<sup>1</sup>.

Due to the massive heat source at a temperature well above the boiling point the water is evaporating very fast and forms a protective layer in between the drop and the metal [115]. This reduces the heat flow dramatically, increasing the lifetime of the drop significantly. The flowing gas also influences the movement of the drop. It decreases the friction allowing it to move very easily. Furthermore asymmetries in the water vapour gas flow (due to irregularities of the surface) can impose a small force on the drop, which can then start moving on the surface of the metal. Most of these effects, and many more, also occur during pellet ablation in a plasma.

The process of pellet ablation is also similar to various phenomena in space plasmas, where large particle sources are present in magnetic fields. For example Io, the volcanically active moon of Jupiter, expels large amounts of gas into space, where they are partially ionized and start moving along Jupiters magnetic field lines.

### 1.2 Why pellet injection ?

The first question to be answered is, of course, why one would do such a strange experiment, combining extreme cold and extreme heat. Pellets are injected into

---

<sup>1</sup>This is known as “Leidenfrost’s phenomena” [27, 44].



plasmas for a number of reasons, but the most important one is that it is the leading candidate to fuel a fusion reactor.

Furthermore pellet injection perturbs the density and temperature profiles. This can be used to study the resulting transport of particles and heat, or to bring the plasma into a different (preferentially better) state of energy confinement.

To achieve good fueling in a fusion reactor accurate predictions of the ablation process and the related particle transport are needed. This can only be done if accurate models are available to describe the ablation process. Therefore the main aim of this thesis is to contribute to the improvement of models that describe the ablation process, and the particle transport related to it.

This leaves the question why one would like to build a fusion reactor, or why one wants to produce a plasma that needs refueling and a good energy confinement. To answer this question a few words have to be said on the general problem of the use of energy in our society.

## 1.3 The energy problem

### 1.3.1 Energy

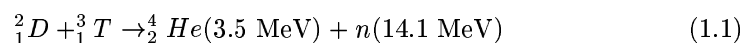
Our present way of life in the western world depends heavily on the availability of (a lot of) energy. It is used for transportation, heating, cooking, entertaining, producing goods, producing food, etc. Energy production depends mainly on burning fossil fuels like oil and coal, from which the heat is used directly, or converted to electricity. It is clear that this energy source will not last forever. Although a precise estimate of the available resources is difficult probably our children or grandchildren will have to face the depletion of this power source. (Oil and gas within the next 50 years, coal within the next 300 years [146]). Also it might be desirable to stop using this energy source in the near future because of the possible influence of the waste (carbon-dioxide) on our climate.

None of the alternative power sources are fit at this time to provide a complete replacement for those fossil fuels. That is why we should try and explore all possible options for new energy sources. One of these options is controlled nuclear fusion.

### 1.3.2 Nuclear fusion

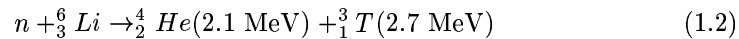
Nuclear fusion is the energy source of our sun and all other stars. By fusing two nuclei of light atoms a large amount of nuclear energy can be released.

The fusion reaction which is easiest to obtain, and which will be used in the first fusion devices, is the one using Deuterium (D) and Tritium (T) [16]:



A big advantage of this kind of energy is the availability of its fuel on earth, enough for many tens of thousands of years [146]. The two essential components

of the fuel are deuterium, which is abundantly present in ordinary (sea)water, and tritium, which can be produced from lithium by the following reaction [16]:



The neutrons produced in the fusion reaction 1.1 can be used for this process.

A second big advantage is that when the proper ingredients are chosen, the waste will be helium, which is totally harmless. A drawback is the activation of the reactor, which produces some radioactive waste. This can be minimized, however, by using the proper materials.

Major difficulties arise in achieving fusion in a controlled and efficient way. This is caused by the repulsive Coulomb force that acts on atomic nuclei when they come close to each other. A potential of 150 keV first has to be overcome before at very short distances the nuclei start to attract each other [102].

Already some decades ago uncontrolled nuclear fusion has been achieved in the hydrogen bomb. In this way the produced energy cannot be used in a controllable but only in a destructive way.

Controlled fusion can be obtained by accelerating beams of ions and letting them collide at sufficiently high velocities, to overcome the repulsive force. This has already been done in the 1930's [103], but this is not at all energy efficient: the chances that a fusion reaction takes place are far too low compared to the number of accelerated particles that slow down by collisions without fusing.

Two options are investigated for achieving nuclear fusion on a sufficiently small scale for controlled energy production: magnetically and inertially confined fusion. Both require the production of a very hot and dense gas, hot enough for the particles to have sufficiently high thermal velocities to overcome the repulsive force between the nuclei, and dense enough to have a sufficient amount of fusion reactions to make the process energy efficient. Automatically this brings up the next difficulty, which is that at the required temperatures all matter is in the plasma state.

Once the fusion reaction is obtained in a controlled way this leads automatically to the subject of this thesis, which is refueling of the burning plasma, especially by pellet injection, and all processes connected to the injection of these pellets in the plasma.

### 1.3.3 Fueling a plasma

At the startup of the plasma the density is mainly produced by ionisation of the gas that has been put in the tokamak before the start of the discharge; the pre-filling.

Inserting fuel or density in a plasma is first of all necessary to reach a sufficiently high density in the plasma to obtain efficient fusion. Also a burning fusion plasma consumes deuterium and tritium and produces helium. This introduces the need for inserting fresh fuel. Several ways of fueling have been applied up to now.

The first and easiest way to implement is just gas puffing at the edge of the plasma. After ionisation the gas spreads through the plasma due to diffusion, con-

vection and charge exchange processes in the plasma. After some time it can reach the center where it can replace the burned up fuel. However, the fueling efficiency of this method is poor, especially for tokamaks using a divertor (varying between 1 and 20 %) [42]. For a fusion reactor this method is not capable of reaching a sufficient central density.

Also the injection of neutral atoms, so called Neutral Beam Injection (NBI), can be applied. Besides heating of the plasma this also fuels the plasma. However, for reactor size plasmas the particles have to be accelerated to very high energies and currents (1 MeV, 40 A) which requires very big and difficult machines [97].

Then of course there is pellet injection, which is the main subject of this thesis. Fueling by means of pellet injection has been proven possible in most present day experiments. However, it is still a question whether this will be possible on an ITER like plasma, because the penetration in the plasma might not be sufficient. The investigation of this penetration, fueling and related processes will be the subject of this thesis.

## 1.4 Objective of this thesis

This thesis contains a study of particle transport in the surrounding plasma related to pellet injection, of movements of the ablation cloud around the pellet, and the diagnostic development required to perform this study. Open questions concerning this particle transport are:

- What is the magnitude of particle transport during pellet injection and how large are the convective and diffusive parts? Which one is dominant? Is there a difference with the unperturbed plasma?
- What influence do both transport components have on important parameters like the fueling profile and efficiency, and the diagnosis of these parameters? Can the results be used to improve the injection scenario for a fusion power plant?
- What is the influence of plasma rotation on the ablation process and its observation, and how does the pellet change the rotation? Can pellet injection be used to manipulate plasma rotation?
- What is the effect of the induced asymmetries in the plasma by the pellet, especially on diagnosing the ablation process?
- Is there a relation between the transport properties of the plasma during pellet injection and the magnetic configuration of the plasma, and how can this be diagnosed?

To find the answers on these questions, measurements of the plasma density profile and its time evolution are needed. The key diagnostics for that are Thomson

scattering and interferometry. Furthermore, the light emission from the neutral gas released by the pellet into the plasma can be used to answer some of these questions. To obtain good spatially and temporally resolved data, which is needed to observe convective transport, a new diagnostic was developed and built. Additional density information was also obtained from ECE-diagnostics from the cut-off phenomenon (these diagnostics are explained in more detail in Chapter 2). The layout of this thesis is described below in Sec. 1.5.

## 1.5 This thesis

### 1.5.1 Outline of this thesis

After this introductory first Chapter, Chapter 2 will describe the hardware used. In Chapter 3 a short review of the present status of the physics of pellet injection in tokamak plasmas will be given. Then the problem of determining the important parameter of penetration will be addressed in Chapter 4. In this Chapter also the related phenomenon of drifting of the ablation cloud and its implications are discussed. In Chapter 5 a study on radial particle transport will be discussed. Chapter 6 will focus on non radial transport effects, especially plasma rotation, that have been observed or have to be assumed to explain observations. Then in Chapter 7 several unrelated subjects will be described.

Finally, in Chapter 8 the results of the previous Chapters will be discussed and a possible continuation of this research and the probable use of pellets in a future fusion device will be discussed.

### 1.5.2 Publications related to this thesis

The work on pellet injection has yielded many results. In this thesis only the work on particle transport is discussed extensively. Below a complete list of publications -in which pellet injection at RTP was involved- is given. The publications marked with a ♣ are included in Chapter 4. The publications marked with a ♠ are included in Chapter 5. The publications marked with a ☺ are included in Chapter 6. The publications marked with a ◇ are included in Chapter 7.

Scientific Journals:

- ♣ “Fast Backward Drift of Pellet Ablatant in Tokamak Plasmas”, **J. de Kloe**, E. Noordermeer, N. J. Lopes Cardozo and A. A. M. Oomens, Phys. Rev. Lett. 82 (13), 1998, p.2685-2688 [60].
- “An International Pellet Ablation Database”, **L. R. Baylor**, A. Geraud, W. A. Houlberg, D. Frigione, M. Gadeberg, T. C. Jernigan, J. de Kloe, P. Kupschus, B. V. Kuteev, P. Lang, A. A. M. Oomens, A. L. Qualls, K. N. Sato, G. L. Schmidt, Nuclear Fusion, Vol. 37, No. 4 (1997), p. 445-450 [4].

- ◇ “Nonlocal transient transport and thermal barriers in Rijnhuizen Tokamak Project plasmas”, **P. Mantica**, P. Galli, G. Gorini, G. M. D. Hogeweij, J. de Kloe, N. J. Lopes Cardozo, and RTP Team, Phys. Rev. Lett., Vol. 82, nr. 25 (1999) p. 5048-5051 [76].
- ◇ “Non-local response of RTP Ohmic plasmas to peripheral perturbations”, **P. Galli**, G. Gorini, P. Mantica, G. M. D. Hogeweij, J. de Kloe, N. J. Lopes Cardozo, RTP Team, Nucl. Fusion, Vol. 39, No. 10 (1999), p. 1355-1368 [32].

## Conference proceedings:

- “Non-adiabatic Pellet Ablation on the RTP Tokamak”, **A. A. M. Oomens**, D. F. da Cruz, C. C. Chu, G. M. D. Hogeweij, J. de Kloe, J. Lok, N. J. Lopes Cardozo, F. J. Pijper, F. C. Schüller and the RTP Team, Proc. EPS Conf. Bournemouth 1995, p. I-129 - I-132 [105].
- ☺ “Pellet disturbed plasmas in the RTP Tokamak”, **J. de Kloe**, J. Lok, M. N. A. Beurskens, J. F. M. van Gelder, B. de Groot, G. M. D. Hogeweij, A. A. M. Oomens and the RTP Team, Proc. 23rd EPS Conf. Kiev 1996, Vol 20C, p. 368-371 [56].
- “Current density profile evolution measured with the triple laser polarimeter at RTP”, **F. A. Karelse**, J. H. Rommers, A. J. H. Donné, G. M. D. Hogeweij, J. Howard, Th. Oyevaar, F. C. Schüller and the RTP-team, Proc. 23rd EPS Conf. Kiev 1996, Vol. 20C, p. 1156-1159 [53].
- “Evidence for fast radial transport during pellet ablation in the RTP Tokamak as measured by Thomson Scattering”, **J. de Kloe**, M. N. A. Beurskens, G. M. D. Hogeweij, J. Lok, N. J. Lopes Cardozo, A. A. M. Oomens and the RTP Team, Proc. 24th EPS Conf. Berchtesgaden 1997, Vol. 21A, p. 593-596 [57].
- ◇ “Non-local plasma response induced by peripheral perturbations in the RTP tokamak”, **P. Mantica**, M. R. de Baar, J. de Kloe, F. De Luca, P. Galli, G. Gorini, , G. M. D. Hogeweij, A. Jacchia, N. J. Lopes Cardozo, A. A. M. Oomens and the RTP Team, Proc. 24th EPS Conf. Berchtesgaden 1997, Vol. 21A, p. 1853-1856 [74].
- ♠ “Radial particle transport during pellet injection in RTP”, **J. de Kloe**, M. M. A. Beurskens, G. M. D. Hogeweij, J. Lok, N. J. Lopes Cardozo, E. Noordermeer, A. A. M. Oomens and the RTP Team, Proc. 25th EPS Conf. Prague 1998, Vol. 22C, p. 734-737 [58].
- ◇ “Non-local electron heat transport effects probed by modulated ECH in the RTP Tokamak”, P. Galli, P. Mantica, **G. M. D. Hogeweij**, J. de Kloe, G. Gorini, N. J. Lopes Cardozo and the RTP-team, Proc. 25th EPS Conf. Prague 1998, Vol. 22C, p. 738-741 [31].

- ♣ “Investigating particle transport during pellet injection in RTP”, **J. de Kloe**, G. M. D. Hogeweyj, N. J. Lopes Cardozo, A. A. M. Oomens and the RTP team, Proc. 26th EPS Conf. Maastricht 1999, Vol. 23J (1999), p.637-640 [59].
- ☺ “The effect of off-axis pellet injection on plasma rotation”, **F. Meijer**, J. de Kloe, R. M. Gravestijn, D. Badoux and the RTP team, Proc. 26th EPS Conf. Maastricht 1999, Vol. 23J, p.633-636 [79].
- ◇ “Cold Pulse Experiments in RTP Ohmic and Electron Cyclotron Heated Plasmas”, **P. Mantica**, G. Gorini, G. M. D. Hogeweyj, J. de Kloe, N. J. Lopes Cardozo and the RTP team, Proc. 26th EPS Conf. Maastricht 1999, Vol. 23J, p.65-68 [75].

conferences without proceedings:

- Poster: “Plasma response on pellet ablation”, **J. de Kloe**, D. F. da Cruz, C. C. Chu, N. J. Lopes Cardozo, A. A. M. Oomens, G. M. D. Hogeweyj, F. J. Pijper and the RTP team, 8e NNV-CPS symposium Lunteren 11-4-1995.
- Poster: “Non-adiabatic Pellet Ablation on the RTP Tokamak”, **J. de Kloe**, A. A. M. Oomens, D. F. da Cruz, C. C. Chu, J. Lok, N. J. Lopes Cardozo, F. J. Pijper and the RTP team, Second Carolus Magnus Summer school on Plasma Physics, Aachen, 1995.
- Poster: “Pellet disturbed plasmas in the RTP Tokamak”, **J. de Kloe**, J. Lok, D. F. Da Cruz, A. A. M. Oomens, M. N. A. Beurskens, and the RTP team, 9e NNV-CPS symposium Lunteren 19-3-1996.
- Oral: “The effect of injected ice-pellets on the RTP-plasma”, **J. de Kloe**, M. N. A. Beurskens, G. M. D. Hogeweyj, J. Lok, N. J. Lopes Cardozo, A.A.M. Oomens, and the RTP Team, 10e NNV symposium Lunteren 12-3-1997.
- Poster: “Observation of pellet penetration”, **J. de Kloe**, **E. Noordermeer**, A. Agterberg, B. Grobber, J. Lok, A.A.M. Oomens, and the RTP team, 11e NNV-CPS symposium Lunteren 17-3-1998

# Chapter 1A

## Plasmas and pellets

### 1A.1 Plasmas

This Chapter is devoted to basic explanations of a plasma, plasma heating, and pellet injection.

#### 1A.1.1 Definition of a plasma

A plasma is a state of matter in which most atoms are in the ionized state, or to be more precise: “A plasma is a quasi neutral gas of charged and neutral particles which exhibits collective behavior”[15]. This means that contrary to an ordinary gas, whose behaviour is dominated by collisions of its atoms, the behaviour of a plasma is strongly determined by the electric and magnetic fields that its particles generate. The quasi neutrality condition means that almost equal numbers of ions and electrons have to be present, at least at longer length scales. The word plasma is from the Greek language and means “something that can be shaped” [134]. Since a plasma in physics is an object that can be shaped by the applied magnetic field, it has been given this name. In biology the same word is applied for the liquid part of blood and the total contents of a living cell (also something that can have different shapes) [33].

#### 1A.1.2 Creating and confining a plasma

A fusion plasma is created by heating hydrogen isotopes, i.e. a mixture of deuterium D and Tritium T, to a temperature in the range of 100 to 300 million degrees Kelvin (10 to 30 keV). A typical burning temperature will be 15 keV. At these temperatures the gas is fully ionized and nuclear fusion will occur. This  $T_i$  is, in fact, higher than in the center of our sun (which is  $14 \times 10^6 K \approx 1 \text{ keV}$ ) but in the sun the density and confinement times are so high that fusion occurs anyway.

To obtain this reaction thermal isolation with the outside world is necessary. This is achieved by magnetically confining the plasma.

When using magnetic confinement the plasma is trapped using a magnetic field. A charged particle in a magnetic field experiences a Lorentz-force perpendicular to the velocity of the particle, and perpendicular to the field direction. This causes the particles to circle around a magnetic field line, leaving only the direction parallel to the magnetic field free for the particles to move.

To ignite a fusion reactor the triple product  $n_i \tau_E T_i$  must be above  $5 \times 10^{21} \text{ keV s m}^{-3}$  ( $n_i$  is the ion density,  $T_i$  the ion temperature and  $\tau_E$  the energy confinement time) [145].

In a magnetically confined plasma the record, is  $3 \times 10^{20} \text{ keV s m}^{-3}$  [160], and was obtained in JET<sup>1</sup>. In RTP<sup>2</sup> the typical value reached is  $7.5 \times 10^{16} \text{ keV s m}^{-3}$ .

### 1A.1.3 Plasma devices

Several different magnetic configurations have been tried to confine plasmas. The most successful ones have been the toroidal devices. Here the freedom of the plasma particles is further limited by bending the magnetic field lines to a circle or a spiral. In that way the particles should be trapped forever (unless they collide with each other). This toroidal magnetic field is achieved using poloidal coils around the torus (see Fig. 1A.1).

To prevent the particles from drifting out of the machine due to the inhomogeneous magnetic field (an effect that will not be discussed here in more detail) a poloidal component of the magnetic field (denoted by  $B_\theta$ ) also is necessary to create a rotational transform. In the two most promising schemes for a fusion reactor this is created in a different way.

In the so-called tokamak device (see Fig. 1A.1) the poloidal field is produced by inducing an electrical current ( $I_p$ ) in the plasma in toroidal direction. This is usually done by applying a transformer yoke, and letting the plasma be the second winding of this transformer. The toroidal field ( $B_\phi$ ) is produced by poloidal coils. A major drawback of this scheme is the fact that the iron yoke can only support a finite magnetic flux, causing the pulse length of the plasma to be finite.

To achieve a stable equilibrium yet an extra force has to be applied in a tokamak: the vertical field ( $B_v$ ), producing an inward force, which counteracts the hoop-force.

The RTP device, on which the results were obtained that are described in this thesis, is a tokamak.

The tokamak device was first proposed by the Russian scientists Tamm and Sakharov in 1951 [132]. The first experimental setup of the tokamak concept, the TMP, was built by Golovin et al. [129]. The name tokamak was also invented by Golovin and Yavlinsky in 1957 [40]. It is an acronym derived from "TOroidal-

<sup>1</sup>Joint European Torus, a joint undertaking of a number of European countries under the auspices of EURATOM

<sup>2</sup>Rijnhuizen Tokamak Project



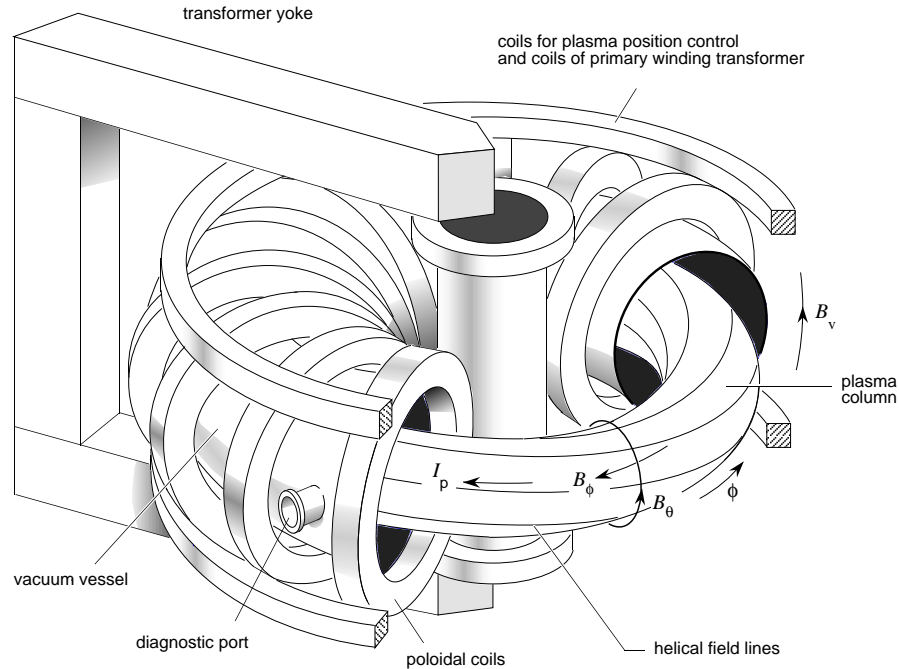


Figure 1A.1: Schematic drawing of a tokamak

ная КАмера и МАгнитная КАтушка” (ТОроидальная КАмера и МАгнитная КАтушка ) meaning “Toroidal chamber with magnetic coils” [147].

The first device producing an ignited plasma will probably be the planned ITER<sup>3</sup> experiment, which will be a tokamak. Its parameters are summarized together with the RTP parameters in Table 2.1 on page 15 for comparison. The first real power plant however, which will be build after that, should operate in steady state, so some kind of stellarator might be more suitable for that.

#### 1A.1.4 Heating a plasma

Both to create a plasma and to obtain temperatures high enough to get fusion reactions, heating has to be applied. For tokamaks the first type of heating is the plasma current which is an inherent part of the tokamak concept. Due to the small but finite resistivity of the plasma the large currents that are flowing cause heating. For additional heating electro magnetic radiation can be used, coupling to the circular motion of the particles around the magnetic field lines: Ion Cyclotron Resonance Heating (ICRH), Electron Cyclotron Resonance Heating (ECRH) and Lower Hybrid waves (LH). Typical frequencies for these waves (for an ordinary

<sup>3</sup>International Thermonuclear Experimental Reactor

plasma with toroidal magnetic field of 3 Tesla) are 23 MHz for ICRH, 0.8 GHz for LH and 80 GHz for ECRH [61] Another kind of additional heating is the injection of an intense beam of highly energetic neutral particles, (NBI, neutral beam injection).

### 1A.1.5 Why don't we have a fusion reactor yet ?

One of the major problems encountered in the attempts to build a fusion reactor is the fact that magnetic confinement is not as good as it was hoped for. The energy loss from the confined plasma is much higher (2 to 5 times via the ions, 10-100 via the electrons) than might be expected if collisions by particles trapped in the magnetic field were the only loss channel.

This transport anomaly is still not yet understood very well, but it is the main reason why a fusion energy power plant has not yet been build. A worldwide effort is going on in trying to understand this phenomenon. That is why the RTP experimental program is largely based on investigating this problem, especially concerning the transport properties of the electrons.

### 1A.1.6 Present status of fusion plasma devices

The largest tokamak at this moment, and also the machine in which the plasma has been brought closest to ignition is JET in Abingdon, UK. End 1997 the world record for fusion power was set in this machine to 16 MW with an input power by external heating of  $\approx 25$  MW. This means that a Q-factor of 0.64 has been reached.

## 1A.2 Pellets

### 1A.2.1 What is a pellet ?

A pellet is a small bullet of solid material [156]. The typical size is a few mm in diameter and it can consist of many different materials. In our case the pellets are small cylinders with a diameter of 0.6 or 0.8 mm and a length equal to the diameter. The material they consist of is solid hydrogen ice.

### 1A.2.2 Short history of pellet injection

The idea of injecting pellets or drops of liquid hydrogen in a burning plasma to refuel it was first proposed by Spitzer et al. in 1954 [127] (see Fig. 1A.2 on page 13).

For many years the problem was only addressed theoretically. One of the first devices to really produce hydrogen pellets was build around 1967 by G. Francis et al. [30] with the objective to use the pellets to produce laser-plasmas.

It took 20 years before the first pellet was experimentally shot into a plasma. This was in 1974 by Jørgensen et al. on a small rotating plasma device called puffatron in de Danish Risø laboratory [52].

Only in 1977 results of the first [13] experiments were published on an experimental study of pellet injection in a tokamak plasma by Foster et al. in the ORMAK tokamak [29].

The pipe-gun type pellet injector with in situ condensation, which is the type in use at RTP, was first used in 1978 by Milora et al. [81]. Because it is one of the simplest to construct it is now widely used for situations in which only a limited number of ( $< 10$ ) pellets are necessary.

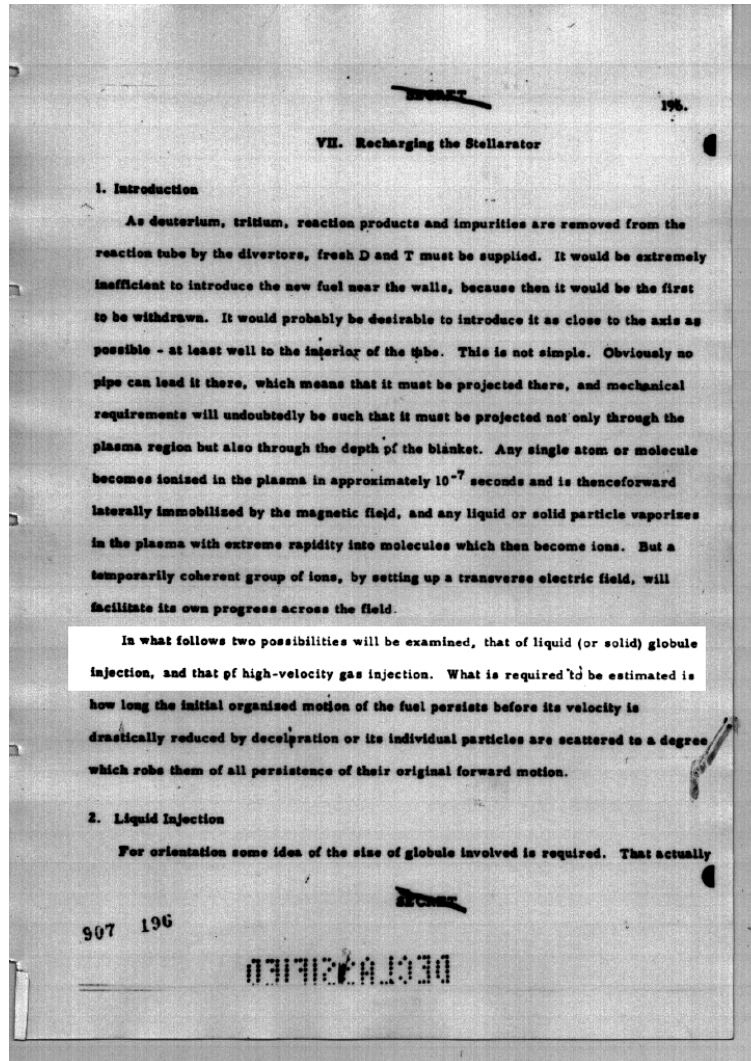


Figure 1A.2: Scanned text of the oldest publication mentioning fueling of a fusion device by solid pellets (globules), (published by L. Spitzer Jr. et al. in 1954 [127]). Note the stamps "secret" at the top and bottom, and "declassified" at the bottom of the page.

## Chapter 2

# Instrumentation

### 2.1 The RTP tokamak

#### 2.1.1 RTP, history and future

The RTP tokamak started its life in Grenoble, France, in 1974 [150], under the name “Petula” [157]. In 1986 the Institute in Grenoble moved to Cadarache and the machine was shipped to Rijnhuizen to replace two in house experiments, Tortur and Spica, which were closed down in 1987 and 1988 [158].

The tokamak received a new name: Rijnhuizen Tokamak Project (RTP). RTP was put into operation in January 1989 [116].

RTP was closed down in September 1998. The base load has been dismantled, most of the additional equipment (heating,diagnostics) has been transferred to the TEXTOR tokamak in Jülich<sup>1</sup>. The coming years the scientific program will be continued both at TEXTOR and at JET.

#### 2.1.2 RTP, parameters

RTP is a nowadays small tokamak with major radius of 0.72 m, a vessel minor radius of 0.230 m and a plasma minor radius of 0.164 m. The plasma is limited by two limiters, a circular limiter at a radius of 18 cm and movable top-bottom limiters which are set at a radius of 16.4 cm in all discussed experiments. A summary of the RTP parameters, compared with those of ITER, is shown in Table 2.1

---

<sup>1</sup>In Dutch also known as Gulik

Table 2.1: Parameters of the RTP tokamak and ITER compared.

| machine                       |                | RTP [20] | ITER [2] |                                 |
|-------------------------------|----------------|----------|----------|---------------------------------|
| major radius                  | $R_0$          | 0.72     | 8.1      | m                               |
| plasma minor radius           | $a$            | 0.164    | 2.8      | m                               |
| plasma current                | $I_{pl}$       | < 150    | <21.000  | kA                              |
| toroidal field                | $B_{tor}$      | < 2.4    | 5.7      | T                               |
| density (centre)              | $n_{e,0}$      | 0.5-14   | 2-10     | $\times 10^{19} \text{ m}^{-3}$ |
| Ohmic temperature (centre)    | $T_{e,0}$      | < 1.0    | <4.0     | keV                             |
| temperature with add. heating | $T_{e,0}$      | < 5.0    | < 10.0   | keV                             |
| safety factor                 | $q_a/q_{95}^*$ | 2.5-8.0  | < 3.0    |                                 |
| eff.ion charge                | $Z_{eff}$      | 1.5-3.0  | 1.5      |                                 |
| shot duration                 | $t$            | < 0.5    | <1000    | s                               |
| additional heating            | $P_h$          | < 0.8    | 100      | MW                              |
| total fusion power            | $P_f$          | 0        | 1500     | MW                              |

\* for RTP this is  $q_a$ , for ITER this is  $q_{95}$ .

### 2.1.3 Coordinate system used

The coordinate system used throughout this thesis is a toroidal one<sup>2</sup>, as is usual in tokamak physics (see Fig. 2.1).

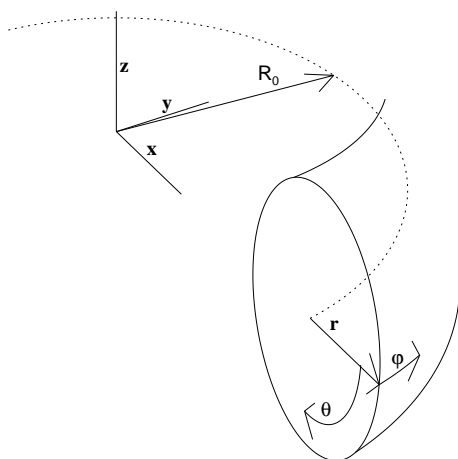


Figure 2.1: The coordinate systems used in this thesis.

The symbols used are the toroidal direction  $\phi$ , the radial direction  $r$ , and the poloidal direction  $\theta$ . Besides these symbols, also often the subscript “pol” or “tor” are used to indicate the poloidal and toroidal directions. For the radial coordinate

<sup>2</sup>This system is somewhat different from the toroidal system used by mathematicians, but only in the naming of the variables and the definition of the sign of the directions.

r often a normalized coordinate  $\rho = r/a$  is used, which varies from 0 in the plasma center to 1 at the plasma boundary..

Sometimes also the z-coordinate of the normal orthogonal coordinate system is used for diagnostics viewing in that direction (for example Thomson scattering) and the x-coordinate is sometimes used for phenomena in the horizontal plane (such as pellet injection).

#### 2.1.4 Additional heating

At RTP 3 gyrotrons are used for Electron Cyclotron Resonance Heating (ECRH). Two of these ECRH sources operate at 60 GHz, the third one operates at 110 GHz. The nominal power is 200 kW for the 60 GHz gyrotrons and 500 kW for the 110 GHz gyrotron. Note that this is much more than the Ohmic power that is deposited at the same time (typically the Ohmic power drops to 50-100 kW during ECRH). The area of deposition of the power can be chosen by applying a magnetic field for which the gyrotron is resonant at the desired position. Depending on the antenna used, the heating can be localized radially in this way (in the order of 1 cm). The ECRH power can also be modulated on a millisecond time scale to do perturbative heat transport experiments.

#### 2.1.5 Fueling systems

To increase the initial density in a controlled way two types of density fueling are available at RTP, feedback controlled gas puffing (the release of gas in the vessel, real-time controlled by a measurement of the plasma electron density) and pellet injection (which will be discussed in more detail in the next Section, Section 2.2).

## 2.2 The pellet injector at RTP

The pellet injector in use at RTP has been designed and built by the Risø laboratory in Roskilde, Denmark [125, 126]. It was installed in 1991 and operational at the end of that year [159, 161]. It has 8 pneumatic single stage gun barrels for hydrogen, thus a maximum of 8 pellets can be fired independently into the same plasma discharge. There are 2 types of gun barrels which differ in inner diameter, resulting in two different pellet sizes. Four of the barrels have a diameter of 0.6 mm and produce pellets containing about  $0.5 \times 10^{18}$  atoms. This is equal to  $8.3 \times 10^{-6}$  gram [140], but the number of atoms is the usual unit in pellet literature. These pellets contain a number of particles which is on the average about equal to the plasma particle content of a typical RTP plasma discharge ( $n_{e,0} = 4 \times 10^{19} \text{ m}^{-3}$ ). This means that the pellets are relatively big, in most other tokamaks the pellets are smaller compared to the plasma particle content. The reason for this is that in most tokamaks pellets are mainly used for fueling purposes, while at RTP pellets are used to perturb the plasma. For the same reason the other 4 barrels have an

even larger diameter of 0.8 mm, leading to an average pellet size of about  $2 \times 10^{19}$  atoms ( $= 33 \mu\text{g}$ ), which is 4 times the plasma particle content.

By changing the power on the different heaters and the driver gas pressure the masses and velocities can be varied somewhat. The range of pellet masses and velocities that can be produced by the two kinds of barrels are given in Table 2.2. The variation from shot to shot for a single gun barrel at the same settings is  $\Delta m = 10\%$  and  $\Delta v = 5\%$  [125].

Table 2.2: Pellet parameters

| Small pellets:   |                |             |                        |
|------------------|----------------|-------------|------------------------|
| diameter         | d              | 0.6         | mm                     |
| velocity         | V <sub>p</sub> | 850-1150    | m/s                    |
| particle content | # atoms        | 0.12-0.5    | $\times 10^{19}$ atoms |
| mass             | M <sub>p</sub> | 2.0-8.3     | $\mu\text{g}$          |
| volume           |                | 0.006-0.024 | mm <sup>3</sup>        |
| Large pellets:   |                |             |                        |
| diameter         | d              | 0.8         | mm                     |
| velocity         | V <sub>p</sub> | 350-900     | m/s                    |
| particle content | # atoms        | 0.5-3.0     | $\times 10^{19}$ atoms |
| mass             | M <sub>p</sub> | 5.5-33      | $\mu\text{g}$          |
| volume           |                | 0.016-0.096 | mm <sup>3</sup>        |

A schematic picture of the construction of the gun barrels is shown in Fig. 2.2. The two outer heaters are used to control the size of the pellet. The center heater

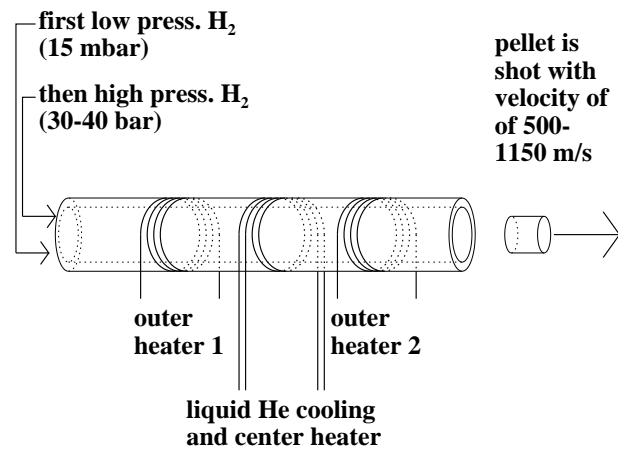


Figure 2.2: Schematic drawing of a gun barrel.



can be used to soften the outside of the pellet partially which affects the injection velocity: it will break free from the tube at a lower gas pressure, so the velocity will be smaller.

The driver gas is removed by two expansion chambers both connected to the flight tube which connect the pellet guns to the tokamak (see fig 2.3).

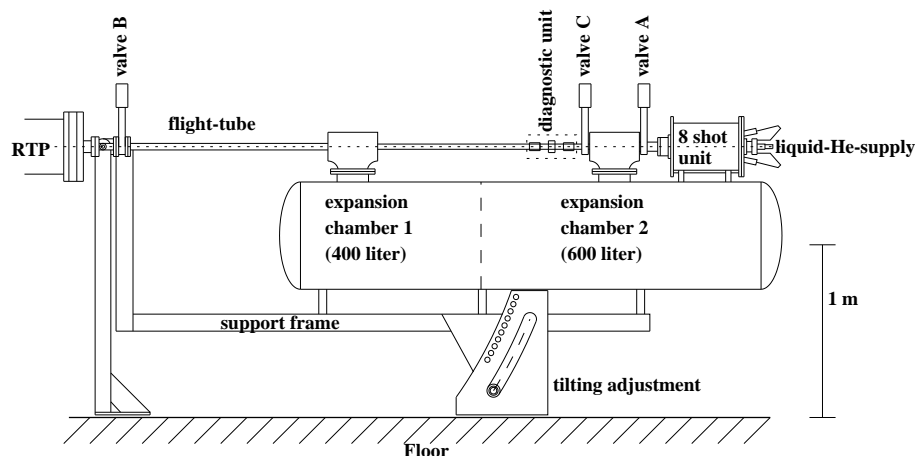


Figure 2.3: Drawing of the complete pellet injector.

A special feature of the RTP pellet injector is the possibility of tilting the angle of injection between  $0^\circ$  and  $8^\circ$  in steps of  $1^\circ$  (see Fig. 2.6). This results in oblique injection which makes it possible to inject pellets far off axis. At the maximum angle the closest approach of the pellet to the magnetic axis is 11.2 cm ( $\rho = 0.68$ ).

After the final shutdown of RTP the pellet injector was moved to the MAST experiment in Culham, England, in March 1999.

## 2.3 Diagnosing the plasma and the pellet

The diagnostics used to study pellet injection in a plasma can be divided in 3 types. Diagnostics observing the pellet before it reaches the plasma, diagnostics observing the pellet while it is inside the plasma and diagnostics observing the plasma itself.

### 2.3.1 Pellet diagnostics

After the pellet has been fired, but before it reaches the plasma, three measurements of the pellet in free flight are done: the pellet velocity  $v_{\text{pellet}}$ , the time of passage in front of an optical detector  $t_{OD1}$  and the pellet mass  $m_{\text{pellet}}$ . In some other tokamaks also the pellet integrity before it enters the plasma is checked by making a picture of it with a very fast CCD or photo camera. At RTP this diagnostic was not available

and only by interpreting carefully the diagnostics that observe the ablation the state of the pellet could be determined (in future experiments this should be considered an essential diagnostic).

### Determining velocity and timing

The timing and velocity of the pellet are measured by means of two optical detectors, OD1 and OD2 (giving times  $t_{OD1}$  and  $t_{OD2}$ ). Light falling on the detectors is blocked for a short time when the pellet flies by (see Fig 2.4). Because the distance between the two detectors is known, the velocity can be calculated from the time difference of the two pulses. This measurement of  $v_{\text{pellet}}$  has an accuracy of  $\pm 1$  m/s, at a typical value of  $v_{\text{pellet}} = 500\text{-}1000$  m/s

Under the assumption that  $v_{\text{pellet}}$  does not change during the ablation process, the pellet position inside the plasma can be computed to an accuracy of 5 mm as a function of time.

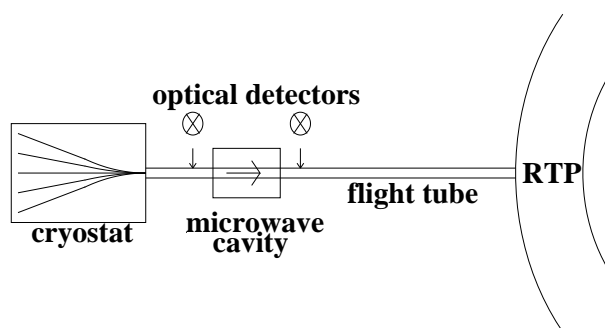


Figure 2.4: Schematic drawing of the diagnostic unit on the injector (not to scale).

The firing time of the pellet can be preprogrammed with steps of 1 ms. After proper conditioning of the machine a shot to shot variation of 100 to 200  $\mu\text{s}$  is seen for the measured time  $t_{OD1}$ . This 100 to 200  $\mu\text{s}$  is, however, not precise enough if we want to synchronize the pellet position with a measurement like Thomson scattering. How this can be improved is described in the next Section.

### 2.3.2 Triggering the Thomson scattering diagnostic by the pellet

To match a Thomson scattering measurement with a specific preprogrammed pellet position a special device was build [51]. Using this device the Thomson scattering laser could be triggered with an uncertainty of 5 mm<sup>3</sup> in the pellet position. Because of the shot to shot variation in pellet velocity and firing time a trigger for the

<sup>3</sup>so in time within 5  $\mu\text{s}$ , when the pellet has a velocity of 1 km/s.

diagnostic has to be determined real time. It is also not possible to wait until the pellet has reached the plasma and use the increase in  $H_\alpha$  signal because the Thomson Scattering laser needs to be pre-triggered at least 1.5 ms before the actual measurement.

This trigger circuit consists of a simple analog computer which calculates the proper time for the trigger pulses it has to give.

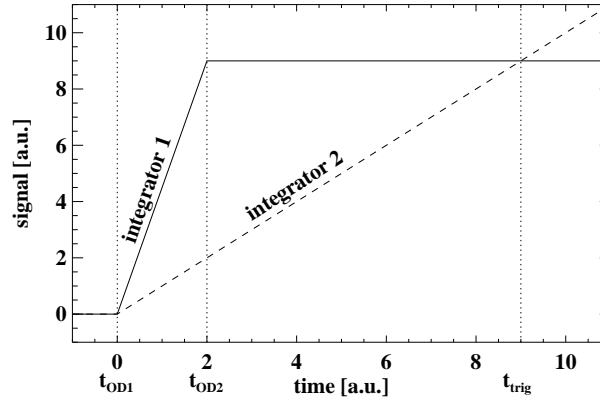


Figure 2.5: Integrator signals inside the pellet trigger box.

The principle used is illustrated in Fig. 2.5. When the pellet passes the first detector (at  $t_{OD1}$ ) two integrators start integrating the same voltage with a different (adjustable) gain. When the second detector is passed (at  $t_{OD2}$ ) the first integrator stops. The second integrator (which has a lower gain) keeps on integrating until it reaches the same voltage as the first (at  $t_{trig}$ ). A comparator is used to determine this condition and gives a trigger pulse at this moment.

The trigger time can be varied by adjusting the gain of the second integrator. The accuracy is determined by the measurement of the distance and width of the two slits of the optical detectors, not by the electronics.

Since this device is meant to be used for triggering the Thomson scattering diagnostic, one special addition is needed. The flash-light inside the laser of the Thomson scattering diagnostic needs a pre-trigger 1.5 ms before the actual measurement can be done. At 1 km/s this means that a trigger has to be generated when the pellet is at a distance of at least 1.5 m from the plasma. Since the optical detectors are at a distance of 3.342 and 3.142 m from the plasma boundary this is possible.

Using this idea, it was possible to build a circuit that gives a trigger pulse with an accuracy of  $\approx 5$  mm in the desired pellet position, independent of the actual pellet velocity and firing time.

### Measuring the pellet mass

The pellet mass is measured during its flight in vacuum by using a microwave cavity. Due to the pellet mass in the cavity, the dielectric condition in the resonating volume, and thus the resonance frequency of the cavity is changed. This change is proportional to the pellet mass so that measuring the frequency gives a measure for the pellet mass. This diagnostic, together with the two optical gates, was developed by the Danish Risø laboratory [126], and came with the pellet injector. The accuracy of the mass measurement is  $\approx 10\%$ .

### 2.3.3 Diagnosing the pellet during the ablation

During its flight through the plasma and its evaporation (or ablation) it is not possible to observe the pellet directly because it is surrounded by a dense cloud of neutral gas and plasma. In fact, the only possibility to diagnose the process of ablation consists of observing this cloud of neutrals and the (cold) dense plasma around the pellet. This is usually done by observing the radiation emitted by this cloud, but it is also possible to probe it with external (laser) radiation.

#### Observation of line emission

A large part of the radiation emitted during the process of pellet ablation consists of line radiation of neutral hydrogen atoms which have been excited due to collisions in the cloud. This radiation is measured by simply mounting a fiber near a window of the tokamak in such a way that it can observe the complete trajectory of the pellet (see Fig. 2.6).

In most experiments the line emission of the Lyman series is not used because the plasma can be optically thick for it in some circumstances. For the Balmer lines this is usually not the case.

On RTP there are 4 fibers close to each other on the same window, looking at the first four Balmer lines of hydrogen, the so called  $H_\alpha$  (656 nm),  $H_\beta$  (486 nm),  $H_\gamma$  (434 nm) and  $H_\delta$  (410 nm) lines [141].

In literature it is often assumed that there exists a direct relation between the intensity of the detected  $H_\alpha$  light and the local particle source in the plasma [90].

An example of the  $H_\alpha$  signal measured as a function of time (but converted to the radial position of the pellet at each time), is given in Fig. 2.7. The time resolution of this signal depends mostly on the properties of the applied photo multiplier, which has a response time of  $0.5 \mu\text{s}$ . This diagnostic has no spatial resolution.

Usually it is assumed that the ablation cloud is located near the pellet and moves with it as the pellet travels through the plasma. In some cases this has been confirmed by fast photo and CCD cameras on other tokamaks [24]. The pictures show that the radial extension of the ablation cloud is in the order of 1 cm.

The toroidal extension can be much larger, up to 10 cm or more, but this is less important for the discussion below. The poloidal extension is almost never observed.

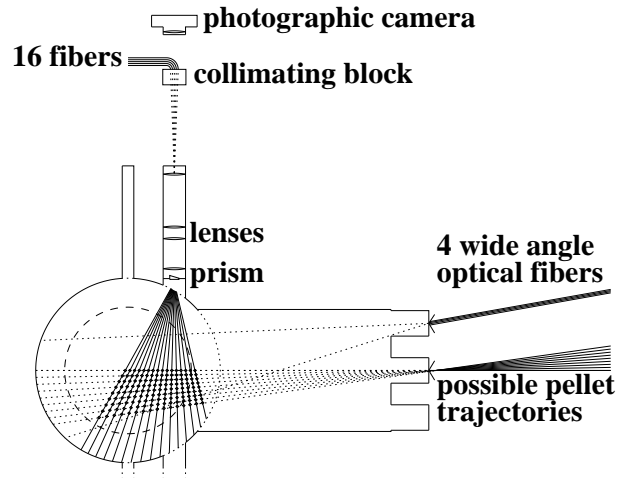


Figure 2.6: Overview of the experimental setup and the viewing lines of the ablation diagnostics in a poloidal cross-section of the tokamak. The dashed circle indicates the plasma position.

The only exception is the Japanese tokamak JIPP T-IIU [120] where a rotation in poloidal direction of the ablation cloud was observed with a tangentially viewing camera.

Using the assumption that the emitted light is emitted close to the pellet, combined with the measured pellet velocity, the time axis of these signals is often converted to pellet position, or pellet radius. This conversion enables comparing the results to other spatially resolved diagnostics, for example Thomson Scattering.

This conversion enables the interpretation of for example the  $H_{\alpha}$  signal in Fig. 2.8. Here a pellet survives the passage through the plasma. It is clearly seen that when the pellet crosses the first half of the plasma the signal is large, while after the pellet has passed the center the signal dramatically drops. This is because of the cooling of the plasma by the pellet. Then the pellet leaves the plasma and hits the wall of the vessel, causing a large gas puff, due to the evaporation of the pellet. This large gas puff is visible in Fig. 2.8 as a burst of signal for pellet positions  $< -27$  cm.

The line emission diagnostic is often used to determine the penetration depth of the pellet, because if no line emission is observed anymore<sup>4</sup> one can be sure that no neutral particles and thus no pellet exists in the plasma. It should be noted, however, that this gives an upper limit to the penetration.

<sup>4</sup>Of course some  $H_{\alpha}$  emission is always seen at the edge of the plasma, but since this is orders of magnitude less than the radiation emitted during pellet injection the end of the process can clearly be discriminated.

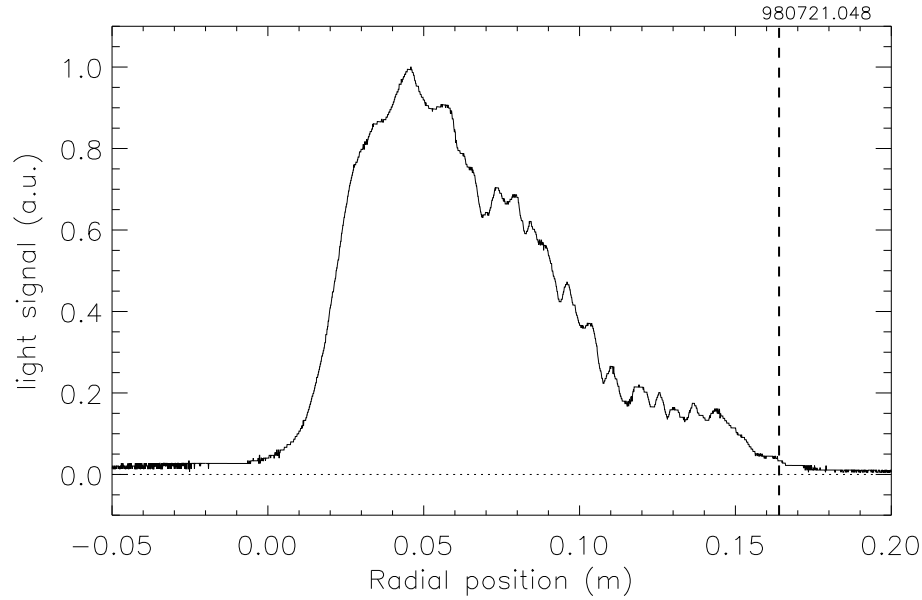


Figure 2.7: Example of the  $H_{\alpha}$  signal for a fully ablated pellet (large pellet in ECRH heated plasma). Time is converted to position by multiplying with the pellet velocity, and increases from right to left in this plot.

### Spatial resolved observations of the ablation

Apart from observing the line emission integrated over a large volume as a function of time, we also have the possibility to observe it spatially resolved but integrated in time. For this purpose we apply a photographic camera, coupled to the plasma by a system of lenses (see Fig. 2.6). Unfortunately, due to the small and long port, we can only see the outer half of the plasma (from the point where the pellet enters the plasma, until the plasma center). The position on the pictures has been calibrated by inserting an illuminated ruler in the vacuum vessel at the position of the pellet trajectory. The resolution of this system is  $\approx 1$  mm for horizontal injection, but no time resolution is obtained since the camera integrates the pictures during  $\approx 25$  ms. An example of a picture taken with this diagnostic is shown in Fig. 3.2 on page 41.

### The fiber-array diagnostic

The two diagnostics described previously yielded conflicting results. Therefore it was decided to build a special diagnostic to obtain a time and spatially resolved measurement of the emitted line radiation. It contains 16 fibers each viewing perpendicularly to the pellet trajectory with very small opening angles. These views were obtained by mounting the ends of the fibers inside the lens system of our photographic system

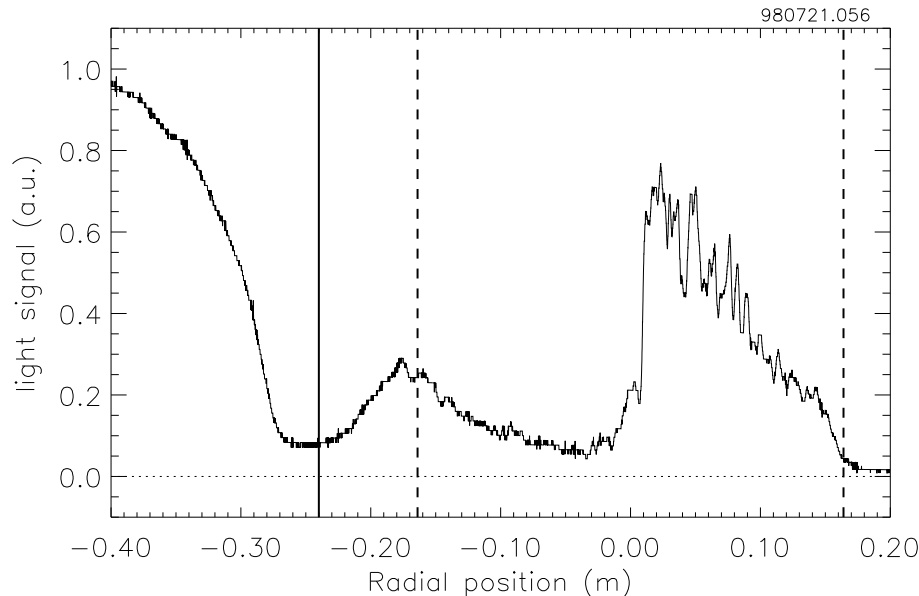


Figure 2.8: Example of the  $H_{\alpha}$  signal of a not fully ablated pellet plotted in the same way as Fig. 2.7 (large pellet in Ohmic plasma). The full vertical line at -24 cm indicates the wall of the RTP vessel. The strong oscillations between 2 and 10 cm are often called striations.

at a plane where the pellet trajectory is imaged. At the other end of the fibers 16 photo diodes are mounted, which enables all fibers to be measured independently. In this way a one-dimensional camera was formed. The temporal resolution of the system was determined by the available ADC's, usually 1 or 2  $\mu\text{s}$ . This is necessary because the shape of the cloud is observed to change within intervals of a few microseconds [84]. A schematic drawing of this setup is included in Fig. 2.6. To narrow the lines of sight of the fibers a collimator consisting of a black 40 mm thick plastic block, with 1 mm diameter holes in it, was mounted in front of the fibers.

The resolution of this system (defined as the part of the pellet trajectory that 1 fiber can observe) is best for central pellet injection, because the lens system is focussed at that trajectory. In this case the resolution is  $\approx 3.5$  mm, and the viewing lines are 9.6 mm apart. For oblique pellet injection the resolution of the fibers stays almost the same thanks to the collimator in the system. It decreases only to about 5 mm for the maximum injection angle of  $8^{\circ}$ , and the distance between the viewing lines increases to 14 mm.

As an additional option, the fiber array can be rotated over 90 degrees to view the timing and extension of the ablation cloud in toroidal direction, and to check the alignment of the fiber array with the pellet trajectory.

Properties that can be measured with this diagnostic are pellet velocity, ablation cloud size and position, and penetration depth. A typical example of a result obtained with this diagnostic is given in Fig. 2.9. The results of this diagnostic are presented in Chapter 4.

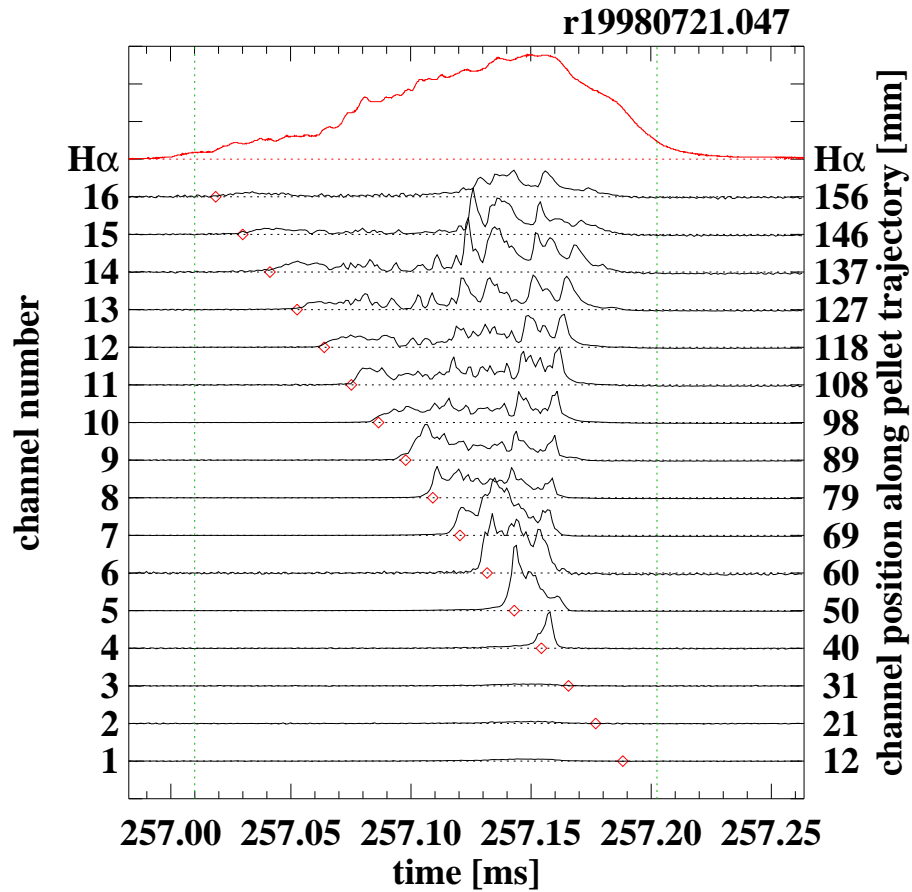


Figure 2.9: Example of the pellet ablation process as observed by the fiber-array diagnostic (this is the same plot as in fig. 4.6 on page 55, see the description there for an explanation of this result).

### 2.3.4 Plasma diagnostics at RTP

The available diagnostics for the plasma itself consist first of measurements of radiation emitted by the plasma, or of light scattered or phase shifted by the plasma.



Furthermore magnetic and electric field measurements are available. Particle diagnostics or probes are not available at RTP.

### Thomson Scattering

A Thomson scattering (TS) diagnostic is available which has a double pulse laser system. It can measure temperature and density profiles along a vertical chord with a spatial resolution of 2 % of the minor radius [10].

Thomson scattering is based on the scattering of photons on the free electrons in the plasma. A powerful laser beam (Ruby laser, 694.3 nm, max. 25 J in a single, 20 ns pulse) is injected into the plasma from top to bottom. The amount of scattered light is a direct measure for the electron density in the plasma. The broadening of the laser line caused by the Doppler effect gives information on the velocity distribution of the electrons, and thus on the electron temperature.

The laser applied in this diagnostic can fire once or twice during a plasma discharge (resulting in one pulse of max. 25 J or 2 pulses of max. 12.5 J). The time between the two laser pulses can be varied between 40 and 800  $\mu\text{s}$ .

This double pulse option is a unique feature of the RTP Thomson scattering system and enables the measurement of two profiles shortly after each other. The available time range is especially suited for study of the pellet ablation process (typical time scale of 200  $\mu\text{s}$ ). Also the high spatial resolution is essential for studying the pellet ablation process, since large gradients are to be expected at the scale of the ablation cloud (typically 10 mm in radial direction). A final big advantage is the short 20 ns laser pulse, which is much faster than all radial profile changes (even the displacement of the drifting clouds described in Chapter 4, in this 20 ns, can be neglected compared to the radial resolution of the TS diagnostic). Thus, one can be sure that the observed structures are real, and not some time averaged artefact. All these advantages make that this diagnostic is one of the two key diagnostics used in this thesis (together with the fiber array diagnostic).

A typical result for a measurement of a  $T_e$  profile in an Ohmic plasma and during pellet ablation are given in fig 4.12 on page 66. A measurement of a  $n_e$  profile in the same two cases is given in fig 4.13 on page 67.

### ECE-radiometer

ECE diagnostics are based on the radiation that is emitted by the electrons because they gyrate around the magnetic field lines. The unique feature of this radiation is that its frequency is related to the gyration frequency of the electrons, which is proportional to the strength of the local magnetic field. Since in a tokamak the magnetic field varies as a function of radius to the tokamak center, this makes it possible to do a localized measurement of this radiation, by observing a certain frequency range. The intensity of the radiation is proportional to  $T_e$ , provided that the plasma is optically thick.

On RTP two diagnostics using this principle are available. The first one is a radiometer which collects the radiation with an antenna viewing along a horizontal chord in the mid plane through the plasma. Either one of two antennas can be used, one located at the low field side (LFS) and one located at the high field side (HFS) of the tokamak. Inside the diagnostic 20 different frequency bands are selected, resulting in 20 local measurements of the radiation intensity. This makes it possible to measure a temperature profile with this diagnostic as a function of time at 20 points in the plasma [34]. This method breaks down if there is a region in the plasma where the radiation cannot propagate. This is called a cut off and occurs above a certain plasma density. An example of a measurement taken by this diagnostic is shown in Fig. 6.3a on page 117.

The second diagnostic based on ECE is the ECE-imaging system. Here a lens system is used to image a vertical chord in the plasma onto a series of detectors all tuned to the same frequency. This results in a measurement of the radiation profile parallel to or coinciding with the TS laser path. By either changing the magnetic field or by changing the detection frequency the observed line can be shifted through the plasma [19]. An example of a measurement taken by this diagnostic is shown in Fig. 6.5 on page 121.

The big advantage of both these diagnostics over Thomson scattering is that a time evolution is obtained, if necessary covering the complete plasma shot with a maximum time resolution of 4  $\mu$ s.

As was mentioned above, for high densities a cut-off occurs and all temperature information is lost. This is usually the case for pellet injection experiments during and shortly after the ablation. However, this yields new information in itself because it reveals the (often very localized) position in the plasma in which the pellet matter has been deposited (see Chapter 6). This localization of the cut-off region makes it often also possible to observe the temperature by using a different antenna (at the HFS).

### SXR-tomography system

A plasma with temperature in the order of 1 keV emits soft-X-ray (SXR) radiation due to “bremsstrahlung”, radiative recombination and line radiation of the impurities in the plasma. This radiation is observed by a system of 5 pinhole cameras each having an array of 16 detectors. These 80 channels in total form a tomographic system which permits converting the line integrated measurements back to the local emissivities. The temporal resolution of the cameras is 5  $\mu$ s and the spacing between the viewing chords of 1 camera in the vessel center is  $\approx$  2 cm. The spectral sensitivity of the cameras ranges from 1 to 10 keV with a maximum sensitivity at 3 keV [17]

The amount of SXR emission is proportional to  $n_e^2$ , and is a more complex function of  $T_e$ . So if  $T_e$  remains constant the diagnostic can in principle be used to determine  $n_e$ , and vice versa.

In many cases a tomographic reconstruction can be done and a two dimensional

cross section of the plasma radiation in this spectral range can be obtained. Therefore this diagnostic is very well suited to observe fast phenomena in the plasma center, like fast MHD and sawteeth. Also the plasma rotation can clearly be observed with this diagnostic, if there are structures that rotate along with the plasma (for example magnetic islands).

During pellet injection, however, both  $T_e$  and  $n_e$  change simultaneously which makes the interpretation of the results very difficult. Another complicating feature is the line integration. This can be misleading when looking at the raw data (without inversion). Because pellet injection can often cause hollow  $n_e$  profiles (and thus hollow radiation profiles) the tomographic inversion becomes much more difficult than for centrally peaked radiation profiles. Because of these problems the signals could not be usefully analyzed for the period of pellet ablation itself.

An example of a measurement of one of the channels of this diagnostic is shown in Fig. 2.10.

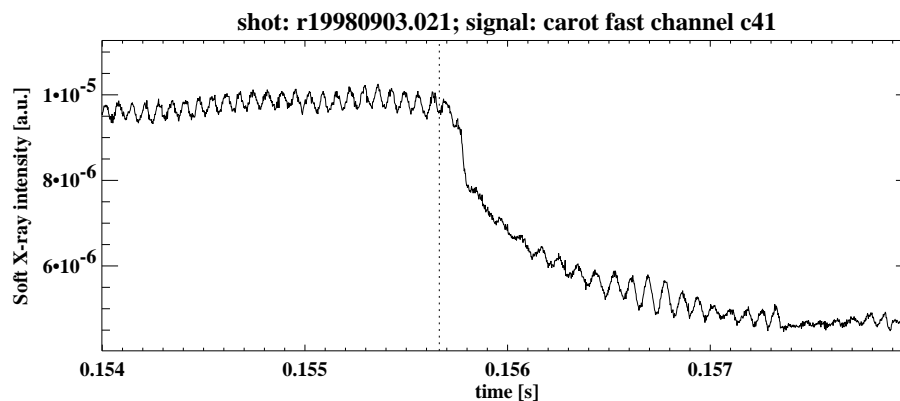


Figure 2.10: Example of plasma MHD rotation as observed by the SXR diagnostic. A clear  $m=1$  mode is seen in the central channel that survives the event of pellet injection (indicated by the vertical dotted line) because the pellet was injected off-axis. Why the mode disappears at  $t=157.35$  ms is not clear.

### Interferometer

Interferometry is based on the change of light velocity in the plasma. This results in a phase shift for light traveling through the plasma, when compared to light traveling the same distance in air. This phase difference is proportional to the electron density in the plasma, and thus forms a measurement of  $n_e$ . The diagnostic at RTP uses 19 channels for monitoring the phase shift [117].

The measurements are line integrated along the laser paths. To obtain local measurements some assumptions on the symmetry of the system have to be made.

Usually one assumes a constant density on a flux surface, which makes it possible to apply a simple tomography method known as Abel inversion.

This diagnostic is in most plasma conditions very well suited to measure the plasma density profile as a function of time (at a time resolution of  $16 \mu\text{s}$ ).

A difficulty that can arise, especially during pellet injection, are fringe jumps. Since the diagnostic measures phase, it gives the same result for densities that give a  $2\pi$  difference in phase shift. A special fringe counter is used (in hardware or software) to count the number of steps that have occurred since the startup of the plasma. In most circumstances this works very reliable. If, however, the signal changes so fast that a  $2\pi$  step, or multiple  $2\pi$  steps occur within a single sampling time interval, the fringe counter can not accurately count the fringes anymore. This situation occurs usually at fast density changes, like during disruptions and pellet injection. If only one such event occurs the signal can be reconstructed using the zero value after the end of the plasma pulse. If two or more such events happen the phase in between them becomes meaningless.

A second difficulty that can arise is refraction of the laser beam. Due to large inhomogeneities the plasma can act like a lens, bending the laser beam. If this becomes so strong that the laser gets out of reach of the detector at the opposite side of the plasma, obviously all information is lost, including the fringe count. This is also only important during pellet injection.

Finally the Abel inversion that is used to convert the line integrated measurements to a local density may break down because it assumes cylindrical symmetry of the plasma. This is clearly not the case during the pellet ablation process.

In spite of the three problems mentioned, the measurements give very reliable and valuable information for most of the plasma shot, and only in the few hundred microseconds of the pellet ablation itself should be treated with extreme care.

An example of a measurement taken with this diagnostic is shown in Fig. 5.3 on page 90.

A second and simpler single channel version, of the diagnostic is also available at RTP. This diagnostic measures the electron density along one vertical chord through the center of the plasma, and is especially used to control the plasma density by gas puffing using a feedback system.

### Other diagnostics

Other diagnostics that are available will only briefly be discussed since they are less important for the results presented in this thesis.

A visible light tomography (Vilt) system is available, consisting of optics and 80 photo diodes (divided in 5 cameras), which can be used to observe visible light emission in the plasma along very narrow lines of sight. Filters can be included in the system to select part of the spectrum, for example a single hydrogen line. The time resolution of the Vilt cameras is  $5 \mu\text{s}$ .

A bolometer is available to observe the total radiation originating from the plasma [139].

Furthermore some spectroscopic diagnostics are present to observe radiation in the visible light, the UV and the SXR region. Also a set of coils and loops is available to probe the magnetic and electric fields around the plasma. These diagnostics all feature very limited time resolution, in the order of  $100 \mu\text{s}$  to  $1 \text{ms}$ , and not the  $1 \mu\text{s}$  that would be needed to do observations on the time scale of pellet ablation. Therefore they are not used in this study, except for one fast magnetic coil (time resolution  $2 \mu\text{s}$ ) that was used to observe the plasma rotation.

### 2.3.5 Location of the diagnostics

The toroidal position of all diagnostics presented is given in Fig. 2.11 [21], relative to the position of the pellet injector. The diagnostics directly observing the pellet ablation (as discussed in Section 2.3.3) are located at the same toroidal position as the pellet injector, and are not shown in Fig. 2.11

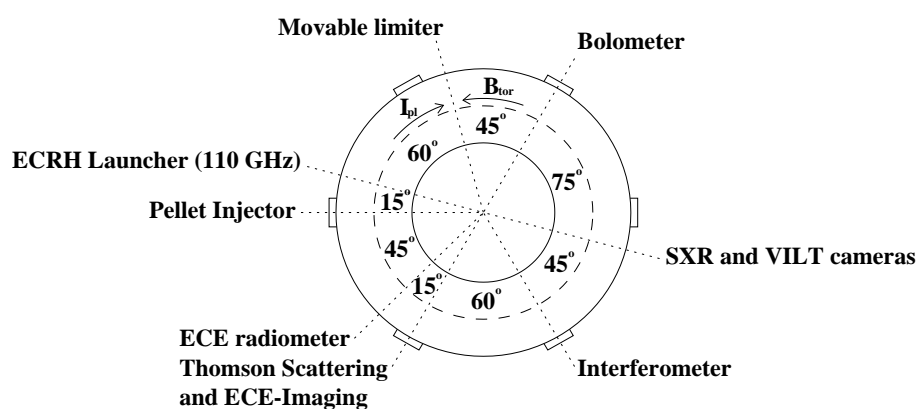


Figure 2.11: Overview of the toroidal position of the pellet injector and the most important diagnostics at the RTP tokamak.

## 2.4 Time and length scales for RTP

A large range of values for both density and temperature occurs during pellet ablation, between the unperturbed plasma and the pellet. This means that a large range of typical time- and length-scales play a role. This is important to realize in the interpretation of many measurements. For example, if one wants to consider the process of pellet ablation as being adiabatic, it is essential to know that the ablation time scale of usually  $100\text{-}200 \mu\text{s}$  is much shorter than the energy confinement time of  $4 \text{ms}$  at RTP. Thus, when studying energy confinement, pellet injection can be regarded to be a delta function, and the resulting  $n_e$  and  $T_e$  changes as step functions in time. Examples of these numbers for RTP are found in Table 2.3.

The current diffusion time is experimentally found to be  $\approx 15$  ms for a typical Ohmic plasma. However, for the cooled plasma after pellet injection this can go down to  $\approx 1$  ms, so some current redistribution could occur in the plasma center during the ablation process.

Time scales that are much smaller than the ablation process are the ion-ion collision time  $\tau_i$  and the electron-ion collision time  $\tau_e$ .

Before a plasma property, like  $T_e$ , can be regarded as a flux function during pellet ablation, it has to be known how fast it spreads out over a flux surface. Only if this relaxation is short on the ablation time scale this is allowed. For  $T_e$  this means the electrons need time to spread on the flux surface and thermalise (as is further discussed in Section 3.3.1. Thermalisation just means that the electron has to experience a few collisions, so a few times  $0.34 \mu\text{s}$  (see table 2.3). Also the mixing time for the electrons can be in the order of a few microseconds so the relaxation time for  $T_e$  will be too. This means that  $T_e$  can be regarded as a flux function, even during pellet ablation.

The ion-thermal velocity divided by the circumference of the torus basically determines the time scale on which the density relaxes on a flux surface. The ion thermal velocity is typically  $1 \times 10^5$  m/s which means a time of  $45 \mu\text{s}$  is needed for a single passage around the torus. Since at least several rounds around the torus have to be made to obtain a constant value of the density on a flux surface, large variations even on a single flux surface can be expected when measuring the density during pellet ablation. This is discussed in more detail in Chapter 6.

The ion-electron heat exchange time normally is in the order of a few ms. However, inside the ablation cloud it goes down to the  $\mu\text{s}$  time scale, so no large differences in ion and electron temperature should be expected after the end of pellet ablation.

Table 2.3: Plasma time and length scales and velocities (remind:  $R=0.72$  m,  $a=0.164$  m, pellet = 0.6-0.8 mm diameter, ablation cloud = 10 mm diameter, 3-10 cm length, ablation time = 100-200  $\mu$ s. A toroidal field of 2 T is taken).

| Kind of plasma:                                | Ohmic         | cooled by a small pellet | inside the abl. cloud |
|--|---------------|--------------------------|-----------------------|
| Plasma parameters used for these calculations: |               |                          |                       |
| $T_e, T_i$ (at $r=0.5$ a)                      | 300 eV        | 100 eV                   | 10 eV                 |
| $n_e$ (at $r=0.5$ a)                           | $2e19 m^{-3}$ | $8e19 m^{-3}$            | $1e21-1e23 m^{-3}$    |
| Coulomb log e-e $\ln(\Lambda)$                 | 14.5          | 12.7                     | 6.8-9.1               |
| Coulomb log e-i $\ln(\Lambda)$                 | 14.8          | 13.0                     | 7.1-9.4               |
| Coulomb log i-i $\ln(\Lambda)$                 | 16.3          | 14.0                     | 6.9-9.2               |
| plasma regime                                  | plateau       | Pfirsch-Schl.            | Pfirsch-Schl.         |
| $\chi_e$                                       | $0.48 m^2/s$  | $2.1 m^2/s$              | $21 m^2/s$            |
| $D_{classical}$ *                              | $0.005 m^2/s$ | $0.03 m^2/s$             | $0.74-57 m^2/s$       |
| $D_{neo-classical}$ *                          | $0.80 m^2/s$  | $0.15 m^2/s$             | $3.7-285 m^2/s$       |
| Time scales:                                   |               |                          |                       |
| energy confinement time                        | 4 ms          | -                        | -                     |
| current diffusion time                         | 15 ms         | 3.3 ms                   | -                     |
| electr.-ion coll. time $\tau_e$                | 6.2 $\mu$ s   | 0.34 $\mu$ s             | 0.016-1.2 ns          |
| ion-ion collision time $\tau_i$                | 333 $\mu$ s   | 18.6 $\mu$ s             | 0.93-71.7 ns          |
| el.-ion energy exch. time                      | 5.6 ms        | 300 $\mu$ s              | 0.015-1.1 $\mu$ s     |
| ion spread time **                             | -             | 95-1100 $\mu$ s          | -                     |
| el. spread time **                             | -             | 15-28 $\mu$ s            | -                     |
| Length scales:                                 |               |                          |                       |
| Debye length                                   | 29 $\mu$ m    | 8.3 $\mu$ m              | 0.074-0.74 $\mu$ m    |
| electron Larmor radius                         | 29 $\mu$ m    | 17 $\mu$ m               | 5.4 $\mu$ m           |
| ion Larmor radius                              | 1.3 mm        | 0.72 mm                  | 0.23 mm               |
| banana width electrons *                       | 1.05 mm       | -                        | -                     |
| banana width ions *                            | 45.0 mm       | -                        | -                     |
| electron mean free path                        | 38.3 m        | 1.1 m                    | 0.02-0.85 mm          |
| Velocities:                                    |               |                          |                       |
| electron thermal velocity                      | $7.3e6$ m/s   | $4.2e6$ m/s              | $1.3e6$ m/s           |
| ion thermal velocity                           | $1.7e5$ m/s   | $9.8e4$ m/s              | $3.1e4$ m/s           |
| ion sound velocity $C_s$                       | $2.4e5$ m/s   | $1.4e5$ m/s              | $4.4e4$ m/s           |
| Alfvén velocity                                | $9.7e6$ m/s   | $4.9e6$ m/s              | $1.4e6$ m/s           |

\* for  $q=2, r=8$  cm

\*\* this is the estimated time needed to get a full spreading on a flux surface of the deposited ablatant, for  $r=8.0$  cm. See Sec. 6.5 for a more detailed explanation.

## Chapter 3

# Status of pellet physics

### 3.1 Introduction

To achieve good fueling in a future reactor one has to be able to predict the outcome of the ablation process. This can only be done if accurate models are available to describe the ablation process and the related particle transport.

In this Chapter the present state of understanding of the interaction of a pellet with a high  $T_e$  plasma is summarized.

The process of pellet ablation and its effects on the plasma is usually divided into four separate processes which can be studied independently (both in experiment and theory), although they are linked to each other of course.

First there is the ablation process itself, i.e. the process of the pellet being exposed to a heat flux, and forming a protective layer of gas and plasma around it (see Section 3.2). Then there is the movement of the ablatant<sup>1</sup> through the plasma (see Section 3.3). Also the forces working on the pellet by the ablation cloud and the plasma can influence the movement of the pellet itself (see Section 3.4). Finally the global response of the plasma to this very local perturbation is studied (see Section 3.5).

Furthermore the viewpoint of studying pellets can be different. First, as was mentioned above, it is studied to achieve better fueling. Second it is studied because pellets can be used as a diagnostic, as a very local probe inside the plasma (see Section 3.6). This is the way pellets were used in RTP.

---

<sup>1</sup>The “ablation cloud” is defined as the region around the pellet in which the ablated material is partially ionized, so that it can be observed by observing the emitted visible line radiation. The word “ablatant” is more general, and includes also the already completely ionized particles that were added by the pellet.



## 3.2 The ablation itself

The main purpose of modeling the ablation itself is to obtain a model of the particle source formed by the pellet as a function minor radius  $r$ . In fact many plasma properties enter in this function, but since they are all supposed to be functions of  $r$  only, this is the remaining variable.

As soon as the pellet enters the plasma it is exposed to the heat flux carried by ions and electrons. The pellet starts to ablate (evaporate, erode) and a cloud of ablated matter is formed around it. This ablation cloud shields the pellet from the incident heat flux. This is the underlying idea of all ablation models.

Experimentally [85] values for  $T_e$  and  $n_e$  inside the ablation cloud are found to be in the range of  $T_e = 1\text{-}20$  eV and  $n_e = 10^{21} - 10^{25} \text{ m}^{-3}$ .

In the simplest models it is assumed that the shielding ablation cloud consists of neutrals only (NGS<sup>2</sup> model) and the heat flux is taken to be radially symmetric (1D) around the pellet. However, many variations exist. The NGS model assumes no cold plasma shielding and a mono-energetic electron population heating the pellet.

In all models the evaporated material flows away from the pellet. Close to the pellet this will be cold neutral gas but further outward its temperature will increase and it will first dissociate and then get more and more ionized (in the NGS model this is a step function). Finally of course it has to match the plasma temperature and densities at large distances from the pellet.

In most models a constant (cold) particle source is taken to represent the pellet, and then for some plasma density and temperature an equilibrium is calculated from the outward flowing particles and the inward flowing energy.

The results of the NGS model can be written as [88, 107]:

$$\frac{\partial r_{\text{pellet}}}{\partial t} = C(r_{\text{pellet}})^{-0.67} (n_e)^{0.33} (T_e)^{1.64} \text{ [cm/s]} \quad (3.1)$$

(with  $C = 1.72 \times 10^{-8}$ ,  $r_{\text{pellet}}$  in [cm],  $n_e$  in [ $\text{cm}^{-3}$ ],  $T_e$  in [eV] and the time  $t$  in [s]).

A result of this model, after inserting RTP parameters, is shown in figure 3.1. From this figure it can be seen that to obtain optimal fueling (=penetration up to, or just beyond the magnetic axis, combined with complete ablation) for a typical Ohmic plasma of 800 eV the pellet has to have a velocity just above 1000 m/s.

Despite its simplicity the NGS model has performed very well in predicting the pellet penetration depth<sup>3</sup> [89]. However, the profile of mass deposition is less well matched. This discrepancy and a possible explanation are further discussed in Chapter 4. Note also that in this class of models all pellet matter is deposited in the plasma, so the fueling efficiency is 100 %. Experimentally it is well known that there are conditions in which this is not true. This shows that after the pellet mat-

<sup>2</sup>The Neutral Gas Shielding model

<sup>3</sup>penetration depth is defined as the distance covered by the pellet when  $r_{\text{pellet}}$  has decreased to zero.

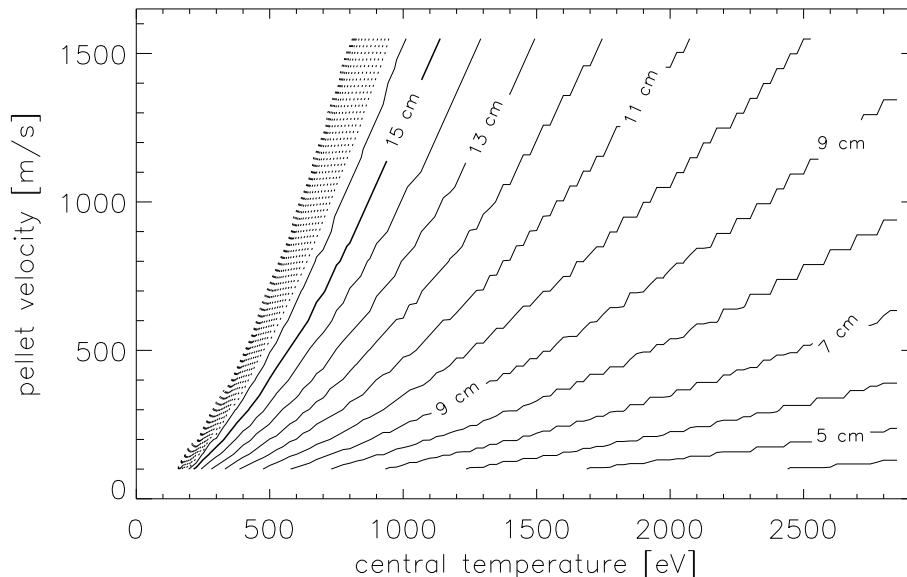


Figure 3.1: Calculated pellet penetration depth from the NGS model as a function of the central plasma electron temperature and pellet velocity (assumptions: pellet size  $m_{\text{pellet}} = 2.0 \times 10^{19}$  atoms, central electron density  $n_e = 3.8 \times 10^{19} \text{ m}^{-3}$ ). The staircase like shape of some of the contours is not real, but an artefact of the limited number of points in the calculation.

ter is deposited redistribution can take place, which is not yet included in these models.

More advanced models include taking 2 or 3 dimensions into account, a realistic (Maxwellian) velocity distribution, cold plasma shielding, both electron and ion heating and the possibility of high energetic particle populations like fast electrons (EC heated or runaway), hot ions (from NBI<sup>4</sup>) or hot  $\alpha$  particles resulting from fusion reactions. A well known example is the NGPS<sup>5</sup> model [48], which is 1D, but includes a cold plasma shield outside the neutral region, a Maxwellian electron distribution and a fast ion contribution.

Also electric and magnetic field changes (possibly resulting in additional shielding) can be taken into account. Finally a choice has to be made which atomic and molecular processes should be included/discarded inside the ablation cloud.

Surprisingly many of these “improvements” of the model do not give a better match to the measurements at all (usually models are compared to the measured penetration depth), or if they improve one dependency<sup>6</sup> they loose another one that

<sup>4</sup>Neutral Beam Injection

<sup>5</sup>The Neutral Gas and Plasma Shielding model

<sup>6</sup>possible dependencies are for example  $v_{\text{pellet}}$ ,  $T_e$ ,  $n_e$ , or the presence of hot electrons or ions

was correct in the simple NGS model [47].

To improve ablation models a database of experimental results, focusing on pellet penetration as a function of a variety of plasma parameters, has been compiled by Baylor et al. [4]. Typical results from RTP have been contributed to this database.

In the range of temperatures from the pellet to the unperturbed plasma, a well defined region exists in which neutral hydrogen atoms can exist. This area is very easy to diagnose since it emits line radiation in the visible light region, and this part usually is called “the ablation cloud”. The radius of this region is usually called the confinement or ionisation radius  $r_i$  and is an important parameter in most models, since it is one other parameter that can be checked in experiments.

The ablation cloud is observed to be elongated along the magnetic field (cigar-shaped) due to the partial ionisation and the high collisionality inside the cloud [24, 71]. Its size at RTP varies between 1 and more than 10 cm along the magnetic field, and between 1 and 2 cm perpendicular to the magnetic field. Furthermore the cloud shape has been observed to vary on a microsecond time scale. This variation is in the width of the cloud along the field lines, as well as in the size perpendicular to the field lines. Examples have even been reported of the cloud splitting up in two separate parts [82]. These variations in toroidal cloud width are known as striations because they appear as stripes on the photographs taken from the process (for an example see Fig. 3.2). Striations are also observed on the  $H_\alpha$  signals as oscillations in the signal (for an example see Fig. 2.8). Sometimes they are divided in two kinds, positive striations (a peak on the  $H_\alpha$  signal) and negative striations (a dip on the  $H_\alpha$  signal), but the difference is hard to see if a number of these events occur closely after each other. These striations have a typical size of 10 mm on the camera images and a frequency of 100 kHz on the  $H_\alpha$  diagnostics [84].

The physical mechanism behind striations is not yet clear. There are several possible explanations.

A first explanation is the limited energy available for the ablation process when the pellet passes certain rational values of  $q$  [23]. This would make the process a possible diagnostic to observe the  $q$ -profile. However, except maybe for some cases near  $q=1$  [37, 110] (see also Section 7.3 for a related measurement of the limited energy reservoir at  $q=1$  at RTP), this has never clearly been demonstrated experimentally [62, 85].

A second possibility is that the ablation clouds sticks to the magnetic field lines because of its partial ionisation (see Section 3.3.2, case 2). In this case the pellet would be shielded as long as it travels through the cloud, but then when it leaves the cloud it would suddenly be exposed to a much larger heat flux and form a new shielding cloud [101]. This would result in a constant distance between coexisting clouds.

A third possibility is suggested by Parks [108]. He suggests that there might occur an instability of the Rayleigh-Taylor type in the ablation cloud because it is rotating due to the high density gradients at the boundary of the ablatant: *“the instability is driven by the  $\vec{E} \times \vec{B}$  rotation of the ablation column about its symmetry axis parallel to the  $B$  field. The radial  $E$  field comes from a radially varying floating potential,*

arising as a result of attenuation of the field-aligned hot plasma electrons streaming through the inhomogeneous ablation cloud density". There is some experimental evidence from impurity pellets that confirms this idea [62].

Finally the drift of the protecting cloud, which will be discussed in Chapter 4, could be a mechanism to explain the striations. When the cloud starts drifting away from the pellet, the pellet is exposed to a higher heat flux, and forms a new cloud.

Maybe also a combination of these four effects is possible.

Due to the ablation the pellet deposits matter very localized in the plasma, and this matter is transformed on a very short time scale to plasma. The rate of ablation determines the lifetime of the pellet in the plasma, and thus the penetration depth.

In fueling a fusion reactor it would be ideal if the pellet penetrates just to the plasma center, depositing a large fraction of its mass in the central plasma region. This is not feasible in these plasma conditions, but a maximum penetration should be pursued. When pellets are used for density profile control a variable penetration is desirable.

For RTP another possibility is that if too large pellets are chosen they will fly through the plasma and smash onto the vessel wall at the opposite side. This means that the solid hydrogen evaporates and causes massive gas puffing at the edge. This is often undesirable because it fuels the plasma at the edge which can have negative effects on plasma properties. Therefore, if at RTP only an edge perturbation is required, very small pellets and/or off-axis injection should be chosen.

If the pellet is completely ablated in the Ohmic regime, then almost the complete pellet is found back in the density increase of the plasma after injection (almost 100 % fueling efficiency). With auxiliary heating the fueling percentage is always observed to go down to about 60 % or less [93], so depositing matter on the proper radius is not the end of the story. This indicates that a fast outward movement of the deposited matter takes places on the time scale of pellet ablation. This is probably caused by the drift processes which will be discussed in Section 3.3.2. The movement has to be outward because otherwise the missing mass would have to pass the hot plasma center. This would be immediately visible because the center would then be cooled, which has never been observed.

### 3.3 Behaviour and movement of the ablatant

It is not at all obvious how the ablatant will behave after it is deposited in the plasma. An expansion parallel to the magnetic field will occur, but whether the ablatant is captured by the field, or moves along with the pellet, or even in opposite direction, is not clear a priori. For each case a model is available. The cloud behaviour can be divided in cloud movement (due to drifting or rotation) and cloud evolution (growth, oscillations). All these effects are closely related to the local electric and magnetic fields inside the cloud. In this Section the most important classes of modeling for these effects are reviewed.

### 3.3.1 Parallel ablatant expansion

After ionisation of the ablatant its movement is limited largely to the magnetic field lines [64]. Along these lines the cloud will expand due to the large pressure that is build up inside it. This parallel expansion probably propagates as a shock wave [73, 112, 119] and goes with a velocity in the order of the ion-sound velocity (so in the order of several  $10^5$  m/s at 10 eV, see table 2.3). This velocity is defined by the low  $T_i$  and  $T_e$  inside the ablatant and is not really influenced by the background plasma,

The expansion is driven by the pressure build up that is caused by the fast redistribution of the hot plasma electrons on a time scale (a few microseconds) on which the ions and thus the density are strongly peaked near the pellet trajectory (see table 2.3).

Since the density inside the ablatant is much higher than in the background plasma, the expansion is slowed down only a little. Only when the pressures and densities have become of the same order of magnitude this becomes important. The velocity of this expansion is usually dominant over the other movements of the ablation cloud as described below, however, since it is along the field lines this expansion is not very important in the view of particle losses.

The time needed to obtain a full equilibration of the plasma density after pellet injection in RTP is calculated in Section 6.5 and probably is somewhere between 95  $\mu$ s and 1.1 ms (at  $r=8$  cm). Because the electron ion energy exchange time is in the same order of magnitude (300  $\mu$ s for 100 eV) the ion temperature will equilibrate on this same time scale.

The equilibration of electron temperature depends on two separate processes. First the different electron populations (cold from the pellet and hot from the background plasma) mix and spread evenly on the flux surface in a typical time of the slowest electrons. Assuming these cold electrons are 10 eV this mixing would take about 4  $\mu$ s (see Section 6.5). Then the velocity distribution thermalises on the energy exchange time scale. This is a very strong function of the electron temperature, and changes from 1.1  $\mu$ s for 10 eV electrons to 5.6 ms for 300 eV electrons (see Table 2.3). However, an additional effect is that almost all of the faster hot electrons will pass through the dense ablation cloud itself, on the mixing time scale (so in a few microseconds). On that position there still is the large  $n_e$  low  $T_e$  ablation cloud, so this will probably dominate the energy loss process of the hot electrons. Inside the ablation cloud the temperature can be below 10 eV which would bring the energy exchange time down to below 1  $\mu$ s inside this cloud. It is not possible to give an estimate for the combined effect of the energy exchange by the background plasma and the ablation cloud<sup>7</sup>

---

<sup>7</sup>since energy exchange times are calculated for 1 temperature only; if 2 temperatures are present, it is not well defined by the simple formula I used. Since the collisionality goes up for lower  $T_e$  and the mean free path gets shorter, it is probably some kind of cascading effect: if an electron loses some energy, the loss will go faster and faster until the background  $T_e$  is reached. This is a large contrast to the exponential decrease that one would expect if this time would be a constant. Thus the energy exchange time I give may be substantially too large. This is very important for the

It was shown in [11], by studying non-thermal features on measured Thomson scattering spectra, that there really seems to be a non-thermal electron distribution function during the pellet ablation.

### 3.3.2 Cloud movement

Three types of drifts in the ablation cloud have been considered in the literature.

Due to the Lorentz transformation, the pure B-field in the laboratory frame is converted to an electric field  $\vec{E} = \vec{v}_{pellet} \times \vec{B}_{tor}$  in the pellet frame. This can give two effects [86]. Under open circuit conditions (case 1) it causes a polarization in the cloud giving rise to an  $\vec{E} \times \vec{B}$  drift with magnitude in the lab frame of

$$\vec{v}_{drift} = \frac{\vec{E} \times \vec{B}}{B^2} = \frac{\vec{v}_{pellet} \times \vec{B} \times \vec{B}}{B^2} = \vec{v}_{pellet} \quad (3.2)$$

This drift is in the direction of the pellet velocity and causes the ablation cloud to stick to the pellet.

In short circuit conditions (case 2) no large charge separation can build up but a continuous current is running through the ablation cloud. This current density  $\vec{j}$  can be described by the local  $\vec{E}$  field and the local conductivity  $\sigma$  as  $\vec{j} = \sigma \cdot \vec{E}$ . If no forces, besides the electric and magnetic field, are present on the particles (with charge  $q$ ) then the force equation reads:  $\vec{f} = \vec{0} = q \cdot \vec{E} + q \cdot \vec{v}_{cloud} \times \vec{B}$  so  $\vec{j} \times \vec{B} = -\sigma \cdot \vec{v}_{cloud} \cdot B^2$  (a possible pressure gradient is neglected here). This force causes a movement of the ablation cloud away from the pellet, and, in fact, lets the cloud stick to the magnetic field, stopping its movement in radial direction.

The third model (case 3) is based on the grad B drift [118]<sup>8</sup>. Due to the gradient in the toroidal field a drift velocity occurs of

$$\vec{v}_{\nabla B} = \frac{1}{2} \cdot v_{\perp} \cdot r_L \cdot \frac{\vec{B} \times \nabla \vec{B}}{B^2} \quad (3.3)$$

(here  $v_{\perp}$  is the velocity of the particles perpendicular to the field lines, and  $r_L$  is the Larmor radius). Due to the high collisionality particles can not complete an orbit around the torus, so the drift is not compensated by the rotational transform. This causes a polarization in opposite direction, compared to case 1, that starts to increase linearly with time as  $\vec{E} = \vec{v}_{\nabla B} \cdot n_e \cdot q \cdot t$ . This causes an  $\vec{E} \times \vec{B}$  drift in an outward direction, opposite to the pellet velocity, with linearly increasing velocity.

In Chapter 4 evidence is presented in favor of the third model.

A further process of interest is the poloidal rotation component of the plasma caused by the radial electric field. This will certainly affect the ablation cloud since

interpretation of the temperature measurements in the following Chapters. Especially the Thomson scattering measurements presented in Chapter 5 suggest that the actual energy exchange time is close to the mixing time.

<sup>8</sup>the possibility of this drift has been pointed out already by Kaufmann et al. [54] in 1986, but they did not report any modeling at that time. Also Parks et al. have modeled this effect [109].

these electric fields exist globally inside the plasma. In the literature experimental results reporting rotation of the ablation cloud are found in [83, 120]. On a fast framing CCD camera it was observed that the ablation cloud of an off-axis injected pellet moves in both poloidal and toroidal direction [120]. At the same time a clear change in radial plasma potential was observed on the ablation time scale. In [83] it is mentioned that a poloidal plasma rotation of 1 km/s is needed, superimposed on the parallel ablatant expansion, to explain measured interferometer density profiles.

### 3.4 Changes in the pellet movement

Due to the plasma rotation and the drift velocities of the plasma particles it cannot be expected that the pellet ablation will always be symmetric. This causes different heat fluxes and has as consequence that the ablation cloud is not symmetric around the pellet. It can also cause a momentum change of the pellet due to the “rocket” effect, especially for small pellets. This means that if one side of the pellet experiences much more ablation than does the other side, the out flowing particles will change the momentum of the pellet in opposite direction. Because the particles flow mostly along field lines the pellet changes momentum perpendicular to its original movement (for perpendicularly injected pellets) and will be bent in toroidal direction. This is quite often observed in tokamaks, especially at the end of the lifetime of the pellet, when the mass is at its smallest [155] (see Fig. 3.2 for an example). According to a model proposed by Egorov the deflection is also a function of the local current density (at least for carbon pellets) [25]. It can be increased when there is a population of fast particles (for example supra thermal electrons) present.

Recently also a radial acceleration of  $4 \times 10^5 \text{ m s}^{-2}$  was reported at ASDEX [99]. In this case the drifts in radial direction (see Chapter 4) probably drag the pellet along, because of a friction between the cloud and the pellet. This is the most likely explanation since pellets injected from the LFS were found to decelerate, and pellets injected from the HFS were found to accelerate.

### 3.5 Plasma response to the pellet

The local response of the plasma to the pellet has to be adiabatic, because a pellet injects only very cold particles, and almost no energy at all<sup>9</sup>. In the picture of a plasma consisting of good conducting flux surfaces this means that energy on a flux surface is conserved (because the pellet ablation time is usually much shorter than the energy confinement time). The plasma response on a flux surface now consists of several distinct steps. First a large mass perturbation is injected. Then the cold and hot electrons mix and thermalise on a very fast time scale of 1  $\mu\text{s}$  (see Sec.3.3.1)

<sup>9</sup>energy transport could happen by radiation or heat conduction by escaping neutral particles. The results presented in Sec. 5.6 show that for the Ohmic regime these effects can be neglected. In other plasma regimes they may be more important.

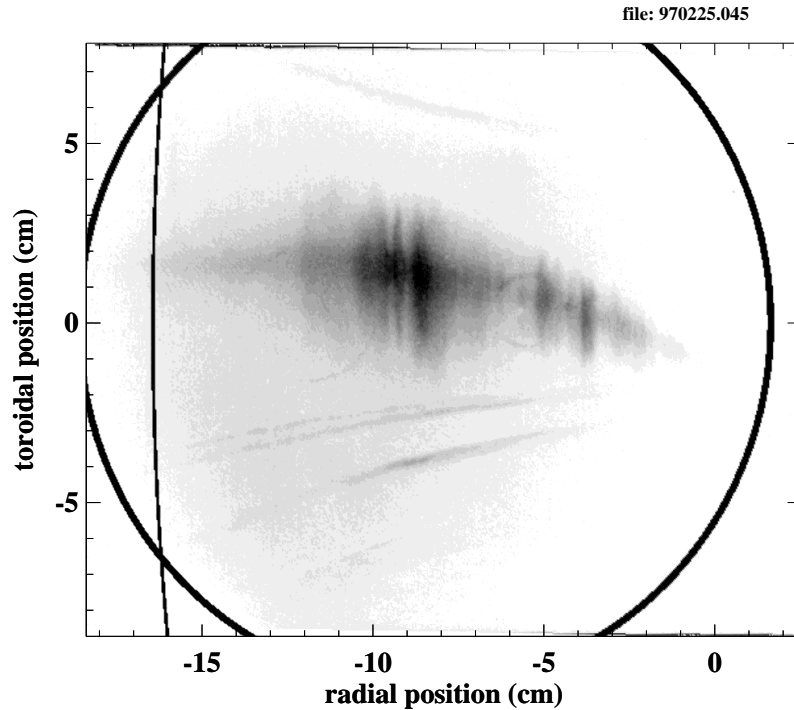


Figure 3.2: Photograph of a small pellet injected in an ECRH heated plasma (negative print). The fat line indicates the port that is used. The thin line indicates the plasma boundary. The pellet moves from left to right, and clearly deflects somewhat in the last part of the ablation. The vertical stripes are the so called striations.

while the density is still highly asymmetric. This causes a pressure gradient that drives the expansion on the flux surface. This also means that the temperature change of the plasma at a flux surface is only due to the spreading of the same amount of thermal energy over an increased amount of particles.

Besides this fueling and adiabatic cooling caused by the pellet, a whole zoo of other phenomena can be triggered by the pellet. This can be divided in global and local changes.

Local changes include the formation of snakes, small island like structures of higher or lower densities than the surrounding plasma, usually located at a rational value of  $q$  ( $1, 3/2, 2$ ) [38, 144]. These seem very stable and can survive for a long time (several seconds). A special class of snakes are the runaway snakes which are reported in [50]. These sometimes even survive a disruption of the plasma.

Another local event that can be triggered by the pellet is the so-called ELM<sup>10</sup>

<sup>10</sup>Edge Localized Mode



[66]: a sudden loss of confinement at the plasma edge for a short time, which only occurs for H-mode <sup>11</sup> plasmas, resulting in a loss of particles and energy of the plasma.

Another example of a local effect is the so called pre-cooling phenomenon. This is an extremely fast cooling of the plasma center on flux surfaces not yet crossed by the pellet [14, 18, 121]. This is usually seen when the pellet crosses/or is near the  $q=1$  surface. The reported inward velocities for this event range from about 1 km/s [121] to 10-20 km/s [14] and can not be explained by an increased diffusion (because then the already anomalous high diffusion has to be increased by another 2 orders of magnitude) [18]. More likely is a convective event, possibly similar to the drifting of the ablation cloud as described in Chapter 4 of this thesis. These fast effects have not been observed by density diagnostics, but since the density needs much more time to become distributed homogeneously on a flux surface than does the temperature [94], the convective event can easily be missed by a diagnostic. If the density is not spread evenly over the flux surface a diagnostic (probing a line integral or a point in space) may probe a spatial region not yet affected. So this is no proof that the two are decoupled, as is suggested for example by Milora [96].

A very intriguing observation is the so called non-local response of the plasma core to an edge perturbation of the plasma. When a pellet only cools the edge (due to shallow penetration, or off-axis injection) the plasma center reacts on a time scale much faster than can be explained by heat or current diffusion. For high  $n_e$  discharges the central  $T_e$  drops. Even more surprising, for low  $n_e$  discharges the central  $T_e$  rises. For ECH heated discharges this rise can be as large as 100 % [74, 75, 76] (for an example see Section 7.2). The most plausible explanation seems the improvement or weakening of the strength of an internal transport barrier in the plasma center, but by which mechanism is not known. In off-axis heated plasmas also a change in heat convection was needed to explain the observations.

Also the global current density profile in the plasma can be drastically altered by pellet injection. A well known example is the PEP-mode<sup>12</sup> [124]. This is an improvement in energy confinement of the plasma by 20-40 % [95] and is due to the production of a reversed magnetic shear region in the plasma center. This is caused by a large increase in central density and pressure due to the central pellet fueling (this shear reversal after pellet injection has also been observed at RTP [41]).

Another well established experimental fact is that the empirical “Greenwald limit” for the plasma density, for plasmas fueled by gas puffing, can be broken by applying pellet injection [68].

<sup>11</sup>H-mode = High confinement mode, a plasma state with a transport barrier close to the edge, reducing energy and particle confinement times. It is obtained by a strong external heating of the plasma.

<sup>12</sup>Pellet Enhanced Performance Mode

## 3.6 Using the pellet as a plasma diagnostic

The process of pellet ablation (hydrogen isotopes/impurity) can be used to diagnose certain plasma properties. In fact, there are as many possible properties that can be studied, as there are factors that influence the ablation process, or the resulting ablation. In order to do this, first a model has to be available that describes the ablation. Then, if all but one parameters are known, as well as the resulting ablation/fueling profile, this can be used to calculate the missing parameter.

A selection of these possibilities will be briefly discussed below to give an impression. This is by no means intended to be a complete overview.

### 3.6.1 Diagnosing the magnetic field

Several possibilities exist to use pellets for the determination of the magnetic field. The most widely used technique is the observation of the direction of the elongated ablation cloud by applying fast framing cameras [98, 135, 136]. Since the toroidal field strength is well known, and only the poloidal field has to be measured, this direction is sufficient since it defines the relative value of the one to the other. From this measurement also the current density profile can be deduced. This is, of course, a destructive measurement, because a pellet penetrating deep enough to obtain a measurement, influences the plasma considerably. The best accuracy that is seen in these measurements of  $q$  is about 10 to 15 % at half the minor radius, and increasing strongly if the plasma center is approached.

Another possibility is using the Zeeman effect, which affects the polarization of the emitted line-radiation as a function of the strength and direction of the magnetic field [77]. The accuracy in the described  $q$  measurement was about 20 %.

A third application uses the possible relation between the striations in the ablation process and the magnetic field (especially the rational values of  $q$ ) [110, 111]. If a specific  $q$ -value can be identified the accuracy of this method is only in the position, not in the  $q$ -value. For a typical RTP measurement this would give an error of  $\approx 7$  % in  $q$  at half radius. Thus it depends only on the determination of the pellet position (and the assumed locality of the line-emission at the pellet radius). As already was mentioned in Section 3.2 this method may only be a valid method in specific plasma conditions, and not applicable for the general case.

A last possibility is observing the pellet deflection (especially for small carbon pellets) which is supposed to be related to the local current density [25, 26]. The accuracy of this method is in the order of 20 %, but it is very sensitive to the presence of fast particle populations. Therefore also this method has limited applicability.

### 3.6.2 Diagnosing temperature profiles

When a model is chosen for the ablation rate, this can be used to determine the plasma temperature profile from the observed ablation rate [137]. This is only possible if all radial transport of heat and particles on the ablation time scale is neglected,

or can be precisely modeled. This measurement is only valid for the region of the plasma traversed by the pellet, so usually some edge region, and if the other factors controlling the ablation, like density and pellet size and velocity are precisely known. Also this method is very sensitive to the presence of fast particle populations, which probably have to be avoided to perform such a measurement.

### 3.6.3 Diagnosing fast particles

A localized concentration of fast particles (for example a beam of fast electrons produced by ECCD <sup>13</sup>) can easily be diagnosed by a pellet thanks to the clearly visible increase in ablation rate. An example of such a measurement is given by Egorov et al. [25]. They observed a narrow beam of fast electrons, probably runaways, when a pellet was shot into a plasma with ECCD. The position of this 2 cm wide beam could be determined with an accuracy of 1 mm.

Another possibility to diagnose the high density inside the ablation cloud makes use of high energetic particles. Ions (for example  $\alpha$ -particles from fusion reactions) that cross this cloud may be neutralized due to charge exchange with the cold neutrals inside the dense cloud, and will leave the plasma. After that they can be detected by an appropriate diagnostic. Fisher et al. showed that this diagnostic in combination with carbon pellets should work [28]. Petrov et al. used this diagnostic in combination with lithium pellets [114]. They could measure the  $\alpha$ -particle radial profile, and from that deduce the confinement and slow-down times of these particles for different energies.

### 3.6.4 Diagnosing fluctuations in E or B

Some attempts have been made to diagnose small structures seen on pellet photographs. These structures are deviations from a straight line, of the observed striations, when observed vertically from above. Drawin and Dubois suggest that these may be caused by pre-existing electric or magnetic field perturbations, and thus that the pellet may be used to diagnose these [22]. The authors think *“that large erratic deviations of the luminous striations from straight lines reflect the electric potential across pre-existing magnetic islands”*.

### 3.6.5 Diagnosing $Z_{\text{eff}}$

Injection of an impurity pellet can be used to measure a profile of the effective ion charge  $Z_{\text{eff}}$  if the  $T_e$  and  $n_e$  profiles are known. This is possible thanks to the known change in relative continuum emission of the plasma in this case [138].

---

<sup>13</sup>Electron Cyclotron Current Drive

### 3.6.6 Diagnosing (impurity) transport

The pellet ablation process results in bringing the plasma away from its equilibrium profile. The relaxation afterwards can be used to study plasma particle transport. This is usually done by simulating the transport and adjusting the model parameters until a good fit with the measured density information is obtained [6]. This method has also been applied at RTP, and the results are discussed in this thesis in Chapter 5.

The same is in principle possible for impurity pellet injection, only here the diagnostics are less precise, a full profile is usually not available<sup>14</sup>. However, also line-integrated or local results for example measured by spectroscopic diagnostics can be compared to transport models, and used to derive transport coefficients [9].

An even more detailed investigation should be possible for studying transport of impurities in the plasma, by using a two layer pellet. This has been tried by Sudo et al. [130, 131]. They produced a double layer pellet consisting of a small lithium-hydride (LiH) core as tracer, surrounded by a layer of polystyrene ( $=n(C_8H_8)$ ). In this way the injection of an impurity species can be done at a very localized radius (a range smaller than 0.03 times the minor radius should be possible theoretically). This would eliminate the uncertainties in the determination of the fueling profile, since the moment that the LiH pellet center starts to ablate can be observed precisely, as well as the moment of the end of the ablation.

---

<sup>14</sup>The mentioned reference uses single channel spectroscopy. In principle a tomographic setup is possible, and this would, after Abel inversion, give a full profile of the injected impurities. However, I don't know of any Tokamak where this has been done in combination with impurity pellet injection.

## Chapter 4

# Diagnosing pellet penetration

### 4.1 Introduction

To obtain reliable predictions for the local ablation rate for pellet fueling in a future fusion device, the validity of the currently applied theoretical models must be investigated. Important checks of a model are the penetration depth and the fueling profile.

The fueling profile has been measured at JET with two independent diagnostics, and this yielded a clear discrepancy. The increase in particle density as measured by Thomson scattering (3 ms after the pellet) showed a fueling located primarily at the edge of the plasma, while the  $H_\alpha$  line emission (Balmer alpha line), which is usually taken as a measure for the ablation rate, indicates a fueling primarily in the inner parts of the plasma [3].

These measurements have been repeated at RTP using three independent diagnostics: the  $H_\alpha$  detector, Thomson scattering and the interferometer<sup>1</sup>. The same discrepancy as at JET was found between the  $H_\alpha$  detector and the other two diagnostics.

At RTP also the penetration depth can be measured using two independent diagnostics. As first diagnostic the duration of the observed  $H_\alpha$  signal is used. An additional penetration diagnostic, a camera taking pictures of the ablation process, is also available. Both diagnostics are quite different in nature. The wide angle  $H_\alpha$  monitor has a high temporal resolution, but no spatial resolution. It must be assumed that the pellet velocity is constant AND that the light emission is very local

---

<sup>1</sup>To obtain a useful result,  $n_e$  profiles have to be taken some time after the end of the ablation, when the density is spread evenly on each flux surface again. At RTP this takes typically 100-200  $\mu s$  (see Section 6.5). At JET profiles are taken typically a few ms after the pellet. The fueling profile is now defined as the difference between a prepellet  $n_e$  profile and the postpellet profile. Note that in this way a net fueling profile is determined, in which fast redistributing effects, such as the fast drifts which are described in this Chapter, are already included. This can be very different from a local fueling profile obtained by modeling, as will be demonstrated in Section 4.4.

around the pellet, to obtain information on pellet penetration. The camera has just opposite properties, it has high spatial resolution but no time resolution, and thus gives a more direct observation of penetration.

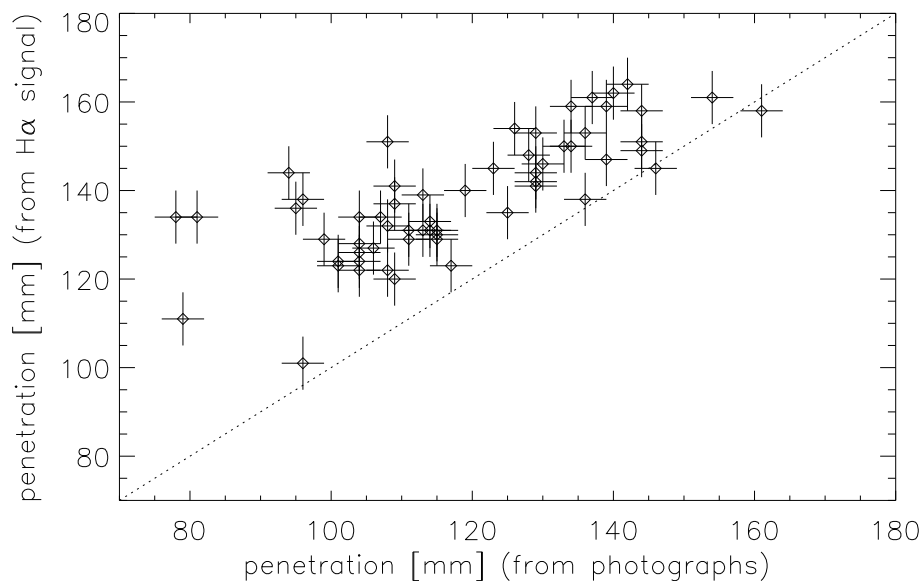


Figure 4.1: Comparison of pellet penetration depth as derived from photographs ( $p_{photo}$ ) and from  $H_\alpha$  signals ( $p_\alpha$ ). A systematic difference is seen with an average of  $\overline{(p_{photo} - p_\alpha)} \approx 20$  mm. The  $H_\alpha$  signal generally yields a deeper penetration than the photographs.

At RTP, the results of both diagnostics taken from identical shots yield a systematic discrepancy in penetration (see Fig. 4.1).

The subject of the remainder of this Chapter is to investigate what the reason is for both the observed discrepancies in fueling profile and penetration depth.

Two possible explanations have been investigated, both concerning modifications in the assumptions used in the interpretation of the  $H_\alpha$  signal.

The first possibility is a change in velocity of the pellet<sup>2</sup>. If the pellet would decelerate, but still ablate in the same time, it would not penetrate as deep into the plasma, compared to the case of constant velocity. Because the  $H_\alpha$  diagnostic only records the time it takes to ablate, it would not see a difference. However, on the photo camera the decreased penetration would be clearly visible. Thus a decrease in velocity would be able to explain the observation of the penetration

<sup>2</sup>A deceleration of LFS injected pellets has been observed at ASDEX [99, 100]. There a value of  $4 \times 10^5 \text{ ms}^{-2}$  was found. This is not high enough to explain the observed discrepancy in the pellet penetration that was observed at RTP.

depth discrepancy. The discrepancy in fueling profile can not be understood in this way.

The second possibility is a light emission not localized at the pellet position. A fast backward movement of the ablatant away from the pellet might explain both discrepancies. Suppose at the point of deepest penetration, a light emitting gas cloud moving away from the pellet is released. If this cloud moves towards the already cooled part of the plasma, than it might exist for some time, and all this time the pellet seems to penetrate further into the plasma if only the  $H_\alpha$  diagnostic is considered. Also the drifting cloud may be the cause for a redistribution of the ablated material, and thus be an explanation for the discrepancy in fueling profiles. Such a drift of the ablation cloud has been predicted on theoretical grounds [118]. In Sec. 4.9 the first experimental demonstration of this phenomenon is presented.

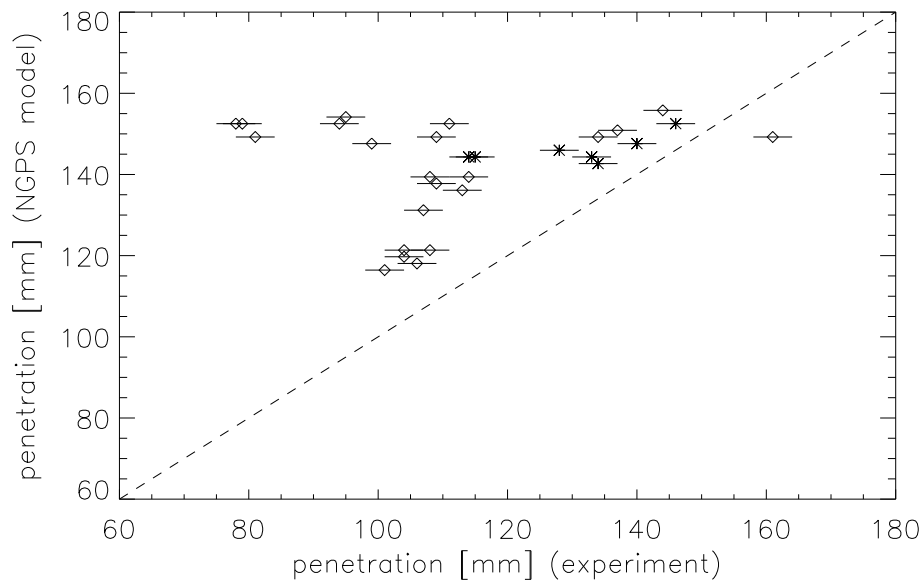


Figure 4.2: Calculated pellet penetration depth from the NGS model (see Section 3.2) compared to experimentally found penetration depth (from the camera diagnostic) for small (stars) and large (diamonds) pellets.

Finally in Fig. 4.2 a comparison is given of the measured penetration depth at RTP from the camera diagnostic and the theoretically calculated values from the NGS model (see Section 3.2). The measured values for  $T_e$  and  $n_e$  from TS have been used as input. Here it can be seen that the model is not even close to describing the measurements. If the penetration depth determined by the  $H_\alpha$  signal is used, the results will improve, but as will be shown further on in this Chapter, the  $H_\alpha$  signal is not a reliable diagnostic for determining pellet penetration. This illustrates that important ingredients of the ablation process are still missing in the model.

## 4.2 Structure of this Chapter

The remainder of this Chapter is divided in two parts, both describing partly the same results but from a different point of view.

First the construction of the new fiber array diagnostic is described, and a series of measurements that illustrate its use, in Sections 4.3 to 4.8.

Then the discovery of the new phenomenon of the drifting ablation cloud is presented in the form of an article in Section 4.9.

## 4.3 The fiber array diagnostic

A new diagnostic was built to check both possible explanations for the found discrepancies in penetration depth and fueling profile: a change in pellet velocity and light emission not local to the pellet position. The new diagnostic is the fiber array described in Sec. 2.3.3.

Measurements with this diagnostic revealed that the ablation cloud breaks loose from the pellet and drift rapidly outward, i.e. in opposite direction of the pellet velocity. This remarkable result was first presented at the EPS conference in Prague [58], and was published in Physical Review Letters [60] (PRL). This PRL is reproduced in Section 4.9.

Similar but less precise diagnostics have been used before. Martin [78] mounted a series of slits in front of an  $H_\alpha$  monitor in an attempt to observe the pellet velocity and possibly its changes inside the plasma. His results were puzzling because the different pulses that he expected when the pellet passes consecutive slits were very poorly resolved (and for some densities not resolved at all). He concluded that  $v_{\text{pellet}}$  remained constant inside the plasma, but his accuracy was poor.

Nishitani [104] used a 10 channel fiber-array to determine  $v_{\text{pellet}}$ , but he had no internal velocity measurement inside the pellet injector to compare with the results.

### 4.3.1 Some history of the fiber-array diagnostic at RTP

The first objective of this new diagnostic was to perform an alternative measurement of the pellet velocity during its flight through the plasma. From published results, and variations in the  $H_\alpha$  signal in our own experiments (striations), we expected the ablation cloud to be small in radial direction ( $\leq 3$  mm). Thus we expected the ablation cloud to be visible at only one channel of the new diagnostic at a time, and we decided initially to combine all 16 fibers into one detector (a photo multiplier tube). This turned out to be a big mistake (as can be seen from the results presented later on in this Chapter). The pulses of the 16 fibers overlapped so much that they could not even be distinguished anymore. The first obvious thought was that we had underestimated the ablation cloud size. We removed 8 fibers, increasing the separation between the fibers by a factor of two. Now some structure became visible but still the results were so irregular that a large overlap had to take place



between the 8 fibers. This ended with removing all but one fiber. Even now light was observed for a large part of the pellets trajectory through the plasma (see for example a signal like channel 12 in Fig. 4.5 in which light is seen for more than 10 cm of the pellet trajectory). After this we decided something special had to be going on, so we built a test setup of 5 detectors (photo diodes, each with its own amplifier and ADC). This revealed the first evidence for the outward drifting clouds, that seem so clear on the 16 channel diagnostic, and persuaded us to monitor all 16 channels independently.

### 4.3.2 Examples of data taken by the new diagnostic

In this Section experimental results from the fiber array diagnostic is presented for 6 different cases (labeled A, B, C, D, E and F) of plasma conditions and diagnostic configuration. In shot (A) a pellet was shot in a low  $T_e$  plasma, in shot (B) in a normal Ohmic plasma, and in shot (C) in an additionally heated plasma. In shot (D) the pellet was injected into a plasma in the slideaway regime. Shot (E) was again a normal Ohmic shot, but now the diagnostic configuration was rotated to view along a toroidal line, instead of the usual radial line. Finally, shot (F) is a special case. It also is a normal Ohmic plasma, but in this case a strange fast drift effect going ahead of the pellet is observed on the Thomson scattering profiles. More detailed shot conditions for each of those 6 cases are given in Table 4.1 on page 51. Each shot in this Chapter is a specimen of a series of similar shots.

Following the usually accepted picture of a cigar shaped ablation cloud which is localized in radial direction around the actual pellet position, we expected each of the channels to give a short pulse. The width of the pulse should then be a measure of the ablation cloud dimensions in radial direction. This is indeed seen for pellets injected in plasmas having electron temperatures below  $\approx 500$  eV. This situation can for example be obtained by injecting the pellet off-axis, or by injecting in a plasma shortly after a period of off-axis ECH [45]. An example of the second type is shown in Fig. 4.4 (shot A).

The  $T_e$  and  $n_e$  profiles for each of these cases are shown in Fig. 4.3. The profiles are taken just before the pellet is injected.

As the pellet passes the viewing lines of the different channels a pulse of light is observed, showing that the ablation cloud is located close to the pellet in radial direction. The onset of these pulses is consistent with the pellet velocity and timing as determined inside the pellet injector.

A second example is given for Ohmic plasma conditions (shot B). This gives a completely different picture (see Fig. 4.5). Here the pulses are much broader in all channels. Besides that, separate peaks can be distinguished after the passage of the pellet, which we will refer to as secondary peaks.

These are clearly correlated in different channels (see for example the parallelogram in Fig. 4.5).

A third example shows the results for a pellet injected in a plasma during central ECH (320 kW) (see Fig. 4.6).

Table 4.1: The plasma and pellet parameters for the shown experimental results. Given are the central density,  $n_{e,0}$ , the central temperature,  $T_{e,0}$ , the plasma current,  $I_{pl}$ , toroidal field,  $B_{tor}$ , safetyfactor  $q_a$ , effective ion charge,  $Z_{eff}$  (all measured just before the pellet was injected), and the pellet velocity,  $v_{pellet}$ , pellet size,  $m_{pellet}$ , pellet radius,  $r_{pellet}$  and pellet penetration,  $l_{penetration}$ . All pellets were injected horizontally, except shot F, which was injected at an angle of  $4^\circ$ .

| shot<br>shot nr   | A (see Fig. 4.4)<br>r19980421.034 | B (see Fig. 4.5)<br>r19980417.019 | C (see Fig. 4.6)<br>r19980721.047               |          |
|-------------------|-----------------------------------|-----------------------------------|---|----------|
| $n_{e,0}$         | $5.7 \times 10^{19}$              | $3.9 \times 10^{19}$              | $5.2 \times 10^{19}$                            | $m^{-3}$ |
| $T_{e,0}$         | 500 †                             | 900                               | 1450 ***  | eV       |
| $I_{pl}$          | 84.3                              | 101                               | -81.5   | kA       |
| $B_{tor}$         | 2.27                              | 2.05                              | 2.01  | T        |
| $q_a$             | 5.03                              | 3.79                              | 4.61  |          |
| $Z_{eff}$         | 1.7                               | 2.6                               | 2.0   |          |
| $v_{pellet}$      | 962                               | 986                               | 852   | m/s      |
| $m_{pellet}$      | $0.5 \times 10^{19}$              | $1.9 \times 10^{19}$              | $1.7 \times 10^{19}$                            | atoms    |
| $r_{pellet}$      | 0.3                               | 0.4                               | 0.4   | mm       |
| $l_{penetration}$ | 15                                | 26 ‡                              | 17*   | cm       |
| shot<br>shot nr   | D (see Fig. 4.7)<br>r19980417.024 | E (see Fig. 4.8)<br>r19980417.025 | F (see Figs. 4.12, 4.13, 4.16)<br>r19980610.031 |          |
| $n_{e,0}$         | $1.9 \times 10^{19}$              | $4.4 \times 10^{19}$              | $2.0 \times 10^{19}$                            | $m^{-3}$ |
| $T_{e,0}$         | 790                               | 820                               | 850   | eV       |
| $I_{pl}$          | 104                               | 101                               | 78.5  | kA       |
| $B_{tor}$         | 2.01                              | 2.01                              | 2.17  | T        |
| $q_a$             | 3.61                              | 3.72                              | 5.16  |          |
| $Z_{eff}$         | 1.6                               | 2.4                               | -   |          |
| $v_{pellet}$      | 910                               | 1003                              | 1013  | m/s      |
| $m_{pellet}$      | $1.8 \times 10^{19}$              | $1.9 \times 10^{19}$              | $1.9 \times 10^{19}$                            | atoms    |
| $r_{pellet}$      | 0.4                               | 0.4                               | 0.4   | mm       |
| $l_{penetration}$ | 9**                               | 23 ‡                              | 5.6 ††  | cm       |

† In this shot the pellet was fired 7 ms after switch off of off-axis dominant ECRH ( $\approx 300$  kW).

‡ these pellets penetrate beyond the plasma center, penetration was determined by end of the  $H_\alpha$  signal (this is beyond the reach of the new diagnostic).

\* this was determined by using the end of the  $H_\alpha$  signal, according to the new fiber array diagnostic the penetration for this shot was only  $\approx 12$  cm.

\*\* penetration determined by using the  $T_e$  profile measured by TS 300  $\mu s$  after the end of the ablation, and looking at the unperturbed part of the profile.

\*\*\* in this shot 320 kW of additional dominant central ECRH was applied.

†† this value is based on the closest approach of the pellet when injected at an angle of  $4^\circ$ . As can be seen in Fig. 4.16 the pellet traveled beyond this point, moving radially outward again until it almost left the plasma again.

Here the secondary peaks are much stronger than in the Ohmic case (the sensitivity along the y-scale is reduced by 50 % compared to Figs. 4.4, 4.5 4.7 and 4.8). In this case the secondary peaks persist longer than the primary ones, and also their luminosity is higher.

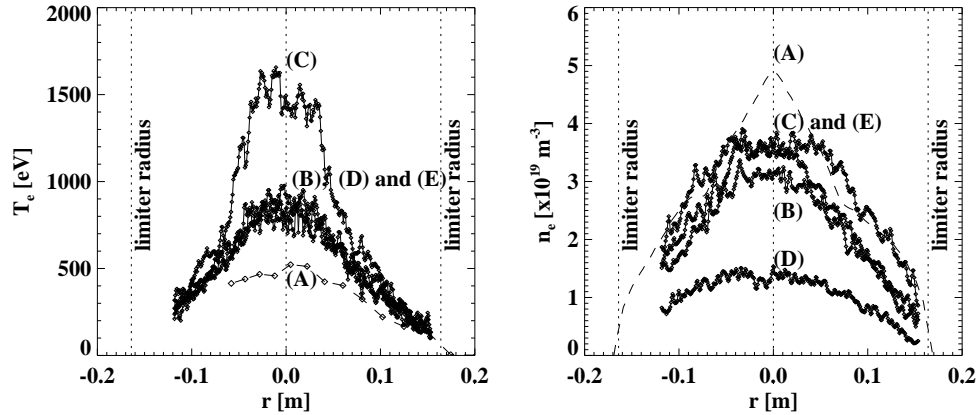


Figure 4.3:  $n_e$  and  $T_e$  profiles just before the pellet was injected into the plasma for each of the 5 discussed cases (A) to (E). The profiles labeled (B) to (E) have been measured by Thomson scattering (not corrected for the Shafranov shift). The  $T_e$  profile labeled (A) (dashed line) was measured by the radiometer. The  $n_e$  profile labeled (A) (dashed line) was measured by the interferometer. The profiles for shot (F) are given in Figs. 4.12 and 4.13.

A fourth example (shot D) shows the results for a pellet injected in a low density plasma (see Fig. 4.7), which was in the slide-away regime. This is a low density plasma in which a large non-thermal electron population exists that carries the majority of the plasma current [122].

Here a completely different situation is seen. The pellet seems surrounded by a very large ablation cloud, and no secondary peaks or substructures at all are seen in the signals. The signals are strongest and have the longest duration near the boundary of the plasma (channel 16). The cloud vanishes first on channel 11, then on channel 12, then on channel 13, etc. These measurements suggest that this could be interpreted as a continuous flow of the ablatant from the pellet towards the plasma boundary. This flow only ends when the pellet is completely ablated, and therefore the light emission stops first at the more central channels. Additional support for this hypothesis is the fact that these low density shots show a very poor fueling efficiency (between 30 and 50 %). For shot (D) the fueling efficiency was

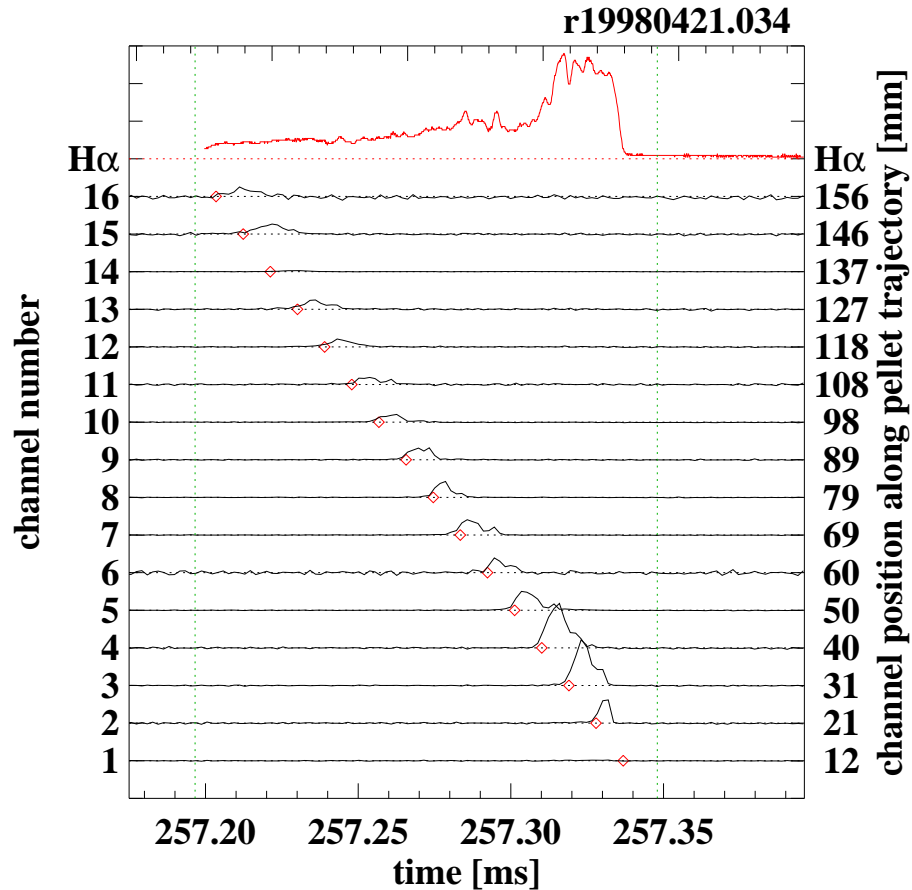


Figure 4.4: Example of the pellet ablation process as observed by the fiber-array (shot A) for a pellet injected in a relatively cold plasma (7 ms after switch off of off-axis ECH [45]). The diamonds indicate the expected passage times of the pellet using the measured pellet velocity and timing in the injector. The vertical dashed lines indicate the moments that the pellet passes the limiter radius and the plasma center (if it would penetrate that far). The top trace is the wide angle  $H_{\alpha}$  monitor. A clear peak is seen at the passage of the pellet at each channel.

35 %, determined by the interferometer 5 ms after ablation. For higher density Ohmic plasmas the fueling efficiency is usually close to 100 %.

Finally an example is given (shot E) in which the fiber array was rotated over 90 degrees. Now the toroidal extension of the cloud can be followed in time at one radial position (see Fig. 4.8). It can clearly be seen that the primary pulse and the secondary pulses have a different toroidal extension and position. Also the last

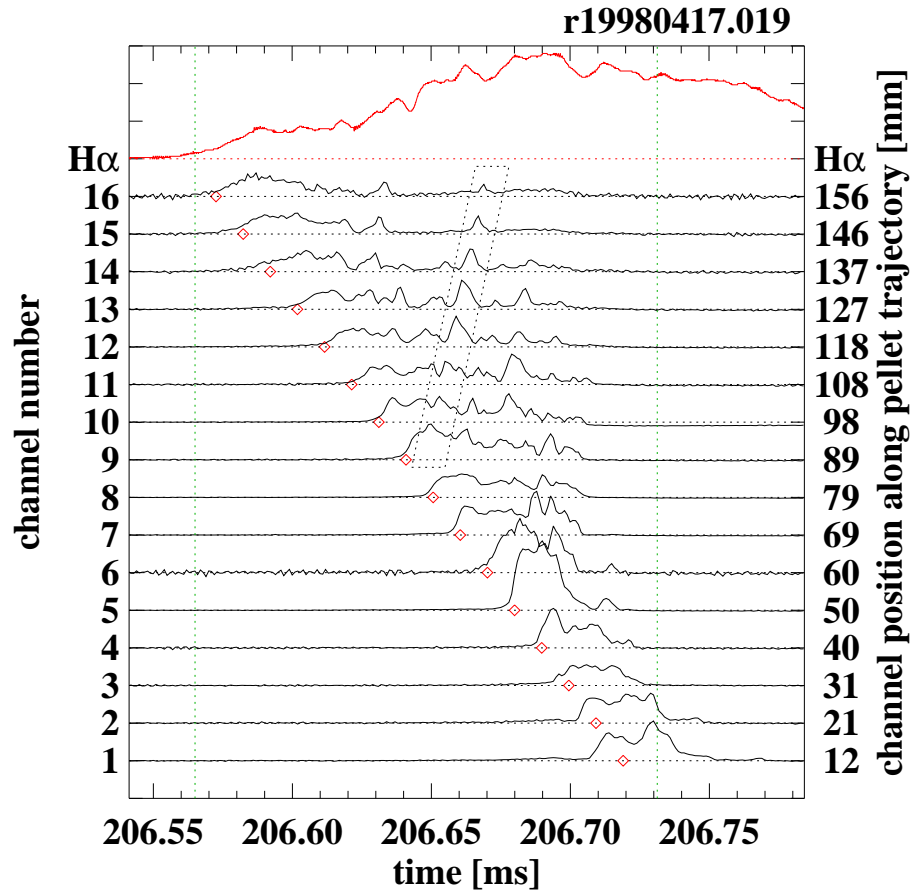


Figure 4.5: Example of the pellet ablation process as observed by the fiber-array (shot B) for an Ohmic plasma, plotted in the same way as in Fig. 4.4. Besides much broader peaks at all channels after passage of the pellet also a sequence of peaks can be recognized which are correlated on separate channels. An example of this is highlighted by the parallelogram. This sequence of correlated peaks shows the presence of a light source which moves faster than the pellet and in opposite direction.

few secondary pulses are shifted in toroidal direction, compared to the first one, in the direction of the toroidal plasma rotation (this is confirmed by photographs, see Section 6.7, Fig. 6.7 on page 130).

To show this more clearly 7 time windows have been defined (see Fig. 4.8). For each channel the maximum signal value was determined in each of the time windows. These maxima have been plotted for each of the chosen times as a function of channel

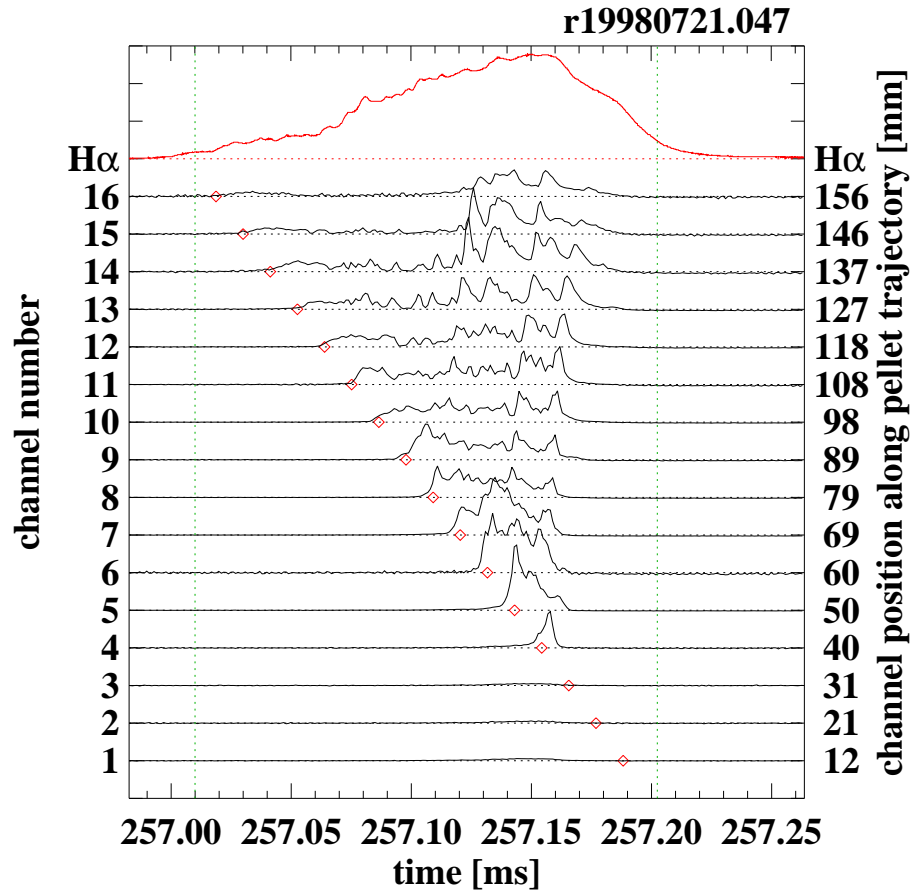


Figure 4.6: Example of the pellet ablation process as observed by the fiber-array (shot C) plotted in the same way as in Fig. 4.4. In this case the pellet was injected in a centrally ECH heated plasma. Clearly the secondary peaks have much higher amplitude on the outer channels, than the primary pulse (channels 10-16).

number in Fig. 4.9.

From this plot it can clearly be seen that the toroidal position of maximum intensity shifts towards negative toroidal direction for later times. This is further discussed in Section 4.3.5.

The secondary peaks do not seem to reproduce in detail. They do not develop at regular time intervals or positions, and have different magnitudes and lifetimes, even with very similar plasma and pellet conditions. The only clear dependences are on

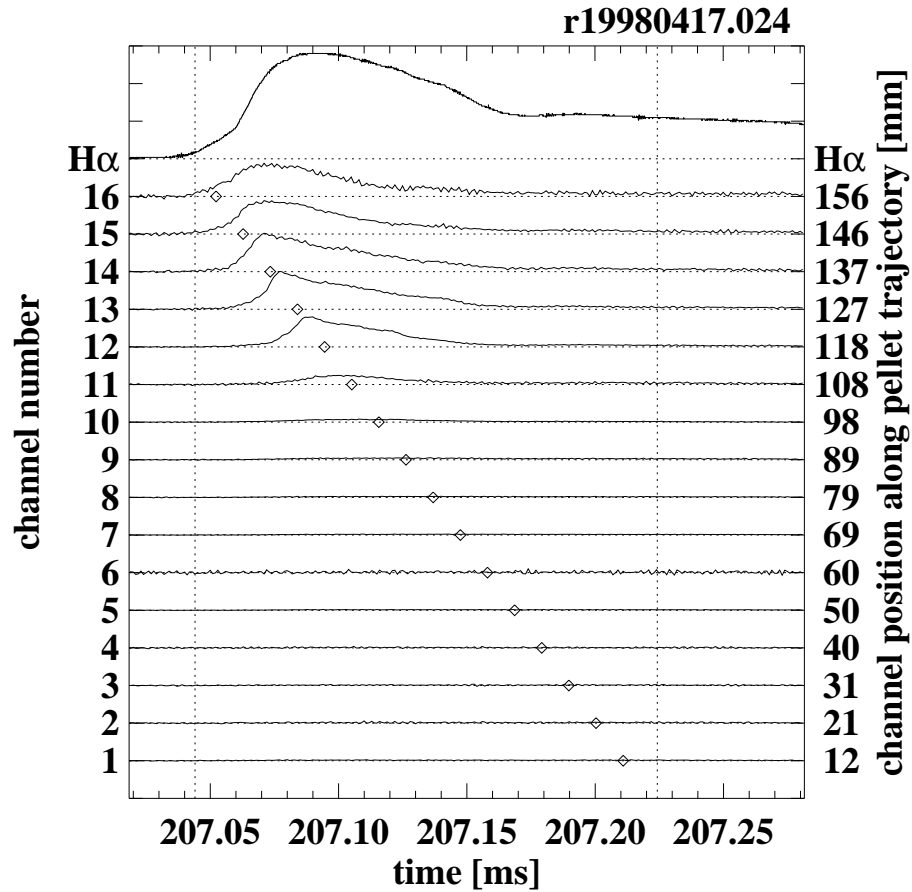


Figure 4.7: Example of the pellet ablation process as observed by the fiber-array (shot D) plotted in the same way as in Fig. 4.4. In this case the pellet is injected in a low density plasma with a large population of supra-thermal electrons. The ablation cloud seems much larger than in the previous cases, and no secondary peaks can be recognized. This may also be interpreted as a continuous stream of ablatant from the pellet to the plasma boundary.

the electron temperature and the absence or presence of supra-thermal electrons<sup>3</sup>.

<sup>3</sup>Recall that only the magnitude in the light emission scales with  $T_e$ . These results do not show directly that the ejected mass is proportional to  $T_e$ . The fact that the fueling efficiency for additionally heated discharges diminishes does point in this direction, however.

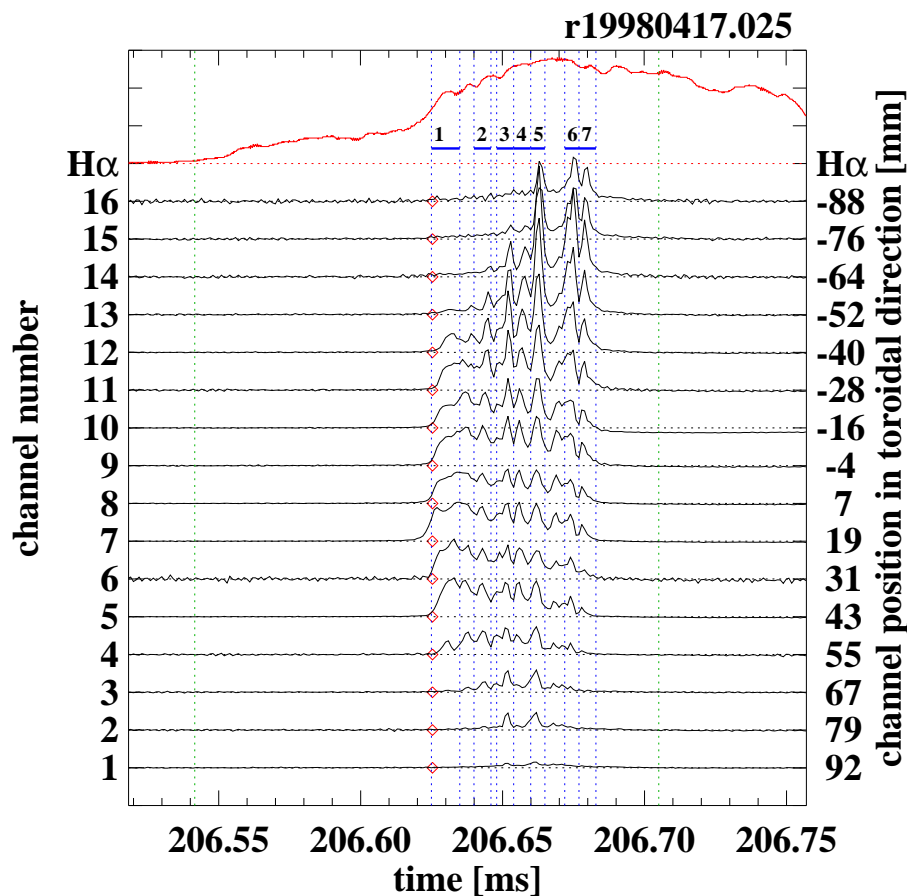


Figure 4.8: Example of the pellet ablation process as observed by the fiber-array (shot E) plotted in the same way as in Fig. 4.4. In this case the pellet was injected in an Ohmic plasma but now the diagnostic was rotated over 90 degrees. Also now it can clearly be seen that first a primary pulse is detected, connected to the pellet passage of this radius. After that a series of secondary pulses is seen. A series of 7 time windows is defined by the vertical dotted lines. This is used to study the toroidal shape of the pulses in more detail, and is further explained in the text.

### 4.3.3 Pellet velocity measured by the fiber array

The pellet velocity for shot (A) measured with the fiber array is  $980 \pm 60$  m/s, in agreement with the value measured inside the injector ( $962 \pm 1$  m/s). The uncertainty is mostly systematic and due to the limited accuracy in the position calibration of the viewing lines.



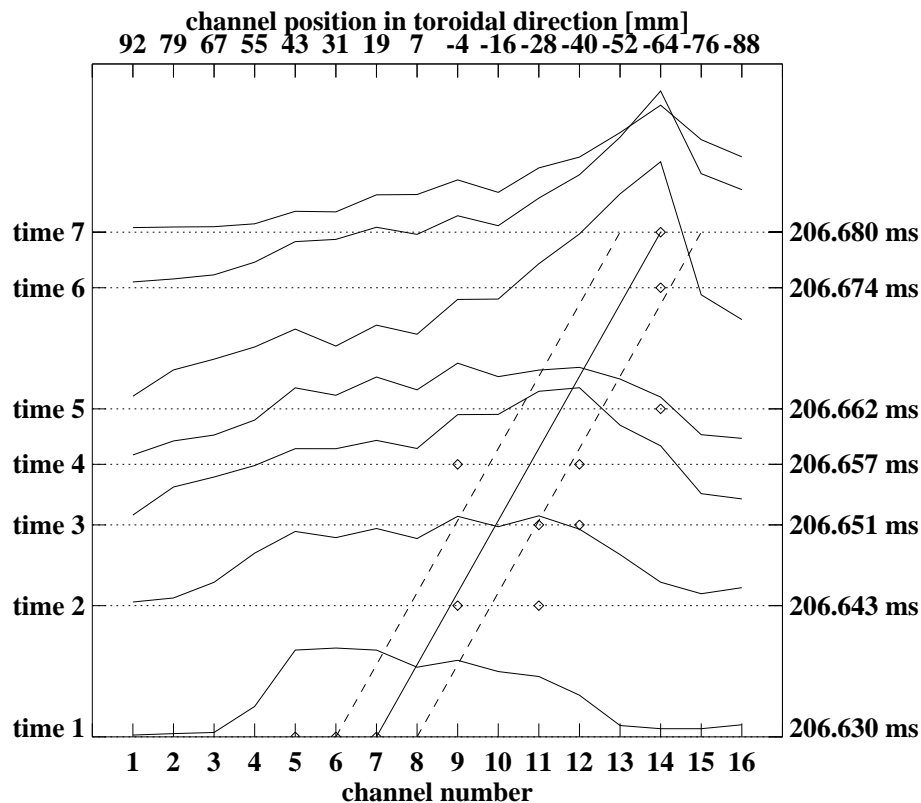


Figure 4.9: Intensity of the observed ablation cloud of shot E (see Fig. 4.8) for a number of pulses. The diamonds indicate the channel numbers with highest intensities for each time. The diagonal lines give an indication of the toroidal displacement of the maximum intensity, which is possibly related to the toroidal plasma rotation.

For shot (B) and (C) the first peak can not easily be recognized, so the rising edge (the value at half peak height) has been taken as moment of pellet passage for each channel. For shot (B) the result was  $1080 \pm 60$  m/s. The velocity measured with the fiber array for shot (C) is  $910 \pm 80$  m/s. The values determined inside the injector were  $986 \pm 1$  m/s (shot B) and  $852 \pm 1$  m/s (shot C). The width of the first peak can not easily be recognized in these cases so this introduces an extra error, which might be responsible for the difference in the result for shot (B). A different interpretation for this discrepancy in velocities may be that the pellet slows down in radial direction. This is reported to happen also in ASDEX [99, 100], where a deceleration of  $4 \times 10^5 \text{ m s}^{-2}$  was found. Within the  $166 \mu\text{s}$  of the ablation that can be observed on the fiber array for shot (B) this would mean a velocity change of 66

m/s, if the same acceleration would occur at RTP. This would be enough to explain the discrepancy.

The same exercise has been tried for shot (D). As can be seen in Fig. 4.7, especially on channels 11 to 14, the light emission starts at several channels already before the pellet has arrived. Several explanations are possible for this observation. The pellet might accelerate, or the ablation cloud might drift in radial inward direction. Another possibility is a poloidal drift of the ablation cloud. Because we observe the process from above this would appear to be in radial inward direction also. Finally a large amount of fast neutrals could be produced by charge exchange. These would then both move ahead of the pellet, causing the light emission in front of the pellet, and move backwards out of the plasma, causing the poor fueling percentage. It cannot be decided, from the data, which mechanism is active in this shot.

Assuming the rising flank of the light pulse coincides with the time of passage of the pellet at each channel, the data yields a velocity of  $1.7 \pm 0.5$  km/s which is way above the velocity of  $910 \pm 1$  m/s detected inside the pellet injector. If this were the case than the pellet would be experience an acceleration in the order of  $10^7$   $m^2/s$ .

The data from shot (E) do not allow determination of the pellet velocity.

#### 4.3.4 Ablation cloud size

We have observed the neutral cloud surrounding the pellet using the fiber array. For pellet injection in a cold plasma (shot A, see Fig. 4.4) the average width of the pulses on each channel is  $16 \pm 5$   $\mu s$  corresponding to a width of the ablation cloud of  $\approx 12 \pm 4$  mm.

In most models the radial cloud size is assumed to be determined by the ionisation radius  $r_i$ . Using an expression derived by Parks [106] we obtain  $r_i \approx 1$  to 3 mm for RTP. This is an order of magnitude smaller than the observed ablation cloud.

In hotter plasmas the cloud size increases and parts of it start drifting away. Since these two processes, the drift and change in size of the cloud, interfere it is not possible to determine the ablation cloud size around the pellet for the data presented for the Ohmic (shot B) and additionally heated cases (shot C).

In shot (D) the pulses are extremely long, lasting 50 to 100  $\mu s$  on the outer 7 channels. This would correspond to a radial size of the ablation cloud of 4.5 to 9 cm. To make this possible the ablation has to be much more intense than for the high density cases. This is thought to be related to the observations of bad penetration for regimes with non-thermal particle populations on other tokamaks [92].

The toroidal view of the fiber array of an Ohmic plasma (shot E) yields information on the toroidal extension of the cloud. Channel 7 is the first one that starts rising, so this one must be closest to the pellet trajectory. The channels above and below show a rise at a somewhat later time. Only the channels 4 to 13 show a clear rise at the passage of the pellet which gives a toroidal length of the primary ablation cloud of about  $107 \pm 10$  mm.

### 4.3.5 Toroidal movement of the ablation cloud

From the time difference in first rise of the first pulse in Fig. 4.8 a toroidal velocity of the ablatant can be determined of  $12.6 \pm 2$  km/s in negative direction (towards channel 13) and  $8.4 \pm 2$  km/s in positive direction (towards channel 4).

The positive direction in Figure 4.8 is directed along the plasma current. Thus the ablation cloud has a higher velocity in the counter current direction and on average moves with  $\approx 2$  km/s in the same direction as the normally observed toroidal plasma rotation. This movement therefore could well be caused by this rotation (see Chapter 6).

Also the secondary peaks are clearly seen. These have a much larger toroidal extension, to one side mostly beyond the limits of the diagnostic. However, the maximum intensity of the clouds can be observed as was shown in Fig. 4.9. From the observation that the pellet is first observed on channel 7 (time window 1), and that the last secondary pulse has its maximum on channel 14 (time window 7) also a cloud velocity can be calculated. When a radial drift of 5 km/s and a straight pellet trajectory are assumed it follows that the clouds causing the secondary pulses move in toroidal direction with a velocity in the order of 10 km/s. A possible reason why this velocity is much larger than the average toroidal velocity of the first pulse, is that there has been much more time for momentum transfer between the cloud and the background plasma. Thus the value of 10 km/s determined from the secondary pulse is probably closer to the actual plasma rotation than the 2 km determined from the primary pulse. An alternative explanation may be that the plasma can have a strongly varying toroidal rotation, depending on minor radius. Since the different pulses were produced in different parts of the plasma they may show evidence for such a rotation profile. From this result it can be concluded that this toroidal configuration of the fiber array could be used as a new plasma rotation diagnostic. Plasma rotation will be further discussed in Chapter 6.

An alternative explanation for the difference between the found rotation velocities of 2 and 10 km/s would be a toroidal deflection of the pellet. There is no experimental evidence available to support this.

### 4.3.6 Radial movement of the ablation cloud

The observation of the secondary peaks is interpreted as a not fully ionized cloud moving away from the pellet through the plasma. The movement has a velocity component along the pellet trajectory but in opposite direction to the pellet velocity. For the highlighted peaks in shot (B) the velocity was determined to be  $3.5 \pm 0.6$  km/s. In other cases it has been observed to be as high as 10 km/s.

The results obtained with the fiber array may be helpful in determining the importance of movements of the ablation cloud. The possibility of these effects have been pointed out by Kaufmann et al. [54] and Rozhansky et al. [118] (case 3 in Section 3.3.2).

The observation of this cloud drifting away from the plasma contradicts the

theories presented in Section 3.3.2 as case 1 and 2. These would yield a sticking of the cloud to the pellet, or a stopping of the cloud, due to a sticking to the field lines.

Applying RTP values in the formulas given by Rozhansky [118] a velocity of  $\approx 3$ -10 km/s is expected. The simulations by Rozhansky yielded the relation  $x = t^2/2$  and  $u_x = t$  in which  $t$  is a dimension less time  $t = t_r c_s / \sqrt{l_i R}$ ,  $x$  is a dimension less position  $x = x_r / l_i$ , and  $u_x$  is a dimension less velocity  $u_x = u_r / (c_s \sqrt{l_i / R})$ . The laboratory time  $t_r$ , position  $x_r$ , and velocity  $u_r$  can be calculated using the ion sound velocity  $c_s = \sqrt{(T_e + T_i) / m_i}$ , the ionisation radius  $l_i$  (=ablation channel width), and the tokamak major radius  $R$ . The result is:  $x_r = t_r^2 c_s^2 / (2R)$  and  $u_r = t_r c_s^2 / R = c_s \sqrt{2x_r / R}$ . With  $R = 0.72$  m, and  $c_s = 44$  km/s (inside the ablation cloud, see Table 2.3), a cloud velocity of 21 km/s is found at  $x_r = 8$  cm. The average cloud velocity over this 8 cm trajectory, which is the observable property, is 10 km/s. The velocity is proportional to  $c_s$ , and  $c_s$  is proportional to  $\sqrt{T}$ . So this velocity changes to 6.5 km/s at 8 cm for  $T=1$  eV, and in that case the average velocity over this 8 cm trajectory is 3.2 km/s.  $T_e$  inside the ablation cloud is not well known, so it could be anywhere in this 3-10 km/s range. This is in good agreement with the observations.

A different view of the same process would be to consider the fluid picture instead of the particle movements. The build up of energy in the cloud caused by equilibration of temperature at a timescale much shorter than the spreading of the particles away from the pellet leads to an increasing beta (dimensionless pressure). If this beta reaches a critical value the plasma equilibrium is lost and the cold ablatant bubble will be pushed outward (to lower magnetic field). The new cloud has to build up its beta again, so the pulsating nature of the process is easy to understand in this picture. It can also be understood why the frequency of ejected clouds is higher for additionally heated plasmas. In that case the build up of beta is faster because of the extra available energy. Beta will also reach a higher value (because drifting away takes some time after the threshold is reached), so the higher drift velocity in this case may be understood.

The observations emphasize the importance of inboard side pellet injection (for which the observed drift would improve the possibility of fueling the plasma center).

### 4.3.7 Size of the drifting cloud

With the known velocity and the known size of the observed region of the system the radial size of the object which moves away from the pellet can be calculated to be  $\approx 14$  mm (channel 12, shot B), comparable to the cloud around the pellet as observed in shot (A).

Also in shot (E) the secondary pulses can easily be recognized. They have an estimated width of about  $3 \mu\text{s}$  which corresponds to a radial width of the cloud of  $\approx 9$  mm (assuming a drift velocity of 3.5 km/s), i.e. in the same order of magnitude as for shot (B).

For most observed clouds, the toroidal width of the drifting cloud can not be determined because they exceed the range of the diagnostic (at one side). Only the peak at 206.642 ms in Fig. 4.9 (shot E) still fits onto the diagnostic. It is

observed from channel 3 to 14 and thus the secondary cloud responsible for it has a toroidal dimension of  $131 \pm 10$  mm. So probably the toroidal dimension grows as the cloud moves further away from the pellet. However, because the cloud also moves in toroidal direction (as was discussed in Section 4.3.5), it moves quickly out of sight of the diagnostic. Another complicating effect is the possible change in toroidal cloud size at the pellet position itself. Thus the toroidal development of the drifting clouds is very uncertain.

If it is assumed that the cloud at the pellet radius has a constant toroidal size of 107 mm (this size was observed for one time in shot (E), see Fig. 4.9) then the toroidal growth rate of the drifting cloud may be estimated. From the time difference between the arrival of the primary pulse and this secondary pulse, it follows from this assumption that the toroidal growth rate of the secondary pulses is  $8 \pm 3$  km/s. This gives a minimum value for the toroidal growth rate of the ablation cloud, which is important for determining transport in the toroidal direction and the mixing time on the flux surface.

### 4.3.8 Penetration depth measured by the fiber array

From the last visible pulse in shot (A) (on channel 2) it follows that the penetration of the pellet was  $\approx 15.0 \pm 0.5$  cm. This agrees with the value obtained by the end of the wide angle  $H_\alpha$  signal yielding a value of  $15 \pm 1$  cm. This shot clearly proves the correct functioning of the fiber array diagnostic.

The pellet in shot (B) penetrates beyond the reach of the fiber array, so for this shot it is not possible to determine the penetration in this way.

For shot (C) the pellet penetration found using the wide angle  $H_\alpha$  signal is  $17 \pm 1$  cm while the fiber array gives a penetration of  $13.0 \pm 0.5$  cm, if it is assumed that the end of the pulse on channel 4 also indicates the end of the pellet ablation. It can also clearly be seen that the last ejected secondary peak lives at least  $15 \mu\text{s}$  longer than does the pellet. This demonstrates that there are cases in which it is impossible to use the wide angle  $H_\alpha$  signal to precisely determine the pellet penetration.

In conclusion, determining pellet penetration from the LFS using the wide angle  $H_\alpha$  signal only gives a maximum possible penetration by assuming that no matter drifts away from the pellet. Better estimates for LFS injection are obtained by using a (photographic) camera.

For shot (D) pellet penetration was very poor, at most  $9.0 \pm 0.5$  cm according to the  $T_e$  profile measured by Thomson scattering  $300 \mu\text{s}$  after the end of the ablation. The fiber array gives a penetration of only  $6.0 \pm 0.5$  cm. This difference is probably a consequence of diffusive radial transport within this time of  $300 \mu\text{s}$ .

The  $H_\alpha$  signal shows a long tail in this case. This is probably  $H_\alpha$  emission by a large amount of hydrogen gas in the scrape off layer. Clearly this signal is not suited at all in this case to determine the penetration depth.

If a neutral cloud can exist for some time after the complete ablation of the pellet, then the determination of the pellet penetration in the plasma using the  $H_\alpha$  signal becomes questionable. This could be an explanation for the discrepancy that we

have observed between the penetrations derived from photographs and from the  $H_\alpha$  signal (see Section 4.1). Let us assume that a cloud departs at the moment the pellet is gone, and travels at 5 km/s, then it would need  $\approx 30 \mu\text{s}$  to travel from the plasma center to the edge. For a pellet with a velocity of 750 m/s this would appear on the large angle  $H_\alpha$  detector as an extra penetration of 25 mm. This matches with the observed discrepancy shown in Fig. 4.1.

#### 4.4 Connection between fueling and drift effects

A consequence of the presented results is that it is not to be expected that the  $H_\alpha$  signal is proportional to the local fueling rate. Also the fueling profile found a few hundred  $\mu\text{s}$  after the pellet is ablated can not be expected to be equal to the local fueling rate.

Direct measurements of the fueling profile from TS and interferometry support this statement<sup>4</sup>. Reference [3] shows an example of the difference between the  $H_\alpha$  signal and the fueling rate at JET. As example for RTP a pellet was selected with only modest penetration (8.0 cm according to the fiber array diagnostic). The  $n_e$  profiles, just before the pellet was injected and just after the end of the ablation, are shown, measured by two independent diagnostics (TS and interferometry, see Fig. 4.10). They agree very well with each other, both before and after the ablation of the pellet. The difference in the profile between those 2 times<sup>5</sup>, which is by definition the resulting fueling profile, is compared to the measured wide angle  $H_\alpha$  signal in Fig. 4.11. They clearly do not match at all. The density increase is peaked around  $r=12$  cm, while the peak in  $H_\alpha$  emission is at  $r=8$  cm.

Furthermore the possibility that ablation clouds drift away from the pellet, can possibly explain some features of pellet fueling that are until now unexplained. Experimentally it is found that additional heating of the plasma reduces the fueling efficiency of pellet injection considerably [36]. A satisfactory explanation for this phenomenon has not yet been given [93].

Looking at the results presented in this Chapter the drifting of the pellet cloud in radial direction is a probable explanation for both the observed discrepancy in the fueling profiles compared to the  $H_\alpha$  signal, and the reduction of fueling efficiency in the case of additional heating.

Since the drifting is only governed by the electric field in the cloud and the magnetic field gradient, there is no reason why it should stop at the plasma boundary.

<sup>4</sup>These measurements are exceptional for RTP since often the interferometer data can not be used because of multiple fringe jumps that occur. In the presented case it was possible to reconstruct the interferometer profile right after the end of the ablation using the zero signal after the end of the plasma discharge. This is needed, because only if interferometer data is available the Thomson scattering profiles can be absolutely calibrated, and only then a fueling profile can be determined from the TS profiles before and after the pellet.

<sup>5</sup>The post-pellet profiles are taken 300  $\mu\text{s}$  after the end of the ablation. This is long enough for the injected mass to spread evenly on the flux surface, and short enough to be able to neglect the radial diffusion.

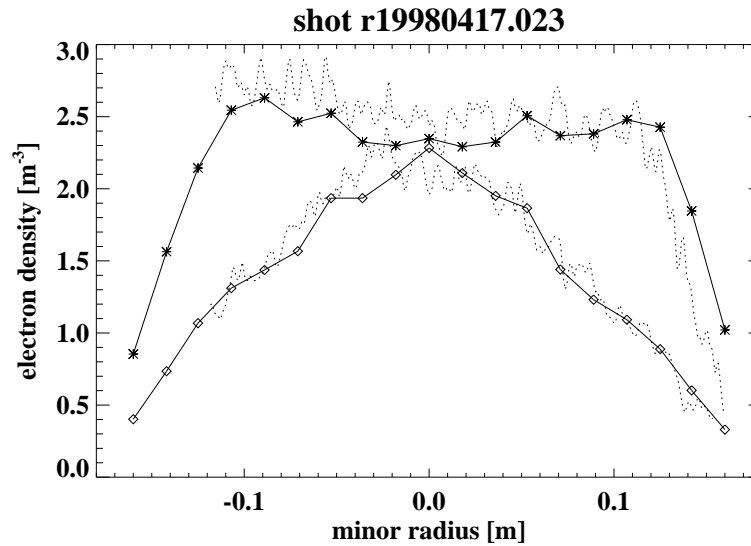


Figure 4.10: Density profiles taken just before pellet injection and just after the end of the ablation by Thomson scattering (dotted lines, at times 205.342 and 205.742 ms) and by interferometry (continuous lines with data points, at times 205.35 and 205.75 ms). The two diagnostics agree very well with each other.

Therefore it seems logical that many cases of lower fueling efficiencies can be related to this process. It remains to be explained, however, why in the additionally heated cases the drifting clouds seem to live much longer, or are at least visible over a much longer radial distance, compared to the Ohmic case.

There is some recent theoretical and experimental work on HFS<sup>6</sup> pellet injection. Theoretically the drift effects are expected to move the ablated matter in front of the pellet, thus improving fueling efficiency and pellet penetration (as long as the pellet does not cross the magnetic axis) [118]. Experimentally this improved fueling and penetration was found, even for modest pellet velocities due to the experimental difficulties arising for HFS injection [5, 67, 70]. Therefore pellet injection is still the first candidate for fueling a reactor plasma.

## 4.5 Radial inward drifts

Finally there are some experimental observations of a radial inward motion of particles during pellet injection. These effects are very difficult to diagnose due to the strong asymmetries in the density (even on the same flux surface) at these time scales. A localized strong density increase can easily escape a diagnostic, when it

<sup>6</sup>High Field Side—from the inboard side of the torus

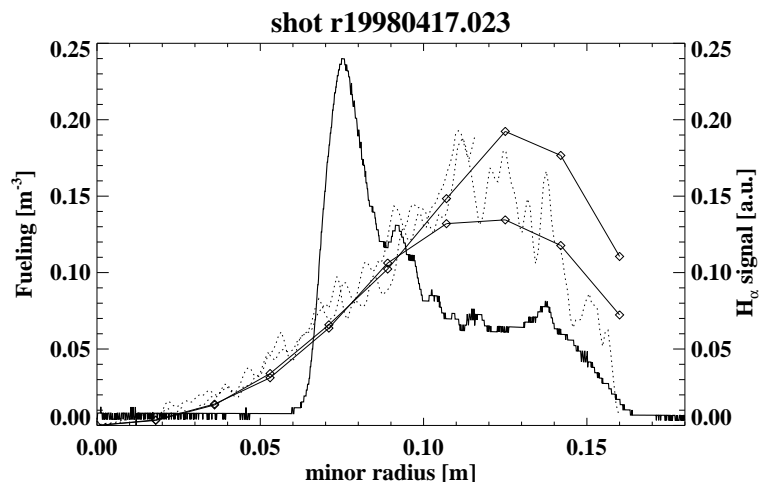


Figure 4.11: Fueling profile, calculated from the difference of the presented  $n_e$  profiles in Fig. 4.10, compared to the  $H_\alpha$  signal (bold continuous line). The TS data is again the dotted line, and the interferometry data is the continuous lines with data points (both sides of the profile are plotted). They clearly do not match with the  $H_\alpha$  signal.

is at another toroidal or poloidal position. In such cases it will appear as a pure temperature perturbation.

We identified conditions in which this density increase in front of the pellet actually showed up on the TS density measurement. An example of such an effect is shown in Figs. 4.12 and 4.13 (shot F) for a pellet injected off-axis on the  $T_e$  and  $n_e$  profiles taken by Thomson scattering at the moment of closest approach of the pellet to the plasma center. In this case the density increase is clearly seen several cm closer to the plasma center than the pellet position. Since this pellet was launched off-axis, it will never approach the plasma center closer than 56 mm. At the same time the temperature has plummeted at the position of the density peak. For completeness in Fig. 4.16 also the fiber-array signals for shot (F) are shown.

The question that remains to be answered is what is the most likely path that this high density region followed from the pellet to the place of observation.

A possible mechanism for this phenomenon is the following. Assume that the ablatant follows the magnetic field lines. The Thomson scattering diagnostic is displaced toroidally by  $60^\circ$  relative to the pellet in counter-current direction and  $300^\circ$  in current direction (see Fig. 4.14).

The times needed to travel the toroidal distance in both directions, assuming an ion thermal velocity of  $10^5$  m/s (at  $T_i=100$  eV), are  $7.5 \mu\text{s}$  and  $37.7 \mu\text{s}$  for these distances (this is with disregard of possible radial drift motions). From this delay it is deduced what the pellet position was at the time of ablation of the matter



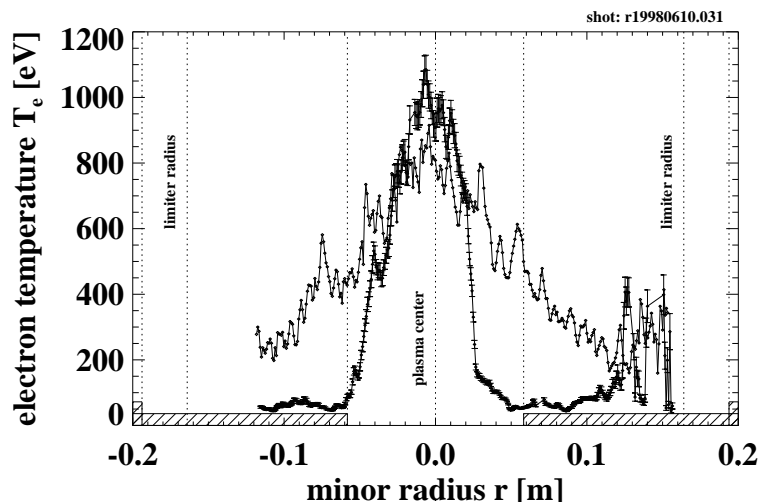


Figure 4.12: Example of two  $T_e$  profiles as observed by the Thomson scattering diagnostic (shot F). The  $n_e$  profiles for this shot are shown in Fig. 4.13. In this case a pellet was injected off axis (angle= $4^\circ$ , which means that the closest approach of the pellet to the center was 56 mm). The bars at the bottom of the plot again indicate the actual pellet position at the time of the measurement. The first TS profile (the triangular one) was taken just before the pellet entered the plasma. The second TS profile was taken when the pellet reached the position indicated by the bar on the bottom of the plot. The temperature perturbation clearly extends several cm in front of the actual pellet position, for positive radii.

forming this high  $n_e$  region. This results in different poloidal angles since the pellet was injected off-axis.

Taking the estimated  $q=1.5$ , a poloidal displacement of the high density may be expected of  $40^\circ$  in the counter-current direction and of  $200^\circ$  in the current direction due to the helicity of the field lines.

For the movement in the current direction this is sufficient to explain why the high density is observed by the Thomson scattering diagnostic in this projection (see Fig. 4.15). Note that the radial coordinate has not yet been taken into account.

For the counter-current direction a further poloidal movement of 13.7 cm ( $160^\circ$ ) is needed before the density is in sight of the diagnostic. This is the case because only the top-half of the TS  $n_e$  profile shows the density increase.

It has to be poloidal and not vertical, because the plasma center is still hot. This would mean an additional poloidal velocity of 18 km/s which seems unrealistic, compared to the typically observed poloidal rotation of 1 km/s (see Chapter 6).

The released matter, which traveled  $300^\circ$  toroidally in the plasma current direction, is located at a radius of 63 mm. This is in contradiction with the TS profile,

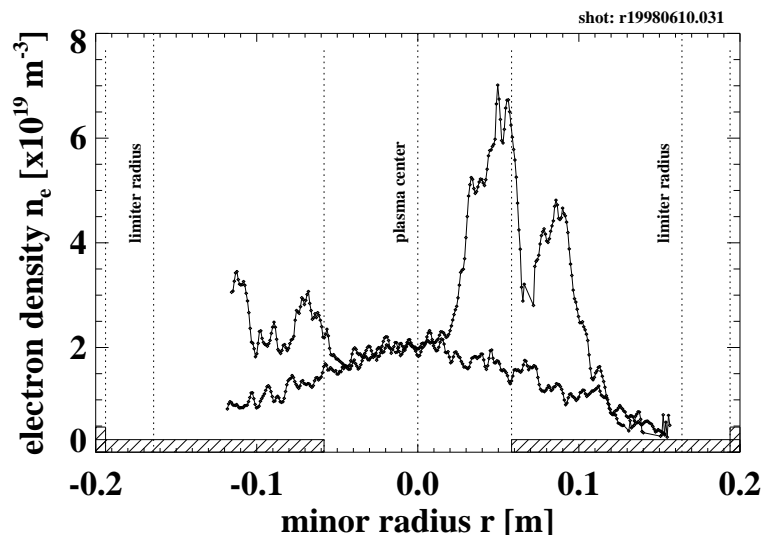


Figure 4.13: The two  $n_e$  profiles as observed by the Thomson scattering diagnostic (shot F) for the same shot as in Fig. 4.12. Also the density perturbation clearly extend several cm in front of the actual pellet position, for positive radii.

on which it is seen to extend up to  $r=25$  mm.

This can be explained if the released matter would start drifting towards the LFS when it is located at the inboard side of the plasma center. It would then move radially inward which explains the observed profiles.

The ablatant may even sweep through the plasma center, which would cause cooling of the plasma center without fueling, because the matter probably drifts away from the center again in the outer half of the plasma.

This could be the explanation for the puzzling pre-cooling phenomenon (which was described in Section 3.5). Here a pure  $T_e$  perturbation seems to travel ahead of the pellet. If, however, there also is a density perturbation that is not yet detected by the diagnostics, this would explain the effect, without the need of fast cross-field heat transport.

Why this only seems to occur when the pellet is at some minimum distance from the plasma center (possibly the  $q=1$  surface, because there the reported pre-cooling phenomenon starts) is not clear yet.

## 4.6 Striations

Another still unexplained feature of pellet injection are the striations, a modulation which is usually observed in the  $H_\alpha$  signals. An example for RTP was shown in

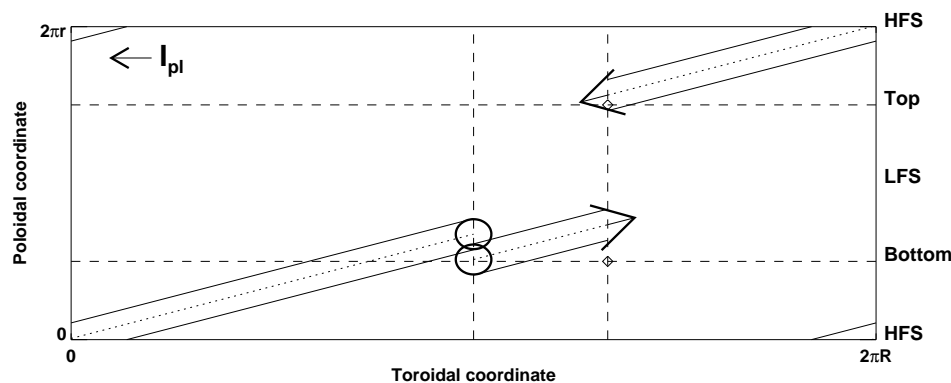


Figure 4.14: Schematic view of a flux surface and of the ablatant that reaches the toroidal position of the TS diagnostic projected on that flux surface (note that it may have drifted in radial direction, so perpendicular to this view). The circles denote the position on which the ablated matter is released. The vertical lines denote the toroidal position of the pellet injector and the TS diagnostic. The horizontal lines indicate the top and bottom of the plasma. The diamonds on these lines denote the positions measured by the TS diagnostic. Because of the different lengths of the path from the pellet to the TS position two different pellet positions have to be used as starting point. The matter that drifts in the current direction can explain why a large density is observed only on the top-half of the  $n_e$  profile in Fig. 4.13.

Fig. 2.7, were they are clearly visible between 5 and 15 cm. This modulation has a typical frequency of 100 kHz.

Two basic ideas have been developed to explain this phenomenon. One, proposed by Neuhauser [101], assumes that the pellet periodically leaves the shielding cloud (see Section 3.2). For RTP this would give a typical cloud radius of 2.0-3.0 mm, calculated from striations in the observed  $H_\alpha$  signals<sup>7</sup>. This is not in agreement with the measured cloud size of  $\approx 12$  mm (see Section 4.3.4).

A second mechanism is proposed by Andelfinger [1] and further investigated by Pégourié and Dubois [110]. This idea assumes that less energy is available at rational q-surfaces to ablate the pellet (the q-effect). If this effect could be observed, it would form a diagnostic for the q-profile.

However, an alternative third explanation is the drift of the ablation cloud. If the ablation cloud periodically drifts away from the pellet it leaves the pellet unprotected and exposed to the hot plasma. This causes a modulation in the ablation rate proportional to the ratio cloud size/ $v_{driftingcloud}$  in stead of the ratio cloud size/ $v_{pellet}$ , and is thus in agreement with the measured cloud size.

<sup>7</sup>The  $H_\alpha$  signal of shot (A) for example shows negative striations at 257.3066 and 257.3116  $\mu s$ , so a time difference of 5.0  $\mu s$ . From the pellet velocity of 962 m/s it then follows from the Neuhauser theory that the cloud diameter is 4.8 mm and the cloud radius is 2.4 mm.

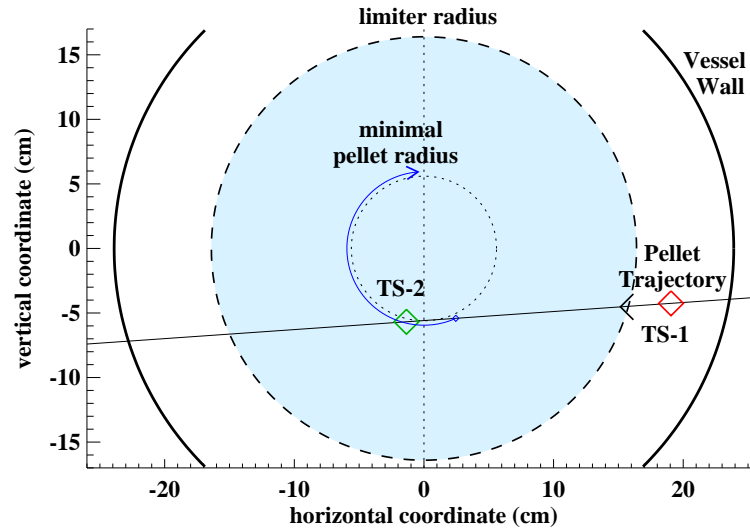


Figure 4.15: Schematic drawing of off-axis pellet injection, projected on a poloidal cross-section of the tokamak. The diamonds indicate the pellet position at the times that the profiles shown in Figs. 4.12 and 4.13 were taken. The vertical dashed line represents the chord viewed by the Thomson scattering diagnostic, but note that this diagnostic is displaced by a toroidal angle of  $60^\circ$  from the pellet injector. The curved arrow indicates a poloidal projection of the most likely 3-dimensional path of the high density.

A complication is, that if both processes (a drifting of the ablation cloud, and a rational  $q$ -effect) do occur simultaneously, the drifting cloud may obscure the  $q$ -effect. If the clouds live longer than the time the pellet needs to pass a region of rational  $q$ , the modulation of the ( $H_\alpha$ ) light would be very difficult to detect. This is especially the case for high  $T_e$  cases, where the light from the drifting cloud is much stronger than the light around the pellet. A search for this  $q$ -effect should therefore be conducted in the low  $T_e$  regime, to suppress the drift effect.

## 4.7 Summary

A clear difference has been observed between the fueling profile after pellet injection and the shape of the  $H_\alpha$  signal. Also a clear discrepancy between pellet penetration, as observed by two independent diagnostics, was observed.

Because of this, a new diagnostic has been build to observe pellet ablation in the RTP tokamak. This diagnostic has proven to be very suitable to observe drift movements of the pellet ablation cloud and pellet penetration. In the absence of such a drift it can be used to determine the pellet velocity and the ablation cloud

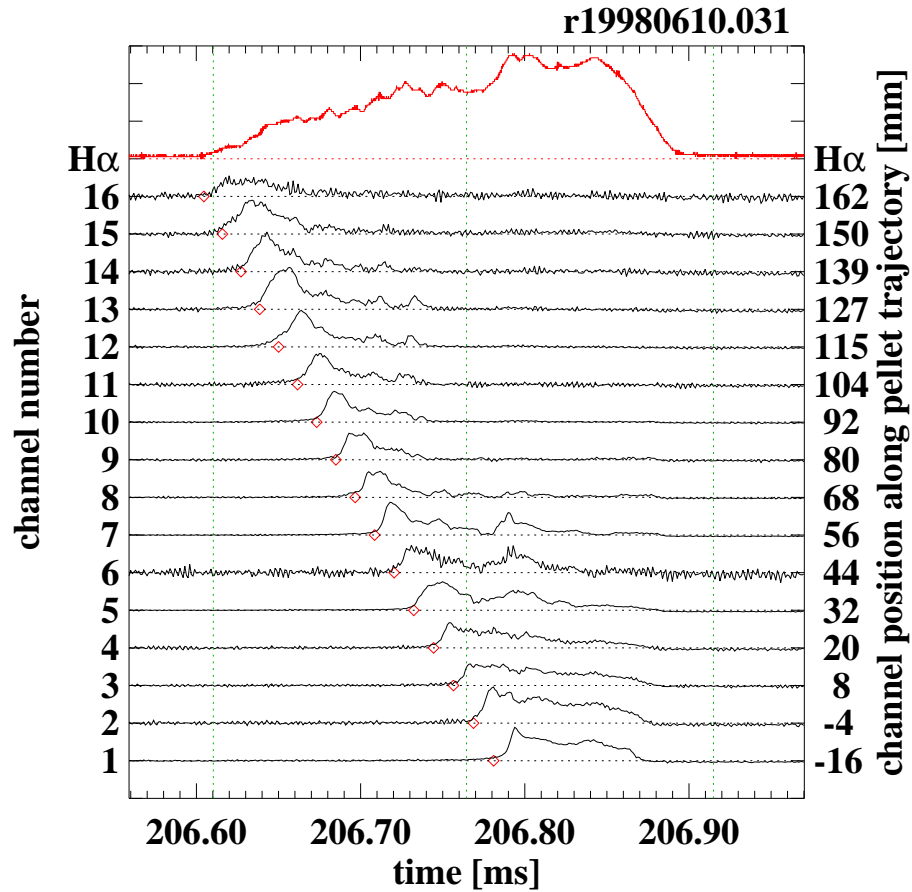


Figure 4.16: The fiber-array signals for shot (F) plotted in the same way as in Fig. 4.4. The dashed lines indicate the limiter radius (at both sides of the plasma) and the plasma center. A noticeable difference with the normal Ohmic results are the long pulse lengths, especially on channels 1 to 5.

size.

We have observed a semi-periodical drifting of (part of) the ablation cloud away from the pellet with a velocity component in major radius direction with a velocity in the range of 2.5 to 10 km/s. This phenomenon has up to now<sup>8</sup> never been observed directly [87] (see also Sec. 4.9). Before this publication, only indirect evidence existed. This has been obtained for example by comparing penetration and fueling

<sup>8</sup>after publishing the first results they were confirmed by measurements at ASDEX [69, 99, 100]. They had the experimental possibility to also perform HFS pellet injection. In that case they observe also a drift towards the LFS side, so now ahead of the pellet.

for pellets injected from the HFS and the LFS of the plasma [66], or from the top and the LFS of the plasma [5].

The drift effect has been studied for different plasma temperatures. It was found that the ablation cloud has a longer lifetime, and emits more light for higher  $T_e$ .

In the slide-away regime no separate drifting clouds could be observed. The cloud around the pellet was unusually large in this case. They may be explained by a continuous drifting of ablatant away from the pellet, or by the production of a large number of fast neutrals from charge exchange.

For the case without drifts the measured pellet velocity agrees well with the velocity measured inside the pellet injector and a cloud size of  $12 \pm 4$  mm was found.

In general, the pellet penetration measured with the fiber array was smaller than the penetration determined from the  $H_\alpha$  signal. Only in some cases they are equal. A penetration determined with the  $H_\alpha$  signal that was less than that determined by the fiber array was never observed.

Also the drift along the magnetic field has been measured using the new diagnostic. The found values, in the range of 8-12 km/s, agree excellently with the value cited in literature of  $10^4$  m/s [83].

The center of the drifting clouds has been observed to move away from the pellet in toroidal direction with a velocity in the order of 10 km/s.

The radial size of the drifting clouds was determined to be in the order of  $\approx$  10-15 mm. The toroidal size of the drifting cloud has been observed to be in the order of 13 cm in one case.

Finally some evidence was presented for a radial drift in inward direction.

## 4.8 Conclusion

The direction and velocity of the observed drift of the ablation cloud can be explained using the mechanism proposed by Rozhansky.

Most of the discrepancy in penetration depth shown in Fig. 4.1 can be explained by the observed drift of the cloud. As long as the drifts are purely in major radius direction, this effect would not be visible on the penetration seen on the photographs, so the observation of these drifts is not in conflict with prior measurements. The results given in Fig. 4.1 confirm that this usually is the case.

A mechanism like this also may be connected to the observation given by Milora [91], that there is a short time scale component to the radial redistribution of ablated mass.

Part of the ablated matter will be located at the HFS of the plasma center due to the rotational transform. If the drift towards the LFS would occur to this matter, this would appear as a radial inward drift. This maybe an explanation for the observed fast cooling (pre-cooling) of the plasma center in front of the pellet.

The observation of a drift of the center of the drifting cloud along the magnetic field lines may be connected to the toroidal plasma rotation. If this is the case

than the fiber array diagnostic may be used as a new diagnostic to obtain more information on the plasma rotation.

A piece of information still missing are movements in the vertical direction. A fiber array looking for those movements can be constructed along the same principles as the existing diagnostic. With such a diagnostic also poloidal rotation could be diagnosed. In the ideal case three fiber arrays looking for movements in all spatial dimensions should be available.

Finally the drift mechanism might be an alternative explanation of the striations that are almost always present in the observed  $H_\alpha$  signals.

## 4.9 Fast backward drift of pellet ablatant in tokamak plasmas

The following four pages display the same text that was published in the **Physical Review Letters** [60] and is reproduced with kind permission of the American Physical Society. They are page 2685-2688 of J. de Kloe et al., Phys. Rev. Lett. 82 (13), 1999. ©1999 by The American Physical Society.

The figure and reference numbers differ from those used in the rest of this thesis. Figure 1 can also be found as Fig. 2.6 on page 22. Figures 2, 3, and 4 can also be found as Figures 4.4, 4.5, and 4.6, on pages 53, 54, and 55.

The references are renumbered as follows: 1 = [3], 2 = [20], 3 = [82], 4 = [10], 5 = [117], 6 = [45], 7 = [106], 8 = [54], 9 = [118], 10 = [101], 11 = [1], 12 = [110].

## Fast Backward Drift of Pellet Ablatant in Tokamak Plasmas

J. de Kloe, E. Noordermeer, N. J. Lopes Cardozo, and A. A. M. Oomens

FOM-Instituut voor Plasmafysica "Rijnhuizen," Association Euratom-FOM, Trilateral Euregio Cluster,  
P.O. Box 1207, 3430 BE Nieuwegein, The Netherlands

(Received 30 November 1998)

Pellet ablation in the Rijnhuizen Tokamak Project has been studied with an array of 16 fibers viewing the pellet trajectory along very narrow lines of sight. Rapid backward drift of the ablation cloud away from the pellet was observed. This has implications for the determination of the fueling profile and the penetration of the pellet in the plasma. Furthermore, this movement of the ablation cloud offers a new explanation for the often observed striations in the light emission. In contrast to the picture of the pellet periodically leaving the ablation cloud, the ablation cloud moves periodically away from the pellet. [S0031-9007(99)08796-7]

PACS numbers: 52.55.Fa, 28.52.Cx, 52.30.-q, 52.70.-m

One of the outstanding problems in thermonuclear fusion research is the fueling of the burning plasma. The high speed (several km/s) injection of pellets of solid hydrogen isotopes is one of the options. To obtain reliable models to predict the local fueling rate, the present pellet ablation theories must be validated. Much experimental and theoretical work still has to be done since large discrepancies have been reported between the ablation rate as measured by different diagnostics. For example, fueling measured by Thomson scattering at the Joint European Torus showed a fueling located primarily at the edge of the plasma, while the line emission (Balmer alpha line), which is usually taken as a measure for the ablation rate, placed the fueling in the inner parts of the plasma [1].

In the Rijnhuizen Tokamak Project (RTP) [2], the ablation of the pellet was monitored by two diagnostics. The intensity of the  $H_\alpha$  emission from the ablation cloud was measured as a function of time by a detector viewing a large plasma volume, and as a function of position by taking time integrating photographs. Between these two measurements sometimes a discrepancy in the observed pellet penetration was found.

A dedicated diagnostic has been built to clarify this discrepancy. It consists of a row of 16 fibers viewing the pellet trajectory along narrow lines of sight, resulting in a very high spatial and temporal resolution. This is necessary because the shape of the cloud is observed to change within intervals of a few  $\mu s$  [3]. Properties that can be measured with this diagnostic are pellet velocity, ablation cloud size and position, and penetration depth.

*Experimental setup.*—The experiments were carried out in the RTP tokamak (major radius  $R = 0.72$  m, minor radius  $a = 0.164$  m, toroidal magnetic field  $B_{tor} \leq 2.4$  T, plasma current  $I_{p1} \leq 150$  kA, effective ion charge  $Z_{eff} \approx 1.5-3.0$ , circular cross section). Typical plasma parameters are central electron temperature and density  $T_{e,0} \approx 0.7$  keV,  $n_{e,0} \approx 5 \times 10^{19} \text{ m}^{-3}$  for plasmas with Ohmic heating (measured with Thomson scattering [4] and interferometry [5]). With central electron cyclotron heating (ECH) ( $\leq 350$  kW, 2nd harmonic heating at 110 GHz)

$T_{e,0} = 1.5-2$  keV is reached at  $n_{e,0} = 5 \times 10^{19} \text{ m}^{-3}$ . With off-axis ECH very broad, flat, or slightly hollow  $T_e$  profiles are obtained with  $T_e \leq 0.5$  keV everywhere [6]. Thus, target plasmas with a large  $T_e$  range can be made, allowing the study of ablation in different conditions.

Pellets of 0.5 and  $2.0 \times 10^{19}$  atoms in size ( $n_{pellet}$ ), with velocities ( $v_{pellet}$ ) between 500 and 1000 m/s, and radius ( $r_{pellet}$ ) of 0.3 or 0.4 mm have been used. The existing diagnostics are the photographic camera (resolution 1 mm, no time resolution) and the wide angle fibers (time resolution 0.5  $\mu s$ , no spatial resolution) viewing the  $H_\alpha$  line emission, as shown in Fig. 1. For the new diagnostic a row of 16 fibers was mounted in one of the image planes of the lens system, on the line where the pellet trajectory is imaged (see Fig. 1).

To narrow the lines of sight of the fibers a black block of 40 mm thickness, with 1 mm diameter holes in it, was

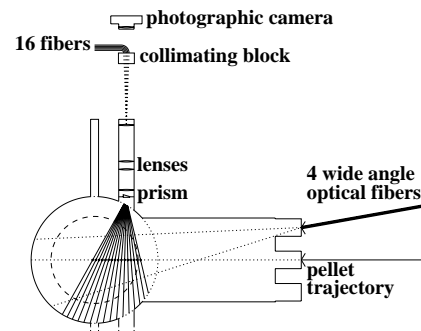


FIG. 1. Overview of the experimental setup in a poloidal cross section of the tokamak. Shown are the photographic camera, the wide angle fibers, and the new diagnostic, consisting of the 16 fibers and a collimating block to narrow the lines of sight. The viewing lines of the new fiber array diagnostic are indicated by the fan of lines originating from the prism. The dashed circle indicates the plasma boundary. The pellet moves inward along the major radius of the torus.



mounted in front of the fibers. This resulted in narrow lines of sight for the fibers, about 3.5 mm on the actual pellet trajectory for horizontal injection. The separation of the fibers was 4.5 mm in the image plane which resulted in a spatial separation of the viewing lines of 9.6 mm on the actual pellet trajectory for horizontal pellet injection.

The toroidal dimension of the viewing spots is also 3.5 mm, the centers of the spots are aligned to within 10 mm of the pellet trajectory. Given the extension of the ablation cloud in toroidal direction, this could lead to a systematic variation of the measured intensity along the array of up to 50%, varying smoothly from channel to channel. Such an error on the amplitude of the signals has no bearing on the analysis and conclusions presented in this Letter. Measurements with the photographic camera showed that the deviation of the pellet trajectory in toroidal direction is negligible in the conditions at hand.

The signals from all 16 fibers are measured independently using photodiodes. The temporal resolution of the system was 1  $\mu$ s, determined by the analog-to-digital converters.

A relative calibration of the channels was determined by taking measurements of a pellet shot with quiet ablation, showing only one peak on most channels (see Fig. 2) and assuming the peak height to be equal to the large angle  $H_\alpha$  signal at the same time.

*Results in different plasma regimes.*—Following the commonly accepted picture of a cigar shaped ablation cloud which is localized in major radial direction around the actual pellet position, we expect each of the channels to give a short pulse. The width of the pulse should then be a measure of the ablation cloud dimensions in major radial direction. This is indeed seen for pellets injected in low temperature plasmas ( $T_e \leq 400$  eV). This situation can be obtained by injecting the pellet off-axis or by injecting in a plasma shortly after a period of off-axis ECH [6]. An example of the second type is shown in Fig. 2. As the pellet passes the viewing lines of the different channels clearly a pulse of light is observed, showing that the ablation cloud is located close to the pellet in major radial direction. The onset of these pulses coincides with the pellet velocity and timing as determined inside the pellet injector. The average width of the pulses on each channel is  $16 \pm 5 \mu$ s corresponding to a width of the ablation cloud of  $\approx 12$  mm. The velocity measured with the new diagnostic is  $980 \pm 25$  m/s, in agreement with the value measured inside the injector ( $962 \pm 1$  m/s). The uncertainty is mostly systematic and due to the position calibration of the viewing lines. From the last visible pulse (on channel 2) it follows that the penetration of the pellet was  $\approx 15.0 \pm 0.5$  cm. This agrees with the value obtained by the end of the wide angle  $H_\alpha$  signal yielding a value of  $15 \pm 1$  cm.

The result shown in Fig. 2 excludes the possibility of reflections playing a role. This has been confirmed by ray tracing calculations.

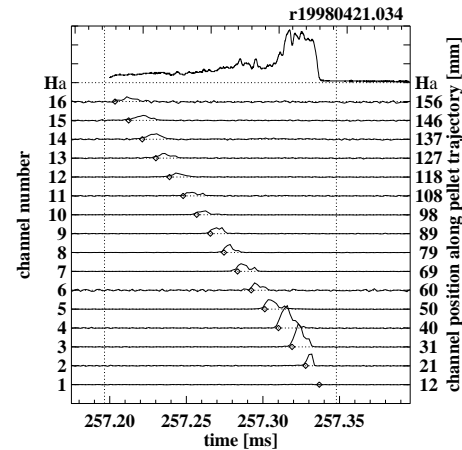


FIG. 2. Example of the pellet ablation process as observed by the fiber array for a pellet injected in a relatively cold plasma (7 ms after switch off of off-axis ECH [6]). The diamonds indicate the expected passage times of the pellet using the measured pellet velocity and timing in the injector. The vertical dashed lines indicate the pellet passes the limiter radius and the plasma center (if it would penetrate that far). The top trace is the wide angle  $H_\alpha$  monitor. A clear peak is seen at the passage of the pellet at each channel. The pellet and plasma parameters are  $n_{e,0} = 5.7 \times 10^{19} \text{ m}^{-3}$ ,  $T_{e,0} = 280$  eV,  $I_{p1} = 84.3$  kA,  $B_{\text{tor}} = 2.27$  T,  $Z_{\text{eff}} = 1.7$ ,  $v_{\text{pellet}} = 962$  m/s,  $m_{\text{pellet}} = 0.5 \times 10^{19}$  atoms,  $r_{\text{pellet}} = 0.3$  mm.

A second example is given for normal Ohmic plasma conditions. This gives a completely different picture (see Fig. 3). Here the pulses are much broader in all channels. Besides that, separate peaks can be distinguished after the passage of the pellet, which we will refer to as secondary peaks. These are clearly correlated in different channels (see, for example, the parallelogram in Fig. 3). Assuming these secondary peaks are caused by an object moving through the plasma along the pellet trajectory a velocity can be calculated. For the highlighted peaks the velocity was 3.5 km/s. In other cases it has been observed to be as high as 10 km/s. With this velocity and the known resolution of the system the size of the object can be calculated to be  $\approx 14$  mm (channel 12). The size decreases as it moves outward on the subsequent channels. In this case the pellet penetrates beyond the reach of the diagnostic so no penetration depth can be determined here.

A third example shows the results for a pellet injected in a plasma during central ECH (320 kW) (see Fig. 4). Here the secondary peaks are much stronger than in the Ohmic case (the sensitivity along the y scale is reduced by 50% compared to Figs. 2 and 3). The secondary peaks persist longer than the primary ones. The pellet penetration found

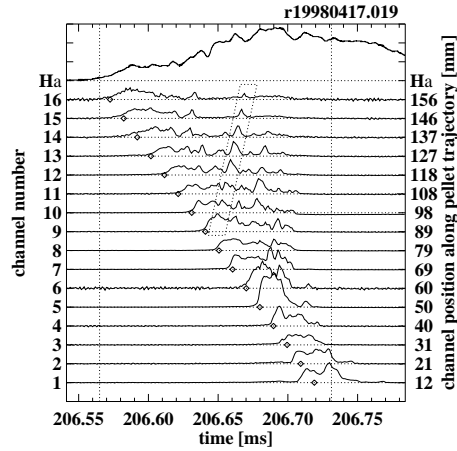


FIG. 3. Example of the pellet ablation process as observed by the new fiber-array diagnostic for an Ohmic plasma, plotted in the same way as in Fig. 2. Besides much broader peaks at all channels after passage of the pellet also a substructure of peaks can be recognized which are correlated on separate channels. An example of this is highlighted by the overlotted parallelogram. This sequence of correlated peaks shows the presence of a light source which moves faster than the pellet and in the opposite direction. The pellet and plasma parameters are  $n_{e,0} = 3.9 \times 10^{19} \text{ m}^{-3}$ ,  $T_{e,0} = 900 \text{ eV}$ ,  $I_{p1} = 101 \text{ kA}$ ,  $B_{\text{tor}} = 2.05 \text{ T}$ ,  $Z_{\text{eff}} = 2.6$ ,  $v_{\text{pellet}} = 986 \text{ m/s}$ ,  $m_{\text{pellet}} = 2.0 \times 10^{19} \text{ atoms}$ ,  $r_{\text{pellet}} = 0.4 \text{ mm}$ .

using the wide angle  $H_{\alpha}$  signal is  $17 \pm 1 \text{ cm}$  while the new diagnostic gives a penetration of  $\approx 13.0 \pm 0.5 \text{ cm}$ .

Up to now the secondary peaks do not seem to reproduce in detail. They do not develop at regular time intervals or positions, and have different magnitudes and lifetimes, even with very similar plasma and pellet conditions.

We have observed the neutral cloud surrounding the pellet using a new diagnostic. For pellet injection in a cold plasma ( $T_e \leq 400 \text{ eV}$ ) the observed cloud size was on average  $12 \pm 5 \text{ mm}$  (see Fig. 2).

In hotter plasmas the cloud size increases and parts of it start drifting away.

In most models the radial cloud size is assumed to be determined by the ionization radius  $r_i$ . Using an expression derived by Parks [7] we obtain  $r_i \approx 1$  to  $3 \text{ mm}$  for RTP. This is significantly smaller than the observed ablation cloud.

The observation of the secondary peaks is interpreted as a not fully ionized cloud moving away from the pellet through the plasma.

The movement has a velocity component along the pellet trajectory but in opposite direction as the pellet velocity. A major radial velocity of  $3.5$  to  $10 \text{ km/s}$  can be deduced from the signals.

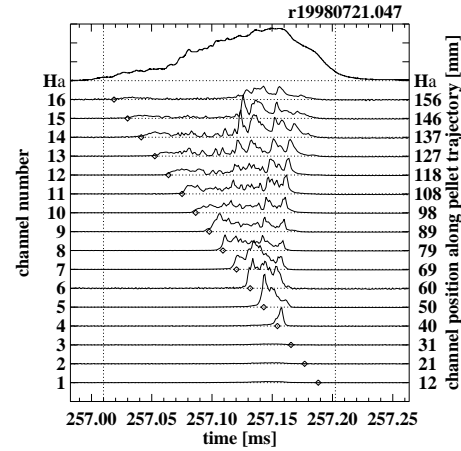


FIG. 4. Example of the pellet ablation process as observed by the new fiber-array diagnostic plotted in the same way as in Fig. 2. In this case the pellet was injected in a centrally ECH heated plasma. Clearly the secondary peaks have much higher amplitude on the outer channels than the primary pulse (channels 10–16). The pellet and plasma parameters are  $n_{e,0} = 5.2 \times 10^{19} \text{ m}^{-3}$ ,  $T_{e,0} = 1450 \text{ eV}$ ,  $I_{p1} = -81.5 \text{ kA}$ ,  $B_{\text{tor}} = 2.01 \text{ T}$ ,  $Z_{\text{eff}} = 2.0$ ,  $v_{\text{pellet}} = 852 \text{ m/s}$ ,  $m_{\text{pellet}} = 2.0 \times 10^{19} \text{ atoms}$ ,  $r_{\text{pellet}} = 0.4 \text{ mm}$ , ECH power =  $320 \text{ kW}$ .

The results obtained with this diagnostic may be helpful in determining the importance of movements of the ablation cloud. The possibility of these effects have been pointed out by Kaufmann *et al.* [8] and Rozhansky *et al.* [9].

In the literature two types of drifts have been considered in the ablation cloud. Because of the Lorentz transformation the pure  $B$  field in the laboratory frame is converted to an electric field  $\mathbf{E} = \mathbf{v}_{\text{pellet}} \times \mathbf{B}_{\text{tor}}$  in the pellet frame. This can give two effects [3]. Under open circuit conditions (case 1) it causes a polarization in the cloud giving rise to an  $\mathbf{E} \times \mathbf{B}$  drift with magnitude  $v_{\text{drift}} = \frac{\mathbf{E} \times \mathbf{B}}{B^2} = \frac{\mathbf{v}_{\text{pellet}} \times \mathbf{B} \times \mathbf{B}}{B^2} = \mathbf{v}_{\text{pellet}}$  in the lab frame. This drift is in the direction of the pellet velocity and causes the ablation cloud to stick to the pellet. This is not consistent with the observations.

In short circuit conditions (case 2) no large charge separation can build up but a continuous current is running through the ablation cloud. This current density  $\mathbf{j}$  can be described by the local  $E$  field and the local conductivity  $\sigma$  as  $\mathbf{j} = \sigma \mathbf{E}$ . If no external forces on the particles (with charge  $q$ ) are present, the only ones are the electric and magnetic field, so the force equation reads  $f = 0 = q\mathbf{E} + q\mathbf{v}_{\text{cloud}} \times \mathbf{B}$  so  $\mathbf{j} \times \mathbf{B} = -\sigma \mathbf{v}_{\text{cloud}} B^2$ . This force causes a movement of the ablation cloud away from the pellet, and, in fact, lets the cloud stick to the magnetic

field, stopping its movement in radial direction. Since we observe the cloud to move backward towards the plasma edge also, this picture cannot be true.

Rozhansky considered a third possibility, the grad  $\mathbf{B}$  drift [9]. Because of the gradient in the toroidal field a drift velocity of  $\mathbf{v}_{\nabla\mathbf{B}} = \frac{1}{2}v_{\perp}r_L\frac{\mathbf{B}\times\nabla\mathbf{B}}{B^2}$  occurs (here  $v_{\perp}$  is the velocity of the particles perpendicular to the field lines, and  $r_L$  is the Larmor radius). Because of the high collisionality particles cannot complete an orbit around the torus, so the drift is not compensated by the rotational transform. This causes a polarization in opposite direction, compared to case 1, that starts to increase linearly with time as  $\mathbf{E} = \mathbf{v}_{\nabla\mathbf{B}}n_eqt$ . This causes an  $\mathbf{E} \times \mathbf{B}$  drift in a direction opposite to the pellet velocity, with linearly increasing velocity. After inserting RTP values in the formulas given by Rozhansky (Ref. [9], Eq. 24) a velocity of  $\approx 5-10$  km/s is expected. This is in good agreement with the observations.

Another still unexplained feature of pellet injection is the striations, a modulation of the observed  $H_{\alpha}$  signals. Two basic ideas have been developed to explain this phenomenon. One was proposed by Neuhauser [10] and assumes that the pellet periodically leaves the shielding cloud. For RTP this would give a typical cloud radius of 1.5–2.5 mm, calculated from striations in the observed  $H_{\alpha}$  signals. This is not in agreement with the cloud size which has been measured.

However, an alternative explanation is possible when the drift of the ablation cloud is taken in consideration. Then the ablation cloud may be periodically drifting away from the pellet (at a velocity up to 1 order of magnitude higher than the pellet velocity), leaving it unprotected and exposed to the hot plasma and causing a modulation in the ablation rate independent of the ratio cloud size/ $v_{\text{pellet}}$ .

An altogether different mechanism was proposed by Andelfinger [11] and further investigated by Pégourié and Dubois [12], which assumes that less energy is available at rational  $q$  surfaces to ablate the pellet. The observations shown in this Letter do not support this hypothesis.

A consequence of the presented results is that it is not to be expected that the  $H_{\alpha}$  signal is proportional to the local fueling rate. Also it follows that it is difficult to determine pellet penetration using the wide angle  $H_{\alpha}$  signal. This gives only a maximum possible penetration by assuming that no matter drifts away from the pellet. Better estimates for low field side injection are obtained by using a (photographic) camera.

If the ablation cloud exists for some time after the complete ablation of the pellet also, determination of the lifetime of the pellet is impossible with the wide angle  $H_{\alpha}$  diagnostic (see Fig. 4).

In conclusion, a new diagnostic has been build to observe pellet ablation in the RTP tokamak. This diagnostic has proven to be well suited to observe movements of (parts of) the pellet ablation cloud. In the absence of such a drift it can be used to determine the ablation cloud size and velocity during the ablation process. We have observed a drifting of the ablation cloud away from the pellet with a velocity component in major radius direction of 3.5 to 10 km/s. The direction and velocity of this cloud can be explained using the mechanism proposed by Rozhansky [9]. This phenomenon has never been observed directly before [3].

The observations emphasize the importance of inboard side pellet injection (for which the observed drift would improve the possibility of fueling the plasma center).

This work was done under the Euratom-FOM association agreement, with financial support from NWO and Euratom.

- 
- [1] L. R. Baylor *et al.*, Nucl. Fusion **32**, 2177 (1992).
  - [2] A. J. H. Donné and the RTP-Team, Plasma Phys. Rep. **20**, 192 (1994).
  - [3] S. L. Milora, W. A. Houlberg, L. L. Lengyel, and V. Mertens, Nucl. Fusion **35**, 657 (1995).
  - [4] M. N. A. Beurskens *et al.*, Rev. Sci. Instrum. **68**, 721 (1997).
  - [5] J. H. Rommers, A. J. H. Donné, F. A. Karelse, and J. Howard, Rev. Sci. Instrum. **68**, 1217 (1997).
  - [6] G. M. D. Hogeweij *et al.*, Phys. Rev. Lett. **76**, 632 (1996).
  - [7] P. B. Parks, Nucl. Fusion, **20**, 311 (1980).
  - [8] M. Kaufmann, K. Lackner, L. Lengyel, and W. Schneider, Nucl. Fusion **26**, 171 (1986).
  - [9] V. Rozhansky, I. Veselova, and S. Voskoboynikov, Plasma Phys. Controlled Fusion **37**, 399 (1995).
  - [10] J. Neuhauser and R. Wunderlich, Max-Planck-Institut für Plasmaphysik, Garching bei München, Report No. IPP 5/30, 1989.
  - [11] C. Andelfinger *et al.*, Max-Planck-Institut für Plasmaphysik, Garching bei München, Report No. IPP 1/219, 1983.
  - [12] B. Pégourié and M. A. Dubois, Nucl. Fusion **29**, 745 (1989).

# Chapter 5

## Radial particle transport

### 5.1 Introduction

The central question in this Chapter is whether or not the particle transport properties in the plasma during and after pellet injection are equal to the transport properties that are observed in the unperturbed pre-pellet plasma.

Many experiments suggest that an increase could occur both in heat transport (pre-cooling, see Section 3.5) and in particle transport (large reduction in fueling efficiency in additionally heated plasmas, see Section 4.4). However, a connection of these phenomena with a change in diffusion coefficient  $D$  is not straightforward, since pre-cooling is believed to be a pure temperature effect <sup>1</sup> and the drift of the ablation cloud (as discussed in Chapter 4) can explain the reduced fueling in some cases.

First the equations that describe particle transport are summarized in Section 5.2. Then several methods of obtaining values for  $D$  and the inward convection velocity  $v_{\text{pinch}}$  are discussed in Section 5.3 and some results obtained previously for RTP are presented. In Section 5.4 a numerical model developed for this analysis, is described. After assuming a profile for  $D$  and estimating a profile that will be used for  $v_{\text{pinch}}$  determined from a plasma in steady state, this model is used to simulate a plasma with modulated gas puff in Section 5.5. Finally, for pellet perturbed plasmas, the values for  $D$  obtained for different plasma time scales are discussed in Sections 5.6 and 5.7. Section 5.8 concludes this Chapter, with a summary, conclusions and the answer to the question posed at the start of this Section.

---

<sup>1</sup>In [96] it is reported that an effect comparable to pre-cooling has never been observed on the particle transport.

## 5.2 The transport equations

To describe the transport of heat and particles in a plasma, a commonly applied model is the assumption that all flows (of heat, particles and current) are driven by the local gradients that exist in the plasma [72]. This results in a transport matrix  $M$  that defines the behaviour of the plasma.

The magnetic configuration of the plasma in a tokamak is assumed to consist of nested flux surfaces, on which the properties like density and temperature are constant. Then the transport equations are simplified to just the radial dimension. This is often allowed since transport on a flux surface is many orders of magnitude faster than transport across flux surfaces, hence often no gradients exist in poloidal or toroidal direction on the considered time scales<sup>2</sup>.

For the toroidal geometry in a tokamak the flows are combined in a vector  $\vec{F}$ , which is usually defined as:

$$\vec{F} = \begin{pmatrix} \Gamma_r \\ q_{e,r} \\ q_{i,r} \\ j_{\parallel} \end{pmatrix} \quad (5.1)$$

With  $\Gamma_r$  the radial particle flow,  $q_{e,r}$  and  $q_{i,r}$  the radial heat flow through the electrons and the ions, and  $j_{\parallel}$  the toroidal component of the current density.

The gradients in the plasma are combined in the vector  $\vec{P}$ , which is defined as:

$$\vec{P} = \begin{pmatrix} \nabla_r n \\ \nabla_r T_e \\ \nabla_r T_i \\ E_{\parallel} \end{pmatrix} \quad (5.2)$$

With  $\nabla_r n$  the radial component of the density gradient,  $\nabla_r T_e$  and  $\nabla_r T_i$  the radial component of the gradients in electron and ion temperature, and  $E_{\parallel}$  the parallel electric field.

The relation between these two vectors is written as  $\vec{F} = M \cdot \vec{P}$  in which  $M$  is the transport matrix:

$$M = \begin{pmatrix} m_{11} & m_{12} & m_{13} & m_{14} \\ m_{21} & m_{22} & m_{23} & m_{24} \\ m_{31} & m_{32} & m_{33} & m_{34} \\ m_{41} & m_{42} & m_{43} & m_{44} \end{pmatrix} \quad (5.3)$$

Some elements in this matrix have special names:  $m_{11} = -D$ ,  $m_{22} = -n\chi_e$ ,  $m_{33} = -n\chi_i$  en  $m_{44} = \sigma$ , with  $D$  the particle diffusion,  $\chi_e$  the heat diffusivity through the electrons,  $\chi_i$  the heat diffusivity through the ions, and  $\sigma$  the electric conductivity.

<sup>2</sup>For the simulation on the pellet ablation time scale this is not true for the density, but it is still a good approximation for the temperature, as will be shown in the experimental results presented in this Chapter. The process of flux surface mixing is studied more closely in Section 6.5.

If this is inserted, the matrix equation  $\vec{F} = M \cdot \vec{P}$  becomes:

$$\begin{pmatrix} \Gamma_r \\ q_{e,r} \\ q_{i,r} \\ j_{\parallel} \end{pmatrix} = \begin{pmatrix} -D & m_{12} & m_{13} & m_{14} \\ m_{21} & -n\chi_e & m_{23} & m_{24} \\ m_{31} & m_{32} & -n\chi_i & m_{34} \\ m_{41} & m_{42} & m_{43} & \sigma \end{pmatrix} \cdot \begin{pmatrix} \nabla_r n \\ \nabla_r T_e \\ \nabla_r T_i \\ E_{\parallel} \end{pmatrix} \quad (5.4)$$

Neo-classical theory gives expressions for all matrix elements, but it is known that many are anomalous. The off diagonal elements may be in the same order of magnitude as the diagonal terms. Well known off-diagonal elements are the Ware-pinch (contained in  $m_{14}$ ) and the bootstrap current (contained in  $m_{41}$ ). In the rest of this Chapter the transport is only considered in an experimental way.

From the given matrix equation it can easily be seen that particle transport is not only driven by the density gradient, but might also be driven by some of the other gradients. This can be written as:

$$\Gamma_r = -D\nabla_r n + m_{12}\nabla_r T_e + m_{13}\nabla_r T_i + m_{14}E_{\parallel} \quad (5.5)$$

in which the last three terms usually are abbreviated into one term (this is the definition of  $v_{pinch}$ , the inward pinch, directed in radial inward direction):

$$-v_{pinch}n = m_{12}\nabla_r T_e + m_{13}\nabla_r T_i + m_{14}E_{\parallel} \quad (5.6)$$

So that:

$$\Gamma_r = -D\nabla_r n - v_{pinch}n \quad (5.7)$$

The first term is usually referred to as the diffusive part, the second term as the convective part.

When one tries to determine the  $D$  and  $v_{pinch}$  terms experimentally two different scenarios must be discussed. In a steady state case, from the particle balance, a  $D^{pb}$  can be calculated from the definition:

$$D^{pb} \equiv \frac{-\Gamma_r}{\nabla_r n} = D + \frac{v_{pinch}n}{\nabla_r n} \quad (5.8)$$

In a perturbative experiment an incremental  $D^{inc}$  can be defined as:

$$D^{inc} \equiv \frac{-\partial\Gamma_r}{\partial\nabla_r n} \quad (5.9)$$

Clearly these two diffusion constants should not be expected to be equal in general.

$D$  often has a value much larger than predicted by neo-classical theory. Only in special situations (in barriers that occur in high-confinement regimes) does it approach the neo-classical value [149]. The observed convective velocity ( $v_{pinch}$ ) can only partially be explained by the Ware pinch effect [63, 143].

Writing the gradients explicitly, the radial diffusion can be described by the following equations [72].

The radial particle flux  $\Gamma_{e,r}$  as a combination of inward pinch and diffusion:

$$\Gamma_{e,r} = -D\frac{\partial n_e}{\partial r} - v_{pinch} \cdot n_e \quad (5.10)$$

and the continuity equation:

$$\frac{\partial n_e}{\partial t} + \left( \frac{1}{r} \frac{\partial}{\partial r} r \right) \Gamma_{e,r} = S_e \quad (5.11)$$

$\Gamma_{e,r}$ ,  $D$ ,  $n_e$ ,  $v_{pinch}$  and  $S_e$  are all functions of radius  $r$  and time  $t$ . The function  $S_e$  is a local source function for particles (from now on only electron transport is considered, since electrons are the only observable species in RTP, hence the subscript “e”).

For a cylindrical geometry 5.10 and 5.11 can be combined into:

$$\frac{\partial n_e}{\partial t} = \left( \frac{1}{r} \frac{\partial}{\partial r} r \right) \left[ D \frac{\partial n_e}{\partial r} + v_{pinch} n_e \right] + S_e \quad (5.12)$$

### 5.3 Strategy for extracting $D$ and $v_{pinch}$

On the basis of the measured profiles for  $n_e$  as a function of time one would like to determine the radial profiles of  $D$  and  $v_{pinch}$ . The following strategies have been applied to obtain these values.

From eq. 5.12 it can immediately be seen that in steady state, (assuming  $S_e = 0$ ) it is impossible to determine  $D$  and  $v_{pinch}$  independently. Only their ratio,  $D/v_{pinch}$ , can be determined. So first the ratio between  $D$  and  $v_{pinch}$  is briefly discussed and estimated in Section 5.3.1.

Determination of both parameters,  $D$  and  $v_{pinch}$ , independently is less straightforward. Two strategies are possible in this case, both take the time evolution of the plasma into account.

If the source profile is known, and a flat region exists on the  $n_e$  profile in the plasma, the term  $\frac{\partial n_e}{\partial r}$  is zero. This is used in the first strategy. In this case, for a dynamic situation like just after a sawtooth crash, the value of  $v_{pinch}$  can be calculated from Eq. 5.12 and the measured  $n_e$  profile. An example of a result of such a procedure using RTP data is given in Section 5.3.2.

A second strategy is to build a numerical model based on Eq. 5.12 for assumed values of  $D$  and  $v_{pinch}$ . The results are then compared to the measured  $n_e$  profile. If the  $D$  and  $v_{pinch}$  values are varied the value that gives the  $n_e$  profile that agrees best with the measured profile is taken as result of this fitting procedure. For this method the source profile has to be well known.

If the plasma is in steady state, or if a steady state is present in the plasma shortly before a perturbation that is to be simulated, these steady state profiles can be used in the calculation of the  $D$ ,  $v_{pinch}$ , or  $S_e$  profile. Only two of the  $D$ ,  $v_{pinch}$  and  $S_e$  profiles have to be assumed. The remaining one can be calculated, when it is assumed that the  $D$ ,  $v_{pinch}$  and  $S_e$  profiles do not change from this steady state phase to the simulated (perturbed) phase. Using this procedure for example  $v_{pinch}$  can be calculated from  $D$  and  $S_e$  as follows:

$$v_{pinch} = -\frac{D}{n_e} \frac{\partial n_e}{\partial r} - \frac{1}{r} \int_{r'=0}^r r' S_e(r') dr' \quad (5.13)$$

An example at RTP of a result of such a procedure is given in Section 5.3.2. This is also the strategy that is followed in the rest of this Chapter, from Section 5.4 onward.

Note that the  $D$  found in this kind of simulations may be different from  $D^{inc}$  if  $D$  itself is a function of  $\nabla n$ . In that case it follows from the definition of  $D^{inc}$  in Eq. 5.9 that:

$$D^{inc} \equiv \frac{-\partial\Gamma_r}{\partial\nabla_r n} = \frac{\partial}{\partial\nabla_r n}(D\nabla_r n + v_{pinch}n) = D + \nabla_r n \frac{\partial D}{\partial\nabla_r n} \quad (5.14)$$

A direct measurement of  $D^{inc}$  by measuring the particle flow and the density gradients would be a third possibility. This has however not been implemented, since no direct diagnostic is available for the particle flow or the particle source.

### 5.3.1 Density scale length

For the given set of equations (5.10 and 5.11) it is easy to extract the ratio  $D/v_{pinch}$  from a steady state plasma. If there is no source term, which in the absence of pellets we usually suppose to be true in the plasma interior, all terms in equation 5.11 are zero, and so is the flux  $\Gamma_e$ . Thus for a measured  $n_{e,eq}$  profile in steady state,

$$\frac{D_{eq}}{v_{pinch}} = -\frac{n_{e,eq}}{\partial n_{e,eq}/\partial r} = \frac{-1}{\partial \ln(n_{e,eq})/\partial r} \equiv L_n \quad (5.15)$$

can be calculated. This defines the radial profile of the density scale length  $L_n$ .

A typical RTP  $n_e$  profile is nearly triangular, so that  $L_n \approx a \approx 0.16$  m close to the plasma center, or  $L_n \approx a - r$  at other radii.

### 5.3.2 Sawtooth density pulse

Often a spontaneous density modulation occurs due to the sawtooth phenomenon in the center of the plasma. The sawteeth are events in which the central part of the plasma is mixed on a very short (100  $\mu$ s) time scale, resulting in flat  $T_e$  and  $n_e$  profiles in the mixing region. The relaxation of the profiles after the sawtooth crash can be described by the same equations. A simulation of this type of data has been done before at RTP by A. van Lammeren [65]. He used a simulation code developed for combined study of heat and particle diffusion at JET (the ACCEPT-code, developed by G.M.D. Hogewei [46]) and found a value of  $D^{inc} = 1.0 \pm 0.3$   $m^2/s$  from the LFS (low field side) interferometer channels.

Later, a calculation by J. Konings, also analyzing the sawtooth collapse, yielded a value of  $v_{pinch} = 1.2 \pm 0.2$  m/s. This could be obtained because just after the sawtooth crash the density profile inside the mixing radius is flat, so the diffusive term is very small and can be neglected (also the internal particle source was neglected). From eq. 5.10 the  $v_{pinch}$  can then be calculated if the particle flux is known. This flux can be determined by integrating the density increase over the volume inside the mixing



radius. This is an upper limit, since if there had been some fueling by an internal particle source the deduced  $v_{\text{pinch}}$  would be lower.

From this  $v_{\text{pinch}}$ , after assuming  $L_n=0.2$  m, a value of  $D^{\text{inc}} = 0.25$  m<sup>2</sup>/s was deduced at  $r/a=0.2$  [63].

## 5.4 Modeling of particle transport

In this Section the numerical simulation of particle transport is described based on eq. 5.12.

First the implementation of the model, the initial and boundary conditions and the particle source functions are discussed in Sections 5.4.1 to 5.4.6. Then in Section 5.4.7 a way is discussed to obtain a measure for the flux surface averaged density on the pellet ablation time scale. Finally in Section 5.4.8 some remarks are made on the expected values of D and the length and time scales needed to be able to observe any effects in transport.

### 5.4.1 Implementation of the numerical model

Based on equation 5.12 a one dimensional numerical model has been built to obtain more information on the values of D and  $v_{\text{pinch}}$  (see Appendix A). The model only includes particle transport, and its purpose is to study the transport around the injection of a pellet.

The differential equation is implicitly solved in first order in dt and dr. Boundary and initial conditions are discussed in detail in the next Sections.

The general idea is to estimate the diffusion D in the unperturbed plasma first (step A). Then the diffusion close to the pellet is estimated (step B). These results are used to simulate a pellet in a plasma on longer time scales (step C).

In all cases an assumption is made for the value of D (or its radial profile) and from this and the initial condition (as if it were a steady state situation) a corresponding  $v_{\text{pinch}}$  profile is calculated.

With these D and  $v_{\text{pinch}}$  profiles, the initial condition and the time dependent boundary condition a time evolution is calculated for step (A) and (C). Then the thus simulated time evolution of the  $n_e$  profile can be compared to the measured interferometer data (after Abel inversion<sup>3</sup>) at a later time. This is done for a series of values for D, and in this way a value of D is found that describes the transport.

In step (B) the pellet is a large localized internal source. An assumption is made for the value of D (or its radial profile) and from this and the initial condition (as if it were a steady state situation) a corresponding  $v_{\text{pinch}}$  profile is calculated.

<sup>3</sup>Starting from scratch it would have been simpler to calculate the line integration from the simulation (and include the necessary refraction correction in that calculation). However, since a reliable Abel inversion program, which included a correction for refraction, already was available, it was faster and more convenient to use that.

With these  $D$  and  $v_{\text{pinch}}$  profiles, the initial condition and the time dependent source function a time evolution is calculated for this step. Then the thus simulated  $n_e$  profile can be compared to the measured Thomson scattering data for the second laser pulse of the Thomson scattering diagnostic.

### 5.4.2 The initial conditions

In all cases a measured initial condition was used (before the pellet). If the simulated results were to be compared with interferometry data, an interferometer  $n_e$  profile was used as initial condition. (Abel inverted, see Section 2.3.4). This was done for two cases, step (A) without a pellet, and step (C) with a pellet. If the simulated results were to be compared with Thomson scattering data, a Thomson scattering  $n_e$  profile was used as initial condition. This is referred to as step (B), and was always done with pellet.

### 5.4.3 The boundary conditions

When comparing with interferometer data (step A,C), an interferometer channel (or in fact the density at that radius, obtained from Abel inversion) was used as boundary condition. Additionally the density gradient at the same position was prescribed. Since this gradient is dependent on the particle source outside this radius it is not precisely known, thus it was taken as a free time-independent parameter in the model.

When comparing with Thomson scattering data (step B)  $\Gamma = 0$  is taken as boundary condition at the plasma edge. This is necessary since the boundary condition can no longer be taken from a measurement in this case. This implies a constant particle content of the plasma and pellet combined, at all times in the model, which seems plausible at this time scale of a few hundred  $\mu\text{s}$ . This is a very useful check on the correctness of the numerics of the simulation.

Also at  $r=0$  the boundary condition is taken to be  $\Gamma = 0$  which is equivalent with  $\nabla n_e = 0$  because also  $v_{\text{pinch}}=0$  at  $r=0$  (see Eq. 5.10).

### 5.4.4 The particle source function

For the particle source in the simulations two assumptions are made. In the simulations without pellet the particle source  $S_e$  is assumed to be only non-zero at the edge of the plasma. This is implemented by simulating only part of the plasma (excluding the edge region in which the particle source is present). The value of the edge particle source can then be imposed by choosing the appropriate density gradient at the boundary of the simulation.

The possibility of having central fueling by ionisation of neutrals will be discussed in Section 5.5.2. It will be shown there that indeed the central fueling is often small.

In the simulations with an ablating pellet in the plasma a source function due to the pellet was derived from the NGS-model (see Sections 5.4.5 and 5.4.6). On

these time scales the internal sources other than the pellet are much smaller than the pellet source, so that they may be discarded, also at the plasma edge. For a typical particle source of  $10^{21} \text{ m}^{-3} \text{ s}^{-1}$  in the plasma center (see Section 5.5.2) the added density in  $100 \mu\text{s}$  is only  $\Delta n_e = 10^{17} \text{ m}^{-3}$ . This is less than 1 % of the pre-pellet central density.

### 5.4.5 The pellet source function

On the time scale discussed above for step (C) the density increase due to the process of pellet ablation can be regarded as a step function. Thus at the time of injection a fueling profile is calculated using eq. 3.1 from Section 3.2, and this profile is added instantaneously to the  $n_e$  profile. No information is available on the behaviour of  $D$  and  $v_{\text{pinch}}$  during or after this event. So they are assumed to keep their pre-pellet steady state values. Note that the simulated plasmas in this case are quiet Ohmic plasmas, so the drift effect of the ablation cloud is probably not very important here.

As a test of the source function the first interferometer profile after pellet injection was used as initial condition. In this case the value for  $v_{\text{pinch}}$  can be calculated from the steady state some time after the end of pellet ablation. This has been tested and did not yield different results for  $D$ , compared to taking the initial condition from the interferometer profile prior to the injection and adding particle deposition derived from the NGS model. Thus the assumed NGS shape of the source function seems reasonable.

### 5.4.6 The pellet source function on shorter time scales

For step (B) the pellet source can no longer be regarded to be a delta function in time (=the complete ablation happens in between two simulated time steps, as was done in Section 5.4.5) since the timesteps are much shorter now than the pellet ablation time. Therefore we apply the NGS model (eq. 3.1) to calculate the particle source at each time step  $dt$ .

To be able to simulate pellets that penetrate beyond the center, or that are injected off-axis, the actual  $T_e$  and  $n_e$  values at the pellet radius are used<sup>4</sup>. This in contrast to the usual method of using the pre-pellet values (which was done in Section 5.4.5). The particles from this source then are deposited in a region of 10 mm around the pellet (between 5 mm before, and 5 mm behind the pellet, in radial direction, to simulate the finite ablation cloud width). This calculation of the instantaneous ablation rate is repeated until the pellet is completely ablated.

Thus in these simulations the essential shape of the particle source function is a peak that moves inward, with a slowly varying magnitude, defined by the NGS model, and a width of 10 mm (as was measured in Chapter 4).

The source function can be fitted to the measured penetration of the pellet by adapting the numerical constant  $C$  in equation 3.1. In this way only the shape of

<sup>4</sup>This gives very good results when compared to the measured  $n_e$  and  $T_e$  profiles by TS for off-axis injected pellets (see Fig. 5.9), which proves the validity of this method.

the ablation rate in the NGS model is used, and not the ablation rate value. The initial diameter of the pellet follows from the measured pellet mass, and the actual fueling efficiency (which is usually close to 100 %). In this way the possible mass loss due to the drifting effect is compensated for.

Since the steep  $T_e$  gradient is only observed in front of the pellet only the front of the cloud is important for these simulations. If the ablation cloud drifts away in backward direction, the  $n_e$  gradient at the back of the cloud changes a lot, but this is not very important since we are observing the flux surface temperature which stays low after it has cooled, even if the cloud drifts away. A second reason why the drift should not influence the measurements strongly is the pulsed character of it. In a typical Ohmic shot the cloud is seen to drift away on intervals of typically 20  $\mu s$ . This means that the pellet is surrounded by a cloud 19 out of each 20  $\mu s$ . In the remaining 1  $\mu s$  the cloud drifts away from the pellet radius and simultaneously a new cloud is formed. The chance that no cloud at all is present at the pellet location at the moment the TS profiles are taken is therefore rather small. Thus no visible effects are expected.

In some cases (in additionally heated plasmas and in the slide-away regime), in which the fueling was much less than 100 %, sometimes as low as 30 %, as observed by interferometry a few hundred  $\mu s$  after the ablation, a smaller pellet mass was taken to adapt the simulation to the actual deposited mass.

#### 5.4.7 Measuring the flux surface averaged density

Since the time resolution of the interferometer is rather limited compared to the pellet ablation process ( $\approx 25 \mu s$  [117]), the data can no longer be used in a meaningful way as an edge condition, or be compared to the simulated  $n_e$  profiles for step (B). Therefore we use as an initial condition the  $n_e$  and  $T_e$  profiles obtained by the first pulse of the double pulse TS diagnostic, which was taken just before the pellet enters the plasma (see Section 2.3.4). The  $n_e$  and  $T_e$  profiles obtained by the second pulse are then used to compare to the output of the simulation.

Another problem in going to a shorter time scale is the fact that the density has not yet reached a constant value on each flux surface (this takes typically 200-400  $\mu s$ , see Chapter 6). The density will locally (around the pellet and in the flux tube crossing the pellet position) be very high, and it may be almost unaffected in some other regions on the same flux surface. Thus it can not be expected that the measured  $n_e$  profile equals the flux surface averaged  $n_e$  profile.

It is likely that a high density region on a flux surface is not intersected by the TS-laser and thus not observed. Even if the localized density is seen, it will probably not have the same value as the flux surface average. This has as a consequence that it is not useful to compare the  $n_e$  profile measured by the second TS pulse with the simulation results.

However, if energy conservation on each flux surface is assumed, the product of the flux surface averaged  $T_e$  and the flux surface averaged  $n_e$  is a constant on each flux surface.

$T_e$  has a much shorter equilibration time on a flux surface than  $n_e$ , because  $T_e$  spreads along field lines typically with the electron thermal velocity, while  $n_e$  moves with the ion thermal velocity, which is about 40 times slower (assuming  $T_e=T_i$ ). Several toroidal revolutions are needed for full equilibration on a flux surface, but this number will be comparable for ions and electrons. Experimentally it is found that the equilibration time for  $n_e$  is about  $200 \mu\text{s}$  (see Section 6.5). So for  $T_e$  a time of  $5 \mu\text{s}$  may be expected, which is short compared to the time scale of the simulation. This can also be seen by observing the (wide angle)  $H_\alpha$  signal during pellet injection (see for example Fig. 2.8). As soon as the pellet has passed the plasma center the light emission drops sharply due to the drop in  $T_e$ . This means that the cooling produced by the pellet has reached the other side of the flux surface. Also a direct calculation yields this result. Assuming that  $T_e=100 \text{ eV}$  the electrons have a thermal velocity of  $4 \times 10^6 \text{ m/s}$ . The toroidal size of the plasma is  $4.52 \text{ m}$ , so several revolutions (say 4) take  $4.5 \mu\text{s}$ .

This makes it plausible to assume that the measured  $T_e$  equals the flux surface averaged  $T_e$  profile.

Thus the simulated density profile (which is by definition flux surface averaged, since the model is one dimensional) should be used to calculate the corresponding flux surface averaged  $T_e$  profile using adiabaticity. This  $T_e$  profile can then be compared to the  $T_e$  profile measured by the second TS pulse (which can be regarded as a function of the flux surface averaged density and the pre-pellet  $n_e$  and  $T_e$  profiles).

#### 5.4.8 Expectations

In Chapter 2, table 2.3, some theoretical values were calculated for the diffusion coefficient  $D$ . Here it was found that according to neo-classical theory  $D$  has a typical value of  $0.8 \text{ m}^2/\text{s}$  in the Ohmic regime, going down to  $0.15 \text{ m}^2/\text{s}$  in the post-pellet cold plasma. The same calculation was done for the ablation cloud. Since the conditions in this cloud are strongly collisional the classical  $D$  should be applied here. This can give much higher values, ranging from  $0.74$  to  $57 \text{ m}^2/\text{s}$ , depending strongly on the local density, which is not precisely known in the experiment.

The time scales on which to expect clearly visible effects on the density profiles can be estimated for a given  $D$  and length scale. For step (A) and (C) we expect an order of magnitude of  $D=1 \text{ m}^2/\text{s}$  which gives for a length of  $\frac{1}{2}a$  a typical time in the order of  $7 \text{ ms}$ . This is well within the spatial and time resolution of the interferometer, so the results of the simulation can very well be compared with the measurement.

For step (B) the ablation cloud radius of  $5 \text{ mm}$  is taken as length scale, and an order of magnitude of  $D=5 \text{ m}^2/\text{s}$  is expected. This gives a typical time scale of  $5 \mu\text{s}$ . Also this length scale is appropriate for the chosen diagnostic, Thomson scattering, in this case. Also the laser pulse of the TS diagnostic is short enough ( $30 \text{ ns}$ ) to resolve the profiles in this case.

It has to be remarked here that radial heat transport is completely neglected in these simulations. An estimate of this heat transport is calculated in Section

5.6.1 which proves that this is allowed in many cases. However some cases do exist in which this is not the case, the most prominent of which is the well known pre-cooling phenomenon. This, however, can not be explained at all by the usually found heat diffusivity, and is more likely of convective nature. A consequence of non-zero radial heat transport is that the value of  $D$  found in these simulations may be overestimated in some cases.

## 5.5 Density evolution without pellet (step A)

The above described simulation procedure (Section 5.4.1) has first been tested on several plasmas without a pellet. Here the interferometer data have been used to calculate the initial and boundary condition.

First, after assuming a profile for  $D$ , estimates are derived for  $v_{\text{pinch}}$  and  $S_e$  an Ohmic plasma without pellet, in Sections 5.5.1 and 5.5.2. Finally a simulation of a plasma with gas puffing is used to estimate  $D$  in Section 5.5.3.

### 5.5.1 Choosing $D$ and $v_{\text{pinch}}$ profiles

Before a simulation can be done profiles have to be taken for  $D$  and  $v_{\text{pinch}}$ . A parabolic  $D$  profile, with  $D=0.5$  in the center and  $D=5$  at the plasma edge was chosen. From this and  $S_e = 0$  an inward pinch was determined using eq. 5.13. The  $n_e$  profile used as initial condition was used to obtain this result. The resulting profiles are shown in Fig. 5.1. The large inward pinch values at the edge are caused by the neglect of an internal particle source in the plasma. This is, especially close to the plasma edge, not valid.

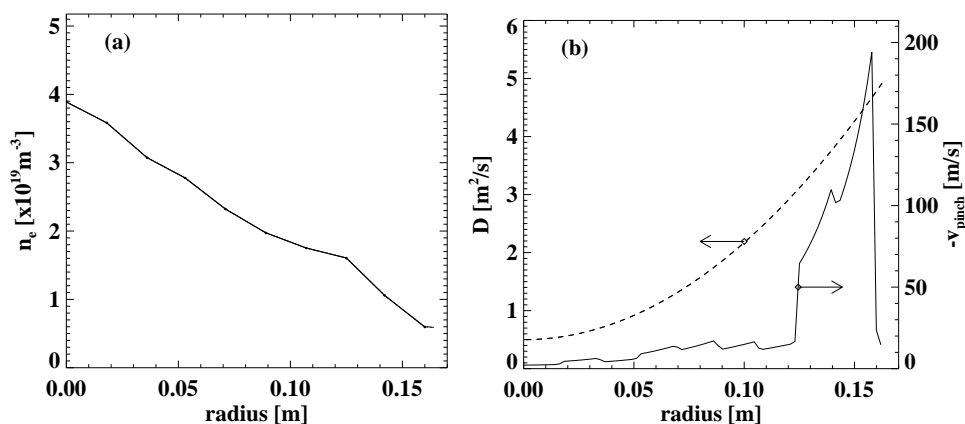


Figure 5.1:  $n_e$  profile as measured by interferometry (a) used as initial condition and a guessed  $D$  profile [(b) dashed line], from which an inward pinch was calculated [(b) solid line] for shotnr. r19960402.018 at  $t=150.005$  [ms].

### 5.5.2 Estimation of the internal particle source

It has to be investigated how large the particle source inside the plasma is (due to ionisation of neutral hydrogen penetrating the plasma) before further numerical results can be obtained. If this is known it can be decided whether it is valid to set it zero in the plasma center.

After assuming a profile for  $D$  and  $v_{\text{pinch}}$  this particle source can be calculated from a measured steady state  $n_e$  profile. For the  $D$  profile the parabolic shape used in the Sec. 5.5.1 is taken. From the absence of steady state hollow  $n_e$  profiles (at least in Ohmic plasmas) it is known that  $v_{\text{pinch}}$  points inward, or at least does not point outward. When  $v_{\text{pinch}}$  is chosen to be zero this gives a safe upper limit for the internal particle source in the plasma.

A result of such a calculation, starting from a measured  $n_e$  profile by Thomson scattering is shown in Fig. 5.2.

From the calculated source profile the neutral hydrogen density is calculated by using the known cross-section for ionisation:

$$S_e = n_e \langle \sigma_{ion} \cdot v_e \rangle n_H \quad (5.16)$$

So with  $\langle \sigma_{ion} \cdot v_e \rangle = 1.5 \times 10^{-14} [m^3/s]$  (for  $T_e=1 \text{ keV}^5$ ) [39] and a known profile for  $S_e$  and  $n_e$  the  $n_H$  profile can be calculated (see Fig. 5.2b). The result shows a density of neutral hydrogen which is clearly peaked in the outer 5 cm of the plasma with a maximum value of about  $7 \times 10^{16}$ . Towards the plasma center the value drops to  $1 \times 10^{16} [m^{-3}]$ . The rising feature at  $r=0$  is an artefact of the calculation.

Ingesson found experimentally (by visible light tomography of the  $H_\alpha$  line emission) a value for the neutral hydrogen density of around  $4 \times 10^{16} [m^{-3}]$  at the edge of the plasma [49]. The order of magnitude of this neutral density agrees with the above performed calculation.

The calculation from the assumed  $D$  and  $v_{\text{pinch}}$  profiles can not be considered to be very precise, but it is an estimate of the order of magnitude of the internal source; nevertheless it still is a very useful result. It shows that the maximum density increase that can be expected in the plasma is below  $1.5 \times 10^{18} [m^{-3}]$  for a simulation of 100  $\mu s$  duration. This means that the effect can be safely neglected for the simulations on the time scale of pellet ablation, which typically lasts 200  $\mu s$ , because the pellet source term is much stronger (typically it gives a density rise of  $5 \times 10^{19} m^{-3}$  in the plasma center). However for simulations on the particle confinement time scale the effect is important and may cause the simulation to deviate from the measured data.

### 5.5.3 Modulated gas puff

A discharge was modeled with a slow modulation in the density due to modulated gas puffing. The simulation was carried out for the indicated time window in Fig.

<sup>5</sup>This assumption introduces only a small error, since the value of  $\langle \sigma_{ion} \cdot v_e \rangle$  is almost constant between 100 eV and 1 keV. At 100 eV it rises to  $2.5 \times 10^{-14} [m^3/s]$ .

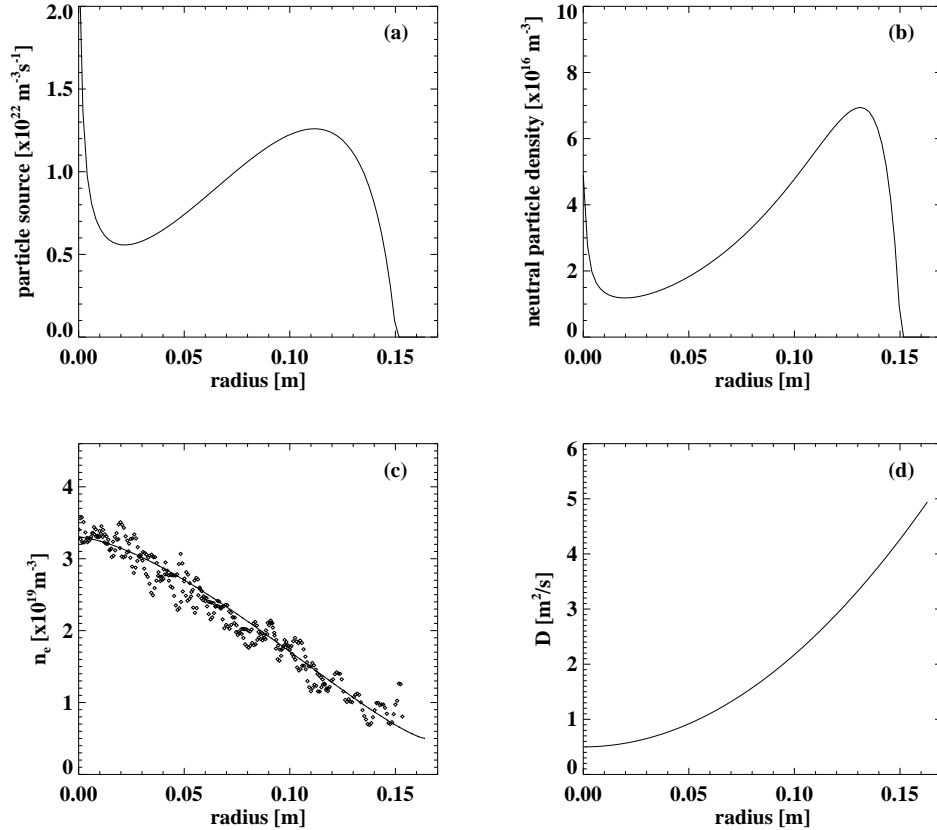


Figure 5.2: Calculated particle source (a) from a theoretical assumed  $D$  profile (d), assuming zero  $v_{\text{pinch}}$ , and a parametrisation [continuous line in (c)] of a measured  $n_e$  profile [dots in (c)] (from shotnr. r19980610.032 at  $t=206.584$  ms). From this and the ionisation cross-section the neutral hydrogen density has been calculated (b).

5.3. The choice for this window is rather arbitrary, except for the initial condition, which was chosen to match the average value over several oscillations in the plasma center. This comparison was done for several values of  $D$  (flat profile). In this way an effective  $D^{inc}$  can be found that describes the data. This was done to obtain a value for  $D^{inc}$  in the unperturbed pre-pellet plasma, so that it can be used in a comparison with the values found during pellet injection.

An example for the resulting simulated density is shown in Figs. 5.4 and 5.5. For this case it was necessary to impose the value measured by the second interferometer channel (at  $r=14.2$  cm) on the plasma to obtain a reasonable fit. This indicates of course the presence of a particle source near the plasma edge that can not be neglected (and is not included in the stationary  $v_{\text{pinch}}$ ).



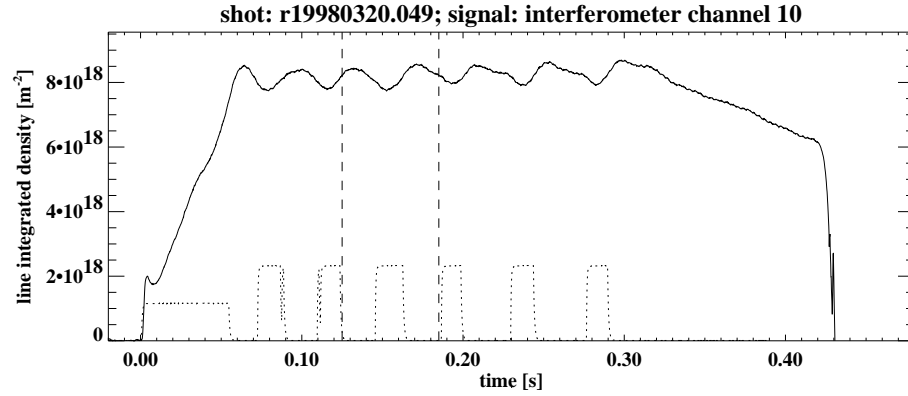


Figure 5.3: Central interferometer signal and the window used for the described simulation (between the dashed lines). The gas puff modulation is indicated by the dotted line at the bottom. Plasma parameters averaged in the chosen time window:  $n_{e,0} = 8.0 \times 10^{19} \text{ m}^{-3}$ ,  $T_{e,0} = 630 \text{ eV}$ ,  $I_{pl} = 78.5 \text{ kA}$ ,  $B_{tor} = 1.89 \text{ T}$ .

The diffusion constant  $D$  has been fit in order to have an oscillation in the simulated central channel with the same phase as the oscillation in the measured data. This is illustrated in Fig. 5.6a.

This is the case for  $D^{inc} = 2.0 \pm 1.0 \text{ m}^2/\text{s}$  (the uncertainty comes from the noise in the measured signal, which causes an uncertainty in the determination of the minimum of the oscillation of about 3 ms). For lower  $D$  the phase difference grows to almost  $180^\circ$  for the  $D^{inc}=0.1 \text{ m}^2/\text{s}$  case. For higher  $D$  the phase difference reverses sign and increases again.

The amplitude could not be fitted to agree with the measurements. At  $D^{inc}=2 \text{ m}^2/\text{s}$  an amplitude of 57 % of the measured data was reached (see Fig. 5.6b). For larger  $D$  the amplitude increases to 67 % at  $D^{inc}=8 \text{ m}^2/\text{s}$

The fact that both the phase and amplitude can not be fitted correctly at the same time may be caused by the presence of a particle source in the plasma that is also modulated by the modulated gas puffing. The large jump in amplitude difference between  $r=12.5$  and  $r=14.2 \text{ cm}$  suggests that the source in that region may be strongest.

#### 5.5.4 Summary

At this point a summary is given of what we have learned about the transport properties of an Ohmic plasma without pellet.

In previous studies all that was known about the values of particle transport in RTP were the values of  $D^{inc}=1.0$  and  $D^{inc}=0.25 \text{ m}^2/\text{s}$  and an inward pinch velocity of  $1.2 \text{ m/s}$  at certain radii in the plasma (see Section 5.3.2).

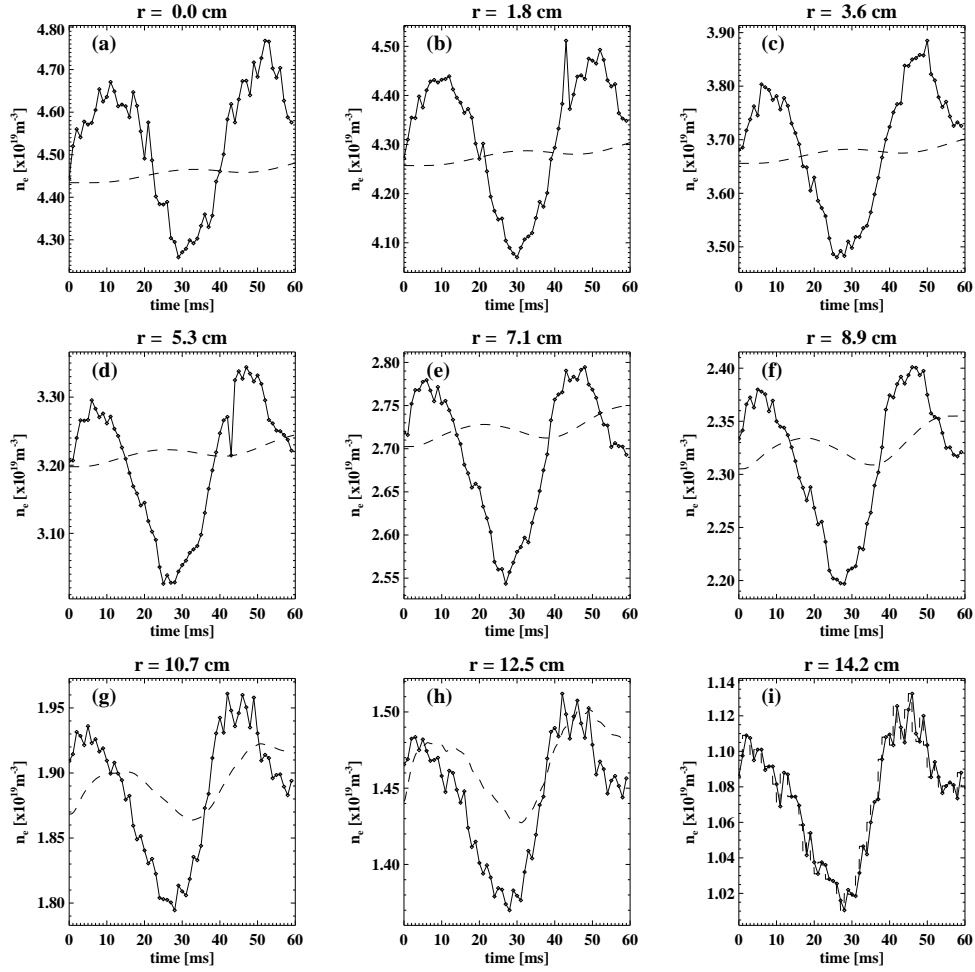


Figure 5.4: Simulated time traces of the electron density at various radial positions (dashed lines) compared to measured (Abel inverted) interferometer data (continuous lines) for  $D=0.1 \text{ m}^2/\text{s}$ . This value of  $D$  is clearly wrong. Both simulated phase and amplitude are very different from the measured data for most channels.

In this Chapter the following has been learned so far. From an analysis of a steady state plasma an upper estimate was found for the profiles of the internal particle source and the related neutral particle density. The internal particle source was found to be below  $1.5 \times 10^{22} \text{ m}^{-3} \text{ s}^{-1}$  for most of the profile. A estimated maximum for the neutral particle density was found to be just above  $1 \times 10^{16} \text{ m}^{-3}$

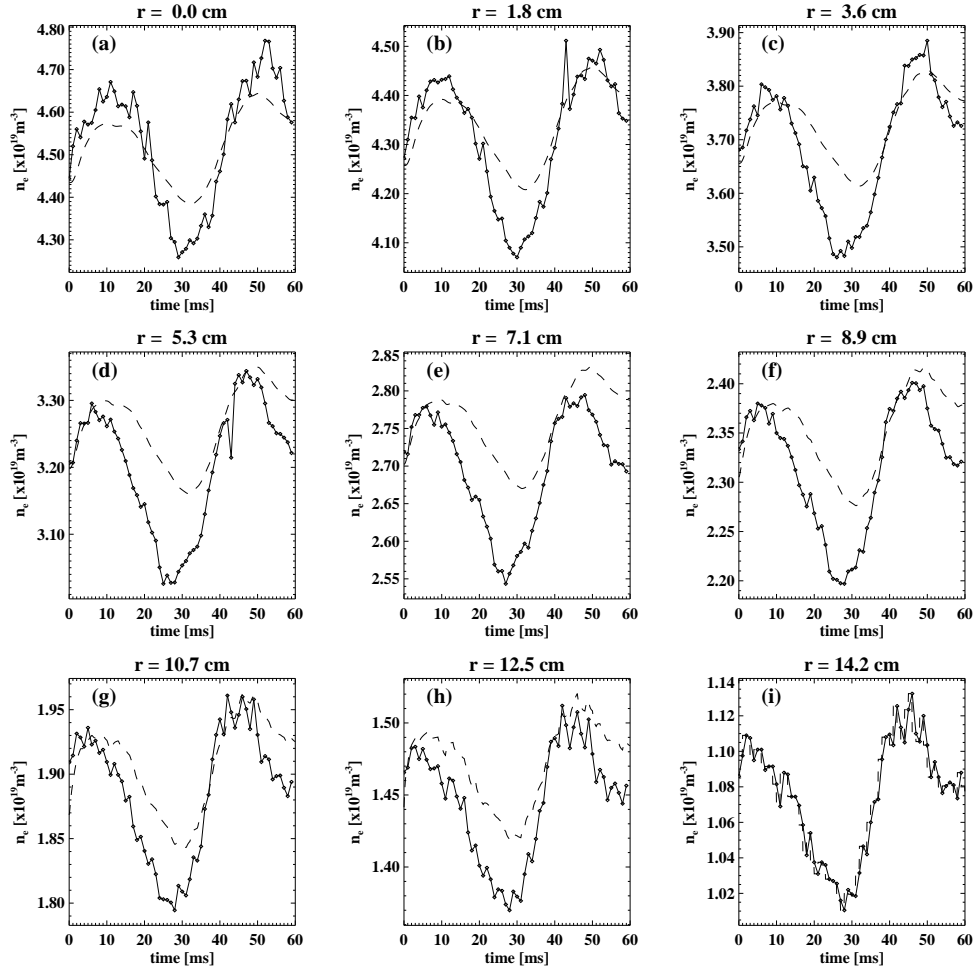


Figure 5.5: Simulated time traces of the electron density at various radial positions (dashed lines) compared to measured (Abel inverted) interferometer data (continuous lines) for  $D=1.5 \text{ m}^2/\text{s}$ . For this value of  $D$  the simulated traces fit the measured data much better, especially the phase of the modulation in the central channels.

at  $r=0$ , rising to  $7 \times 10^{16} \text{ m}^{-3}$  close to the plasma edge.

It is described how a model was implemented to simulate particle transport. The results of these simulations for an Ohmic plasma with modulated gas puff were that a value of  $D^{inc} = 2.0 \pm 1.0 \text{ m}^2/\text{s}$  describes the observed phase behaviour of the inward diffusing density.

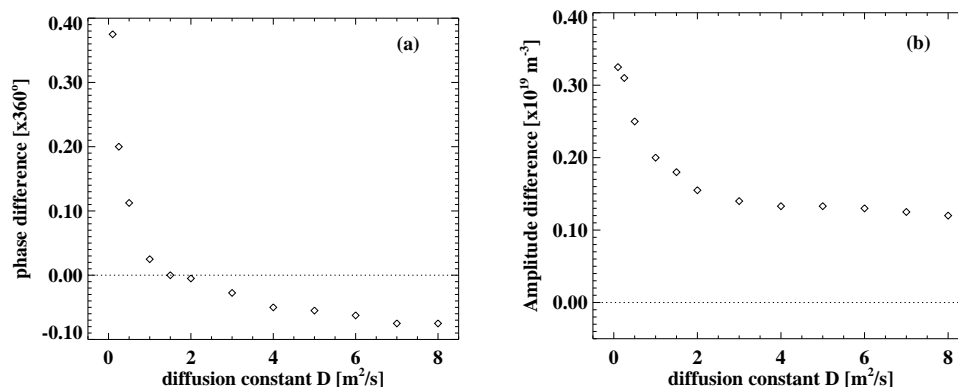


Figure 5.6: Phase (a) and amplitude (b) difference between the measured data at  $r=0$  and the simulation for different values of  $D$ . The phase of the simulation agrees with the measurement at  $D=2.0 \pm 1.0 \text{ m}^2/\text{s}$ . The experimental amplitude was  $0.36 \pm 0.04$  in the plasma center and was never reached in the simulation.

The amplitudes of the simulated modulated density differ, but that may be caused by neglecting the internal particle source, which may play a significant role at the used time scale.

The main objective of the past Sections was to obtain an order of magnitude estimate of particle transport in the plasma in or close to steady state. This Chapter will now be continued with studying the influence of pellets on the plasma, to see what influence that has on the transport properties of the plasma.

## 5.6 Short time scale simulation (step B)

In this Section simulations on the pellet ablation time scale are discussed, and compared to Thomson scattering data (as was explained in Section 5.4).

As initial condition the measured (smoothed) pre-pellet  $n_e$  and  $T_e$  profiles are taken. This gives a smooth  $v_{\text{pinch}}$  profile, a zero gradient at the plasma center, and eliminates small fluctuations in the plasma and statistical errors in the measurement. The internal particle source is assumed to be zero again in the following series of simulations, because of the small influence on this short time scale, as was discussed in Section 5.5.2.

Because it is expected that the density on each surface is not yet equilibrated at the pellet ablation time-scale it is not useful to compare a measured density to the simulation (the expected equilibration time for the ions is in the order of  $95 \mu\text{s}$  to  $1.1 \text{ ms}$ , see Section 6.5). It makes much more sense to use a temperature measurement to compare to the simulation, as was explained in Section 5.4.7. since the temperature is expected to equilibrate much faster (the expected equilibration

time for the temperature of the electrons is in the order of 15 to 28  $\mu\text{s}$ , as is also deduced in Section 6.5).

The simulations are compared to  $T_e$  profiles measured by Thomson scattering (2nd pulse) during or shortly after the pellet ablation. This assumes besides the already discussed very fast heat transport inside the flux surfaces also adiabaticity on each flux surface, so a negligible radial heat transport in between flux surfaces. The validity of the assumptions of negligible radial heat transport will be discussed in Section 5.6.1.

Experimentally it has been observed that the largest changes in the  $T_e$  profile always occur around the actual pellet position. This means that close to the pellet the value of  $D$  is very important, and in the rest of the plasma it is not, since there the plasma is either still in the pre-pellet steady state, (in the region not yet perturbed by the pellet) or the plasma is already very cold and almost without gradients (in the plasma region traversed by the pellet). Or more general:  $D$  is only important in the region of high  $T_e$  gradient. Therefore in all simulations in this Section (5.6) a constant flat  $D$  profile was taken.

Thus by comparing these simulations to TS profiles the local value of  $D$  around the pellet position can be probed during the process of ablation. This may of course be very different from the unperturbed  $D$  in the pre-pellet plasma at that same position.

Different plasma and pellet steps have been studied. First an example of a pellet shot into a quiet Ohmic plasma (shot a) was simulated in Section 5.6.2. Second, an example of an off-axis injected pellet (shot b) is considered in Section 5.6.3. Third, the special case of a plasma in the slide-away regime (with a supra-thermal electron population) is simulated (shot c) in Section 5.6.4. Finally an overview of all considered shots of the three mentioned types is presented and some conclusions are drawn from that in Section 5.6.5.

### 5.6.1 Validation of assumptions

In order to be able to extract the (flux surface averaged)  $n_e$  evolution from the measured  $T_e$  profiles several assumptions were made. A very important assumption is that radial heat transport can be neglected on the time scale considered. If this is not true, than the observed gradient in the  $T_e$  profile may partially be a consequence of this heat flow. This means that the assumed  $D$  to explain the observations is too high. The found  $D$  thus is an upper limit, approaching the real  $D$  value when the radial heat transport may be neglected.

The validity of the assumption of low radial heat transport can be checked by a simple argument. Take for a start the steep gradient in  $T_e$  in Fig. 5.7d (shot a). The jump in  $T_e$ ,  $\Delta T_{e,gradient}$ , is  $\approx 400$  eV and the width of the gradient region is  $\Delta r \approx 3$  cm. This can be used to calculate the resulting heat flow, taking a reasonable value for the diffusivity of  $\chi_e = 3 \text{ m}^2/\text{s}$  [113].

The subset of the energy conservation equation reads:

$$\Delta T_{e,bottom} = \frac{2}{3} \times \frac{\text{surface}}{\text{volume}} \frac{\Delta T_{e,gradient}}{\Delta r} \chi_e \Delta t \quad (5.17)$$

This gives for the typical time scale of the process of  $dt=10 \mu s^6$ :

$$\Delta T_{e,bottom} = \frac{2}{3} \times \frac{1.137 \text{ m}^2}{0.0128 \text{ m}^3} \times 3 \text{ m}^2/\text{s} \times 13.3 \text{ keV}/\text{m} \times 10 \mu\text{s} = 24 \text{ eV} \quad (5.18)$$

if the surface is taken at  $r=4$  cm (at the foot of the gradient) and the volume between  $r=4$  and  $r=5$  cm (so the first layer of 1 cm plasma outside the foot of the gradient). This shows that for the Ohmic case (shot a) the effect in  $T_e$  is small (6 % of the jump in  $T_e$ ). For the other two shots the effect is more important. For the off-axis case (shot b) in Fig. 5.9 the gradient is much steeper, and the typical time scale is longer (since the pellet is no longer moving inward, up the gradient). The same holds for the slideaway case (shot c) in Fig. 5.11, except that here the time scale is much longer since there is no pellet at all at the time at which the profile was measured ( $dt \approx 275 \mu s$  because the gradient has been located at almost the same position since the pellet was completely ablated,  $275 \mu s$  before the second TS profile was taken). In these cases the assumption of no radial heat transport may break down, and the found D may be much higher than the actual D in the plasma.

### 5.6.2 On-axis pellet in Ohmic plasma (case a)

The result of a simulation of a pellet in an Ohmic plasma (case a) is shown in Fig. 5.7. The parameters of this shot are summarized in Table 5.1. The upper plots (a,b) show the initial conditions for the simulation ( $t=0 \mu s$ ). The result of the simulation after 100 time steps of  $1.22 \mu s$ , so at  $t=122 \mu s$ , is shown in the lower plots (c,d). Clearly, the  $n_e$  profile is not well fitted, probably because of asymmetries of the density on each flux surface, as explained earlier. The simulated  $T_e$  profile, however, gives a fairly good approximation of the measurement. Especially the steep gradient between  $r=2$  and  $r=4$  cm is well reproduced. The cooled part of the plasma is somewhat more irregular than the simulation which might be caused by movements of the ablatant after deposition, or by a different fueling profile than predicted by the NGS model. The plasma in front of the pellet, so inside  $r=2$ , even has a somewhat increased temperature, compared to the situation just prior to pellet injection. This may be connected to the non-local central heating that was mentioned in Section 3.5 after cooling of the plasma edge [74, 75, 76].

The thin noisy line on the bottom of Fig. 5.7d is the absolute value of the difference between the simulation and the TS measurement. A least squares fit of the  $T_e$  profile was done with respect to the value of D. The best fit to the data is given by  $D=5.3 \text{ m}^2/\text{s}$ . When looking closer at Fig. 5.7 it can be seen that the

<sup>6</sup>time-scale =  $2r_{cloud}/v_{pellet} = 10 \text{ mm} / 1 \text{ km}/\text{s} = 10 \text{ mm} / 1 \text{ mm}/\mu\text{s} = 10 \mu\text{s}$

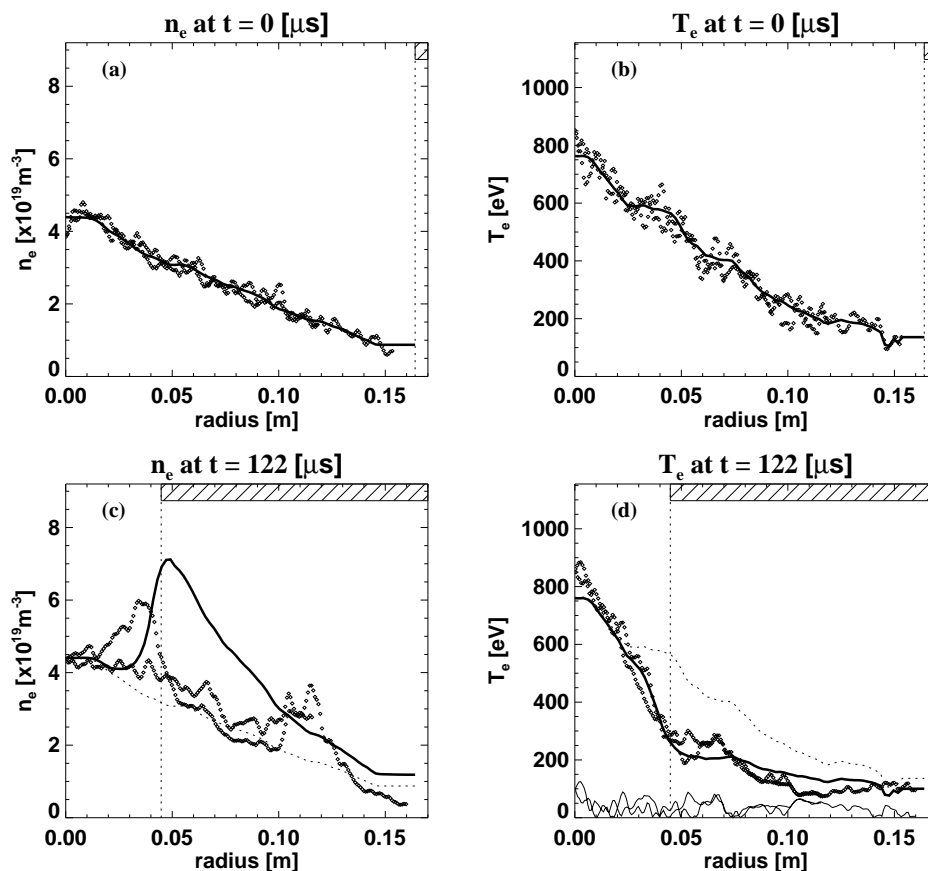


Figure 5.7:  $n_e$  and  $T_e$  profiles before (a,b) and during (c,d) pellet ablation measured by Thomson scattering, compared to simulated profiles during pellet ablation for  $D=5.3 \text{ m}^2/\text{s}$ , in an Ohmic plasma (case a). The fat dots are the TS measurements, the full line in (a,b) is a smoothed version of this data, taken as initial condition for the simulation. The bar on top of the plots indicates the actual penetration of the pellet. The dotted profile on plots (c,d) represents the pre-pellet profiles (so they are the same as the full line in plots (a,b)). The noisy black line at the bottom of plot (d) is the absolute value of the difference between the simulation and the TS measurement. This is used to calculate an error measure, which is then minimized by varying  $D$  to obtain a good fit. Both sides of the profile are shown, so that it appears as if there are two datasets in each of the plots.

simulated steep gradient now is just in between the two gradients measured by TS at the top and bottom of the plasma.

A disturbing feature is the increase in density at radii smaller than predicted by

this simulation. This means that either the ablation cloud is on the move, towards the plasma center, or the ablation cloud has a radius much larger than the 5 mm that has been assumed. It is not possible to decide which option is the correct one on basis of this data. However, based on the measured cloud radius of  $6 \pm 2$  mm that was found in Section 4.3.4, and the knowledge that drifts do occur (as was presented in Chapter 4, also towards the plasma center) the movement of the ablation cloud is the more plausible explanation.

Using an ablation cloud radius of 5 mm (close to the experimentally found value of 6 mm) a number of shots like this one, for different pellet positions have been simulated. The results are shown in Fig. 5.8. A wide range of values for  $D$  is found, between 1.3 and  $9.6 \text{ m}^2/\text{s}$ . The average result of the 11 simulated profiles was  $D=5.2 \pm 2.7 \text{ m}^2/\text{s}$ . The number of available points is not sufficient to decide whether or not there is a relation between  $D$  and the radial position of the foot of the steep gradient. This is confirmed by the fact that the deviation of these points is comparable to the error bar for each point.

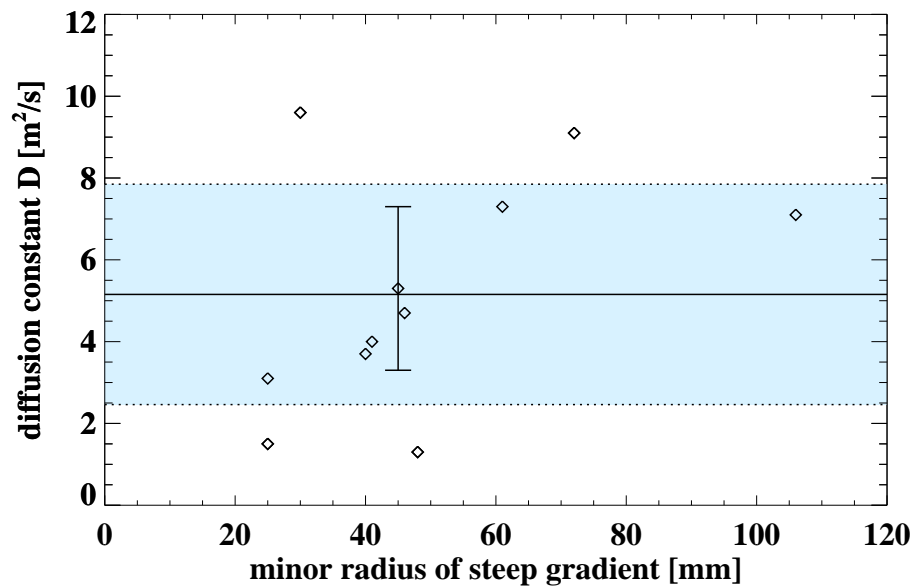


Figure 5.8: Overview of the found  $D$  for all processed Ohmic shots (similar to case a) as a function of the pellet position. The shaded area indicates the value of 1 standard deviation above and below the average (indicated by the full line). A typical error bar for a single simulation is overplotted at  $r=45$  mm.



Table 5.1: Plasma and pellet properties of the examples given of simulated cases.

| Plasma type:                                | Ohmic (case a)              | Ohmic (case b)              | Slide away (case c)         |
|---|-----------------------------|-----------------------------|-----------------------------|
| Plasma parameters used for these cases :    |                             |                             |                             |
| TS-shot nr                                  | r19980721.010               | r19980610.033               | r19980417.024               |
| D   | 5.30 $m^2/s$                | 0.90 $m^2/s$                | 0.05 $m^2/s$                |
| $I_{pl}$                                    | -80.2 kA                    | 77.8 kA                     | 104 kA                      |
| $B_{tor}$                                   | 2.34 T                      | 2.16 T                      | 2.01 T                      |
| $q_a$                                       | 5.45                        | 5.18                        | 3.61                        |
| Pellet parameters used for these cases:     |                             |                             |                             |
| Mass  | $0.60 \times 10^{19}$ atoms | $1.96 \times 10^{19}$ atoms | $0.60 \times 10^{19}$ atoms |
| Velocity                                    | 969 m/s                     | 1028 m/s                    | 910 m/s                     |
| Angle                                       | $0^\circ$                   | $4.2^\circ$                 | $0^\circ$                   |
| NGS factor                                  | $1.5 \times 10^{-13}$       | $1.8 \times 10^{-13}$       | $7.5 \times 10^{-13}$       |
| Simulation parameters used for these cases: |                             |                             |                             |
| dt  | 1.23 $\mu s$                | 1.73 $\mu s$                | 2.5 $\mu s$                 |
| #time steps                                 | 100                         | 100                         | 150                         |
| dr  | 2.05 mm                     | 2.05 mm                     | 2.05 mm                     |
| #points                                     | 81                          | 81                          | 81                          |

### 5.6.3 Off-axis pellet in Ohmic plasma (case b)

The next case that was simulated was an Ohmic plasma in which a pellet was shot off-axis (case b). The result of this simulation is shown in Fig. 5.9. The parameters of this case are also summarized in Table 5.1. As an extra degree of freedom the injection angle of the pellet was varied somewhat (in the simulation) to get a better fit of the steep gradient position. The best fit was obtained with a diffusion constant of  $D=0.9 m^2/s$ . It can clearly be seen that the pellet has almost no radial velocity anymore (it moves parallel to the flux surface), since the measured density in several places already approaches the simulation.

Using an ablation cloud radius of 5 mm also a number of shots like this one, for different pellet positions and injection angles (between  $2^\circ$  and  $6^\circ$ ), have been simulated. The results are presented in Fig. 5.10. A range of values for D is found, between 0.4 and  $2.9 m^2/s$ . The number of simulations is too small to decide if there is a relation between D and the minor radius of the steep gradient position. An increase may be present going to smaller radii (which in this case also means going to smaller injection angles, so getting more close to horizontal injection), but this is only based on the single point of  $D=2.9 m^2/s$  at  $r=28$  mm. The average result of the 9 simulated profiles was  $D=1.2 \pm 0.7 m^2/s$ , and again this deviation is very close to the estimated uncertainty in the individual simulations. This result is significantly lower than the result for horizontal pellet injection (case a).

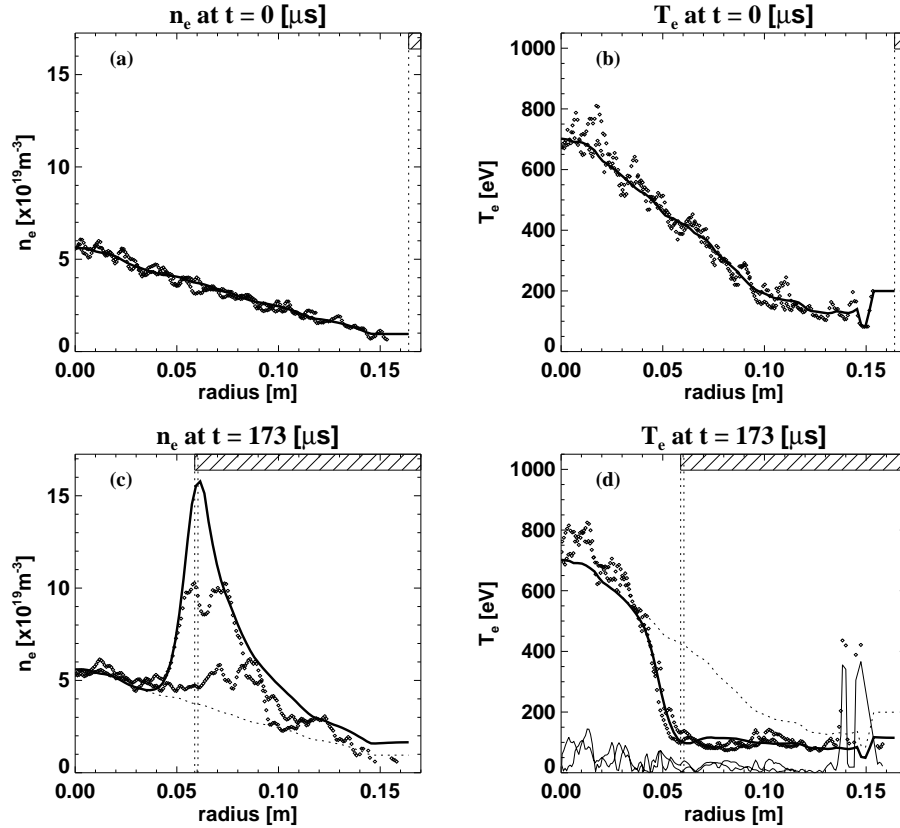


Figure 5.9:  $n_e$  and  $T_e$  profiles before (a,b) and during (c,d) pellet ablation measured by Thomson scattering, compared to simulated profiles during off-axis pellet ablation for  $D=0.9 \text{ m}^2/\text{s}$ , in an Ohmic plasma, plotted in the same way as Fig. 5.7. Since this pellet was injected off-axis it will not penetrate the plasma any further, and, in fact, is on its way now to larger radii. This is depicted by the two vertical dashed lines. The left one indicates the closest approach of the pellet to the plasma center. The right one indicates the pellet position at the end of the simulation.

#### 5.6.4 On-axis pellet in slide-away plasma (case c)

One case was simulated in which a pellet was shot on-axis in a slide-away plasma, i.e. a low density plasma in which a large non-thermal electron population exists that carries the majority of the plasma current [122] (case c).

The result of this simulation is shown in Fig. 5.11. The parameters of this case are also summarized in Table 5.1. In this case first the numerical constant in the NGS model was fitted to get the proper pellet penetration. Then the pellet mass

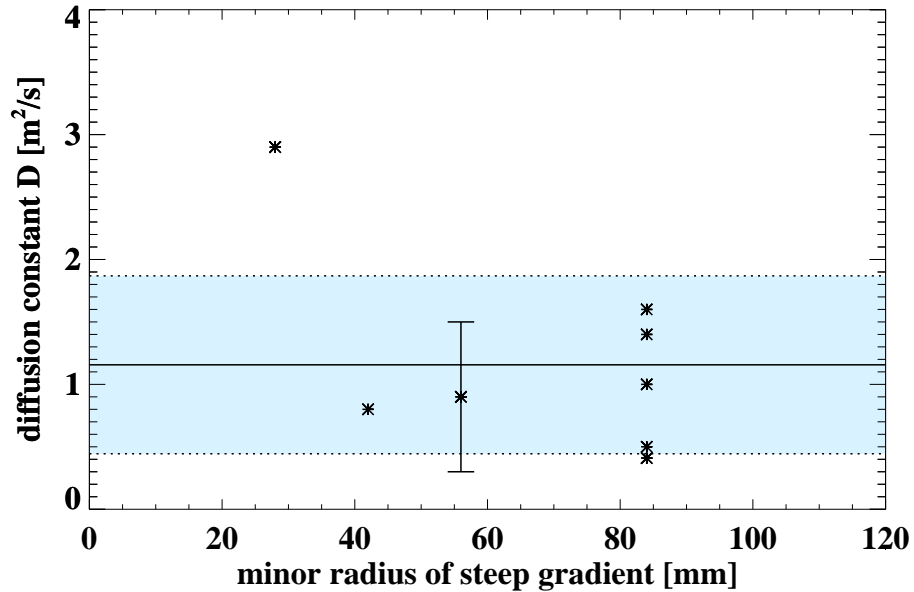


Figure 5.10: Overview of the found  $D$  for all processed Ohmic shots with off-axis pellets (similar to case b) as a function of steep gradient position. The shaded area indicates the value of 1 standard deviation above and below the average (indicated by the full line). A typical error bar for a single simulation is overplotted at  $r=56$  mm.

was fitted to the low  $T_e$  level in the region traversed by the pellet. This showed that the fueling efficiency only was 33 %. This agrees very well with the experimentally determined fueling efficiency of 35 % (determined 5 ms after the end of the ablation by the interferometer).

Finally the value of  $D$  was fitted to the steep gradient in  $T_e$  and a diffusion constant was found in this case of  $D=0.05 \pm 0.04 \text{ m}^2/\text{s}$ . The validity of this can be understood by recalling the fact that the pellet already has been completely ablated for  $275 \mu\text{s}$  at the time the second TS-profile was taken. This means that the steep gradient has to survive  $275 \mu\text{s}$  which is a much longer time scale than the changes we have seen thus far in front of the pellet. In most other RTP plasma conditions no steep gradient would remain after such a time. Another argument which shows that particle transport must be very slow is the fact that the density responsible for the temperature drop is not (yet) visible on the TS profile. This can have two causes. Either no equilibrium is reached at the flux surfaces (this is confirmed by the asymmetry of the  $n_e$  profile), or part of the matter responsible for cooling the plasma has drifted to larger radii, or even outside the plasma (this is confirmed by the low fueling efficiency; compare also to the observations described in Section

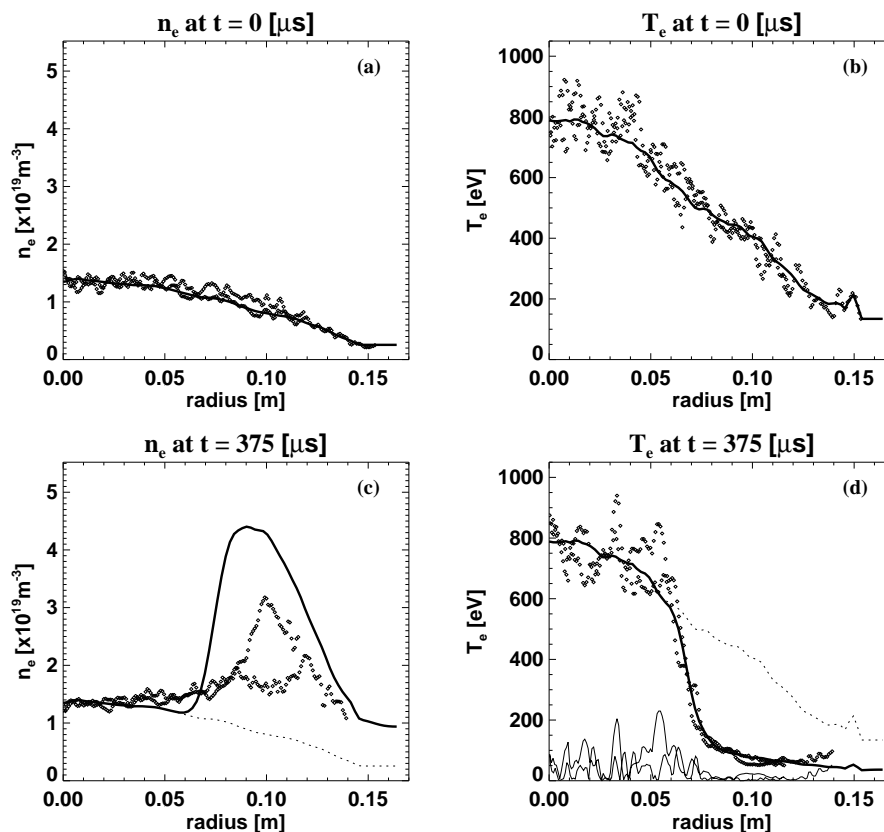


Figure 5.11:  $n_e$  and  $T_e$  profiles before (a,b) and after (c,d) pellet ablation measured by Thomson scattering, compared to simulated profiles after pellet ablation for  $D=0.05 \text{ m}^2/\text{s}$ , in the slide-away regime, plotted in the same way as Fig. 5.7. This pellet was injected on-axis but penetrated only up to  $r=71$  mm. This means that at the time at which the second TS profile was taken the pellet had vanished already for  $275 \mu\text{s}$ .

4.3.2, case d). Probably both effects occur simultaneously.

The fact that this steep gradient is seen also gives a clue to the interpretation of the large ablation cloud in this regime. Remind that in Section 4.3.2 it was found that the ablation cloud is very large in this case, possibly by a continuous drift instead of a pulsating drift, or by charge exchange produced neutrals. A consequence of both possibilities is that a large amount of fueled material directly leaves the plasma, and the fueling percentage is very low (typically 35 %). However, if the drift indeed is continuously outward it is easy to understand why such a steep gradient in  $T_e$  as was observed can build up. If the large cloud is produced by fast neutrals, it is much

more difficult to explain why there would be a sharp edge on the plasma cooling caused by it.

A further interesting effect that can be seen on the  $n_e$  profile (Fig. 5.11c) is the small but clear increase of the density inside  $r=6$  cm, so well inside the sharp gradient in  $T_e$ . Probably this density increase is due to the internal particle source from ionisation of neutrals (as was discussed in Section 5.5.2). From the maximum density increase at  $r=6$  cm of  $0.3 \times 10^{19} m^{-3}$ , which must have occurred in the mentioned  $275 \mu s$ , an estimate for the particle source inside the plasma is found of  $1.1 \times 10^{22} m^{-3}s^{-1}$ . This agrees perfectly with the values found in Section 5.5.2 (see Fig. 5.2a), for an Ohmic plasma without pellet.

The fact that a steep gradient in  $T_e$  is still seen in this last case means that also  $\chi_e$  has a much lower value than in a normal Ohmic plasma. Recall that the value of  $D=0.05 m^2/s$  that was determined actually is an upper limit. It will be lower if there is any radial heat transport. With such a low  $D$  this means that also the heat transport must be very low (this has been observed before for this regime in RTP [123]). Using the same reasoning as in Section 5.6.1 an estimate was made of  $\chi_e$ . If it is assumed that the pellet cooled the plasma to 100 eV, and that the measured value at the foot of the gradient, of about 150 eV is caused by heat transport only, then a value of  $\chi_e \approx 0.1 m^2/s$  is found. This is indeed much lower than the value of  $\chi_e = 3 m^2/s$  typically found in an Ohmic plasma.

### 5.6.5 Summary of all simulated cases

The results obtained for the fast time scale simulation are summarized in Fig. 5.12. The steep gradients observed in the  $T_e$  profile were successfully simulated using only particle diffusion for a number of different plasma and pellet parameters. For horizontal injection in Ohmic plasmas an average value was found of  $D=5.2 \pm 2.7 m^2/s$ . For off-axis injection a lower average value of  $D=1.2 \pm 0.7 m^2/s$  was found.

No clear dependence of  $D$  on the position of the steep gradient was found.

Finally when a pellet is injected in a plasma in the slide-away regime a very low diffusion of only  $D=0.05 m^2/s$  is observed. This has to coincide with a low value of  $\chi_e \approx 0.1 m^2/s$ , lower than in a normal Ohmic plasma.

### 5.6.6 Interpretation of the difference in $D$ with on-axis and off-axis pellet injection

Below a possible explanation is given for the different values of  $D$  found for on- and off-axis pellet injection in Ohmic plasmas.

First it is observed that the diffusion close to the pellet will be classical because of the high plasma density. Since this region probably dominates the particle transport the rest of the flux surface is less important.

$D$  can be written as the square of the ion-Larmor radius  $\rho_i$  divided by the ion-ion

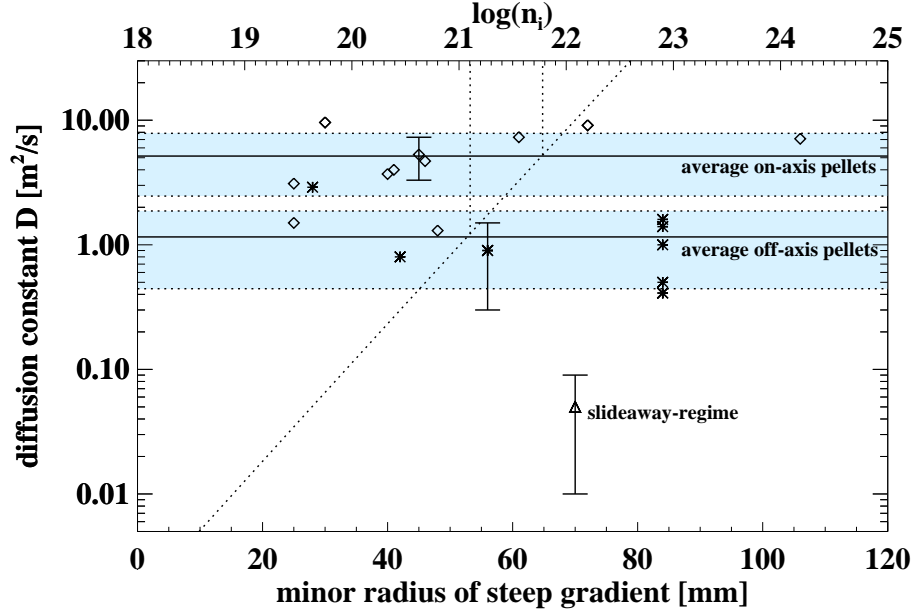


Figure 5.12: Overview of the found  $D$  for all processed shots. The diamonds result from on-axis injected pellets. The stars result from off-axis injected pellets (with injection angles between 2 and 6°). The shaded areas indicate the value of 1 standard deviation above and below the average (indicated by the full line) both for the on- and the off-axis case. The single triangle is the very low value found in the slideaway regime. The diagonal dotted line is the classical diffusion for  $T_e = 4$  eV as a function of the ion density (given on top of the figure). The experimental averages of  $D$  occur at  $n_i = 1.3 \times 10^{21}$  and  $n_i = 6.0 \times 10^{21}$  (indicated by the vertical dotted lines).

collision time  $\tau_i$  [148, 152, 153]:

$$D = \rho_i^2 / \tau_i = 3.16 \times 10^{-23} \frac{n_i \ln(\Lambda_i)}{B^2 \sqrt{T_i}} \quad (5.19)$$

(with  $B$  in Tesla,  $n_i$  in  $m^{-3}$  and  $T_i$  in keV).

$\ln(\Lambda_i)$  is given by [151]:

$$\ln(\Lambda_i) = 17.3 - \frac{1}{2} \ln(n_e / 10^{20}) + \frac{3}{2} \ln(T_i) \quad (5.20)$$

As was mentioned already in Section 3.2, values for  $T_e$  and  $n_e$  inside the ablation cloud are found to be in the range of  $T_e = 1\text{-}20$  eV and  $n_e = 10^{21} - 10^{25} m^{-3}$  [85]. The values of  $T_i$  and  $n_i$  will be comparable.

Since the classical  $D$  scales only with the inverse of the square root of  $T_i$  and  $T_i$  spans only a small range, the value of  $T_i$  is not very important in this calculation. However  $n_i$  is important since it can be in a large range of 4 orders of magnitude, and  $D$  scales linearly with  $n_i$ . Therefore it is assumed that  $T_i = 4$  eV and  $B = 2$  T. With these two numbers it is possible to calculate the density that corresponds to the average  $D$  values found. In this way it was found that  $D=5.2$   $m^2/s$  corresponds to a density of  $6.0 \times 10^{21} m^{-3}$  and  $D=1.2$   $m^2/s$  corresponds to a density of  $1.3 \times 10^{21} m^{-3}$ .

In this way a kind of average density inside the ablation cloud can be estimated. The difference between the on-axis and off-axis pellet injection can now be reduced to a difference in density inside the ablation cloud.

Thus in the simulations with horizontally injected pellets indeed the transport inside the cloud was dominant. In the simulation with off-axis injected pellets  $D$  is already close to the prepellet value. This means that in that case the transport in the cloud is no longer dominant over that on the rest of the flux surface.

This difference in cloud density is also observed experimentally in an indirect way. The cooling of the plasma by the pellet seems limited. In Thomson scattering profiles a typical minimum value of 100 eV after passage of the pellet is observed, both for on- and off-axis pellet injection (compare Figs. 5.7d and 5.9d). This is directly related to the amount of matter deposited on each flux surface, using the assumption of adiabaticity on a flux surface. Now, because of its trajectory, the pellet crosses the flux surfaces much slower for off-axis injection (especially near the point of deepest penetration). Thus, an equal amount of deposition in a longer time gives a lower ablation rate and a lower average density inside the ablation cloud.

## 5.7 Long time scale simulation (Step C)

Finally for a long time scale (the particle confinement time scale, so several ms), the  $D$  found in the previous Sections is used to simulate the plasma behaviour. The idea of a  $D$  profile that is constant in time has to be abandoned, and a step function of  $D$  in time at certain radii appears necessary to explain the data.

### 5.7.1 Stationary $D$ profile

As a next step pellet injection was added to the simulation described as step (A) in Section 5.5. This was done by imposing the pellet fueling profile at one time step. As initial condition the measured interferometer  $n_e$  profile before the pellet is used, and as boundary condition one of the interferometer channels is chosen.

First, the simulation was done using a parabolic  $D$  profile similar to the one shown in Fig. 5.1b, which is kept fixed in time. A central value of  $D=1$   $m^2/s$  was taken as a kind of compromise between the value of  $D = 2.0 \pm 1.0$   $m^2/s$  found in Section 5.5.3, and the values of  $D = 1.0$   $m^2/s$  and  $D = 0.25$   $m^2/s$  found in Section 5.3.2

The value of  $D = 5.2 \pm 2.7 \text{ m}^2/\text{s}$  as found in Section 5.6.2 is not used since this probably occurs only very localized inside the ablation cloud. As soon as the pellet has passed a surface or is gone the value of  $D$  probably is back at the lower value of  $D \approx 1 \text{ m}^2/\text{s}$  (in the inner part of the plasma). The main effect of the high  $D$  around the pellet on this time scale is a smearing out of the deposition profile with the ablation cloud width ( $\approx 10 \text{ mm}$ ). Such details in the applied source function are not relevant since the lower diffusion of  $D=1 \text{ m}^2/\text{s}$  dominates over this effect on this time scale.

The  $v_{\text{pinch}}$  profile was determined using this  $D$  profile and assuming zero  $S_e$  in the equilibrium state before the pellet was injected.

The results of this simulation are shown in Fig. 5.13. The interferometer channel at  $r=10.7 \text{ cm}$  is imposed to exclude any additional gas puffing that may happen simultaneously with the pellet injection in the outer parts of the plasma. For some channels (for example at (e)  $r=7.1 \text{ cm}$  and (f)  $r=8.9 \text{ cm}$ ) the data are nicely reproduced. Also all channels do approach the proper steady state value at 30 ms. However large differences can be seen for the central channels.

After the first 200  $\mu\text{s}$  after injection the simulated density rises much faster than the measured one, and as a consequence reaches the maximum value much too early. To verify that this was not a consequence of a mistake in the pellet fueling profile, in a second run of the simulation instead of the NGS model (eq. 3.1) the actually measured fueling has been used to impose this source function. This was done by using the interferometer profile just after pellet ablation as initial condition (so at  $t=0.2 \text{ ms}$ ), while still using the pre-pellet profiles to determine the inward pinch profile from the chosen  $D$  profile. The behaviour of the model stayed the same, which proves that this is an indication that the central plasma properties are not described by the applied  $D$  and  $v_{\text{pinch}}$  profile.

Also the difference in the central channels cannot be a consequence of some fast transport event (such as the drifting effect of the ablation cloud) that happened during the ablation process itself. First because this would probably give an increase in transport, and not a decrease compared to the model. Second because the drifting effects only occur during the pellet ablation (so within the first 116  $\mu\text{s}$  after the start of the pellet ablation in the used shot). And third because these fast events basically cause the fueling function to be lower, and are thus incorporated in the model by setting the fueling percentage to the measured one.

This shows that probably some ingredient in the model is still missing. In the following Section the  $D$  profile is changed in time in an effort to obtain a better fit for the central 3 channels (a-c).

### 5.7.2 Time dependent $D$

In order to find an explanation, especially for the behaviour of the central channels in Fig. 5.13, a strong time dependent variation in the  $D$  profile was implemented. To make sure that the deposited particles do not penetrate too fast towards the center the value of  $D$  is lowered. At a time 0.2 ms after the addition of the pellet



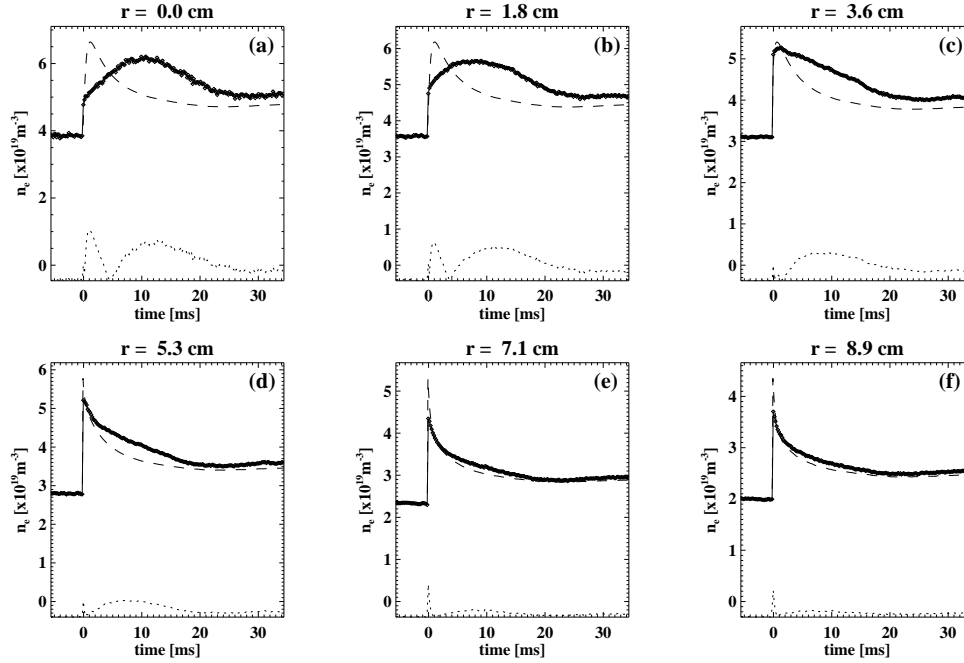


Figure 5.13: Simulated electron density at different radii (dashed lines) compared to measured (Abel inverted) interferometer data (full lines) for shot nr. r19960402.018. The time is set at 0 ms at the moment that the pellet was injected in the plasma. The value of the interferometer channel at  $r=107 \text{ mm}$  is imposed on the profile at each time step, and the evolution inside this radius is observed. A parabolic D profile from  $1 \text{ m}^2/\text{s}$  in the center to  $5 \text{ m}^2/\text{s}$  at the edge was taken. The dotted line at the bottom is the absolute value of the difference between the simulation and the measurement. Clearly the 2 central channels have a much faster and higher density increase than the measurement. Also they reach their maximum too soon. The outer 3 channels give a reasonable resemblance to the measured data. The pellet and plasma parameters are:  $n_{e,0} = 4.1 \times 10^{19} \text{ m}^{-3}$ ,  $T_{e,0} = 0.8 \text{ keV}$ ,  $I_{\text{pl}} = 76.6 \text{ kA}$ ,  $B_{\text{tor}} = 2.24 \text{ T}$ ,  $q_a = 5.46$ ,  $v_{\text{pellet}} = 939 \text{ m/s}$ ,  $m_{\text{pellet}} = 0.42 \times 10^{19} \text{ atoms}$ , pellet penetration = 109 mm (so up to  $r=55 \text{ mm}$ )

fueling profile (so 2 time steps later, determined by trial and error) the D profile was changed in a stepwise manner (see Figs. 5.14 and 5.15).

For all radii inside  $r=50 \text{ mm}$  D was lowered to  $0.04 \text{ m}^2/\text{s}$ . A new, lower, inward pinch velocity was calculated from that, and the pre-pellet, steady state  $n_e$  profile. The resulting time traces for the central two channels match now much closer to the actual measurements (see Fig. 5.16). The value of  $D=0.04 \pm 0.01 \text{ m}^2/\text{s}$  could

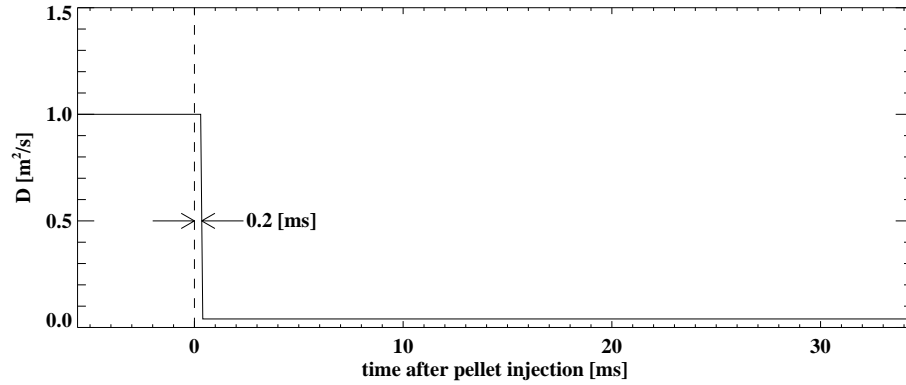


Figure 5.14: Assumed time behaviour of the central diffusion  $D$  for the region inside  $r=50$  mm. The vertical dashed line indicates the time at which the pellet fueling profile is added instantaneously.

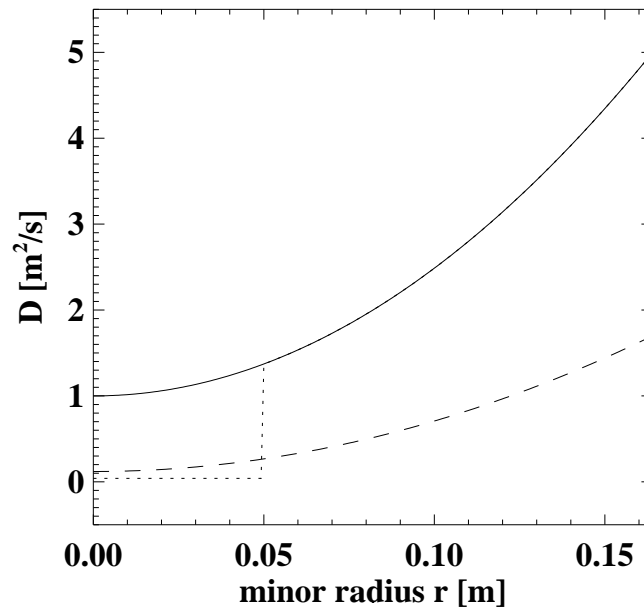


Figure 5.15: The  $D$  profiles that have been used in the described simulations. The full line for Fig. 5.13, the dotted line for Fig. 5.16 (after the step, depicted in fig. 5.14), and the dashed line for Fig. 5.17.

actually be fitted because the rate of change of the simulated density in the central channel (a) in Fig. 5.16 after the step depends strongly on the chosen  $D$ . This is, in

fact, very close to the neo-classical value for D which is  $0.02 \text{ m}^2/\text{s}$ .

The decay, however, between 15 and 30 ms is too slow compared to the measurement so probably D is rising again in this stage.

If a low central D ( $=0.12 \text{ m}^2/\text{s}$ ) is taken for all times, the result does not give the steep increase in the first  $200 \mu\text{s}$  after injection (see Fig. 5.17, in this case both the edge and center value of the parabolic D profile were optimized for the best fit on channel (c) and (d)). The resulting edge value was  $D=1.7 \text{ m}^2/\text{s}$ ). If a center value of  $D=0.04 \text{ m}^2/\text{s}$  was taken the two central channels remained much lower, and never reached the observed maximum density.

Several cases have been implemented with a stepwise change in  $v_{\text{pinch}}$  but no proper fit of the data could be obtained in that way.

It has also been tried to do the simulation using a barrier model (for example a barrier between  $r=4$  and  $r=5$  cm), but also this was unsuccessful. That this can not be the case can also be seen directly from the data. The density in the channel at  $r=0$  cm (see Fig. 5.13a) increases slower than the density in the channel at  $r=1.8$  cm (see Fig. 5.13b). The average increase in the first 3 ms after the fast first jump are  $1.4 \times 10^{21} \text{ m}^{-3}\text{s}^{-1}$  at  $r=0$  cm and  $1.6 \times 10^{21} \text{ m}^{-3}\text{s}^{-1}$  at  $r=1.8$  cm. This can never be the case if there is a region of low D in between the region of pellet ablation and these channels, combined with a higher D at the actual region of these channels.

All this points in the direction that a change does occur in the diffusive transport properties of the central part of the plasma during or shortly after a pellet is injected. The applied D profiles are summarized in Fig. 5.15.

Summarizing it can be said that the key features are first the fast rise in central density followed by a slow continuation of this rise. To model this, D must be reduced inside  $r_{\text{dep}}$  (the maximum deposition radius), shortly after injection, to a value close to neo-classical.

From these long time scale simulations it can be concluded that in the first  $200 \mu\text{s}$  after pellet injection (so mostly during the ablation) a diffusion constant close to  $1 \text{ m}^2/\text{s}$  describes accurately the fast step that is observed. After that only a drop in central D to very low values ( $0.04 \text{ m}^2/\text{s}$ ) describes the data. The value of D at the edge could not be determined very precisely because the boundary condition for the simulation had to be placed rather far into the plasma.

## 5.8 Conclusion and discussion

From this Chapter the following conclusions may be drawn:

- A maximum value for the particle source inside the plasma due to ionisation of neutral particles has been estimated. This maximum source is in the order of  $10^{22}$  particles  $\text{m}^{-3}\text{s}^{-1}$  in a large part of the plasma in a steady state Ohmic plasma without pellet. In the slide-away regime just after a pellet was injected an independent estimate was made, which surprisingly gave almost the same result. A maximum value for the neutral particle density in the order of  $2 \times 10^{16} \text{ m}^{-3}$  in the plasma center up to  $7 \times 10^{16} \text{ m}^{-3}$  near the edge is deduced from

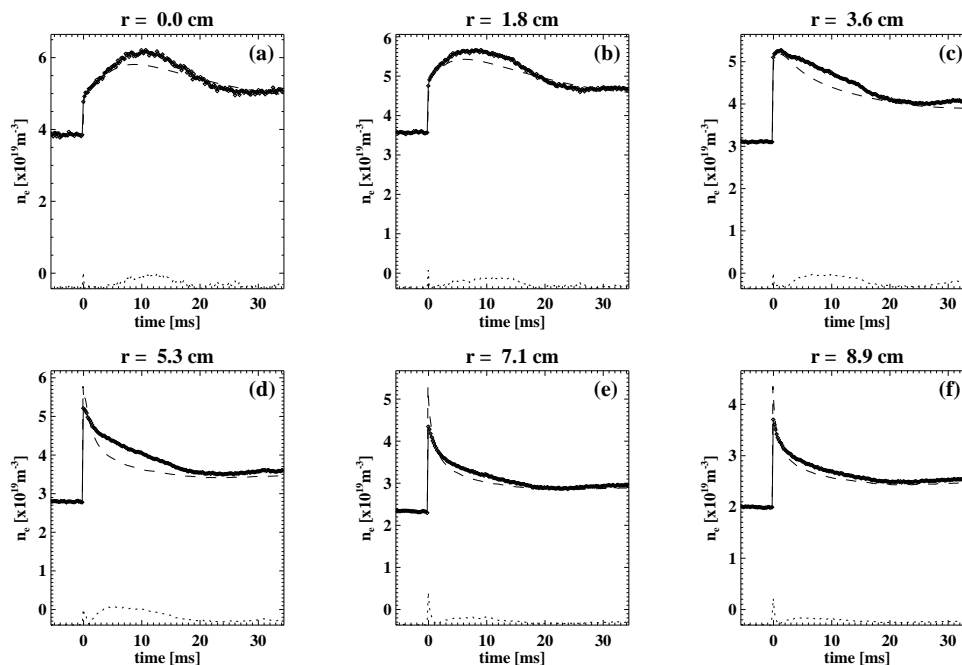


Figure 5.16: Simulated electron density at different radii (dashed lines) compared to measured (Abel inverted) interferometer data (full lines). Now a sudden step in  $D$  is implemented in the model (see Fig. 5.14), which makes the behaviour of the center channels much closer to the measured data.

this source for the Ohmic case (assuming that  $v_{\text{pinch}}=0$ ). This agrees with the value found by Ingesson [49] by VILT measurements at RTP.

Recall, however, that this is an upper estimate, assuming a zero inward pinch velocity. When calculating what effect this particle source would have on the energy balance in the plasma center it can be seen that the found value indeed is somewhat high. For example assuming the neutrals inside  $r=10 \text{ cm}$  have an average energy of 100 eV and are heated to an average temperature of 500 eV after ionisation this would require a power of  $\approx 90 \text{ kW}$ . This is in the same range as the Ohmic input power of the plasma (which usually is in the order of 100 kW for an Ohmic RTP plasma). So this estimate of the internal neutral particle source is probably too high, which would be good for the simulations since there the source is usually assumed to be zero. However, this is not certain. The situation during pellet injection could be different.

- From a simulation on a time scale of 40 ms of a plasma with modulated gas-

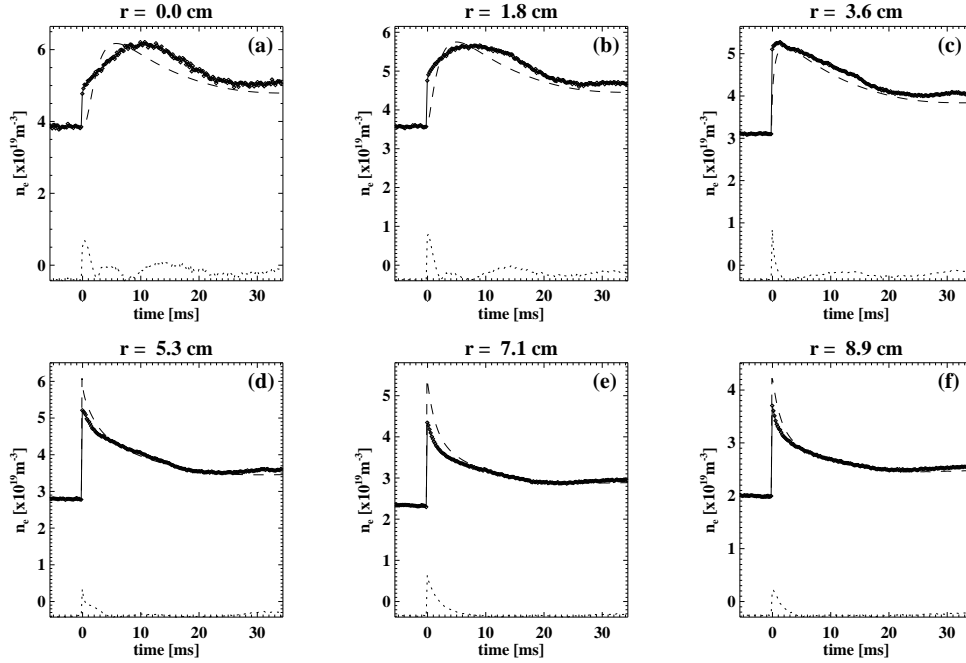


Figure 5.17: Simulated electron density at different radii (dashed lines) compared to measured (Abel inverted) interferometer data (full lines). This case is included to show that the central channels can not be simulated by a stationary low  $D$  value, because the step in the first millisecond after pellet injection in the channels at  $r=0$  and  $r=18 \text{ mm}$  (a and b) are not reproduced in this case.

puffing (step A) it was found that the incremental diffusion constant in the Ohmic plasma is in the order of  $D^{inc} = 2.0 \pm 1.0 \text{ m}^2/\text{s}$ . This may be somewhat too high due to the neutral particle source in the plasma center that was neglected in this calculation. Previously values of  $D^{inc} = 0.25 \text{ m}^2/\text{s}$  and  $D^{inc} = 1.0 \pm 0.3 \text{ m}^2/\text{s}$  have been reported for RTP. These different values are not necessarily conflicting, because they maybe results from observing different parts of the same  $D$  profile.

- The short time scale simulations of a few hundred  $\mu\text{s}$  (step B) showed that determining a flux surface averaged value of the density during the pellet ablation is often possible by using the  $T_e$  profile from Thomson scattering.
- Horizontally injected pellets showed that an increase in  $D$  to  $D=5.2 \pm 2.7 \text{ m}^2/\text{s}$  is necessary to explain the data. This may reflect the diffusion inside the ablation cloud, which is expected to be this large because of the high density

in this cloud. Data taken during off-axis pellet injection could be explained by  $D=1.2 \pm 0.7 \text{ m}^2/\text{s}$  which is similar to the pre-pellet  $D$  value. The ablation in this case is probably too low to dominate particle transport on the flux surface. Therefore the pre-pellet  $D$  value is observed.

- In case of a plasma in the slide-away regime a  $D$  of  $0.05 \text{ m}^2/\text{s}$ , much lower than in a normal Ohmic plasma, is found. However, no value is known for the slide-away plasma without pellet, although according to [123] improved plasma confinement is present in a plasma in the slide-away regime. A crude estimate for  $\chi_e$  yielded in this case an upper limit of  $\chi_e \approx 0.1 \text{ m}^2/\text{s}$
- After simulating the density evolution, on the 40 ms time scale (step C), of a plasma in which a small pellet was injected it was found that during the pellet ablation a central value for the diffusion constant of  $D=1.0 \text{ m}^2/\text{s}$  describes the data. Note that this is the  $D$  value in the central plasma, so not the value of  $D$  inside the ablation cloud. However, only  $200 \mu\text{s}$  after the injection the central value of  $D$  has to drop almost to the neo-classical value of  $0.04 \text{ m}^2/\text{s}$  to describe the data.

So in most cases a normal value for  $D$  was found, only with the exception of the slide-away regime and the central  $D$  inside the radius of pellet penetration. These two exceptions will be discussed below. Inside the ablation cloud a higher value of  $D=5.2 \pm 2.7 \text{ m}^2/\text{s}$  was found, which is not surprising because of the high densities in this cloud.

Especially the very low values that were found,  $D=0.04 \text{ m}^2/\text{s}$  in the plasma center, in Section 5.7.2, and  $D=0.05 \text{ m}^2/\text{s}$ , in Section 5.6.4, are interesting. They may be caused by a plasma state in which particle transport is close to the neo-classical value.

A possible explanation for both cases of low  $D$  is that at the point of deepest penetration of the pellet a region is formed with a high rotational shear.

This happens because the pre-pellet toroidal rotation in the plasma is slowed down in the region crossed by the pellet, but remains at full speed in the plasma center (at least for some time).

It has already been reported that a shear in rotation may lower the transport in the ion part of the plasma, especially at the plasma edge (connected to the transition from L to H-mode) and at internal transport barriers in the ion channel [12] down to the neo-classical value. This may temporarily cause a region of low transport just at the radius of maximum pellet penetration. Unfortunately there is no experimental data on rotation available for these RTP shots.

Why the low  $D$  region has to be extended up to the plasma center in the 40 ms simulation to get good agreement, and why a barrier like localized low  $D$  does not fit the data, is not clear. For the slide-away regime the low  $D$  was combined with a very low  $\chi_e \approx 0.1 \text{ m}^2/\text{s}$ . An explanation for this low  $\chi$  is not available.

Coming back to the question posed in Section 5.1, changes in transport are in some cases necessary to explain the observations. An increase in particle transport,

compared to the unperturbed pre-pellet phase, has been deduced during pellet injection for on-axis injection. The values found probably reflect the high density inside the ablation cloud. High values should be expected here because if, for the parameters in Table 2.3 on page 32, the value of  $D$  is calculated (using the equations for classical transport in this collision dominated plasma), a typical value up to  $D \approx 57 \text{ m}^2/\text{s}$  is found inside the ablation cloud for a density of  $n_e=10^{23} \text{ m}^{-3}$ . Furthermore some unexpected low values have been found for  $D$  in the plasma center just after pellet injection, and for the slide-away regime.

So summarizing the main conclusions of this Chapter: the values for  $D$  are as expected for most conditions, only at the radius of maximum pellet penetration unusual low values were found, acting as transport barriers induced by the pellet.

## Chapter 6

# Transport on a flux surface

### 6.1 Introduction

In the previous two Chapters particle transport in the radial direction was addressed. In this Chapter it will be investigated how fast particles move on a flux surface, during pellet injection. Especially the influence of rotation on this process is studied, as well as the influence of the pellet on the rotation.

These details are important for the interaction between the pellet and the plasma, and thus for understanding the pellet ablation process itself.

Furthermore, although this matter may be less important for global transport properties of the plasma, it is essential for understanding the behaviour of most plasma diagnostics on the short time scale of pellet ablation.

First, measurements of flux surface mixing are presented in Sec. 6.2, and in Sec. 6.3 it is argued that these can not be explained by parallel particle transport only. In Sec. 6.4 experimental results are discussed that show that rotation is important, also for the pellet ablation. In Sec. 6.5 the results are summarized and used to deduce the particle mixing times. The relevant theoretical background of rotation is summarized in Sec. 6.6, and the changes in the rotation induced by the ablating pellet are deduced. This is followed by Sec. 6.7 in which some experimental results on plasma rotation during pellet injection, from photographs of the ablating pellet and from impurity spectroscopy of the plasma, are presented. Finally, a summary and conclusion are given in Sec. 6.8.

### 6.2 Mixing on a flux surface: experiment

As a start of the discussion of transport on a flux surface it is useful to look at the experimental evidence that is available on mixing on a flux surface, i.e. how fast differences in particle density and/or temperature mix on these surfaces and when they reach a constant level on the surface.



Experimentally, many diagnostics can be used to see at what time after pellet injection a symmetric profile is obtained. Interferometry, the soft X-ray and visible light tomography cameras all show a clear symmetrisation within 1 ms. These diagnostics all look at the density symmetrisation time.

The most convincing data has been obtained by taking  $n_e$  and  $T_e$  profiles measured by Thomson scattering. From the  $n_e$  profile in Fig. 4.10 on page 64, which was taken  $274 \mu\text{s}$  after the end of the ablation of the pellet it can clearly be seen that the profile is already very symmetric.

Some more examples of density profiles measured at different times after pellet injection are given in Fig. 6.1a, b, and c.

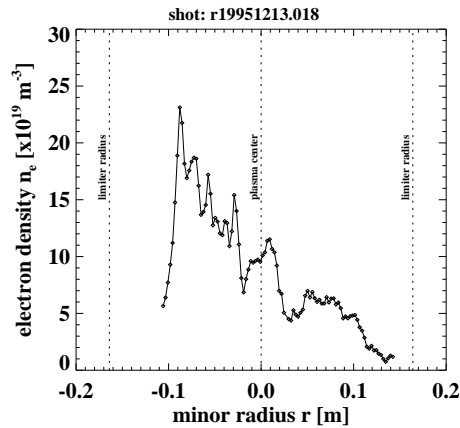


Figure 6.1a:  $n_e$  profile as measured by the Thomson scattering diagnostic at  $29 \mu\text{s}$  after the end of the ablation. Large asymmetries are still present.

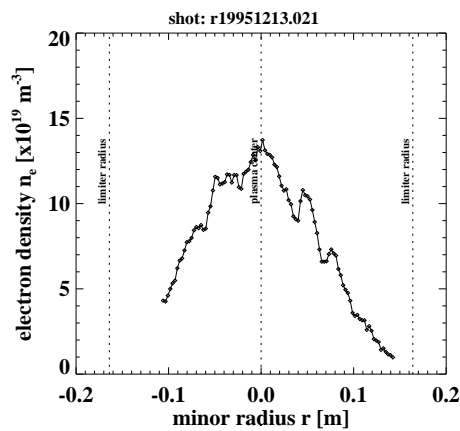


Figure 6.1b:  $n_e$  profile as measured by the Thomson scattering diagnostic at  $102 \mu\text{s}$  after the end of the ablation. The profile is almost symmetric now, only some small structures deviate.

From these results it can be seen that the symmetrisation time for the density is in the order of 100 to  $150 \mu\text{s}$  after the end of the ablation<sup>1</sup>.

<sup>1</sup>The end of the ablation is defined as the end of the interaction between the pellet and the

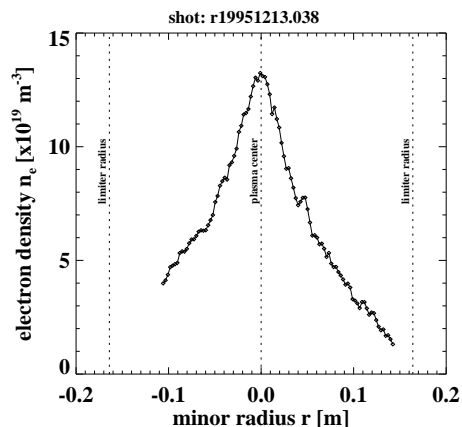


Figure 6.1c:  $n_e$  profile as measured by the Thomson scattering diagnostic at  $174 \mu\text{s}$  after the end of the ablation. An almost perfect symmetry is observed.

At other machines symmetrisation of the density on a flux surface on a time scale of  $\approx 1 \text{ ms}$  has been reported [112].

Symmetrisation of the electron temperature is more difficult to determine because of its fast time scale. In fact, it is too fast for almost any diagnostic available at RTP. The only clue that was obtained, came from  $T_e$  profiles measured by Thomson scattering. These, however, give just a snap-shot, and no time information. From Fig. 5.7 on page 96 it can be seen that even in this very dynamic situation the  $T_e$  profile is almost perfectly symmetric around the plasma center. This is an indication that the equilibration indeed is happening on the time scale of  $10 \mu\text{s}$  at most.

### 6.3 Mixing on a flux surface: a challenge

The measurements presented in the previous Section are not at all easy to explain. If the ablated particles would only move parallel to the magnetic field lines, as is usually assumed, mixing times very different from the measured ones might be expected. This can easily be calculated in the following way.

The parallel expansion will be in the order of the ion sound velocity and driven by the gradients in pressure along the field line. This toroidal velocity is for ions expected to be in the order of  $3 \times 10^5 \text{ m/s}$  for the unperturbed Ohmic plasma (for  $T_e=1 \text{ keV}$ ) and around  $10^5 \text{ m/s}$  for the plasma after it has been cooled (to  $100 \text{ eV}$ ) by the injected pellet (see Table 2.3 on page 32; see also ref. [112]).

A very simple and straightforward first estimate can be made for the time needed to reach a symmetric situation after fueling with the very localized particle source formed by the pellet. Suppose the source is deposited in a circle with a realistic plasma. This can be either when the pellet is completely ablated, or when the pellet leaves the plasma.

diameter of  $d=10$  mm (see Fig. 6.2). The ion sound velocity in toroidal direction is taken to be 100 km/s. Now the area  $A$  covered by the ablatant grows with :

$$A = \int_{t'=0}^t d \cdot v dt' = 10 \text{ mm} \times 100 \text{ km/s} \times t. \quad (6.1)$$

From this it follows that this area will be equal to the total area of the flux surface (assuming  $r=8$  cm and no overlapping) for  $t=2.3$  ms, so this gives the lowest possible time after pellet injection at which a completely symmetric  $n_e$  profile may be expected if only the parallel expansion is important.

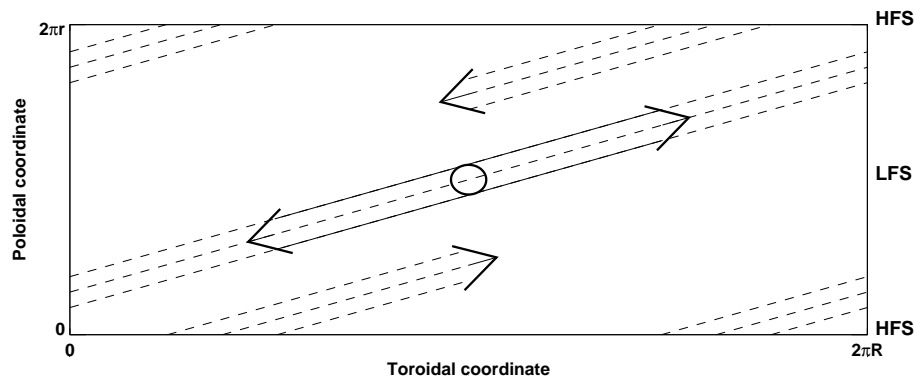


Figure 6.2: Schematic drawing of the spreading of the pellet ablatant on a flux surface. The central circle depicts the density source, which after deposition expands along the magnetic field lines until a constant  $n_e$  is reached on the surface.

For electrons the thermal velocity is about 40 times larger, so consequently the mixing time is 40 times shorter, so this should be about  $55 \mu\text{s}$ . However, the electron density can not deviate very much from the ion density (otherwise the ambipolar diffusion, i.e. the electric field caused by this charge separation would come into play, and stop the mixing process). This number of  $55 \mu\text{s}$  therefore should be seen as a typical time of mixing for the electrons with different velocity (and temperature) without large change of electron density. It is thus a measure for equilibration of the electron velocity distribution on a flux surface. For temperature equilibration also collisions have to be taken into account to thermalize the particles. As can be seen in table 2.3 on page 32 the collision times for a 100 eV plasma are below  $1 \mu\text{s}$  for electron-ion collisions, so this will not change the time scale very much.

The numbers found for equilibration in this way, 2.3 ms for ions, and  $55 \mu\text{s}$  for electrons are clearly much higher than the actual measured numbers (i.e.  $150 \mu\text{s}$  and  $10 \mu\text{s}$ ) presented in Sec. 6.2. This means that an important ingredient leading to cross-field transport on the flux surface is still missing in this model.

## 6.4 Cross-field transport: experiment

An important experimental clue in finding what kind of cross-field transport is responsible for this enhanced mixing is presented in this Chapter. Two types of transport can be imagined to be responsible for this: diffusion and convection. Diffusion would result in symmetric transport in both poloidal directions. Convection would cause transport in one direction, and in fact this would be some kind of poloidal or toroidal rotation.

An estimate of the cross-field transport due to diffusion with  $D=1 \text{ m}^2/\text{s}$  gives a radial distance  $dr=1.2 \text{ cm}$  in  $150 \text{ }\mu\text{s}$ . This triples the initial width of the ablation cloud of  $1 \text{ cm}$  and thus gives a mixing time of one third of the mentioned  $2.3 \text{ ms}$ , so  $0.8 \text{ ms}$ . This still is not sufficient to explain the observed mixing time of  $150 \text{ }\mu\text{s}$ . So the only remaining possibility is a cross-field convection.

### Cut-off observation

An important clue for the explanation of the cross-field transport during pellet injection in the plasma was obtained from ECE data from the radiometer.

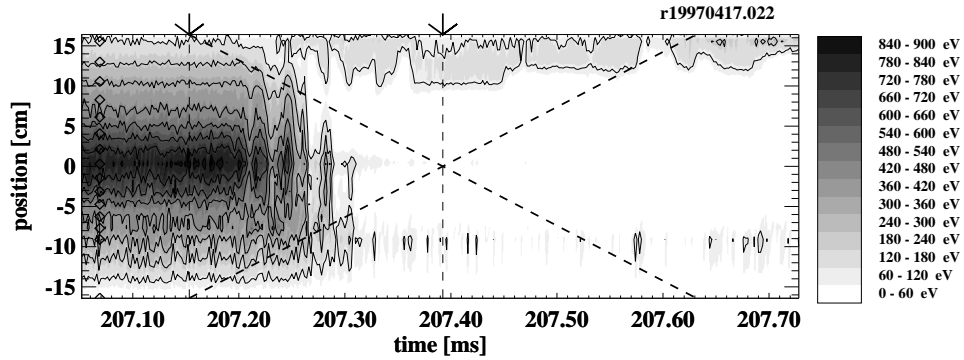


Figure 6.3a: Example of observed radiometer signals (converted to temperature) for positive current and field direction (case A of Fig. 6.4). A clear change in signal of the central channel is seen already starting at  $207.21 \text{ ms}$  while the TS profile taken at  $207.29 \text{ ms}$  clearly shows the same central temperature as ECE did before the pellet. The vertical dashed lines and arrows depict the times that the pellet reaches the plasma edge and the plasma center (if it would live that long). The diagonal dashed lines depict the radius of pellet penetration as a function of time.

The signals of this RTP diagnostic often suffer from the effect of cut-off<sup>2</sup> of the radiation in the plasma due to a very localized high  $n_e$  (see Fig. 6.3a).

<sup>2</sup>The upper cut-off frequency is given by:  $\omega^+ = \frac{1}{2}\omega_c + \sqrt{\left(\frac{1}{2}\omega_c\right)^2 + \omega_p^2}$  in which  $\omega_c$  is the electron cyclotron frequency and  $\omega_p$  is the plasma frequency [35]. For constant magnetic field  $\omega_c = \frac{eB}{\gamma m_e}$  is

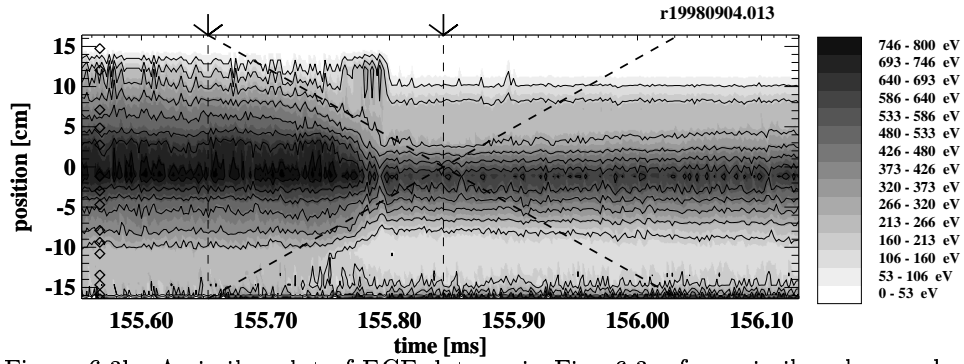


Figure 6.3b: A similar plot of ECE data as in Fig. 6.3a, for a similar plasma shot but with reversed plasma current and reversed toroidal magnetic field (case D of Fig. 6.4). This case also had a smaller pellet than the previous shot, so the pellet does not penetrate until the plasma center. The fact that the highest temperature appears not to be located in the center anymore after the injection, is an effect of the changed optical depth of the plasma due to the density increase (which was not corrected for). No cut-off is present (except maybe for a very short time around 155.79 ms).

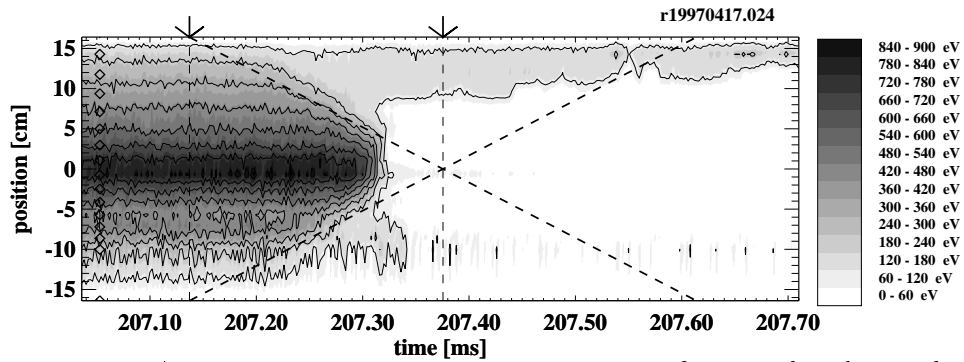


Figure 6.3c: A similar plot of ECE data as in Fig. 6.3a, for a similar plasma shot but now with reversed plasma current (case B of Fig. 6.4). It is clearly seen that the pellet cools the plasma only outside the radius of penetration, and not inside (except when it gets closer than 4 cm to the plasma center). No cut-off is present here before the pellet reaches  $r=4$  cm.

This was clearly determined by comparing  $T_e$  profiles obtained by TS and ECE during pellet ablation. Cut-off occurs very early in the penetration of the pellet,

a constant, except for very relativistic electrons, but  $\omega_p = \sqrt{\frac{n_e e^2}{\epsilon_0 m_e}}$  clearly depends on the electron density. So for each radiometer frequency a different density exists for which the channel is blinded by cut-off.

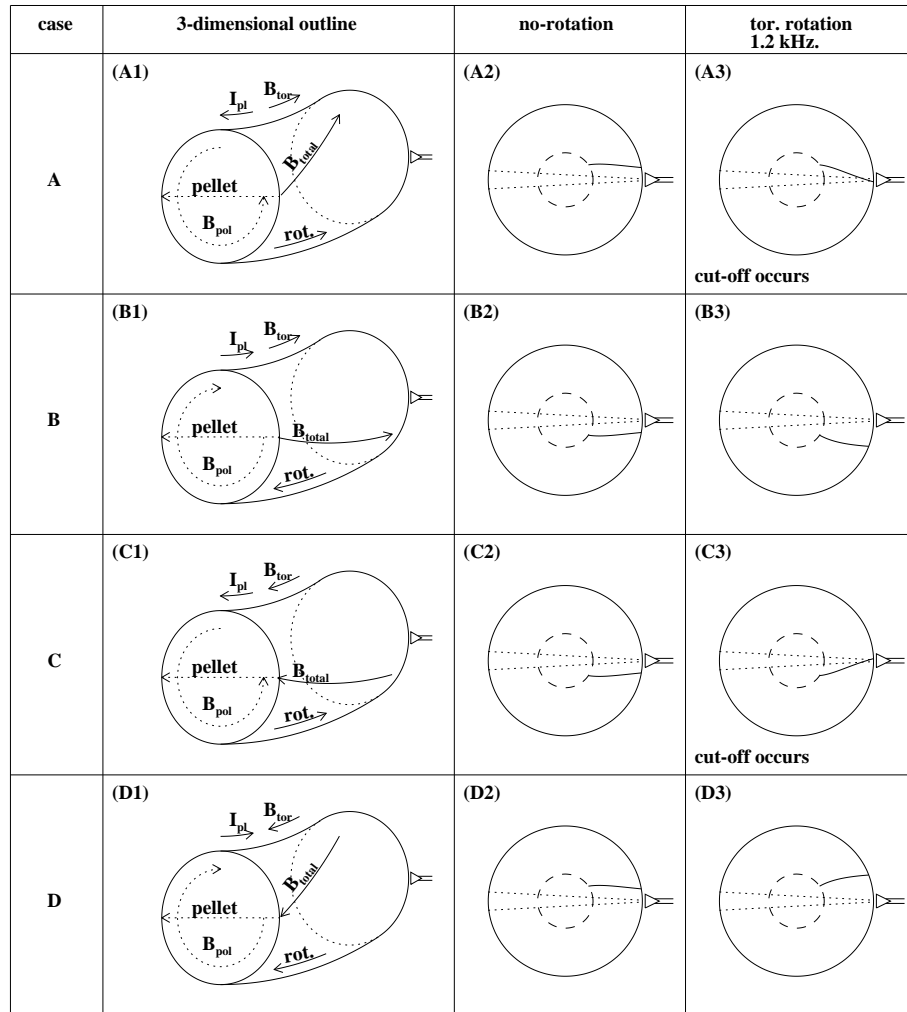


Figure 6.4: Explanation for the observed cut-off effect after pellet injection. The left four plots, A1 to D1 show the possible directions of plasma current and magnetic field in a small section of the torus. A1 is the situation defined to have positive current and toroidal field in RTP. Without rotation, in the poloidal cross-section at the radiometer position the pellet ablatant would not pass in front of the radiometer antenna which is indicated by the little triangle at the right of each cross-section (A2-D2). If rotation is included, A3 and C3 do show cut-off effects, and B3 and D3 not.

usually in the first  $50 \mu\text{s}$ . However, this is still much longer than the  $5 \mu\text{s}$  needed for the ablatant to move the 57 cm between the pellet injector and the ECE-antenna,

along the field lines.

Another confirmation that cut-off occurs was obtained by using an ECE antenna positioned at the HFS of the plasma. In that case no clear cut-off was observed. These measurements showed that the plasma was only cooled close to the pellet radius (within 2 cm), as was published in [56].

First this cut-off was considered to be a problem for the radiometer, since it makes determining  $T_e$  profiles during pellet injection with this diagnostic impossible. Later it was realized that this fact could be used to study the movement of the high density ablatant (because the cut-off effect is caused by high  $n_e$ ) so, in fact, in this situation the radiometer turns into a density diagnostic.

A second clue needed to understand what is happening was obtained by reversing both the plasma current and the toroidal magnetic field. This does not change the direction of the field lines. Assuming the the particles still mainly flow along the magnetic field lines, no difference should occur in the ECE measurement compared to the previous case. This is schematically shown in Fig. 6.4, cases A2 and D2.

However, the measurement of this case, shown in Fig. 6.3b clearly shows a very different behaviour. Also an example is given in which only the plasma current has a reversed direction (see Fig. 6.3c).

The cut-off effect disappears mostly in both cases, only some small effects are seen when the pellet approaches the plasma center (see Figs. 6.3b and 6.3c). The ablatant clearly does not pass between the hot plasma center and the antenna anymore in this case. This clearly points towards an effect caused by rotation or convection.

The important observation on this diagnostic is thus that particles do not only flow along the magnetic field lines, which results in the asymmetric behaviour under reversal of current and magnetic field. This is a clear indication that this effect is connected to convection or rotation, rather than to cross-field diffusion.

Additional information was obtained by observing the same phenomenon with the ECE-imaging diagnostic. By shifting the resonance frequency on a shot to shot basis time information was obtained for (part of) the poloidal cross-section of the plasma. The results for both positive and negative current at the time that the pellet is at a radius of 80 mm are shown in Fig. 6.5 for positive plasma current and in Fig. 6.6 for negative plasma current.

In Fig. 6.5 a clear decrease in signal is seen in the upper part of the plasma inside the radius of pellet penetration. This again points to the presence of cut-off in the plasma. After current reversal the situation is mirrored. As can be seen in Fig. 6.6. Now from the lower part of the plasma inside the radius of pellet penetration clearly less ECE radiation is detected.

### **Explanation of the cut-off observation**

The disappearance of the cut-off effect on the radiometer diagnostic after current or field and current reversal revealed that we were dealing with a local phenomenon in the plasma. This could, however, not be understood by assuming that the ablatant just moves along the magnetic field lines (see Fig. 6.4, A2, B2, C2 and D2). If this

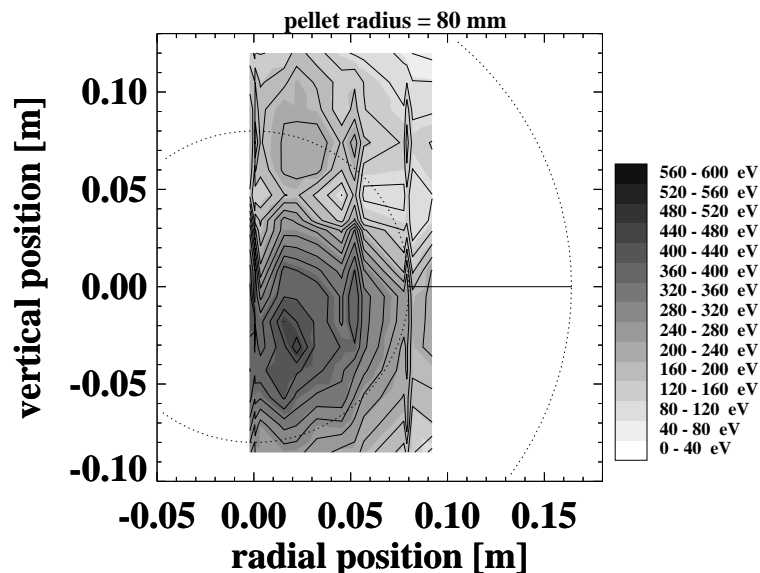


Figure 6.5: Plasma radiation temperature as measured by the ECE-imaging diagnostic during pellet injection (taken from 14 plasma shots, at the time that the pellet reached a radius of 80 mm). The large circle indicates the plasma boundary, the small circle indicates the radius at which the pellet is located. The horizontal line indicates the path of the pellet (but remind: it moves on a different toroidal position). A clear asymmetry is seen in the temperature inside the radius of pellet penetration. Especially on top the plasma seems cooled much more than at the bottom.

were the case the ablatant would not pass in front of the radiometer antenna at first passage. Also there would be no effect of field and current reversal, and the effect of field or current reversal would be completely symmetric. Thus no difference should be expected in the observations of these different cases.

It would take 3 to 5 toroidal turns for the material to pass in front of the antenna, and this is impossible within  $50 \mu\text{s}$ .<sup>3</sup>

When, however, rotation of the plasma is considered the situation changes (see Fig. 6.4, A3, B3, C3 and D3). When a rigid toroidal rotation  $f_{tor}$  is assumed (identical to a poloidal rotation profile of  $f_{tor}/q$ ) a toroidal rotation frequency of at least 1.2 kHz. is needed to explain the occurrence of the first cut-off at  $50 \mu\text{s}$ . At the edge, this would coincide with a poloidal rotation of 250 Hz ( $q_a = 4.8$ ). Both values give a minimum rotation frequency, of which at least one has to be present to explain the observation.

<sup>3</sup>one toroidal turn takes about  $45 \mu\text{s}$  at a spreading velocity along the magnetic field lines of  $1 \times 10^5 \text{ m/s}$ .



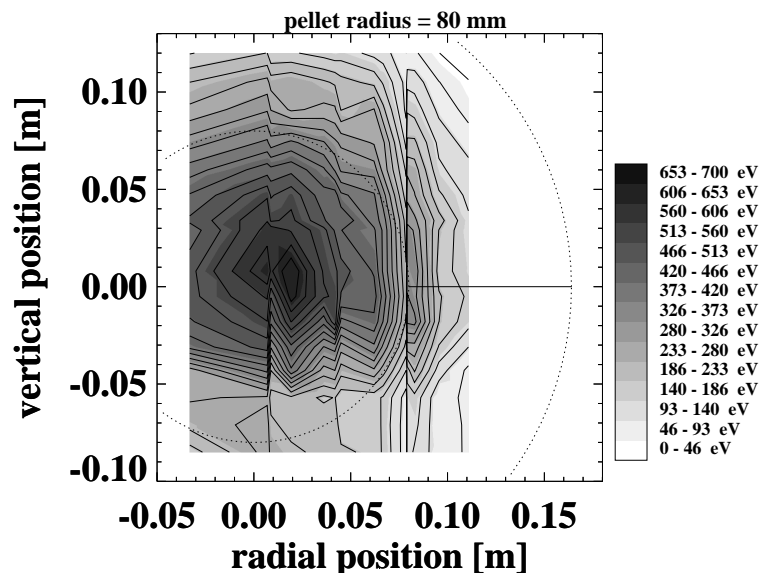


Figure 6.6: Plasma radiation temperature as measured by the ECE-imaging diagnostic during pellet injection (taken from 14 plasma shots, at the time that the pellet reached a radius of 80 mm) plotted in the same way as in Fig. 6.5. In this case the plasma current was negative. Still a clear asymmetry is seen in the temperature inside the radius of pellet penetration. Now especially the bottom of the plasma seems cooled much more than at the top.

In conclusion, a toroidal rotation somewhere above 1.2 kHz (so with a velocity above 5.4 km/s) or a poloidal rotation somewhere above 250 Hz (so a velocity above 260 m/s) close to the plasma boundary must be present (at least for a short time) to explain the observed cut-off effect for case A. Both would give a cross-field drift velocity in the order of 250 m/s.

If this drift is caused by an  $\vec{E} \times \vec{B}$  drift then an electric field of 0.5 kV/m is needed. This is just a modest field, compared for example to what is calculated in Sec. 6.6.1.

The absence of cut-off in cases B and D can be explained by the configuration of the field and rotation direction. The magnitude of the rotation does not play a role in this case.

For case C unfortunately no experimental data is available.

The results obtained with the ECE-imaging diagnostic confirm this interpretation. Fig. 6.5 shows cut-off in the upper half of the plasma, just as is expected from case A3 in Fig. 6.4. The ECE-imaging diagnostic is located somewhat further away from the pellet injector than the radiometer, which explains why the effect is seen a little higher in the plasma. Fig. 6.6 shows cut-off in a narrow region in the lower

half of the plasma, exactly as was expected from case B3 in Fig. 6.4. In this case most of the high density shields an already cooled part of the plasma, so the effect is less pronounced. The second example is clearly not the mirrored image of the first example.

## 6.5 Cross-field transport: summary

In the previous Section it was observed that a cross-field motion of the pellet ablatant occurs during pellet injection. To establish whether this is the same mechanism responsible for the fast mixing on the flux surface of  $n_e$  as discussed in Sec. 6.2 or not, the mixing times are estimated again.

When also the effect of the cross-field motion is taken into account the estimation changes in the following way. A cross-field motion consistent with a toroidal rotation of 10 kHz, or a poloidal rotation of 5 kHz is taken (at  $r=8$  cm,  $q=2$ ). This gives a cross-field velocity of 2.5 km/s.

First an upper estimate of the mixing times is calculated. It is assumed that cross-field motion is only important as long as the particle source is on the considered flux surface, otherwise the flux surface rotates as a whole (provided that the momentum transfer from the background plasma to the ablatant is fast, compared to the particle mixing time). The pellet has a typical velocity of 1 km/s and the ionisation radius typically is 5 mm, so the particle source is only present for 5  $\mu$ s. In this 5  $\mu$ s a cross-field motion of 2.1 km/s would widen the deposited cloud by 10 mm. The assumed cloud diameter is 10 mm, and this becomes now 20 mm, and thus the total mixing time will be halved.

Everything combined the effective cloud width would be 20 mm and a time of around 1.1 ms for the density ( $dt=A/(20 \text{ mm} \times 100 \text{ km/s})$  with  $A=4\pi^2 r R$ , and  $r=8$  cm,  $R=72$  cm) and 28  $\mu$ s for the electron temperature is expected to give a complete mixing of the ablatant on the flux surface.

If the mixing of the momentum of the background plasma and the ablatant takes more time than assumed this would mean that the effect of rotation becomes more important, and may last until the density on the flux surface is completely mixed. Thus the particle mixing times will be smaller. The numbers found should therefore be considered an upper estimate.

A lower estimate can be found assuming that there is no transfer at all of momentum between the background plasma and the ablatant on this time scale. Now the rotation stays an important component until the density on this surface is completely mixed. The surface covered by the ablatant is now given by:

$$\begin{aligned} A &= (10 \text{ mm} + 2.5 \text{ km/s} \times dt) \times 100 \text{ km/s} \times dt \\ &= 10^3 \text{ m}^2/\text{s} \times dt + 2.5 \times 10^8 \text{ m}^2/\text{s} \times dt^2 \end{aligned} \quad (6.2)$$

which gives a time of  $dt=95 \mu$ s needed to fill the complete flux surface for the density. Thus, depending on the efficiency of the transfer of momentum from plasma

to ablatant, a particle mixing time of 0.1-1 ms is expected. The experimental value is 0.15 ms and falls in the lower end of this range.

For the electron temperature (with a sound velocity of  $v_{sound} \approx 4 \times 10^6$  m/s) the covered surface grows as:

$$\begin{aligned} A &= (10 \text{ mm} + 2.5 \text{ km/s} \times dt) \times 4 \times 10^6 \text{ m/s} \times dt \\ &= 4 \times 10^4 \text{ m}^2/\text{s} \times dt + 1.0 \times 10^{10} \text{ m}^2/\text{s} \times dt^2 \end{aligned} \quad (6.3)$$

which gives a time of  $dt=15 \mu\text{s}$  needed to spread the electron temperature perturbation over the complete flux surface.

For the electron temperature a value between 15 and 28  $\mu\text{s}$  is found. These values are still slightly too high to explain the observed mixing of 10  $\mu\text{s}$ , so possibly an ingredient is still missing here.

The conclusion is that parallel expansion combined with the estimated cross-field motion can explain the fast particle and most of the fast temperature mixing of the plasma that has been observed.

The effect of rotation on the mixing of the ablation cloud with the plasma lasts probably much longer than the time needed by the pellet to pass the flux surface. This follows from the observed mixing times, which are very close to the lower limits that were estimated.

## 6.6 Plasma rotation theory

To obtain an insight in which rotation component is responsible for the observed cut-off effect, shown in Sec. 6.4, some theory has to be presented about general plasma rotation first.

### 6.6.1 Stationary rotation

The same forces that cause the bulk plasma to rotate, the radial electric field and the radial pressure gradient [142], also cause rotation of the pellet ablatant. Besides these forces also transfer of momentum from the bulk plasma to the ablatant (due to the high collisionality in the ablation cloud) will occur on the short time scale of pellet ablation (this is related to the mixing time, which was discussed in Section 6.2 and has a value in the order of 100  $\mu\text{s}$ ).

Tokamak plasma rotation can be divided into two components that behave rather differently: a component parallel to the magnetic field and a component perpendicular to the magnetic field.

The rotation perpendicular to the magnetic field consists only of guiding center drifts of the particles, mainly due to the radial electric field and pressure. For the rotation parallel to the field the driving forces include the magnetic induction<sup>4</sup> and

<sup>4</sup>This induces the current in the plasma and causes rotation for the different species in the plasma, but has no significant contribution to the net toroidal rotation of the entire plasma.

the parallel component of the poloidal rotation damping<sup>5</sup>.

The drift velocity  $\vec{v}_\alpha^\perp$  perpendicular to the magnetic field (for species  $\alpha$ ) can be written for a steady state plasma as [142]:

$$\vec{v}_\alpha^\perp = \frac{\vec{E} \times \vec{B}}{B^2} - \frac{1}{n_\alpha q_\alpha} \frac{\nabla p_\alpha \times \vec{B}}{B^2} \quad (6.4)$$

Here  $n_\alpha$ ,  $q_\alpha$  and  $p_\alpha$  are the density, charge and pressure of the considered species of particles. The first term is the  $\vec{E} \times \vec{B}$  drift due to the radial electric field, and the second term is the drift due to the radial pressure gradient.

For the rotation velocity  $v_\alpha^\parallel$  along the magnetic field line generally no simple equations can be given (but fortunately this component is of less importance for the interpretation of the experiments described in this thesis).

From equation 6.4 it can immediately be seen that different species can have different perpendicular rotations, depending on their charge, density profile and pressure profile.

Due to the magnetic configuration the parallel and the perpendicular component both contribute to both poloidal and toroidal rotation.

In the plasma center the net ion poloidal rotation is experimentally observed to be zero [142] in steady state indicating that the poloidal components of  $v_\alpha^\perp$  and  $v_\alpha^\parallel$  cancel each other. This is sometimes ascribed to the existence of strong poloidal damping of rotation due to viscous forces [55], or to the existence of friction with trapped particles [142].

This can be used to determine the radial electric field  $E_r$  from a measured value of the toroidal rotation  $v_{tor}$ .

$$v_{pol} = v_\alpha^\perp \cos(\delta) - v_\alpha^\parallel \sin(\delta) = 0 \quad (6.5)$$

and

$$v_{tor} = v_\alpha^\perp \sin(\delta) + v_\alpha^\parallel \cos(\delta) \quad (6.6)$$

in which  $\delta$  is the angle between the magnetic field line and the toroidal direction:  $\tan(\delta) = \frac{r}{R} \frac{1}{q}$  with  $r$  the minor radius,  $R$  the major radius and  $q$  the safety factor.

Combining 6.4, 6.5 and 6.6 yields:

$$E_r = v_{tor} \frac{r}{R} \frac{B}{q} \frac{1}{\sqrt{1 + \frac{r^2}{R^2 q^2}}} + \frac{\nabla_r p_\alpha}{n_\alpha q_\alpha} \approx v_{tor} B_{pol} + \frac{\nabla_r p_\alpha}{n_\alpha q_\alpha} \quad (6.7)$$

In this equation the first term is positive, the second is negative. For RTP typical numbers are  $v_{tor} B_{pol} = 7.7$  kV/m (for  $q=2$ ,  $B_{tor} = 2$  T and  $r=8.2$  cm) and  $\frac{\nabla_r p_\alpha}{n_\alpha q_\alpha} = -12.5$  kV/m (for  $\nabla p_\alpha = -10^4$  Pa/0.164 m =  $-6 \times 10^4$  Pa/m,  $n_\alpha = 3 \times 10^{19}$  m<sup>-3</sup> and  $q_\alpha = 1.6 \times 10^{-19}$  C).

---

<sup>5</sup>Other possible forces include NBI and ECCD, but since they are not used during the described experiments in this thesis they are not discussed in detail.

This toroidal plasma rotation can be interpreted in a different way for an observer moving along with the bulk toroidal plasma rotation. Because of the Lorentz transformation there exists no radial electric field in this moving frame. From Fig. 6.4 it can be seen that this means that the magnetic field lines move along with the rotating plasma for this observer.

If a strong change in parallel rotation occurs (i.e. after pellet injection) this balance is disturbed and the plasma will also start to rotate in poloidal direction, since the profile of  $E_r$  probably stays constant during this short time scale of the ablation process. This is further discussed in Section 6.6.2.

Furthermore as long as the ablation is more or less adiabatic (which is expected if the drift effects as described in Chapter 4 are small, and no pre-cooling or other fast radial mixing process is present) the pressure profile stays constant also on a longer time scale, and no change at all is expected in the  $\frac{\nabla p_\alpha}{n_\alpha q_\alpha}$  term.

The relaxation to the old situation with zero poloidal rotation depends on the strength of the poloidal damping. This relaxation has been observed by viewing the fast magnetic perturbations in the plasma and has a typical time scale of 30 ms at RTP. Since this is also similar to the time in which the injected pellet mass is lost by the plasma, also that effect may be of importance.

### 6.6.2 Pellet induced rotation change

When a pellet is ablated in the plasma the main effect is a large increase in (local) density. This leads, due to parallel momentum conservation, to a (strong) slowing down in parallel plasma motion, so also in toroidal direction.

To be able to calculate this quantitatively an important assumption has to be made. It is assumed that the region of the plasma under consideration has parallel magnetic field lines, which means that there is no coupling between the perpendicular (gyrating) motion and the parallel motion of the considered particles. Only with this condition the parallel momentum of the particles is conserved. Note also that no such conservation law holds for the poloidal drifting (rotation) that may be present.

As was discussed in Section 6.6.1 the density change has no direct effect on the global pressure and plasma rotation for adiabatic ablation on the time scale of pellet ablation. If it also is assumed that the radial electric field profile does not change globally, then this means that the equality between the poloidal components of  $v^\perp$  and  $v^\parallel$  is lost. Consequently a net poloidal rotation occurs. This assumption of a constant radial electric field profile is justified by the spectroscopic results presented later in this Chapter, in Sec. 6.7.<sup>6</sup>

The magnitude of this rotation can be estimated as follows. If the toroidal and poloidal components of the rotation before pellet injection are  $v_{tor,pre}$  and  $v_{pol,pre}$  and after pellet injection  $v_{tor,post}$  and  $v_{pol,post}$  (which both can be decomposed in

<sup>6</sup>The only direct (line integrated) measurement of this property that I know of shows the same behaviour [43]. Only after the end of the ablation the potential starts to change (for the case of horizontal injection, see fig. 2 on page 1049 of this paper).

$v_{pre}^\perp$  and  $v_{pre}^\parallel$  before the pellet and  $v_{post}^\perp$  and  $v_{post}^\parallel$  after the pellet) than momentum conservation along the field lines gives:

$$m_{flux}v_{pre}^\parallel = (m_{flux} + \Delta m)v_{post}^\parallel \quad (6.8)$$

with  $m_{flux}$  the mass sitting on the considered flux surface and  $\Delta m$  the mass added to the considered flux surface. This momentum conservation has actually been measured at DIII-D [7].

Also

$$v_{pre}^\perp = v_{post}^\perp \quad (6.9)$$

because of the assumed constant  $E_r$  and  $p_\alpha$ . This means for the rotation after the pellet (and after equilibration of all momentum of all the plasma on a flux surface):

$$v_{tor,post} = v_{post}^\perp \sin(\delta) + v_{post}^\parallel \cos(\delta) = v_{pre}^\perp \sin(\delta) + \frac{m_{flux}}{m_{flux} + \Delta m} v_{pre}^\parallel \cos(\delta) \quad (6.10)$$

which is in good approximation (since  $\delta$  is very small):

$$v_{tor,post} = \frac{m_{flux}}{m_{flux} + \Delta m} v_{pre}^\parallel \cos(\delta) \quad (6.11)$$

and (using equation 6.5):

$$v_{pol,post} = v_{post}^\perp \cos(\delta) - v_{post}^\parallel \sin(\delta) = v_{pre}^\perp \cos(\delta) - \frac{m_{flux}}{m_{flux} + \Delta m} v_{pre}^\parallel \sin(\delta) = (6.12)$$

$$v_{pre}^\parallel \sin(\delta) - \frac{m_{flux}}{m_{flux} + \Delta m} v_{pre}^\parallel \sin(\delta) = \frac{\Delta m}{m_{flux} + \Delta m} v_{pre}^\parallel \sin(\delta)$$

So:

$$v_{pol,post} = \frac{\Delta m}{m_{flux} + \Delta m} v_{tor,pre} \sin(\delta) \cos(\delta) \quad (6.13)$$

A typical numerical value for these effects can now easily be calculated. For a value of  $q=1.5$  at  $r=5$  cm the angle is  $\delta = 2.65^\circ$ . Assuming  $\Delta m = m_{flux}$  we find  $v_{tor,pre} = 54$  km/s (12 kHz),  $v_{tor,post} = 27$  km/s and  $v_{pol,post} = 1.25$  km/s. So the poloidal rotation may increase due to pellet injection from zero to a value in the order of 1 km/s if the assumptions are correct, and is especially a function of  $r$ ,  $q$  and the fueling ratio  $\frac{\Delta m}{m_{flux} + \Delta m}$ . From this it follows that there is a maximum induced rotation for pellets much heavier than the plasma of  $v_{pol,post} = \sin \delta v_{tor,pre}$  or  $f_{pol,post} = f_{tor,pre}/q_a$  at the edge.

Because of the damping of the rotation on a longer time scale the pre-pellet situation of zero poloidal rotation is restored. For this it is needed that the radial electric field changes. On the same time scale the toroidal rotation gains momentum again, until it is back to the unperturbed situation.

Another possible mechanism resulting in a poloidal displacement of the ablation cloud is discussed in [112]. Here it is said that *“this motion, which is induced by*

the pellet itself, results from the conservation of kinetic momentum: the convective motion in the sheet of ablated material (due to its positive potential with respect to the plasma) is compensated by a global drift of the whole magnetic surface." This could very well be the same mechanism as proposed above.

A consequence of this poloidal rotation is that the equilibration time on a flux surface is shortened considerably, compared to the case with only parallel expansion of the ablatant.

Another consequence of this result is that in regions with strong change in deposited mass  $\Delta m$ , so close to the end of the pellets life, strong gradients in both toroidal and poloidal rotation are induced. This may lead to a local improvement of confinement, and it has even been suggested that this will lower the power threshold for H-mode in a plasma [7] if the mass is deposited only near the plasma boundary. The experiments reported in Section 7.2 on the so called non-local effect may be related to this effect.

The followed argumentation can be expanded to pellets that are injected off-axis. The only thing that is changed here is that the inserted mass does bring some poloidal momentum into the plasma. As soon as the ablated material is ionized most of this momentum is converted to the gyrating movement of the formed ions and electrons. There is, however, a small component of this poloidal injected momentum in parallel direction. If  $v_{\text{pellet,flux}}$  is the component of the pellet velocity parallel to the flux surface than the injected parallel momentum is  $\Delta m \times v_{\text{pellet,flux}} \times \sin(\delta)$ . This changes equation 6.8 in the following way

$$m_{\text{flux}} v_{\text{pre}}^{\parallel} \pm \Delta m v_{\text{pellet,flux}} \sin(\delta) = (m_{\text{flux}} + \Delta m) v_{\text{post}}^{\parallel} \quad (6.14)$$

(+ for co-injection and - for counter injection).

So this adds or subtracts typically (if  $\Delta m = m_{\text{flux}}$  and  $v_{\text{pellet,flux}} = 1$  km/s, and  $\delta = 2.65$ ) an amount of 23 m/s, which is of no importance at all compared to the typical toroidal rotation velocity of at least 10 km/s, and may safely be neglected (see Sec. 4.3.5).

The induced poloidal rotation deduced in this Section is probably related to what is reported in the literature [83, 112]. There the parallel expansion of the ablatant along the magnetic field lines is simulated and the results are compared to the measurements of a 5 channel interferometer. To explain observed data it was necessary to assume a poloidal movement/rotation in the order of 1 to  $5 \times 10^3$  m/s of the ablatant. This matches with the values found for RTP.

## 6.7 Ion rotation measurements

Several diagnostics give at least an idea of the behaviour of the ion rotation in the plasma during pellet injection. Subsequently the results of the photographs of pellet ablation, and spectroscopy are discussed.

### 6.7.1 Movement on photographs

An indication of the importance of toroidal rotation can be observed on the photographs taken of the ablation process. In Fig. 6.7 the ablation cloud clearly extends to larger negative toroidal direction ( $I_{p1}$  is running in positive toroidal direction). In Fig. 6.8 a photograph from a similar shot is shown, only with reversed  $I_{p1}$ . The effect points in the opposite direction, showing that the plasma current is the important factor here. So the observed toroidal rotation is counter the plasma current direction, consistent with the assumed rotation in the explanation for the observed cut-off as was described above. This observation is consistent with the results found using the fiber array diagnostic in Section 4.3.2 Fig. 4.8. Because the photographs are time integrated no temporal information is available, so no frequencies or velocities can be deduced, only the direction of the rotation<sup>7</sup>.

A next observation from the presented photograph in Figure 6.7 is that if it is assumed that the pellet moves on a straight line it penetrates up to  $r=4$  cm. However, light is still observed at radii closer to the plasma center (between  $r=4$  and  $r=0$  cm, and possibly further outside the view of this diagnostic). The toroidal position of the center of this light is at  $-2.5$  cm. It seems very unlikely that the pellet would jump 25 mm in toroidal direction and then assume its straight path again so something different must be happening here. There are many cases in which this effect does not occur, which proves that reflections of the observed light are not causing this effect.

A sudden poloidal rotation of (part of) the ablation cloud might actually explain this. The first few cm of the movement would then be parallel to the view of the photo camera, so would not be detected. A simultaneous toroidal movement (which is present and manifests itself in the asymmetry of the cloud in toroidal direction) would then cause a seemingly “sudden jump in toroidal position”.

An alternative explanation would be a sudden discontinuity in the toroidal plasma rotation. Such an effect could occur if for example a barrier in momentum is present at this position.

As was discussed in Section 6.6.2 a poloidal rotation is induced by the pellet. It only remains to be explained why the lifetime of this light emitting cloud seems to be suddenly much longer here. The pre-cooling phenomenon might be related to this, because when the plasma center suddenly loses its high temperature this would probably greatly enhance the lifetime of the cloud. In order to be able to observe it as was done in Fig. 6.7 it is also necessary that this central cooling happens just as the pellet is fully ablated, otherwise the poloidal rotated cloud would be behind the cloud around the pellet and not visible.

Similar effects have been observed on another tokamak. At the JIPP T-IIU tokamak in Japan using a tangentially viewing CCD camera a cloud moving away in a poloidal direction from the pellet was observed (called the “tail” structure) [120].

<sup>7</sup>in fact, only neutrals are observed in this way, but due to the high collisionality they will move in the same direction as the cold ions in this cloud.



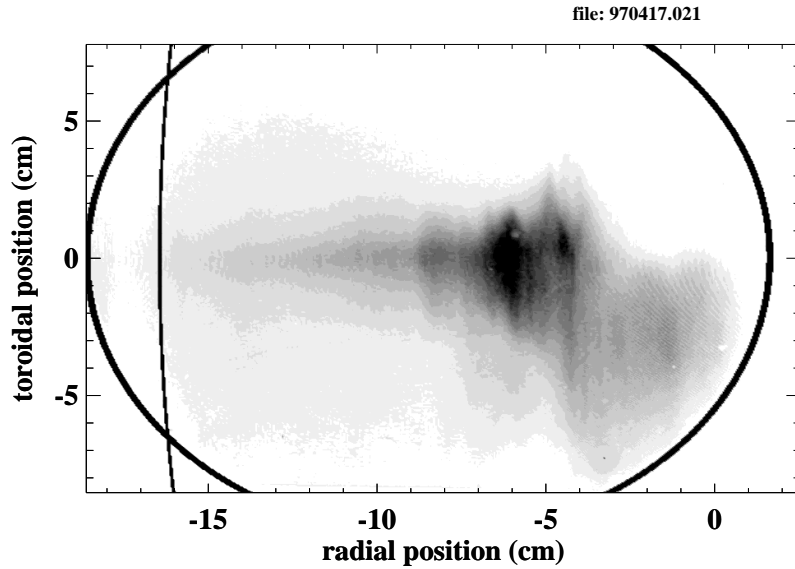


Figure 6.7: Photograph of pellet injected in a plasma with positive current. The fat line indicates the port that is used. The thin line indicates the plasma boundary. The two dots at  $[-10, -7]$  cm and  $[-3, -7]$  cm are defects resulting from the development of the photographic film. Clearly the ablatant has a tendency to move towards the negative toroidal direction. Also the “sudden” toroidal jump of the center of the cloud at  $r=4$  cm is clearly visible.

### 6.7.2 Spectroscopic measurements

A direct measurement of ion rotation can be obtained by observing the Doppler shift in the line radiation emitted by impurities in the plasma. This was done at RTP for poloidal rotation using the carbon IV ion (CIV) [79]. Remind, however, that this may differ from the bulk ion rotation due to different pressure profiles of the different species.

A complicating factor here is that no absolute calibration is available, so that no absolute velocity can be measured, but only a velocity change. The results of such a measurement for a series of plasma shots is shown in Fig. 6.9 for different angles of pellet injection. The negative pellet injection angles were obtained by reversing both the plasma current and the toroidal magnetic field (which effectively puts the tokamak upside down). The result shows for horizontal injection a rotation change of  $1.1 \pm 0.1$  km/s which is in good agreement with the expected estimated increase (see Section 6.6.2) of 1.25 km/s. The lower values at  $-8$ ,  $-4$  and  $+4$  degrees might be attributed to a lower fueling efficiency from the not completely ablated pellet. The result at  $+8$  degrees, however, is very puzzling, since it is not just a stronger change, but also a change in sign of the effect. A possible explanation for this is the

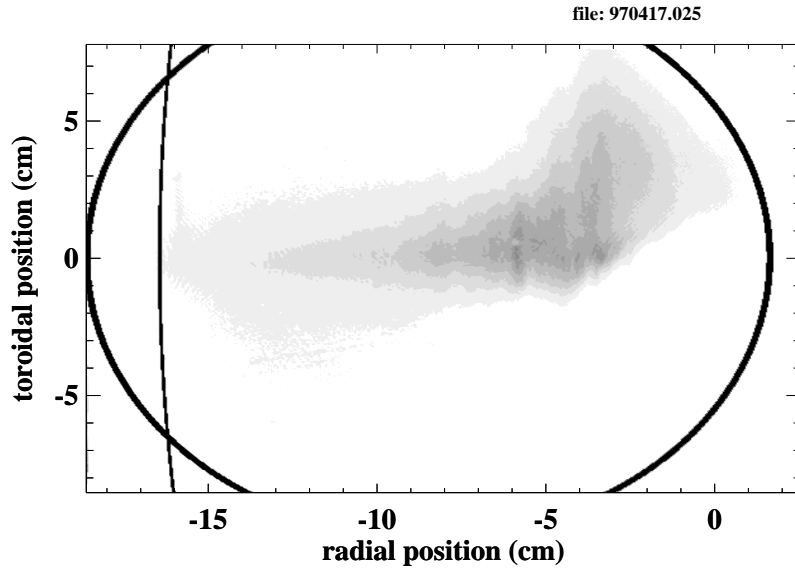


Figure 6.8: Photograph of pellet injected in a plasma with negative current.

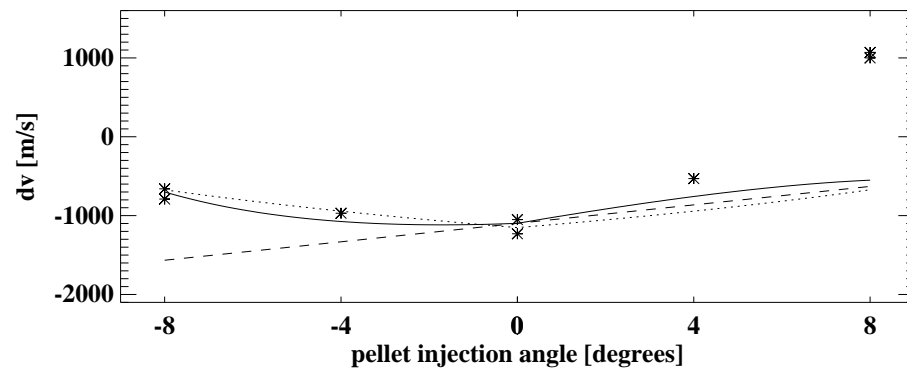


Figure 6.9: Change in velocity of the poloidal CIV rotation in the plasma obtained by comparing the difference between the pre and post pellet Doppler-shift (stars). The dashed line is calculated assuming 100 % fueling and poloidal angular momentum conservation. The continuous line is calculated by lowering the fueling percentage for off-axis pellet injection. The dotted line is calculated assuming toroidal momentum conservation and varying fueling percentage.

injection of poloidal momentum by the pellet. Even though it was not expected that the injected momentum of the pellet could be converted to poloidal rotation (based on a constant radial electric field profile; if this field is changed by the injected pellet

the situation may change completely).

A very crude model was made in an attempt to describe the effect. In this model the plasma is treated as a rigid rotating body. The effective pellet mass is inserted at the radius of closest approach of the pellet to the plasma center. Then using an assumed conservation of poloidal angular momentum the rotation after pellet injection can be calculated. The result is shown as the dashed line in Fig. 6.9 for a constant 100 % fueling rate. A pre-pellet poloidal rotation had to be assumed of 2.5 kHz. The horizontal injected pellet case can be explained very well with this model, but the off-axis injected pellets not.

Then the fueling efficiency is changed from 90 % for central injection down to 10 % for the maximum injection angle. The result is shown as the solid line in Fig. 6.9. This explains the smaller effect for -8, -4 and +4 degrees, but still does not explain the +8 degrees case.

Because of the prepellet poloidal rotation of 2.5 kHz that is needed for these calculations, which is in contradiction with the results from [142], this is probably not the correct scenario.

Finally the effect of toroidal momentum conservation was calculated. Here the radial electric field profile is kept constant so that after the pellet is injected the balance that causes the zero poloidal rotation in steady state is destroyed. Also the fueling is decreased to 45 % at maximum injection angle to get a better fit. An initial impurity ion rotation of 11 kHz was assumed in toroidal direction. This leads to the poloidal rotation shown as the dotted line in Fig. 6.9. The result agrees as good for the -8, -4 and 0 degree cases as did the model of poloidal angular momentum conservation. The +4 degree case deviates a little more and the +8 degree case is still not well explained.

The measurement at +8 degrees can not be explained by any of the models. Maybe the effect is exclusive to the CIV ions, but that can not be proven with the available diagnostics.

Toroidal rotation can also be measured by spectroscopy. For RTP the CIII line radiation and its Doppler-shift in the plasma was measured in toroidal direction. Preliminary results from these experiments show a toroidal rotation change of -0.6 to -1.0 km/s for a horizontally injected pellet. This is very different from the expected value of several tens of km/s (based on almost stopping of a toroidal rotation in the order of 10 kHz.) which again points towards a very different behaviour between bulk and impurity ions.

## 6.8 Summary and conclusion

Fast mixing of both ions and electrons has been observed just after pellet injection. The ion density reaches a constant value on a flux surface on a typical timescale of 100  $\mu$ s. The electrons are much faster and probably need a time in the order of 10  $\mu$ s before the electron temperature is equilibrated.

This could not be explained using only parallel expansion along the magnetic

field. However, when plasma rotation was taken into account the expected values are very close to the measured values. The presence of this rotation, also in the deposited matter from the pellet, was demonstrated by the observation of cut-off effects on two different diagnostics. Up to this point all that is known is that the rotation needed to explain the data has a cross-field component. No information is obtained on the parallel component.

Furthermore it is argued that the pellet causes a large change in the parallel rotation component. The parallel (and thus the toroidal) rotation will be slowed down by 50 % when the deposited mass equals the mass on the flux surface itself. This could not directly be observed in impurity rotation measurements. It is probably caused by a difference in bulk and impurity ion (CIII) behaviour.

Simultaneously the cross-field component of the rotation stays the same, which manifests itself as a (change in) poloidal rotation. This has for the given example a velocity in the order of 1 km/s. This follows both from theory, and from spectroscopic measurements. The change in poloidal rotation was directly observed from impurity spectroscopy.

Finally the photographic results also supports that the ablatant rotated both in toroidal and poloidal direction.

## Chapter 7

# Other pellet related research at RTP

### 7.1 Introduction

In this Chapter some preliminary work that did not fit in one of the previous Chapters is briefly discussed. Some of this work has mainly been done by colleagues but it is nevertheless included in order to give a complete overview of pellet related research at RTP.

In Section 7.2 the results on the pellet induced cold-pulse experiments are discussed. Then, in Section 7.3 the effect of a rational value of  $q$  on pellet ablation is shown. Finally in Section 7.4 a special feature on the  $H_\alpha$  radiation during pellet injection in off-axis heated plasmas is discussed.

### 7.2 Cold pulse experiments

The work that is described in this Section was done in cooperation with P. Mantica and coworkers. The results have been published in [31, 32, 74, 75, 76]

#### 7.2.1 Description of the experiments

A fast cooling localized in the outer parts of the plasma is introduced in the plasma in these experiments, and the reaction of especially the plasma center to this perturbation is studied. This is usually done by injecting a pellet far off-axis in the plasma (usually  $8^\circ$  is used, which gives a closest approach of the pellet to the center of 11.2 cm). It can, however, also be done by injecting a very small pellet or using very hot plasmas, in which case the horizontal injected pellet has a penetration that is so poor that the effect is the same. Also the gas puff that occurs when a not fully

ablated pellet hits the vessel wall, or when a pellet is destroyed in the guiding tube before it reaches the plasma, cools the plasma edge, and can be used.

This has been done in plasmas with different properties, sometimes combined with modulated ECH (MECH) to study the heat transport properties of the plasma during the experiment.

### 7.2.2 Observations

When the plasma edge is cooled usually a fast response of the plasma center is seen. For high densities the center also cools. For low densities the temperature of the plasma center increases strongly on a time scale of 5 to 10 ms and then falls down again on the same time scale to the value it had before.<sup>1</sup> An example of this effect is shown in Fig. 7.1.

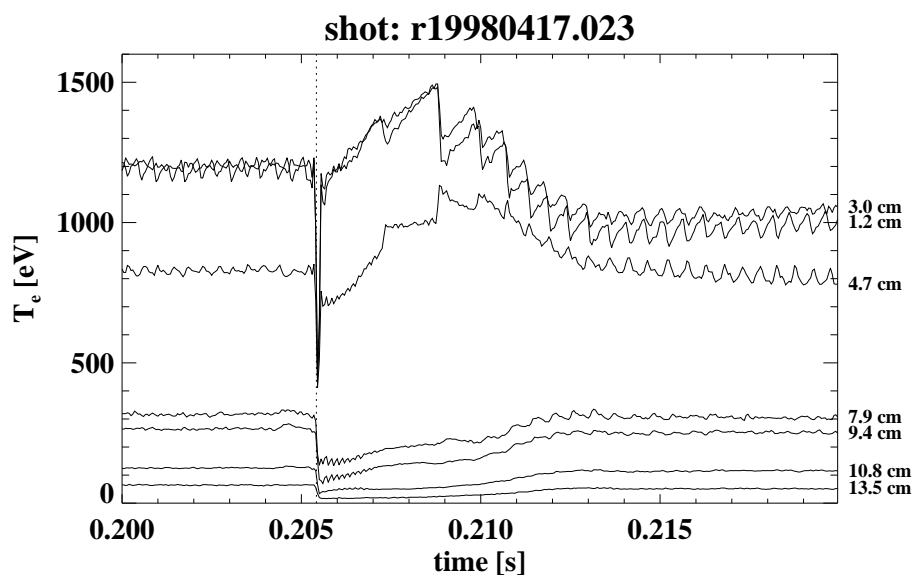


Figure 7.1: Example of central heating in an Ohmic plasma after the plasma edge is cooled by a horizontally injected small pellet (ECE-channels). The vertical dotted line indicates the time of pellet injection. The plasma and pellet parameters are:  $n_{e,0} = 2.7 \times 10^{19} \text{ m}^{-3}$ ,  $T_{e,0} = 1.0 \text{ keV}$ ,  $I_{pl} = 101 \text{ kA}$ ,  $B_{tor} = 2.02 \text{ T}$ ,  $v_{pellet} = 961 \text{ m/s}$ ,  $m_{pellet} = 0.26 \times 10^{19} \text{ atoms}$ , penetration =  $85 \pm 5 \text{ mm}$ .

An interesting accompanying effect is the clear change in the behaviour of the sawtooth instability in the plasma. The period increases strongly during the heating and the amplitude increases. The strong decrease of the central channels just at the

<sup>1</sup>This type of effects have been called non-local because the mechanism that connects the edge perturbation with the change in the centre is not precisely known.

time of pellet injection is just an artefact due to cut-off, and not a real temperature change.

The effect can be increased by adjusting the plasma parameters. It was found that especially in off-axis heated plasmas the central heating is strongly increased, and can sometimes almost double the electron temperature after the edge cooling occurred. The optimum is reached at the largest ECH deposition radius for which still a  $q=1$  surface exists in the plasma. An example of this effect is shown in Fig. 7.2. In this case the strange effect is seen that the central channel increases somewhat slower than the channel next to it, which is more off-axis. This means that for a short time the temperature profile becomes hollow.

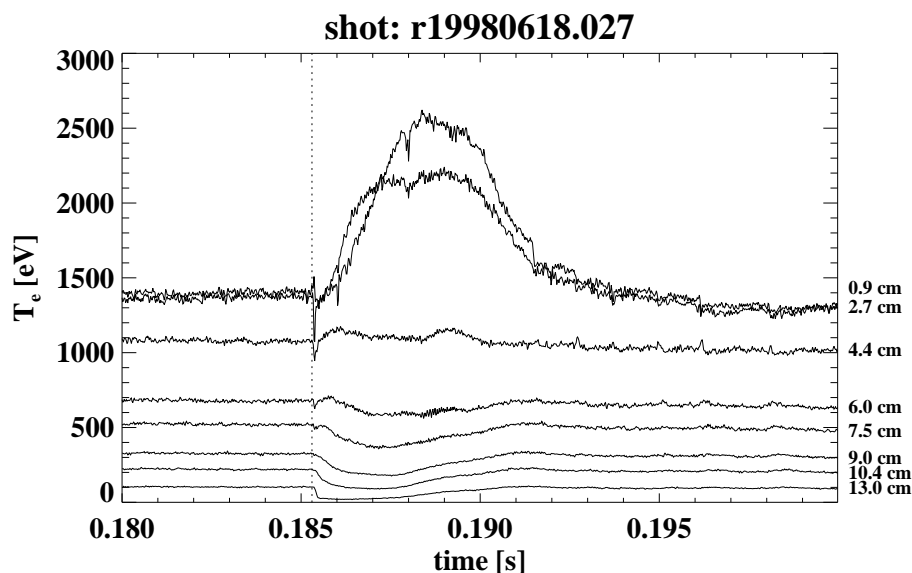


Figure 7.2: Example of a large heating effect in the plasma center after injection of an off-axis pellet in an off-axis heated plasma. The plasma and pellet parameters are:  $n_{e,0} = 3.8 \times 10^{19} \text{ m}^{-3}$ ,  $T_{e,0} = 1.4 \text{ keV}$ ,  $I_{pl} = 82.7 \text{ kA}$ ,  $B_{tor} = 2.08 \text{ T}$ , ECRH 350 kW at  $r=4 \text{ cm}$ ,  $v_{pellet} = 957 \text{ m/s}$ ,  $m_{pellet} = 0.19 \times 10^{19} \text{ atoms}$

By applying MECH it was found that in these experiments a region is induced in the plasma which causes a strong decrease in the propagating heat pulse. This was both observed for heat pulses going from the plasma center outwards, and pulses traveling from far off-axis towards the plasma center.

In far off-axis heated plasmas, that show a steady state hollow temperature profile, the heating effect was observed at the position of the off-axis temperature maximum, and not in the plasma center.

When the plasma edge is heated, instead of cooled, the effect reverses. When for example due to a current ramp-up the edge is heated, a clear drop of temperature

is seen in the plasma center.

### 7.2.3 Interpretation

All evidence gathered thus far points towards the formation of a transport barrier in the plasma, located between  $q=2$  and  $q=1$ . The change in transport is mostly in the diffusive heat transport, however, for ECH heated plasmas also a change in the convective component does occur. More details on the results of these experiments can be found in [31, 32, 74, 75, 76]. The actual mechanism causing this change in transport is still a mystery.

### 7.2.4 Extremely fast temperature rise

Another experiment in which the plasma center can heat due to pellet injection is shown in Fig. 7.3. Here a strong increase from 1200 to 1900 eV has occurred in the

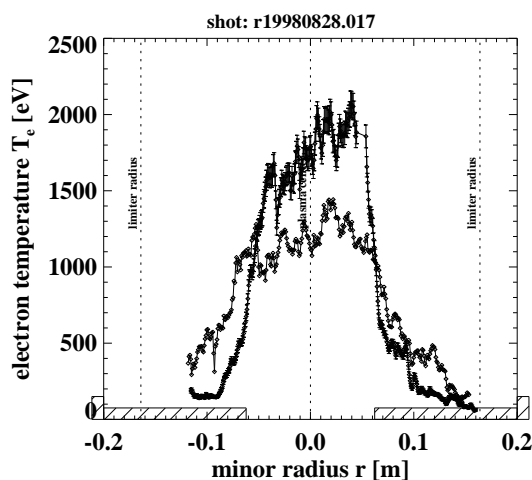


Figure 7.3:  $T_e$  profiles as measured by the Thomson scattering diagnostic (double pulse) just before the pellet enters the plasma (diamonds), and just as the pellet is fully ablated ( $200 \mu\text{s}$  later, crosses). A strong increase in  $T_e$  is seen in the region not reached by the pellet. The plasma and pellet parameters are:  $n_{e,0} = 6.2 \times 10^{19} \text{ m}^{-3}$ ,  $T_{e,0} = 1.2 \text{ keV}$ ,  $I_{pl} = 118 \text{ kA}$ ,  $B_{tor} = 2.06 \text{ T}$ , ECRH  $350 \text{ kW}$  at  $r=3 \text{ cm}$ ,  $v_{\text{pellet}} = 746 \text{ m/s}$ ,  $m_{\text{pellet}} = 1.47 \times 10^{19} \text{ atoms}$

plasma center within the  $200 \mu\text{s}$  of pellet ablation. Unfortunately no density profiles are available for this shot, so it is not known whether also the pressure shows the increase, or not. This effect is only seen for shots with strong additional heating, and may be caused by an improved confinement due to the strong rotation shear that is introduced by the pellet (as was discussed in Chapter 6). The heating effects do look rather similar to the cold pulse experiments described above, so there may be a similar mechanism in both cases. The time scale of this effect, however, is much shorter, which makes it hard to believe that this actually is heating. If this  $T_e$  rise is caused by perfect confinement of the injected ECRH power then still a power of  $\approx 1.7 \text{ MW}$  is needed to explain the  $T_e$  rise of  $700 \text{ eV}$  in  $200 \mu\text{s}$  (assuming the central density stays constant at  $6 \times 10^{19} \text{ m}^{-3}$ ). Therefore this is still not well understood.



## 7.3 Limited energy reservoir

In Section 3.2 it was already mentioned that the structure of the magnetic field may limit the amount of energy available for pellet ablation. Although this effect could not be connected to the often observed striations in the  $H_\alpha$  signals, it has been observed in another way.

### 7.3.1 Description of the experiment

During a scan of plasma current and toroidal magnetic field some conditions were found for which the  $T_e$  profile (as measured by Thomson scattering) showed an unusual shape after the passage of the first half of the plasma by the pellet (in all these cases the pellet penetrated almost up to the plasma center but not beyond). Two clear peaks in  $T_e$  are observed, in contrast to most other shots, in which the resulting  $T_e$  profile was more or less flat, directly after the end of pellet ablation (for similar penetration depths). This phenomenon was found at rather low values of  $q_a$  ( $q_a=3.4$ , at  $I_{pl}=118$  kA and  $B_{tor}=2.17$  T). All discharges with these parameters showed the effect.

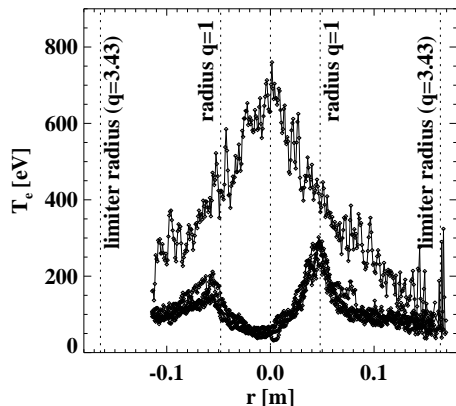


Figure 7.4:  $T_e$  profiles measured by Thomson scattering. Four profiles were taken just after the pellet (which penetrated almost to  $r=0$ ) was fully ablated. The fifth profile is a prepellet profile from the same experimental session for comparison. The plasma and pellet parameters are:  $n_{e,0} = 5.0 \times 10^{19} \text{ m}^{-3}$ , [ $T_{e,0}$  not available, estimated to be  $\approx 0.9$  keV],  $I_{pl} = 118$  kA,  $B_{tor} = 2.17$  T,  $v_{pellet} \approx 0.7$  km/s,  $m_{pellet} \approx 2 \times 10^{19}$  atoms

The plasma center is in all of these shots cooled down to 50 eV (see Fig. 7.4), but the region around  $q=1$  remains at much higher  $T_e$  (around 350 eV). Further outside  $q=1$  the cooling is again stronger, and reaches around 100 eV. These plasmas show clear sawteeth with strong precursors, which demonstrates the presence and location of the  $q=1$  surface.

There is no evidence for a density snake for these shots, after the pellet ablation.

For comparison some  $T_e$  profiles from shots from the same day with different  $q_a$  value are shown in Fig. 7.5 ( $q_a=5.3$ , at  $I_{pl}=77.4$  kA and  $B_{tor}=2.19$  T). The effect is clearly not present here.

The observed  $n_e$  profiles for these shots are very asymmetric and do not reproduce at all. This indicates that still large local densities exist in the plasma.

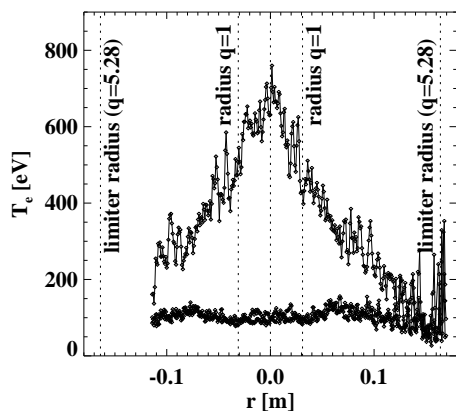


Figure 7.5:  $T_e$  profiles measured by Thomson scattering. Two profiles were taken just when the pellet penetrated almost to  $r=0$ . The third profile is a prepellet profile from the same experimental session for comparison. The plasma and pellet parameters are:  $n_{e,0} = 4.9 \times 10^{19} \text{ m}^{-3}$ , [ $T_{e,0}$  not available, estimated to be  $\approx 0.7 \text{ keV}$ ],  $I_{pl} = 77.4 \text{ kA}$ ,  $B_{tor} = 2.19 \text{ T}$ ,  $v_{pellet} \approx 0.7 \text{ km/s}$ ,  $m_{pellet} \approx 2 \times 10^{19} \text{ atoms}$

### 7.3.2 Interpretation

Clearly the observed effect is related to the expected limited availability of energy to the ablating pellet when a rational value of  $q$  is passed. This effect is not only present exactly at  $q=1$  but also in a region around it, because the number of rotations for the hot particles around the torus, needed to drain all available energy from the flux surface, increases strongly when  $q=1$  is approached. Thus, due to the finite time a pellet needs to cross a flux surface, this automatically leads to less ablation in a region around  $q=1$ . For the same reasons this effect should occur near other rational values of  $q$ , but should be less pronounced there.

Another noticeable feature in these profiles is the clear asymmetry between the two sides of the  $T_e$  profile. Not using all energy on a flux surface automatically leads to asymmetries in the temperature of this surface, which will be removed on a slow timescale related to perpendicular heat transport in this case. Therefore an asymmetry can be observed on the vertical chord of the Thomson scattering diagnostic.

## 7.4 Ablation pattern in off-axis heated plasma

In most cases the fine structure ( $< 3 \text{ cm}$ ) in the observed  $H_\alpha$  emission during pellet injection does not reproduce. It disappears when a number of similar pellet shots are averaged, and leaves only the general, increasing, trend from the plasma edge to the moment of full ablation. This illustrates that the phases of these structures are independent and vary from shot to shot, even if the frequency is often comparable. However, for some conditions, in which a pellet was injected centrally in an off-axis heated plasma, a clear pattern was found.

### 7.4.1 Description of the experiment

In this experiment a number of identical pellets were shot into a series of similar target plasmas. Then the observed  $H_\alpha$  traces (converted to pellet position) were averaged to see how reproducible they were. The result for an Ohmic plasma is shown in Fig. 7.6. Due to this averaging all small scale structures disappear, and only the

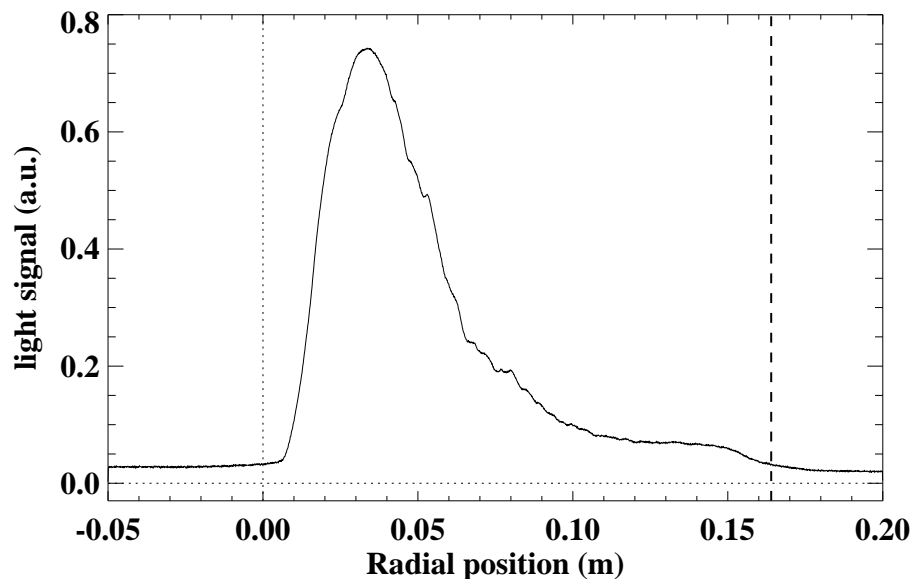


Figure 7.6: Average of 26  $H_\alpha$  traces for pellets injected in to almost identical Ohmic target plasmas. All small structures disappear. The pellet and pre-pellet plasma parameters are:  $n_{e,0} = 6.1 \pm 0.7 \times 10^{19} \text{ m}^{-3}$ ,  $T_{e,0} = 0.9 \text{ keV}$ ,  $I_{pl} = 96.3 \pm 1.4 \text{ kA}$ ,  $B_{tor} = 2.205 \pm 0.020 \text{ T}$ ,  $v_{\text{pellet}} = 707 \pm 8 \text{ m/s}$ ,  $m_{\text{pellet}} \approx 2 \times 10^{19} \text{ atoms}$ .

general trend of increasing line emission due to increasing ablation and/or increasing plasma temperature remains. In this case no striations that could theoretically be caused by rational  $q$ -values are observed.

The same experiment was done for pellets injected into off-axis heated plasmas. This yielded the very different result shown in Fig. 7.7. Here a clear structure of 4 peaks is seen when the pellet crosses the first half of the plasma, the largest one at  $r=9.5 \text{ cm}$ , than a smaller one at  $6.5 \text{ cm}$ , and two little ones at  $2.0$  and  $14.0 \text{ cm}$ . In the second half of the plasma the ablation is quiet until the pellet reaches the outer parts of the plasma again. There the light emission increases again when the pellet crosses the  $r=-10 \text{ cm}$  mark, and only drops when the pellet has left the plasma.

A typical  $T_e$  profile for this plasma before and during pellet injection, measured by Thomson scattering, is shown in Fig. 7.8. Using the pre-pellet  $T_e$  profile an

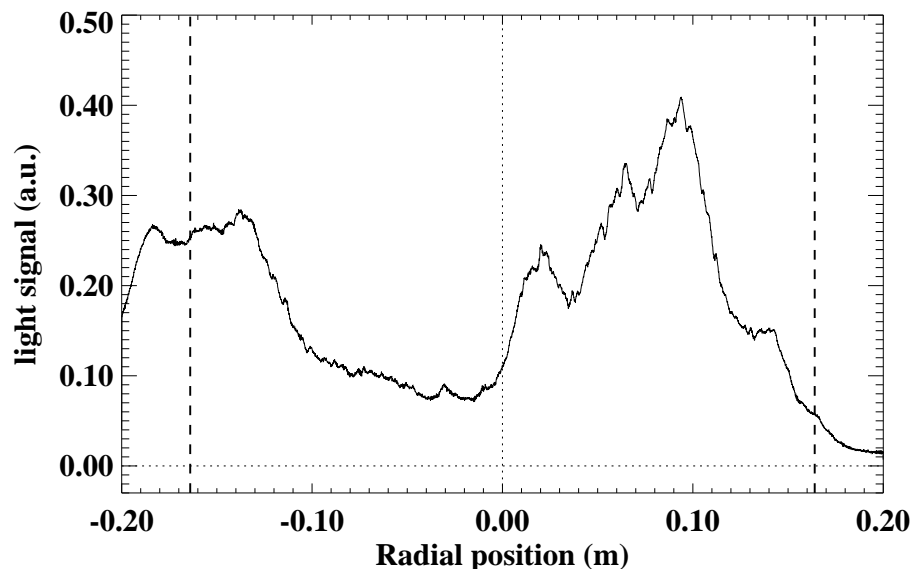


Figure 7.7: Average of 15  $H_\alpha$  traces for pellets injected in to almost identical target off-axis heated plasmas. Now some clear structures remain. The pellet and pre-pellet plasma parameters are:  $n_{e,0} = 7.5 \pm 0.5 \times 10^{19} \text{ m}^{-3}$ ,  $T_{e,0} = 0.45 \text{ keV}$ ,  $I_{pl} = 76.9 \pm 0.3 \text{ kA}$ ,  $B_{tor} = 2.257 \pm 0.009 \text{ T}$ ,  $q_a = 5.5$ , ECRH 350 kW (resonant at  $r=11 \text{ cm}$ ),  $v_{pellet} = 667 \pm 14 \text{ m/s}$ ,  $m_{pellet} = 2.4 \pm 0.1 \times 10^{19} \text{ atoms}$ .

estimate was made for the  $q$  profile, which yielded a large flat region of  $q$  just below 2.5 for the center part of the plasma (inside  $r=6 \text{ cm}$ ), going up to 5.5 at the edge.

#### 7.4.2 Interpretation

The reasons for the observed behaviour are not yet clear at this moment. The effect can be split in two features. First the global trend of increasing  $H_\alpha$  emission when the pellet travels from the plasma edge up to  $r=10 \text{ cm}$ , after which it decreases again strongly towards the plasma center. Then the fine structure on top of this signal, which remains even after averaging a number of different shots.

It would be tempting to assume a fast event which cools the plasma after the pellet crosses a certain radius of say  $r=10 \text{ cm}$ . This would explain the decrease in  $H_\alpha$  signal after the passage of this point. This, however, can not be the case, as is proven by the Thomson scattering profile taken when the pellet is at  $r=4.5 \text{ cm}$  (see Fig. 7.8). This profile shows that the center of the plasma has not yet changed, and that there is a strong gradient in  $T_e$  just in front of the pellet.

The global trend may be understood by considering the energy content of the

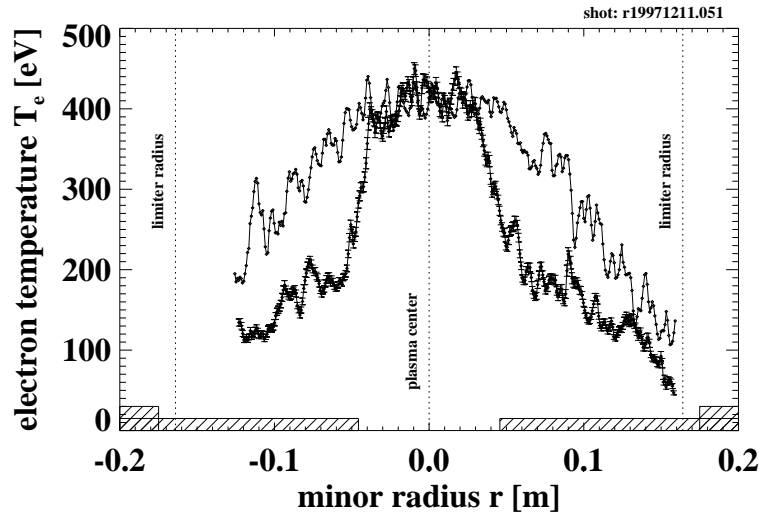


Figure 7.8: Example of a  $T_e$  profile as observed by the Thomson scattering diagnostic for the discussed off-axis heated plasma during pellet injection compared to a profile from the same shot just before the pellet was shot. Clearly the plasma center remains at the prepellet temperature, even if the pellet is as close as 5 cm.

flux surfaces in the plasma. This is of course a restraining factor in pellet ablation, and since this energy goes to zero in the plasma center (because the surface of the flux surfaces scales with  $r^2$ ) a decrease towards the center may be expected.

This leaves us with the question why this is not seen in Ohmic plasmas. This can be the case if the parallel transport along the flux surface is not fast enough to access all energy on it. In that case the available amount of energy is not an important factor. This may actually be caused because the  $q$  value is nearly rational.

Or it can be the case if there is considerable cross-field heat and/or particle transport in the Ohmic case.

Also the “fine structure” on top of the signal is difficult to understand. There may be a connection with crossing rational values of  $q$  as was discussed above in Section 7.3. This is not very likely, however, because these off-axis heated plasmas have a high center value of  $q$  of just below 2.5, and keep that value for a large region of the plasma (up to  $r=6$  cm). A second explanation might be a drift of the ablation cloud (as was discussed in Chapter 4) at certain preferred radii. Why this would happen is not clear at all. Sometimes this effect can be observed also on the fiberarray diagnostic but it is not always clearly present in the data.

A last thing that has to be explained is the increase in signal when the pellet reaches the edge of the plasma at the inboard side. This may be caused by the fact that the low initial ablation of the pellet has only slightly cooled this region of the plasma. Why in this second passage of this plasma radius the light emission is

actually much larger than at the first passage (at  $r=13$  cm for example it is  $\approx 35$  % larger) is not clear. Again this could be connected to the drifting effect. When the ablated material drifts towards the low field side, the material released at for example  $+13$  cm is quickly removed from the plasma. The material that is released at  $-13$  cm may drift for a much longer time through the plasma, which might explain the higher light emission. Remember that the  $H_\alpha$  diagnostic actually has no spatial resolution, and that the conversion to radius, as was done in these plots, is only valid if the light emission is localized around the pellet.

When summarizing this Section it can only be said that the results presented here are very puzzling. They may contain clues on the transport behaviour of the plasma, but this could not be extracted. These plasma conditions certainly should be studied more closely in the future.

## Chapter 8

# Discussion and future work

In the previous Chapters a number of different aspects of pellet ablation has been studied. Those results will be shortly summarized below. These processes are, however, not independent. They occur simultaneously and may interact with each other. Still, from studying these processes separately a number of useful conclusions can be drawn, and some of the questions posed in Section 1.4 can be answered. Finally some possibilities for future research are described.

### 8.1 Conclusions

From the results given in Chapter 4 the most important conclusion is that the ablated material from the pellet can drift away from the pellet towards the LFS in a tokamak. This effect explains the discrepancies found in the observed penetration depth of the pellet when observed by different diagnostics. These drifts can have velocities in the range of 2.5 to 10 km/s, and when present they probably form the dominant part of the particle convection. In combination with the rotational transform that is present in the plasma, this drift may move towards the plasma center, even for pellets located at the LFS. This might be an explanation for the puzzling precooling effect that has been reported on many tokamaks.

Why the drift is sometimes pulsating and sometimes seems to be continuous is not clear. When a pulsating drift occurs this may explain the striations that are almost always present in the observed  $H_\alpha$  signals. It is concluded from the diagnostics used in this Chapter that the pellet penetration depth can not be measured reliably by a measurement of the  $H_\alpha$  signal without spatial resolution. A much better measurement is done by photographic observations (localized  $H_\alpha$  measurements).

A very important consequence from the observation of the drift effect is that this largely increases the fueling efficiency of HFS pellet injection on large tokamaks, because the ablated material is deposited closer to the plasma center. This probably solves the refueling problem for future fusion devices.

In Chapter 5 it is concluded that in a normal Ohmic RTP plasma the maximum particle source inside the plasma due to ionisation of neutral particles can be estimated to be in the order of  $10^{22}$  particles  $m^{-3}s^{-1}$ . The maximum neutral particle density needed to explain this is in the order of  $7 \times 10^{16} m^{-3}$ . The particle diffusion in an Ohmic RTP plasma is in the order of  $D^{inc} = 2.0 \pm 1.0 m^2/s$

Short (200  $\mu s$ ) time scale simulations showed that during the ablation process itself an increased value of D of  $5.2 \pm 2.7 m^2/s$  is needed to explain the observations. This is caused by the local high density in the ablation cloud which will cause locally a higher value of D. For off-axis injected pellets this increase was not observed, and a value of  $D=1.2 \pm 0.7 m^2/s$  can explain the observations. They are consistent with collisional transport that is to be expected inside the ablation cloud. This difference between on- and off-axis pellet injection maybe related to a difference in particle density inside the ablation cloud.

When a pellet is injected the diffusive transport on the ms time scale can be described by assuming a  $D=1.0 m^2/s$  in most cases. Only in the center of the plasma after pellet injection a region with very low D of  $0.04 m^2/s$  is needed to explain the data.

An interesting observation in the slide-away regime is the extremely low value for D of  $0.05 m^2/s$  that was observed. This must be accompanied by a very low  $\chi_e$ , which was estimated to be in the order of  $\chi_e \approx 0.1 m^2/s$

An important diagnostic conclusion that can be drawn is that very often the  $T_e$  profile can be used to determine a flux surface averaged value of the plasma density during pellet injection, i.e. at a time scale of 200  $\mu s$ . The locally measured  $n_e$  profiles can deviate far from this average during pellet injection.

An important result of Chapter 6 is the fact that the pellet induces a strong poloidal rotation by (partly) stopping the toroidal rotation. This has both been measured, and deduced by assuming a constant electric field on the flux surface on the considered time scale. The combination of parallel movement and rotation is sufficient to explain the observed mixing times on a flux surface.

## 8.2 Answers to the posed questions

At this point some of the open questions concerning this particle transport that were posed in Section 1.4 can be answered.

- What is the magnitude of particle transport during pellet injection and how large are the convective and diffusive parts? Which one is dominant? Is there a difference with the unperturbed plasma?

Particle diffusion in the RTP tokamak was found to be around  $D^{inc}=2.0 \pm 1.0 m^2/s$  in the Ohmic case, and increases in the ablation cloud to  $D=5.2 \pm 2.7 m^2/s$ . In the plasma center a region with much lower D was found just after pellet injection. Also in the slide-away regime D is much lower, and maybe neoclassical. This is possibly connected to a transport barrier induced by a strong gradient in the plasma rotation.



Transport due to convection is dominated by the cloud drift that occurs during pellet injection. Drift velocities in the order of 10 km/s occur. In cases with quiet ablation without drift the radial diffusion is the dominant term, in cases with the cloud-drift, the outward convection dominates the region passed by the pellet, but diffusion usually still determines the profiles in front of the pellet.

- What influence have both transport components on important parameters like the fueling profile and efficiency, and the diagnosis of these parameters? Can the results be used to improve the injection scenario for a fusion power plant?

The observed diffusion causes the density to diffuse slightly in front of the pellet, but this is not of importance for the net fueling profile. The important factor is if drifts occur, and in which direction they move the ablatant. For the LFS pellet injection in RTP the drift effect gives a deposition further outward than would result from the local deposition of matter by the pellet. In some cases (additionally heated plasmas and slideaway regime) a considerable amount of matter is expelled from the plasma. For HFS injection the drift would have an opposite effect. It would move the net deposition of matter towards the plasma center, and has already been proven to be a favorable scenario for fueling in larger Tokamaks [67].

- What is the influence of plasma rotation on the ablation process and its observation, and how does the pellet change the rotation? Can pellet injection be used to manipulate plasma rotation?

The important effect of plasma rotation is the fast mixing of both particles and temperature on a flux surface, much faster than could be expected by parallel movement alone. This has as consequence that the energy that is available for pellet ablation, especially in the presence of rational q-values (with only a few exceptions) is much larger than expected by just parallel movement of the electrons along the field lines. Furthermore this equilibration makes it possible to actually observe a profile for  $T_e$  which is representative for the whole flux surface, even during pellet ablation. The effect of the pellet on rotation is that it slows down the toroidal rotation and induces a poloidal rotation. Especially for pellets that do not penetrate the plasma up to the center this means that a large gradient in both rotation components occurs as a function of radius. This could have a strong effect on the confinement of the plasma, and may induce a transport barrier at the position of maximum pellet penetration.

- What is the effect of the induced asymmetries in the plasma by the pellet, especially on diagnosing the ablation process?

Asymmetries especially occur in the density profile and this causes two effects in the interpretation of the diagnostics. First it makes measuring the local density during pellet injection of little use. Secondly the local high densities that can exist during a short time are far above the maximum density after equilibration. This will cause cut-off effects on ECE diagnostics, at least for a short time.

When a local high density flows towards the HFS of the torus then a drift effect may cause this density to move through the plasma center. This may be an explanation for the well known pre-cooling phenomenon.

- Is there a relation between the transport properties of the plasma during pellet injection and the magnetic configuration of the plasma, and how can this be diagnosed ?

An effect that was expected in the plasma is the limited availability of energy at rational values of  $q$ . On the  $H_\alpha$  signals no evidence has been found for this effect, although this emission was expected to be at least some function of the available energy to ablate the pellet. This may be caused by the drifting clouds, that dominate the observed fluctuations, and make such rational  $q$  effects impossible to observe. A second way to diagnose the energy is to observe the remaining energy (and thus  $T_e$ ) after the pellet has passed. In this way an effect of limited available energy near  $q=1$  has been observed, but only in a very specific plasma configuration (see Section 7.3). As was mentioned before the rationality of  $q$  is not of large importance, probably because of the strong cross-field mixing that exists on a flux surface during and shortly after pellet injection.

### 8.3 Future work

To obtain a better and more detailed understanding of the processes during pellet injection in a plasma it is vital to have local information (preferably radial profiles) of the magnitude and direction of the electric field in the plasma. The possibility for new diagnostics to obtain this information should be investigated. Besides the drift effect during pellet injection, also plasma rotation and the (inward-) pinch effect are closely related to the electric fields in the plasma, so also for the study of those plasma properties this would be very useful.

A next step may be an attempt to control those electric fields, which would enable the possibility of controlling radial plasma transport (at least the convective part). If we can have a better view of these fields than maybe they can be altered in such a way as to decrease the convection. It may be difficult to influence this field directly, but manipulation of the flow/rotation and the pressure may be a handle for this. This has already been used in advanced tokamak scenarios.

Before the ablation cloud can be taken into account in modeling it has to be studied in more detail. This is needed to be able to extrapolate to a future fusion reactor. Especially information is needed on the lifetime of the drifting cloud, and how this depends on the plasma parameters crossed by the cloud. Also the mechanism for the pulsating character of the drift should be looked for.

The drifting cloud effect clearly favours the HFS injection over LFS injection of pellets, especially for larger tokamaks.

# References

- [1] C. Andelfinger et al., report IPP 1/219 (1983), Max-Planck Institut fur Plasma Physik, Garching.
- [2] R. Aymar, IEEE Transactions on Plasma Science, vol. 25 (6) 1997, p.1187-1195.
- [3] L. R. Baylor et al., Nuclear Fusion, Vol. 32, No. 12, (1992), p. 2177-2187, Fig. 6.
- [4] L. R. Baylor et al., Nuclear Fusion, Vol. 37, No. 4, (1997), p. 445-450.
- [5] L. R. Baylor et al., proc. 26th EPS conf. Maastricht, june 1999, Vol 23J, p. 297-300.
- [6] L. R. Baylor et al., Nuclear Fusion, Vol. 31, No. 7, (1991), p. 1249-1259.
- [7] L. R. Baylor et al., abstract for 2nd Europhysics Workshop on Role of Electric Field in Plasma Confinement and Exhaust, Maastricht, june 1999, (satellite meeting of EPS).
- [8] L. R. Baylor et al., Nuclear Fusion, Vol. 37, No. 1, (1997), p. 127-144.
- [9] K. Behringer et al., Report Max-Planck Institut fur Plasmaphysik, (1988), IPP III/137 IPP 1/246.
- [10] M. N. A. Beurskens et al., Rev. Sci. Instrum 68 (1), January 1997, p.721-724.
- [11] F. M. A. Box, Nuclear Fusion, Vol. 39, No. 9 (1999), p.1193-1203.
- [12] K. H. Burrell et al., Phys. Plasmas 1 (5), may 1994, p. 1536-1544.
- [13] Chang, C. T., et al., Nucl. Fusion, Vol. 20, No. 7 (1980), p. 859-892.
- [14] A.D. Cheetham et al., proc. 14th EPS conf. Madrid (1987), part 1, Vol. 11D, p. 205-208.
- [15] F. F. Chen, Introduction to Plasma Physics, Plenum Press, New York and London, 1974, page 3.
- [16] idem, chapter 9, page 279.
- [17] D. F. da Cruz, thesis University of Utrecht, 1993 (fig. 4.7, p.62).
- [18] D. F. da Cruz et al., Phys. Rev. Lett. 75 (20) 1995, p.3585-3688.

- [19] B. H. Deng et al., proc. 25th EPS conf. Prague 1998, Vol. 22C, p. 1454-1457.
- [20] A. J. H. Donné et al., plasma Physics Reports, Vol. 20 (2) 1994, p.192-202.
- [21] A. J. H. Donné et al., Report FOM Rijnhuizen, 91-207 (december 1991).
- [22] H. W. Drawin et al., Nuclear Fusion, Vol. 32, No. 9 (1992), p. 1615-1623.
- [23] M. A. Dubois et al., Nuclear Fusion, Vol. 32 No. 11 (1992) p. 1935-1940.
- [24] R. D. Durst et al., Nuclear Fusion, Vol. 30, No. 1 (1990), p.3-9, figure 4.
- [25] S. N. Egorov et al., Nucl. Fusion, Vol. 32, No. 11, (1992), p. 2025-2028.
- [26] S. M. Egorov et al., Proc. EPS conf. Lisboa (1993), p. 255-258.
- [27] K. H. Finken, "Interaction of pellets with hot plasmas", report Jül-2980, p. 3.
- [28] R. K. Fisher et al., Rev. Sci. Instrum. 61 (10), Oct. 1990, p. 3196-3198.
- [29] C. A. Foster et al., Nuclear Fusion 17, 5 (1977), p.1067-1075.
- [30] G. Francis et al., Physics Letters, 25A (6) 1967, p.486-487.
- [31] P. Galli et al., proc. 25th EPS conf. Prague, Vol. 22C (1998) p. 738-741.
- [32] P. Galli et al., Nucl. Fusion, Vol. 39, No. 10 (1999), p. 1355-1368.
- [33] G. Geerts et al., "van Dale, groot woordenboek der Nederlandse Taal", 12e druk, deel 2 (j-r), p.2304, "plasma".
- [34] J. F. M. van Gelder et al., Rev. Sci. Instrum. 66 (1), January 1995.
- [35] J. F. M. van Gelder, Thesis University Utrecht, 1996, chapter 2.
- [36] A. Geraud et al., Proc. 19th EPS conf. Innsbruck 1992, p. 159-162.
- [37] R. D. Gill et al., Nuclear Fusion, Vol. 29, No. 5 (1989) p. 821-825.
- [38] R. D. Gill, proc. 21st EPS Conf. on Contr. Fusion and Plasma Phys., Montpellier, 1994, Vol. 18B, part 1, p.198-201.
- [39] R. J. Goldston and P. H. Rutherford, "Introduction to plasma physics", Institute of physics publishing Bristol and Philadelphia, chapter 10, p. 152.
- [40] I. N. Golovin, letter from him to prof. C. B. Braams (from personal communication with prof. Braams).
- [41] J. van Gorkom, Student verslag, Intern Rapport Rijnhuizen, nov. 1997 (IR 97/010).
- [42] M. J. Gouge, Fusion Technology, Vol. 34, nov. 1998, p.435-440.
- [43] Y. Hamada et al., Nucl. Fusion, Vol. 36, No. 8 (1996) p. 1047-1052.
- [44] C. F. Hix jr. and R. P. Alley, "Physical Laws and effects", 1958, (John Wiley & sons, inc., New York and Chapman & Hall, ltd., London), p. 130-131.
- [45] G. M. D. Hogeweyj et al., Phys. Rev. Lett. 76 (1996) p.632-635.
- [46] G. M. D. Hogeweyj et al., Proc. 17th EPS conference, Amsterdam 1990, Vol. 14B, Part 1, p. 158-161.

- [47] W. A. Houlberg et al., Nuclear Fusion, Vol. 32, No. 11 (1992).
- [48] W. A. Houlberg et al., Nuclear Fusion, Vol. 28, No. 4 (1988), p. 595-610.
- [49] L. C. Ingesson, thesis university of Eindhoven 1995, p.156.
- [50] R. Jaspers et al., Phys. Rev. Lett., Vol. 72, No. 26 (1994) p. 4093-4096.
- [51] Raymond de Jongh, student report Rijnhuizen, 3-5-1995.
- [52] L. W. Jorgensen et al., Plasma Physics, vol. 17, (1974) p.453-461.
- [53] F. A. Karelse et al., proc. 23rd EPS conf Kiev, 1996, Vol. 20C, p. 1156-1159.
- [54] M. Kaufmann et al., Nuclear Fusion, vol. 26, No.2, (1986), p.171-178.
- [55] Y. B. Kim et al., Phys. Fluids B, 3 (8), aug. 1991, p. 2050-2060.
- [56] J. de Kloe et al., proc. 23th EPS conf. Kiev, 1996, Vol. 20C, p. 368-371.
- [57] J. de Kloe et al., proc. 24th EPS conf. Berchtesgaden, 1997, Vol. 21A, p. 593-596.
- [58] J. de Kloe et al., proc. 25th EPS conf. Prague, 1998, Vol. 22C, p.734-737.
- [59] J. de Kloe et al., proc. 26th EPS conf. on Contr. Fusion and Plasma Physics, Maastricht, 1999, Vol. 23J, p. 637-640.
- [60] J. de Kloe et al., Phys. Rev. Lett. 82 (13), 1998, p.2685-2688.
- [61] R. Koch, Transactions of Fusion Technology, vol. 29, (1996), p.227-236 (proc. 2nd Carolus Magnus Summer School on Plasma Physics).
- [62] G. Kocsis et al., Plasma Phys. Control. Fusion 41, (1999), p. 881-898.
- [63] J. A. Konings, Thesis University of Utrecht 1994, p.65.
- [64] G. Kristof, report Max-Planck-Institut fur Plasmaphysik Garching, IPP 5/73, (1996).
- [65] A. C. A. P. van Lammeren, Thesis University of Utrecht, 1991.
- [66] P. T. Lang et al., Proc. EPS conf. Bournemouth, 1995, Vol. 19c, part II, p.449-452.
- [67] P. T. Lang et al., Phys. Rev. Lett., Vol. 79, No. 8, (1997), p. 1487-1490.
- [68] P. T. Lang et al., Nuclear Fusion, Vol. 36, No. 11 (1996), p. 1531-1545.
- [69] P. T. Lang et al., proc. 25th EPS conf. Prague 1998, Vol. 22C, p. 293-296.
- [70] P. T. Lang et al., proc. 26th EPS Conf. Maastricht, june 1999, Vol. 23J, p.1389-1392.
- [71] L. L. Lengyel, IEEE Transactions on Plasma Science, Vol. 20, no. 6, Dec. 1992, p.663-668.
- [72] N. J. Lopes Cardozo, Plasma Phys. Control. Fusion 37 (1995), p.799-852.
- [73] K. N. Mansfield et al., Phys. Rev. Lett., Vol. 66, no. 24 (1991), p.3140-3143.
- [74] P. Mantica, proc. 24th EPS Berchtesgaden, Vol. 21A, (1997), p. 1853-1856.

- [75] P. Mantica et al., proc. 26th EPS conf. Maastricht 1999, Vol. 23J, p.65-68.
- [76] P. Mantica et al., Phys. Rev. Lett. Vol. 21, nr. 25 (1999) p. 5048-5051.
- [77] E. S. Marmar et al., Rev. Sci. Instrum. 60 (12), dec. 1989, p. 3739-3743.
- [78] Y. Martin, thesis Ecole Polytechnique Federale de Lausanne, Suisse (1993), (page 51, fig. 3.3).
- [79] F. Meijer et al., proc. 26th EPS conf. Maastricht 1999, Vol. 23J, p.633-636.
- [80] J. Meyer-ter-Vehn, Proc. EPS Berchtesgaden 1997, Plasma Phys. Control. Fusion 39 (1997), p. B39-B45.
- [81] S. L. Milora et al., Rev. Sci. Instrum. 50 (4), Apr. 1979, p.482-487.
- [82] S. L. Milora et al., Nucl. Fusion, 35 (6), 1995, p. 657-754, chapter 2.1.1, p. 661.
- [83] idem, chapter 2.1.1, p. 662.
- [84] idem, chapter 2.1.1, p. 664.
- [85] idem, chapter 2.1.1+2.1.3, p. 659+663+668.
- [86] idem, chapter 2.1.4, p. 669.
- [87] idem, chapter 2.1.4, p. 670.
- [88] idem, chapter 2.2.1, p. 671.
- [89] idem, chapter 2.2.1+2.2.2, p. 673+678.
- [90] idem, chapter 2.2.2, p. 676.
- [91] idem, chapter 2.2.2, p. 677.
- [92] idem, chapter 2.2.2, p. 679.
- [93] idem, chapter 3.1.1, p. 683+684.
- [94] idem, chapter 3.1.2, p. 685.
- [95] idem, chapter 4.1.2, p. 720.
- [96] idem, chapter 4.2, p. 724.
- [97] K. Miyamoto, poster abstract (p-22.2), 17th IEEE/NPSS symposium on Fusion Engineering, San Diego, Ca, USA, october 6-10, 1997.
- [98] H. W. Müller et al., Proc. 23rd EPS conf. on Controlled Fusion and Plasma Physics, Kiev, (1996), Vol. 20C, part III, p. 1019-1022.
- [99] H. W. Müller et al., proc. EPS conf. Maastricht june 1999, Vol.23J, p.109-112.
- [100] H. W. Müller et al., Phys. Rev. Lett. 83 (11) 1999, p. 2199-2202.
- [101] J. Neuhauser et al., report IPP 5/30 (1989), Max-Planck Institut fur Plasma Physik, Garching.
- [102] A. Nijsen-Vis et al., "Fusie-energie bij magnetische opsluiting", 1985, FOM instituut voor plasmafysica Rijnhuizen, Nieuwegein, p.11.

- [103] idem, p.13.
- [104] Nishitani et al., Rev. Sci. Instrum. 61 (10), October 1990, p.3090-3092.
- [105] A. A. M. Oomens et al., Proc. EPS conf. Bournemouth 1995, p. I-129 - I-132.
- [106] P.B. Parks, Nuclear Fusion, vol.20, no.3, (1980), p.311-320.
- [107] P.B. Parks, Phys. Fluids 21(10), October 1978, p. 1735-1741, eq.40.
- [108] P. B. Parks, Plasma Phys. Control. Fusion, 38 (1996) p. 571-591.
- [109] P. B. Parks et al., proc. 26th EPS conf. Maastricht, june 1999, Vol. 23J, p.1217-1220.
- [110] B. Pégourié et al., Nucl. Fusion, Vol. 29, No. 5 (1989), p. 745-751.
- [111] B. Pégourié et al., Nucl. Fusion, Vol. 30, No. 8 (1990), p. 1575-1584.
- [112] B. Pegourie et al., Phys. Plasmas 3 (12), december 1996, p.4594-4605.
- [113] M. Peters, Thesis Technical University of Eindhoven 1996, p. 107.
- [114] M. P. Petrov et al., Nuclear Fusion, Vol. 35, No. 12 (1995), p. 1437-1443.
- [115] L. Poels, Intermediair, jaargang 32, nr. 16 (19-4-1996).
- [116] R. W. Polman et al., proc. EPS conf. Amsterdam 1990, p. 1121-1124.
- [117] J. H. Rommers, Rev. Sci. Instrum. 68 (2), 1997, p.1217-1226.
- [118] V. Rozhansky et al., Plasma Phys. Control. Fusion 37 (1995), p.399-414.
- [119] V. A. Rozhanskij et al., Nuclear Fusion, Vol. 34, No. 5 (1994), p.665-674.
- [120] H. Sakakita et al., proc. EPS conf. Bournemouth (1995), p.125-128.
- [121] M. Sakamoto et al., Plasma Phys. and Contr. Fusion, Vol. 33, No. 6, (1991), p. 583-594.
- [122] B. C. Schokker et al., proc. EC-9 workshop, Borrego Springs, 1995, p.199-207.  
Here it is shown that in RTP at densities below  $2 \times 10^{19} \text{ m}^{-3}$  supra thermal electron populations occur.
- [123] B. C. Schokker, thesis university of Eindhoven 1996, section 10.3, page 160.
- [124] P. Smeulders et al., Nucl. Fusion, Vol. 35, No. 2, (1995), p. 225-242.
- [125] H. Sørensen et al., Fusion Technology, 1992 (647-650).
- [126] H. Sørensen et al., Rev. Sci. Instrum. 61 (11), 1990, p.3464-3466.
- [127] L. Spitzer et al., Problems of the Stellarator as a Useful Power Source, Report NYO-6047, USAEC (1954).
- [128] L. Spitzer jr., Atomic Energy Commission, NYO-993, PM-S-1, (1951).
- [129] V. S. Strelkov, Nuclear Fusion, Vol. 25, No. 9 (1985), p.1189-1194.
- [130] S. Sudo, Journal of Plasma and Fusion Research, Vol. 69, No. 11 (1993), p. 1349-1361.
- [131] S. Sudo et al., report NIFS-560, Oct. 1998.

- [132] I. E. Tamm, Theory of a thermonuclear reactor (part I and III), and A. D. Sakharov (part II), in: "Plasma Physics and the problem of controlled thermonuclear reactions", (parts of this work were done already in 1951) Vol. I, editor: M. A. Leontovich, Pergamon Press 1961, p. 1-47.
- [133] H.F. Tammen, Thesis University of Utrecht, 1995, p. 109.
- [134] C. P. Tanzi, thesis university of Utrecht 1996, p.2.
- [135] J. L. Terry et al., Rev. Sci. Instrum. 63 (10), October 1992, p.5191-5194.
- [136] TFR Group, Nucl. Fusion, Vol. 27, No. 12 (1987), p. 1975-1999.
- [137] N. L. Vasin et al., Sov. J. Plasma Phys. 12 (2) Feb. 1986, p. 73-77.
- [138] N. L. Vasin et al., Sov. J. Plasma Phys. 10 (6) Nov. 1984, p. 650-654.
- [139] G. C. H. M. Verhaag, Internal Report Rijnhuizen 94/006, may 1994.
- [140] G. Verkerk et al., "Binas, Informatieboek VWO/HAVO voor het onderwijs in de Natuurwetenschappen", published by: Wolters-Noordhoff Groningen, 1992, tabel 17, p.7, ISBN 90 01 89372 4.
- [141] idem, tabel 21 A, p.36.
- [142] P. C. de Vries, Thesis university of Utrecht, 1997, chapter 5.
- [143] A. A. Ware, Physical Review Letters, Vol. 25, No. 1 (1970), p. 15-17.
- [144] A. Weller et al., Phys. Rev. Lett. 59 (20) 1987, p. 2303-2306.
- [145] J. Wesson, "Tokamaks", Clarendon press, Oxford, 1987, chapter 1.4, p.8.
- [146] idem, chapter 1.8, p.16.
- [147] J. Wesson, "Tokamaks", 2nd edition, Clarendon press - Oxford, 1997, Chapter 1.10, p.27.
- [148] idem, chapter 4.2, p.147.
- [149] idem, chapter 4.15, p.187.
- [150] idem, chapter 11.20, p.555.
- [151] idem, chapter 14.5, p.661.
- [152] idem, chapter 14.6, p.663.
- [153] idem, chapter 14.7, p.664.
- [154] G. H. Wolf et al., Transactions of Fusion Technology, vol. 29, (1996), p.17-22 (proc. 2nd Carolus Magnus Summer School on Plasma Physics).
- [155] G. A. Wurden et al., proc. EPS Venice 1989, p. 1561-1564.
- [156] Webster's third new international dictionary, G. & C. Merriam Company, publishers, Springfield, Massachusetts, U.S.A., 1964, "Pellet".
- [157] FOM jaarboek, 1986.
- [158] FOM jaarboek, 1987.



- 
- [159] FOM jaarboek, 1991.
  - [160] JET Joint Undertaking, Progress Report 1997, section “High Fusion Power and High Q in D-T”, p. 114-115.
  - [161] Annual progress report 1991, work in Controlled Thermonuclear Research performed in The Fusion Research Unit under the Contract of association between Euratom and Risø National Laboratory, report: Eur/Risø Steer. Com. 21/4/1.

# Appendix A: Implementation of the model

The diffusion model implemented here is the one dimensional model as was described by eq. 5.12 in section 5.2, using the idea of constant plasma properties on concentric flux surfaces.

The plasma is built up from a small torus with minor radius  $\frac{1}{2}\Delta r$ , with around it n-1 shells added with thickness  $\Delta r$  (see fig 8.1). All volume properties of the plasma are defined at positions r that are a multiple of  $\Delta r$  and all surface properties are defined at positions r that are a multiple of  $\Delta r + \frac{1}{2}\Delta r$ .

So the plasma electron density  $n_e(r, t)$  [ $m^{-3}$ ] and temperature  $T_e(r, t)$  [ $eV$ ], and the particle source function  $S_e(r, t)$  [ $m^{-3}s^{-1}$ ] are defined at  $r = i.\Delta r$  (so in between the circles drawn in Fig. 8.1). The particle flux  $\Gamma_e(r, t)$  [ $m^{-2}s^{-1}$ ] is defined at  $r = (i - \frac{1}{2}).\Delta r$  (so at the circles drawn in Fig. 8.1). Where i is an integer between 0 and n-1. The time coordinate is t [s], which is divided into time steps of  $\Delta t$ .

Some care has to be taken on the implementation at the edge of the plasma. Since outside r=a no plasma is defined in the model, the last shell does not extent from  $r=a-\frac{1}{2}\Delta r$  to  $r=a+\frac{1}{2}\Delta r$  but only from  $r=a-\frac{1}{2}\Delta r$  to  $r=a$ . It also means that this last shell only interacts and only has its fluxes defined at its inner side. The fluxes at  $r=a$  are by definition zero in the model, which defines the edge condition.

In the plasma center this has as an extra advantage that  $v_{pinch}$  is not applied at  $r=0$  but only at  $r=\frac{1}{2}\Delta r$ . This may not seem to be of large importance, but it means that no singularities can arise for non-zero values of  $v_{pinch}$  in the plasma center

In this geometry the differential equation eq. 5.11 can for each plasma volume between two circles be written as:

$$\vec{V}_{cc} \frac{\partial \vec{n}_e(t)}{\partial t} = \vec{O}_c \vec{\Gamma}_e(t + dt) - [\vec{O}_c \vec{\Gamma}_e(t + dt)]_{(shifted\ by\ \Delta r)} + \vec{V}_{cc} \vec{S}_e(t + dt) \quad (8.1)$$

Here  $\vec{O}_c$  is the surface and  $\vec{V}_{cc}$  is the volume of a unit shell.

This is just the equation for particle conservation. The volume of the considered shell times the change in particle density equals the influx and out flux times the inner and outer surface of the shell, added to the source function.

The  $t+dt$  at the right side of the equation defines that we are solving the problem implicitly.

In this form all variables may be considered to be vectors, so this one equation describes all shells in the plasma at once. For this the following definitions are used:

$$\bullet \vec{V}_{cc} = 2\pi^2 R_0 \Delta r^2 \begin{pmatrix} \frac{1}{4} \\ 2 \\ 4 \\ \vdots \\ 2(n-3) \\ 2(n-2) \\ (n-\frac{5}{4}) \end{pmatrix} \text{ the volume of each of the shells}$$

$$\bullet \vec{O}_c = 2\pi^2 R_0 \Delta r \begin{pmatrix} 1 \\ 3 \\ 5 \\ \vdots \\ 2(n-2\frac{1}{2}) \\ 2(n-1\frac{1}{2}) \end{pmatrix} \text{ the surface at the edge of each of the shells.}$$

$$\bullet \vec{n}_e(t) = \begin{pmatrix} n_e(0) \\ n_e(1) \\ n_e(2) \\ \vdots \\ n_e(n-2) \\ n_e(n-1) \end{pmatrix} \text{ the density inside each of the shells.}$$

$$\bullet \vec{S}_e(t) = \begin{pmatrix} S_e(0) \\ S_e(1) \\ S_e(2) \\ \vdots \\ S_e(n-2) \\ S_e(n-1) \end{pmatrix} \text{ the particle source inside each of the shells}$$

$$\bullet \vec{\Gamma}_e(t) = \begin{pmatrix} \Gamma_e(\frac{1}{2}) \\ \Gamma_e(1\frac{1}{2}) \\ \Gamma_e(2\frac{1}{2}) \\ \vdots \\ \Gamma_e(n-2\frac{1}{2}) \\ \Gamma_e(n-1\frac{1}{2}) \end{pmatrix} \text{ the particle flux at the edge of each of the shells}$$

The diffusion equation 5.10 which defines the flux  $\Gamma_e$  in vector form is implemented as follows:

$$\vec{\Gamma}_e = \text{GM} \cdot \vec{n}_e \quad (8.2)$$

Here GM is a matrix:

$$\text{GM} = \begin{pmatrix} \frac{D(\frac{1}{2})}{\Delta r} + \frac{v_p(\frac{1}{2})}{2} & \frac{-D(\frac{1}{2})}{\Delta r} + \frac{v_p(\frac{1}{2})}{2} & 0 & \dots & \dots \\ 0 & \frac{D(\frac{1}{2})}{\Delta r} + \frac{v_p(\frac{1}{2})}{2} & \frac{-D(\frac{1}{2})}{\Delta r} + \frac{v_p(\frac{1}{2})}{2} & \dots & \dots \\ 0 & 0 & \frac{D(\frac{2}{2})}{\Delta r} + \frac{v_p(\frac{2}{2})}{2} & \dots & \dots \\ \dots & \dots & \dots & \dots & \dots \\ \vdots & \vdots & \vdots & \vdots & \vdots \\ \dots & \dots & \dots & \dots & \dots \\ \emptyset & \dots & \frac{-D(n-2\frac{1}{2})}{\Delta r} + \frac{v_p(n-2\frac{1}{2})}{2} & 0 & \dots \\ \dots & \frac{D(n-1\frac{1}{2})}{\Delta r} + \frac{v_p(n-1\frac{1}{2})}{2} & \frac{-D(n-1\frac{1}{2})}{\Delta r} + \frac{v_p(n-1\frac{1}{2})}{2} & \dots & \dots \end{pmatrix} \quad (8.3)$$

defining that the diffusion is just a function of the difference between the densities of two adjacent shells, and the inward pinch a function of the average density of two adjacent shells.

This can be written in a simpler way as:

$$\text{GM} = v_p \cdot \text{MD} - \text{D} \cdot \text{AM} \quad (8.4)$$

in which the matrix MD is used to calculate an average between two adjacent shells:

$$\text{MD} = \frac{1}{2} \cdot \begin{pmatrix} 1 & 1 & 0 & 0 & \dots & \dots \\ 0 & 1 & 1 & 0 & \dots & \dots \\ 0 & 0 & 1 & 1 & \dots & \dots \\ \dots & \dots & \dots & \dots & \dots & \dots \\ \dots & \dots & \dots & \dots & 1 & 1 & 0 & 0 \\ \dots & \dots & \dots & \dots & 0 & 1 & 1 & 0 \\ \dots & \dots & \dots & \dots & 0 & 0 & 1 & 1 \end{pmatrix} \quad (8.5)$$

and the matrix AM to calculate a derivative between two adjacent shells:

$$\text{AM} = \frac{1}{\Delta r} \cdot \begin{pmatrix} -1 & 1 & 0 & 0 & \dots & \dots \\ 0 & -1 & 1 & 0 & \dots & \dots \\ 0 & 0 & -1 & 1 & \dots & \dots \\ \dots & \dots & \dots & \dots & \dots & \dots \\ \dots & \dots & \dots & \dots & -1 & 1 & 0 & 0 \\ \dots & \dots & \dots & \dots & 0 & -1 & 1 & 0 \\ \dots & \dots & \dots & \dots & 0 & 0 & -1 & 1 \end{pmatrix} \quad (8.6)$$

Also a matrix DS can be constructed to combine both  $\vec{O}_c \vec{\Gamma}_e(t+dt)$  and  $\vec{O}_c \vec{\Gamma}_e(t+dt)]_{(shifted\ by\ \Delta r)}$  into one matrix. This DS matrix defines the difference between in- and out flux of a shell:



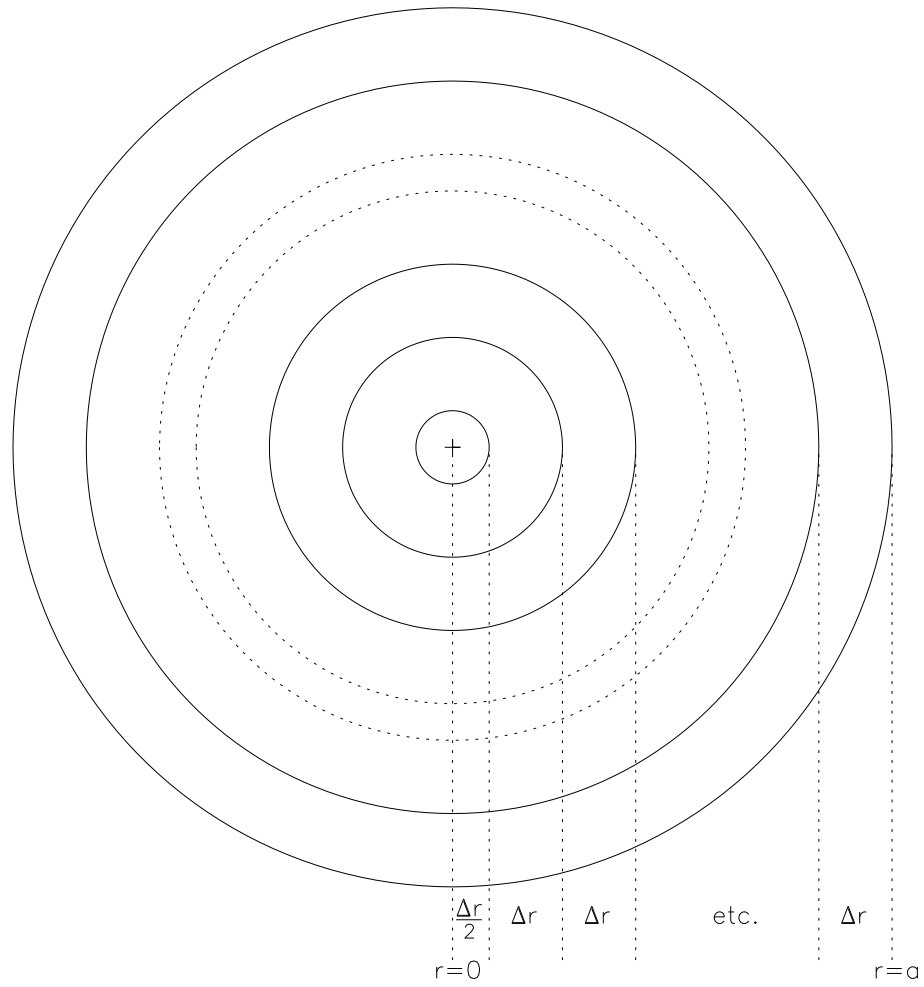


Figure 8.1: Chosen coordinates in a poloidal cross section of the plasma.

# Dankwoord

Werken op Rijnhuizen is iets bijzonders. Het was interessant, vaak moeizaam, maar toch ook erg leerzaam. Vooral de schitterende omgeving en tuin waren regelmatig onontbeerlijk als inspiratiebron. Nu het RTP team al weer anderhalf jaar geen gezamenlijke inspanning meer hoeft te leveren om moeizaam gegevens aan het ongrijpbare plasma te onttrekken besef ik pas hoe goed de samenwerking was binnen die groep.

Graag wil ik dit boekje afsluiten met het bedanken van al die mensen die mijn onderzoek mogelijk hebben gemaakt. Ik kan niet iedereen opsommen die heeft meegewerkt, want dan vergeet ik er ongetwijfeld enkelen, maar toch wil ik er een aantal bij naam noemen.

Allereerst uiteraard mijn directe begeleiders Noud Oomens en Niek Lopes Cardozo. Daarnaast Dick Hogewey, Frans Meijer, Jaap Lok en Rolie Barth die op verschillende onderwerpen in deze studie met mij hebben samengewerkt. Verder al mijn mede OIO's, en in het bijzonder mijn kamergenoten Michiel Peters en Francisco Salzedas. Ook de medewerkers uit de diverse technische afdelingen, in het bijzonder Joop Bode, Peter Wortman, Ad. Agterberg en Ben Grobber. En verder alle anderen die deel hebben uitgemaakt van het RTP-team, en met name Cor Tito, Ogé Kruijt en Bart de Groot.

Verder enkele studenten die ieder op hun manier een waardevolle bijdrage hebben geleverd aan dit werk: Edo Noordermeer, Fabian Akerboom, Maarten Klarenbeek en Gaby van Oyen.

Tot slot dank aan mijn echtgenote Mariska voor haar steun en hulp tijdens dit hele project, en ook bij het proberen duidelijk uit te leggen aan niet ingewijden wat ik nu eigenlijk heb gedaan.

# Curriculum Vitae

Ik<sup>1</sup> ben geboren op 7 oktober 1968 in Gameren (nu gemeente Zaltbommel, destijds gemeente Kerkwijk). Mijn middelbare schoolopleiding (atheneum) heb ik gevolgd aan de scholengemeenschap “Buys Ballot” (tegenwoordig “Cambium”) te Zaltbommel. Na het behalen van mijn VWO diploma in 1987 heb ik experimentele Natuurkunde gestudeerd aan de Rijks Universiteit Utrecht (tegenwoordig Universiteit Utrecht) van 1987 tot en met 1992. Mijn afstudeeronderzoek betrof het bestuderen van roosterafstanden van de atomen in een koperkristal met behulp van ionen verstrooiing. Verder heb ik mij tijdens een kort onderzoek verdiept in de laserkoeling van atomen, wat resulteerde in een baan van 3 maanden aan de Rijks Universiteit Utrecht in het voorjaar van 1993. Daaropvolgend heb ik gedurende 9 maanden mijn militaire dienstplicht vervuld als huzaar 1e klas in het 11e Tankbataljon te Oirschot. Mijn werk daar bestond uit het laden van het kanon van een Leopard 2 tank. Op 1 januari 1995 begon mijn promotie-onderzoek aan het FOM instituut voor plasmafysica Rijnhuizen. Dit onderzoek, zoals beschreven in dit boekje, betrof het op zeer korte tijdschaal bestuderen van de interactie tussen een kogeltje van vast waterstof ijs en een heet tokamak plasma.

---

<sup>1</sup>Joost de Kloe (Jos), geb. 7-10-1968 te Gameren,  
gehuwd 19-12-1997 te Kerkwijk met Maria Louise (Mariska) van Veeren  
zoon van: Antonie de Kloe (geb. 17-2-1940 te Gameren) en Pieterella Naaijen  
kleinzoon van: Joost de Kloe (geb. 23-4-1914 te Gameren) en Mina Cornelia Donker  
achterkleinzoon van: Willem de Kloe (geb. 27-1-1889 te Gameren) en Jenneke van Steenberg  
hij was een zoon van: Joost de Kloe (geb. 25-5-1854 te Andel) en Willemijntje Kraaij  
hij was een zoon van: Jacob de Kloe (geb. 7-9-1824 te Andel) en Leske van Helden  
hij was een zoon van: Joost de Kloe (geb. 12-3-1777 te Giessen) en Wilhelmina Piek  
hij was een zoon van: Joost de Kloe (ged. 26-5-1737 te Andel) en Maaijke van Wijngaarden  
hij was een zoon van: Hardenberg de Kloe (ged. 8-3-1705 te Woudrichem) en zijn 3e vrouw Jenneke Hoeckx  
hij was een zoon van: Joost de Kloe (ged. 30-1-1670 te Delft) en Pellegrina Stael van Holstijn  
hij was een zoon van: Isaac du Cloux/de Kloe (ged.20-4-1642 te Delft) en (Mar)Grietgen Cornelisdr. van Gijssen  
hij was een zoon van: Daniel du Cloux (mogelijk geb. ca. 1623 te Sedan, Frankrijk) en Maria Dalichamp/Dalichang  
Daniel is de oudste bewezen voorvader van de Nederlandse familie de Kloe.